N75-26192

NASA CR 134759

VOLUME I
LIGHTWEIGHT VACUUM JACKET FOR CRYOGENIC INSULATION

FINAL REPORT

By

D. L. Barclay, J. E. Bell, E. W. Brogren & J. W. Straayer

BOEING AEROSPACE COMPANY

Prepared for

NATIONAL AERONAUTICS AND SPACE ADMINISTRATION

NASA Lewis Research Center

CONTRACT NAS3-15848

J. R. Barber, Project Manager

1. Report No.	2. Government Accession No.	3. Recipient's Catalog No.
NASA CR 134759		

4. Title and Subtitle	5. Report Date
LIGHTWEIGHT VACUUM JACKET FOR CRYOGENIC INSULATION	April 1975
	6. Performing Organization Code

7. Author(s)	8. Performing Organization Report No.
D. L. BARCLAY, J. E. BELL, E. W. BROGREN & J. W. STRAAYER	D180-18476-1
	10. Work Unit No.

9. Performing Organization Name and Address	11. Contract or Grant No.
BOEING AEROSPACE COMPANY (A division of The Boeing Company) P.O. Box 3999, Seattle, Washington 98124	NAS3-15848
	13. Type of Report and Period Covered

12. Sponsoring Agency Name and Address	
National Aeronautics & Space Administration Lewis Research Center	Final Contractor Report
	14. Sponsoring Agency Code

15. Supplementary Notes

J. R. BARBER, PROJECT MANAGER

16. Abstract

This program demonstrated the feasibility of producing a lightweight vacuum jacket using state-of-the art technology and materials. Design and analytical studies were made on a full scale, i.e., 4.57 m (15 ft) inside diameter with a volume of 65.1 m^3 (2300 ft. ^{3}), OMS fuel (LH_2) tank. Preliminary design details were completed for the tank assembly which included an optimized vacuum jacket and MLI system. A half scale LH_2 test model was designed and fabricated. A Force/Stiffness (F/S) proof test was conducted on the vacuum jacket. The vacuum jacket designed and fabricated on this program achieved a vacuum leak rate of 1×10^{-5} atmosphere ml of helium per second, sustained approsimately 1500 hours of vacuum pressure and experienced 29 vacuum pressure cycles prior to failure.

17. Key Words (Suggested by Author(s))	18. Distribution Statement
Evacuated MLI System, Vacuum Jacket, Space Shuttle Orbiter OMS Fuel (LH_2) Tank Force/Stiffness (F/S) Proof Test Vacuum Annulus Preconditioning	UNCLASSIFIED-UNLIMITED

19. Security Classif. (of this report)	20. Security Classif. (of this page)	21. No. of Pages	22. Price*
Unclassified	Unclassified		$3.00

* For sale by the National Technical Information Service, Springfield, Virginia 22151

FOREWARD

This report describes a design, fabrication and test program which investigated a lightweight vacuum jacket and the associated evacuated multilayer insulation system for the OMS fuel tank. The work was performed by the Boeing Aerospace Company from June 19, 1972 through November 20, 1974, under Contract NAS3-15848. The work was administered by Mr. J. R. Barber of NASA Lewis Research Center.

Mr. D. K. Zimmerman was the supervisor during the early program stages; Mr. J. W. Straayer during the later stages. Mr. D. L. Barclay was program technical leader. Mr. J. E. Bell performed the structural analysis and directed the F/S proof test. Mr. E. W. Brogren performed the thermal analysis and developed the system evaluation test program and the associated instrumentation plan. Dr. R. E. Jones, originator of the F/S proof test method, assisted in the development of test procedures and interpretation of the data. Mr. E. B. Kinnaman was chairman of the Boeing Aerospace Company's failure evaluation committee.

Other major participants in the program include:

Manufacturing Technology

F. Tipton

R. Nelson

Engineering Laboratories

H. Lenhart - Sandwich Beam Tests

E. M. Balog - F/S Proof Tests

D. McKenney - Vacuum Acquisition

P. Gauthier - Vacuum Acquisition

H. Olden - System Evaluation Test Planning

TABLE OF CONTENTS

TABLE OF CONTENTS (Cont.)

TABLE OF CONTENTS (Cont.)

LIST OF ILLUSTRATIONS

LIST OF ILLUSTRATIONS (Cont.)

LIST OF ILLUSTRATIONS (Cont.)

LIST OF ILLUSTRATIONS (Cont.)

LIST OF ILLUSTRATIONS (Cont.)

LIST OF ILLUSTRATIONS (Cont.)

LIST OF ILLUSTRATIONS (Cont.)

LIST OF ILLUSTRATIONS (Cont.)

LIST OF TABLES

LIST OF TABLES

LIST OF TABLES

1.0 SUMMARY

The objective of this program was to verify the feasibility of producing a lightweight vacuum jacket using state-of-the-art technology and materials. It was established by the work performed on the Contract NAS3-14369 (NASA CR 121105) that an efficient vacuum jacket design was the key element in developing a high performance evacuated multilayer insulation (MLI) system for the Space Shuttle Orbiter OMS fuel (LH_2) tank. The goal for the program reported in this document was to develop an evcuated MLI system which combined maximum performance with minimum weight and provided a constant level of performance for at least 100 flights, each of 30 days duration.

The work completed included (1) design and analytical studies, (2) detail design of a half scale LH_2 test model, (3) fabrication of the half scale LH_2 test model, (4) materials and component testing, and (5) a failure analysis.

A test program to evaluate the thermal performance of the evacuated MLI system was planned but did not commence due to failure of the vacuum jacket during vacuum annulus preconditioning.

The design and analytical studies consisted of the following:

1) Design studies which investigated preliminary detail design of the major elements for the OMS fuel (LH_2) tank.

2) Structural studies which (a) optimized the vacuum jacket sandwich configuration, and (b) analyzed the pressure vessel design and the pressure vessel support system.

3) Thermal studies which (a) predicted the heat flow through the MLI system; (b) established the relationship between heat flow to the pressure vessel interior and pressure rise in the closed pressure vessel; (c) investigated maximum MLI temperatures, MLI lateral

conductivity, and effects on heat leak from three support strap materials; and (d) studies the effects of GH_2 and air leakage and vacuum pump capability upon vacuum annulus pressure, heat flow boil-off and MLI temperatures.

The detail design of the half scale LH_2 test model completed the following:

1) A set of detail drawings for manufacturing the LH_2 test model.

2) Structural analyses which (a) optimized the vacuum jacket sandwich and girth ring configurations; (b) stress checked the pressure vessel support system, and (c) established the Force/Stiffness (F/S) proof test loading requirements for the vacuum jacket.

3) Thermal analyses which (a) predicted heat flow through the MLI system and (b) sized the vent line to meet test objectives and satisfy safety requirements.

The LH_2 test model assembly was fabricated to the requirements specified on the detail design drawings.

Material and component testing investigated the following:

1) Material performance at the required loading and temperature conditions for (a) the vacuum jacket sandwich, (b) the support strap, and (c) the MLI panel.

2) The structural and vacuum integrity of the vacuum jacket and the pressure vessel.

The failure analysis isolated two possible causes of failure and made recommendations for future lightweight vacuum design programs.

The vacuum jacket designed and fabricated on this program achieved a vacuum leak rate of 1×10^{-5} atmospheric ml of helium per second, sustained approximately 1500 hours of vacuum pressure and experienced 29 vacuum pressure cycles prior to failure. These results shown that the lightweight vacuum jacket is within the scope of present day design and fabrication technology.

2.0 INTRODUCTION

The Space Shuttle Orbiter, future reentry space vehicles, hydrogen fueled aircraft, and other hydrogen fueled vehicles all clearly must continue to evaluate the merits of evacuated insulation systems for LH_2 storage. Opportunities for improved vehicle life cycle costs, system simplicity, performance, and weight saving exist when it has been verified that lightweight vacuum jackets can be designed and fabricated to withstand reliably the rigorous cyclic operational requirements of a vehicle such as the Orbiter.

Previous work reported in NASA CR 121105 identified the vacuum jacket as the key element in developing a high performance evacuated MLI system. Aluminum honeycomb sandwich was recommended as the most efficient construction method for low and medium length/diameter L/D tanks. Also, the bonded aluminum gore, vacuum sealing inner face skin was recommended as a cost effective, repetitive manufacturing process to produce vacuum jackets to the contour accuracy and face skin thickness requirements.

The purpose of the program reported herein was to design, fabricate, and test a lightweight evacuated MLI system capable of maintaining vacuum, structural, and thermal integrity throughout repeated temperature and pressure cycles. The main program emphasis was on verifying the feasibility of producing a lightweight vacuum jacket using state-of-the-art technology and materials. The experimental design, fabrication and test program discussed in Volume I of this report addressed itself to this task.

Initial studies developed a near spherical 4.57 m (15 ft) diameter, 65.1m^3 (2300 ft^3) orbital maneuvering system (OMS) fuel (LH_2) tank preliminary design with optimized aluminum honeycomb sandwich construction for the vacuum jacket and an optimized MLI system which included the effects of GH_2 and air leakage on thermal performance. The results from these initial studies were used to design a half scale LH_2 test model which was then fabricated in parallel with a component test program.

This program provided additional data on the successful use of the force/stiffness (F/S) method for predicting the buckling pressure of shells as a valuable tool for achieving minimum weight shells. Techniques were developed to seal vacuum leaks on high temperature use, aluminum honeycomb sandwich, vacuum jacket structure.

Cleaning and preconditioning procedures were established for processing all surfaces exposed to the vacuum annulus. This effort was a precautionary measure to reduce outgassing contamination and thereby reduce the preconditioning time necessary to read the required vac-ion pump stablized vacuum pressure on the LH_2 test model assembly.

Volume II is the appendix for this report and contains:

1) Appendix A - OMS Fuel Tank Preliminary Drawings

2) Appendix B - Modified Theoretical Effective Gas Conductivity

3) Apprndix C - Analytical Thermal Modesl

4) Appendix D - Half Scale LH_2 Test Model Drawings

5) Appendix E - Instrumentation Plan For the LH_2 Test Model

6) Appendix F - System Test Plan For the LH_2 Test Model

3.0 OMS FUEL TANK DESIGN AND ANALYSIS

3.1 DESIGN REQUIREMENTS

The OMS fuel tank was controlled by the criteria outlined below. These criteria were based on the contract work statement and on applicable Space Shuttle design criteria, References 1 and 2. The vibration criteria were estimated.

3.1.1 Life

One hundred operational flight cycles (launch, orbit, reentry and ground turn around).

3.1.2 Time in Orbit

Thirty (30) days.

3.1.3 Thermal Performance

The total propellant boil off losses for the 30 day mission will be limited to a maximum of 10% of the loaded propellant. Thermal protection system will be optimized on a heat flow, weight trade-off basis for a 30 day mission.

3.1.4 Residual Gas Pressure in Multilayer Insulation (MLI)

$6.65\ mN/m^2$ (5×10^{-5} torr)

3.1.5 Propellant Weight

Pressure vessel and support structure design will be based on a propellant weight equal to (pressure vessel internal volume-4% ullage) x fluid density at maximum relief valve pressure setting.

3.1.6 Net Positive Suction Pressure (NPSP)

Engine (NPSP)	=	$13.8 kN/m^2$ (2 psia)
Time Loss	=	$20.7 kN/m^2$ (3 psia)
Total at pressure vessel outlet		$34.5 kN/m^2$ (5 psia)

3.1.7 Loading Conditions

Load Factors

Load factors critical to tank and support structure design are specified in the following table. All load factors except crash are limit values. The crash load factors are ultimate values. The flyback, landing, and crash load factors are applied with the tank carrying 30 percent of its maximum propellant weight. All other load factors are applied with a full propellant load.

LIMIT LOAD FACTORS FOR OMS FUEL TANK

	Longitudinal n (g) x	Lateral n (g) y	Vertical n (g) z
Launch Release	1.5	± 0.25	± 0.25
Max Q & Atmosphere	2.0	± 0.5	± 0.8
Abort			- 0.4
Orbiter Boost	3.0	± 0.2	± 0.6
Reentry	-1.0	± 0.5	- 3.0
Flyback	-0.2	± 1.0	± 2.5
Landing	-1.0	± 0.5	- 3.0
Crash (Ultimate Load)	-9.0	- 1.5	+ 2.0

POSITIVE COORDINATE SYSTEM

3.1.8 Pressure Vessel Supports

The pressure vessel support system will be optimized on a heat flow, weight trade off basis for a 30-day mission.

Factors of Safety

Yield	1.1
Ultimate	1.5

Vibration

Design frequency of loaded pressure vessel on the supports will be 12 cps or higher

3.1.9 Vacuum Jacket

Minimum weight design.

Limit design external pressure = 101.4 k N/m^2 (14.7 psia)

Factor of Safety

Yield	1.1
Ultimate	1.4

3.1.10 Temperature Conditions

Vacuum Shell External Temperature

Ground hold, launch and on-orbit	=	311°K (+100°F)
Reentry	=	450°K (+350°F) maximum

Shuttle Primary Structure Temperature at Tank Support Locations

On-orbit	=	339°K (+150°F)

Minimum Interior Insulation Temperature

20.4°K (-432°F)

3.1.11 Pressure Vessel

Minimum weight design.

Relief Valve Maximum Pressure Setting = 241.3 kN/m^2 (35 psia)

Configuration

4.57 m (15 ft.) inside diameter with a volume of 65.1 m^3 (2300 ft^3)

Design Conditions

Room temperature proof test with membrane stress at 95% yield = 241.3 kN/m^2 (35 psia)

20.5K (-423°F) proof test with membrane stress at 95% of yield = 1.5 x 241 kN/m^2 (35 psia)

3.1.12 Plumbing Lines

Factor of Safety

Proof	=	1.5
Ultimate	=	2.5

Sizes

Fwd	=	63.5 mm (2.5 in) diameter
Vent	=	76.2 mm (3.0 in) diameter

3.2 PRELIMINARY DESIGN

The OMS fuel tank preliminary design (Figure 3.2-1) was developed from the recommended low L/D, LH_2 tank design shown in Figure 3-46, Reference 3. The major differences in the two designs was (1) a longer cylindrical section in the OMS fuel tank due to increased tank volume requirements; (2) Kevlar (PRD)/epoxy, a more efficient material than fiberglass/epoxy was used for the OMS fuel tank pressure vessel support straps; (3) four trunnions were used at the girth ring to attach the OMS fuel tank to the shuttle structure instead of the eight trunnions shown in Figure 3-46, Reference 3. This change also meant sixteen support strap attachment bosses on the OMS fuel tank pressure vessel in place of eight. This change was made in order to minimize the OMS fuel tank attach points to the shuttle, and to spread out support loads over a larger area on the thin membrane pressure vessel; (4) a 0.44 radian (2^{o} 30') conical section was used on the OMS fuel tank vacuum jacket in place of the cylindrical section in order to allow head removal from the layup and bond cure mandrel after completion of vacuum jacket head assembly; and (5) the girth ring and trunnion arrangement was modified for the OMS fuel tank as the design developed in order to simplify manufacturing processes.

3.2.1 Design Features

The drawings in Appendix A describe the OMS fuel tank components in detail.

Pressure Vessel (Figure A-11)

2219-T81 aluminum gores, polar caps, cylindrical section, and fittings made up the pressure vessel weld assembly. Material in the weld area was sized for the "as welded" condition. Testing required for the finished pressure vessel assembly were LN_2 cold shock, hydrostatic pressure tested at room temperature and a helium leak check.

Pressure Vessel Support System (Figure A-13)

Sixteen Kevlar/epoxy (PRD/epoxy) tension straps supported the pressure vessel from four girth rings trunnion fittings. The straps were sized for the shuttle loading conditions discussed in Section 3.1. Turnbuckles attached the support straps to the trunnion fittings, providing assembly adjustment and pre-tensioning.

The pressure vessel was locally reinforced around the support strap attachment boss to distribute the loads into the pressure vessel wall.

Multilayer Insulation System (MLI) (Figures A-3 through A-5)

The multilayer insulation system was comprised of twenty-four inner MLI panel assemblies and twenty-four outer MLI panel assemblies. The inner MLI panel assembly was composed of alternate layers of 0.15 mil aluminized Mylar and Dacron net (B4A) at 2.95 layers per mm (75 layers per in.) to a thickness of 13.97 mm (0.55 in). The outer MLI panel assembly was identical to the inner assembly except that in the outer 2.50 mm (0.10 in) thickness the aluminized Mylar was replaced with 0.30 mil aluminized Kapton, due to high shuttle reentry temperature of 450°K (350°F). At the 2.50 mm (0.10 in) depth calculations showed that the outside aluminized Mylar layer would experience a maximum temperature of less than 294.3°K (250°F), well within the capability of the aluminized Mylar.

The assembly fasteners for the MLI panels are shown in Figures A-13 through A-21 . Experience in fabricating and installing the MLI panels on the LH_2 test model assembly suggests that the same single type of Nylon pin arrangements could be used on the OMS fuel tank MLI panels.

The MLI panels were attached to the pressure vessel and the other panel layer with Velcro hook and pile fasteners. The outer layers of Dacron net (B4A) on adjacent panels were sewn together along the seam.

Vacuum Jacket Heads (Figures A-6 through A-10)

The vacuum jacket was assembled from two vacuum jacket heads. The apex fitting opening was a different size for each head. Other than this difference the heads were the same. Vacuum jacket assembly consisted of bolting the heads together at the girth ring. The mechanical fastening arrangement included attachments to the four trunnion fittings. Vacuum closeout at the girth was by welding the vacuum sealing strip to the girth rings and the trunnion fittings. Welded joints also closed out the vacuum jacket at the apex fittings.

The vacuum jacket heads were a honeycomb sandwich construction. The aluminum 5056/F40-0.0014, 33.64 Kg/m^3 (2.1 lb/ft^3) Flex-Core was a uniform thickness of 35.5 mm (1.40 in). The inner and outer face skins were made up of eight gores each of 2024-T81 aluminum. A continuous basic gage of 0.51 mm (0.020 in) was used for both inner and outer face skins. In the cylindrical area a 0.20 mm (0.008 in) thick foil was bonded to the basic skin to achieve the required thickness (Reference Section 3.3). These reinforcing skins stopped short of the gore joining strips, simplifying this joint. Metlbond 320 adhesive was used to bond the face skins to the core.

Girth Ring (Figures A-12)

The girth ring was designed (1) to provide edge restraint for the vacuum jacket heads, (2) to transfer the pressure vessel support loads to the primary structure support, and (3) as a final closeout for the vacuum annulus.

Plumbing Penetrations (Figure A-2)

Detail II in Figure A-2 describes the vent line penetration arrangement. The vent valve was mounted externally on the pressure vessel inside an enclosure to protect the vacuum annulus from hydrogen leakage. The enclosure was a stainless steel core welded at one end to the stainless steel vent line. At the other end, an aluminum collar was diffusion

bonded to the core, for welding to the pressure vessel. A line from the enclosure vents gas leakage overboard. A conical, sandwich shell closeout 635.0 mm (25.0 in.) long sealed the vacuum jacket with sufficient clearance for vent line insulation.

A conical fiberglass/epoxy collar supported the MIL around the vent valve and line. Fiberglass spacers prevented the radiation shields from shorting across the joint at the intersection of the cone and pressure vessel MLI.

Detail III in Figure A-2 shows the submerged feed line shut-off valve mounted to the manhole cover. A conical sandwich shell access cover similar to the vent line closeout discussed above closed out the vacuum jacket. A double metal seal with venting provision was used on the pressure vessel manhole cover. The vent line between the seals served a dual purpose. It provided a venting path overboard for leakage past the first seal and provides a small ΔP across the outer seal which improved its reliability.

The disc shaped MLI blanket on the manhole cover was installed after assembly of the vacuum jacket to the girth ring. The interface with the pressure vessel MLI blanket was through a staggered circular butt joint. The 635.00 mm (25.0 in.) diameter opening in the vacuum jacket provided adequate access to the MLI joint for fitup. A fiberglass MLI support collar was used around the feedline. Details are similar to the vent line arrangement.

Vacuum Acquisition

Six pumpdown ports are shown in Figure 3.2-1. Three were 101.6 mm (4.0 in.) diameter fabrication pumpdown ports. After the initial pumpdown, these ports would be pinched-off and welded closed. Three other 101.6 mm (4.0 in.) diameter pumpdown ports were provided for vacuum maintainability during service. These ports contained Vac-ion pumps for service operation and an outlet with a vacuum shut-off valve for connection to a ground pumping system.

3.2.1 Estimated Weight

Estimated weight of the OMS fuel tank assembly was

	kg	lb
Vacuum Jacket	550	1211
Pressure Vessel	366	806
MLI	84	185
Support Strap	13.6	30
Plumbing Lines	2.4	5
Total	1016.0	2237

3.2.3 Remaining Uncertainties

Before an OMS fuel tank is committed to fabrication, additional analytical and experimental studies should be undertaken to investigate

1) Whether additional pressure vessel support in the form of sway braces at the inlet and outlet ports would be needed.

2) The effectiveness of the vented double metallic seal arrangement at the manhole cover to meet the H_2 leakage requirements.

3.3 STRUCTURAL ANALYSES

3.3.1 Vacuum Jacket Analyses

OPTRAN Analysis

An OPTRAN (Reference 11) analysis was run on the 2.4 m (94.5 in.) radius vacuum jacket hemispherical head. This radius is to the inner face skin of the sandwich construction for the 65.13 m^3 (2300 ft^3) OMS fuel tank as shown in Figure 3.2-1.

The sandwich construction used in the analysis was 33.64 kg/m^3 (2.1 lb/ft^3), 5056 aluminum Flex-Core with 2024 T3 aluminum alloy face skins. The limit design external pressure of 101.35 kN/m^2 (14.7 psi) with the ultimate factor of safety of 1.4 as specified in Section 3.1 was used. The maximum shell temperature of 450°K (350°F) was used and assumed to be uniform. Weight allowances for fittings and joints were not made. All weights presented included the face skins, core and bonding adhesive. An adhesive weight of 20.34 $\mu kg/m^2$ (0.006 lb/in^2) for each surface was used.

The results of this analysis are shown in Table 3.3-1.

Case 1 used a knockdown factor derived from the sandwich shell test results on one 1.14 m (45.0 in.) diameter head tested on contract NAS 3-14369, (Reference 3). Cases 2, 3 and 4 used knockdown factors derived from Boeing statistical data.

Table 3.3-1 shows that the case 1 shell weights lie in the range of weights between 0.5 and 0.9 probability of not failing based on Boeing statistical data. Since the sandwich construction used on the test head (Reference 3) was similar to the OMS fuel tank vacuum jacket, the case 1 results were used to develop the preliminary design for a detailed BOSOR 3 analysis.

Table 3.3-1: Optimum Designs for OMS Fuel Tank Vacuum Jacket Hemispherical Heads

$T = 450^{o}$ k (350^{o}F)

PULT. = 142.03 kN/m^2 (20.6 psi) EXTERNAL

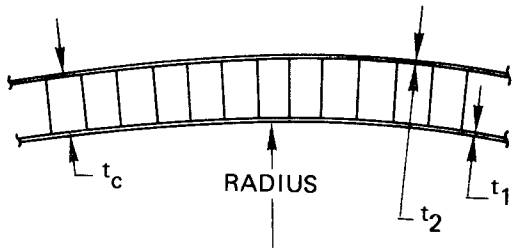

CASE	PROBABILITY OF NOT FAILING	RADIUS		t_1		t_2		t_c		ρ_c		WEIGHT OF 2 HEADS	
		m	in.	mm	in.	mm	in.	mm	in.	kg/m^3	lb/ft^3	kg	lb
1	0.5 [1]	2.40	94.5	0.605	0.0238	0.292	0.0115	19.69	0.775	32.64	2.1	290.62	640.7
2	0.5 [2]	2.40	94.5	0.579	0.0228	0.315	0.0124	14.86	0.585	32.64	2.1	277.74	612.3
3	0.9 [2]	2.40	94.5	0.592	0.0233	0.307	0.0121	22.68	0.893	32.64	2.1	298.87	658.9
4	0.99 [2]	2.40	94.5	0.612	0.0241	0.295	0.0116	34.32	1.351	32.64	2.1	330.40	728.4

[1] KNOCKDOWN FACTOR DERIVED FROM REFERENCE STUDIES

[2] KNOCKDOWN FACTOR FROM BOEING STATISTICAL DATA

Preliminary BOSOR 3 Analysis

The OPTRAN analysis considered the hemispherical head as a separate component which had a simple support at the interface with the adjacent component. The BOSOR 3 stress and buckling analysis, Reference 4, a more comprehensive analytical tool than OPTRAN, considered the interaction of the hemispherical heads with the cylinder and girth ring. Also, this BOSOR 3 analysis included the conical access cover, the vacuum seal stiffener rings and the closeout cone.

The results of the BOSOR 3 analysis of the preliminary vacuum jacket design indicated that:

1) A minimum 2.54 mm (0.100 in) thickness was necessary for the aluminum alloy conical access cover and closeout cone to prevent local buckling of the vacuum jacket. Alternatively, a sandwich construction of equivalent stiffness could be used.

2) The buckling strength of the vacuum jacket preliminary design which used a 0.5 probability of not failing (Case 1 Table 3.3-1) was insufficient to meet the loading condition. Additional stiffness was needed to reinforce the hemisphere to cylinder joint area. Due to the length of the cyclinder section, the stiffening influence of the girth ring was not as effective as was assumed in the OPTRAN analysis.

3) Some sections of the girth as presently designed were overstressed when used with the Case 1 preliminary design.

As a result of the Preliminary BOSOR 3 analysis, three design changes were made. The conical access cover and the closeout cone were changed to sandwich construction, to provide a lightweight design with the required stiffness. The vacuum jacket core thickness was increased from 19.81 mm (0.78 in) to 27.94 mm (1.10 in) to improve the shell bending stiffness. The outer skin thickness of the sandwich was increased over the cylindrical section and on part of the hemisphere to increase the buckling strength.

Stability Analysis

A eigenvalue and an axisymmetric buckling analysis were made for the vacuum jacket. These analyses assumed a 27.94 mm (1.10 in) thick core 450°K (350°F) material properties and used the BOSOR 3 analysis method, Reference 4.

The minimum eigenvalue for the critical external pressure was 533.7 kN/m^2 (77.4 psi) for 10 circumferential waves. The allowable external pressure was calculated using the experimental knockdown factor derived from Reference 3 studies for the BOSOR 3 analysis method. The allowable was calculated as,

$$P_{allowable} = 0.28 \times P_{eigenvalue} = 0.28 \times 533.7 - 148.9 \text{ kN/m}^2 \text{ (21.6 psi)}$$

The Margin of Safety for this mode of buckling was

$$M.S. = \frac{P_{allowable}}{P_{applied}} - 1 = \frac{148.9}{142} - 1 = +0.05$$

The axisymmetric buckling analysis did not assume any circumferential buckles. It did include the axisymmetric displacements due to the applied load. The top half of the jacket had a critical external pressure of 520.6 kN/m^2 (75.5 psi). With the 0.28 knockdown factor, the allowable critical pressure was calculated to be,

$$P_{allowable} = 0.28 \times 520.6 = 145.5 \text{ kN/m}^2 \text{ (21.1 psi) and the}$$

Margin of Safety was calculated to be,

$$M.S. = \frac{P_{allowable}}{P_{applied}} - 1 = \frac{145.5}{142} - 1 = +0.02$$

Both of these analyses indicated that the critical section of the vacuum jacket was the hemisphere to cylinder transition area. A core thickness of at least 27.94 mm (1.10 in) was required to provide the necessary buckling strength.

Stress Analysis

The design of the vacuum jacket assumed that it would be buckling critical. The stress analysis was conducted to determine the material stress and check some of the local modes of failures such as face wrinkling, intercell buckling, and shear crimping for the sandwich shell.

Preliminary calculations showed that the 2024-T81 bare aluminum alloy would be a better face skin material than 2024-T3 for meeting the program goal of a minimum weight vacuum jacket design using state-of-the-art materials. The allowable materials stresses for bare 2024-T81 aluminum alloy were taken from the Boeing Design Manual. The critical material properties are plotted as compression stress-modules curves in Figure 3.3-1. "B-Basis" allowables were selected for the compression yield strength values because it was planned to proof test the vacuum jackets prior to use. The allowable stress for the sandwich face skins was arbitrarily limited to 206.8 MN/m^2 (30 ksi) at 450°K (350°F). This does not constitute a failure criterion; however, it is a practical material limitation for the analysis. Stresses higher than 206.8 MN/m^2 (30 ksi) will decrease the tangent modulus and require a nonlinear analysis. The BOSOR 3 analysis method assumed a constant material modulus and is not valid for material nonlinearity. Therefore, a constant modulus of 6.55 GN/m^2 (9.5 x 10^6 psi) was assumed for the BOSOR 3 stress analysis.

The BOSOR 3 analysis method was used to calculate the in-place loads, N_{10} and N_{20}, and the bending moment loads, M_{10} and M_{20}. From these loads (for 142 kN/m^2 (20.6 psi) external pressure) the material stresses were calculated from the equations.

$$f_{1i} = N_{10}/(t_i + t_o) + M_{10}/(d \times t_i)$$

$$f_{1o} = N_{10}/(t_i + t_o) - M_{10}/(d \times t_o)$$

$$f_{2i} = N_{20}/(t_i + t_o) + M_{20}/(d \times t_i)$$

$$f_{2o} = N_{20}/(t_i + t_o) - M_{20}/(d \times t_o)$$

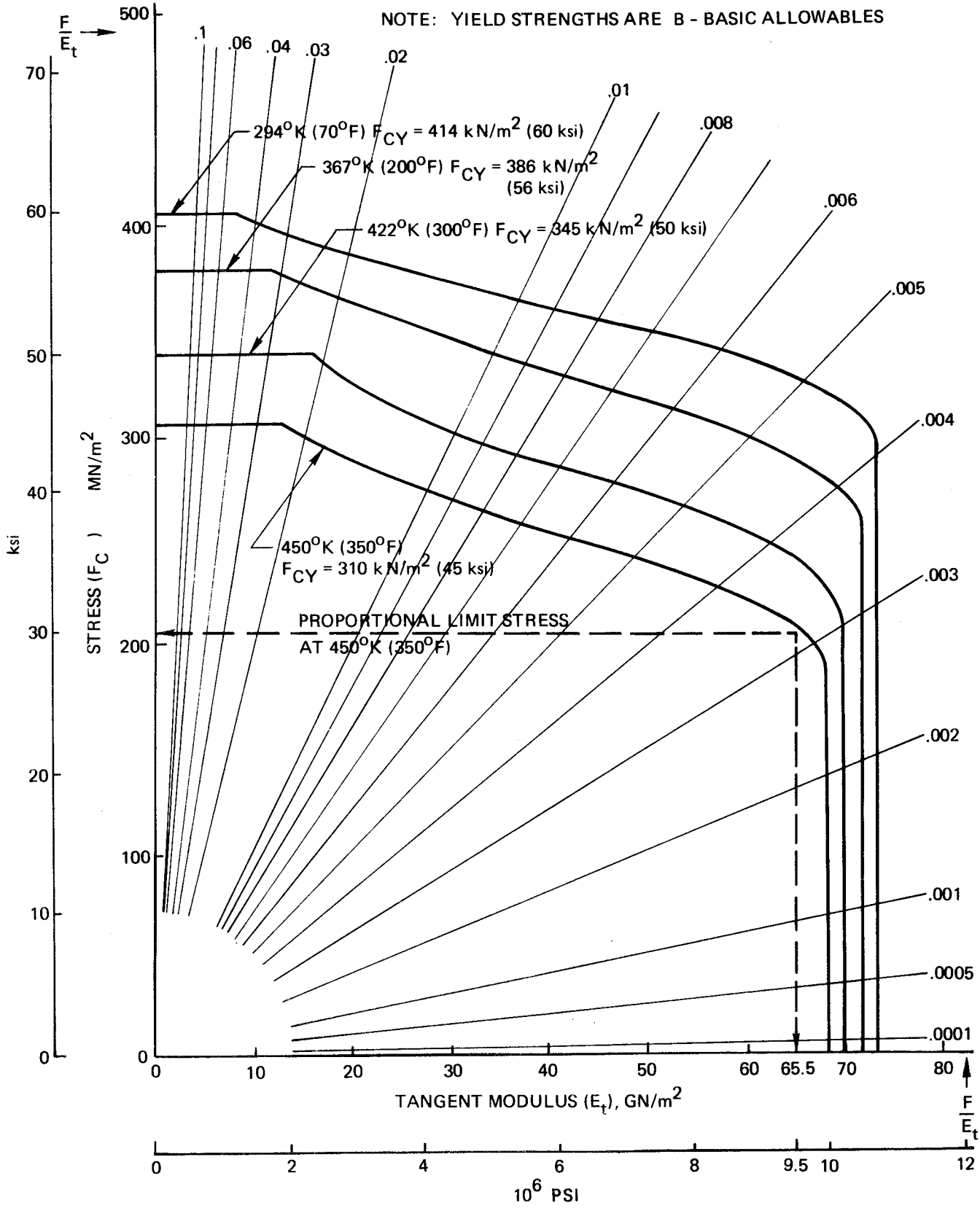

Figure 3.3-1: Stress-Modulus Curve for Bare 2024-T81 Aluminum Alloy

where,

f_{1i} = meridional stress, inner skin

f_{1o} = meridional stress, outer skin

f_{2i} = circumferential stress, inner skin

f_{2c} = circumferential stress, outer skin

and $d = t_o + \frac{1}{2} t_i + \frac{1}{2} t_o$.

Figure 3.3-2 shows the positive sense of the N_{10}, N_{20}, M_{10} and M_{20} loads plus the thickness dimensions t_i, t_o, and t_c for a sandwich section. For thin face skins on a thick core

t_c d.

and the core thickness was used to calculate the face skin stresses.

The stress analysis revealed that the face skin stresses for the 27.9 mm (1.10 in) thick core design would exceed the 206.8 MN/m^2 (30 ksi) limitation. This was a result of the bending stresses due to the M_{10} and M_{20} loads. To alleviate this condition, the core depth t_c, was increased to 35.5 mm (1.40 in) and the stress analysis was repeated several times to find a good combination of face gages that did not exceed the 206.8 MN/m^2 (30 ksi) allowable stress. In the process three other changes were incorporated in the analysis:

1) The new girth ring design properties were used,

2) The core thickness of the conical access cover was increased to 35.56 mm (1.40 in) and,

3) The core thickness of the closeout cone was increased to 12.7 mm (0.50 in).

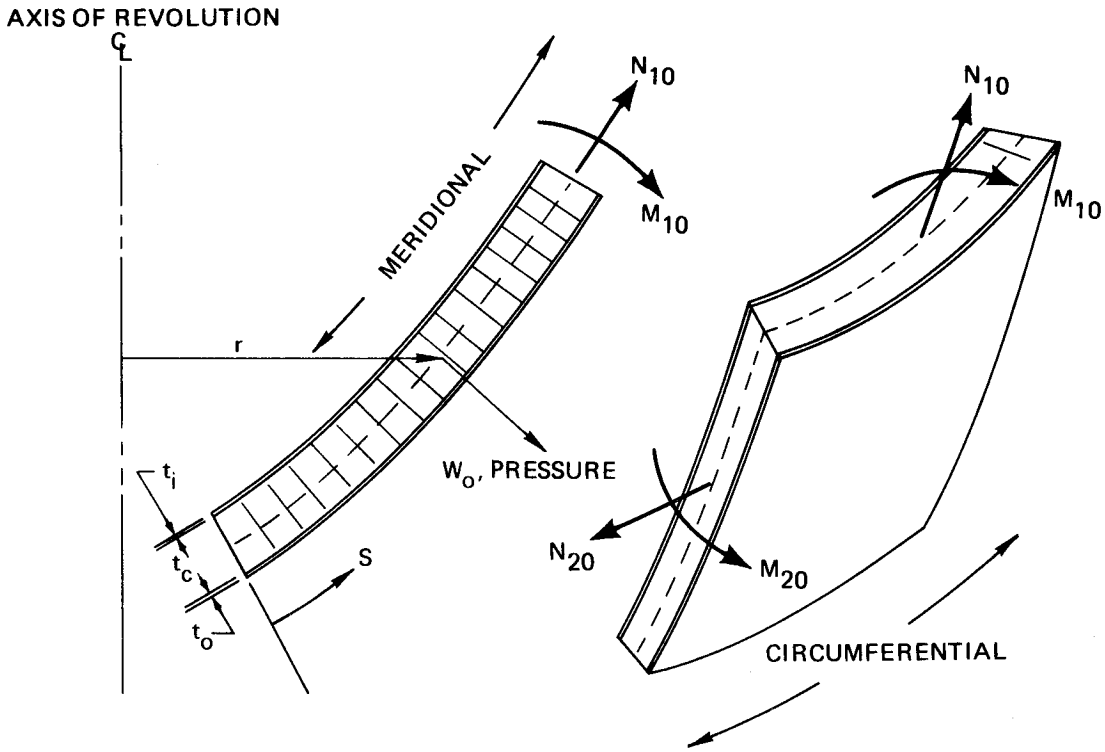

Figure 3.3-2: Sandwich Shell Element with Positive Displacements and Forces for BOSOR3

The final analysis loads, the face skin gages and core thicknesses, and the minimum Margin of Safety for the ultimate load condition at 450°K (350°F) are tabulated in Table 3.3-2. The segment numbers refer to the analysis sections used in the BOSOR 3 analysis method. Location of the segments on the vacuum jacket is shown schematically in Figure 3.3-3. Segment ② is the conical access cover Segment ⑮ is the closeout cone. Segments ① and ⑯ were used as closeouts for the fill and vent lines and were not included in the stress analysis. The girth ring was located between segments ⑧ and ⑨.

The nominal stresses in the vacuum jacket will be about 71 percent of the maximum stresses shown in Table 3.3-2 or about 137.9 MN/m^2 (20 ksi) aluminum stress. No significant creep is expected at this stress level over the life of the vacuum jacket at ambient temperatures.

Intracell Buckling

The allowable intracell buckling stress was calculated using the equation from Boeing Design Manual, Section 253.6,

$$\frac{F_{cr}}{E_t} = \frac{k\pi^2}{12\,(1 - \nu^2)}\left(\frac{+}{S}\right)^2$$

where

k = 2 for biaxial compression stresses

E_t = Tangent Modulus

ν = Poisson's ratio

t = Face skin gage

S = Honeycomb cell size

Table 3.3-2a: BOSOR3 Stress Analysis of Vacuum Jacket Design for OMS Fuel Tank

SEGMENT NO.	SEGMENT LENGTH (mm)	BOSOR3 ANALYSIS LOADS				FACE SKIN GAGES AND CORE DEPTH			MAXIMUM STRESS (MN/M^2)	MINIMUM MARGIN - OF - SAFETY [1]
		N_{10} (kN/m)	N_{20} (kN/m)	M_{10} (N)	M_{20} (N)	t_i (mm)	t_o (mm)	t_o (mm)		
2	498	-48.0	-133.6	+2388.6	+836.0	0.51	0.51	35.5	-180.0	+0.14
3	409	-173.0	-174.1	-204.6	0	0.51	0.51		-180.6	+0.14
4	2342	-171.6	-170.4	-89.0	-31.1	0.46	0.46		-193.0	+0.07
5	526	-171.6	-176.5	-137.9	-48.9	0.51	0.51		-191.7	+0.08
6	203	-171.8	-250.0	+903.0	+298.0	0.69	0.69		-194.4	+0.06
7	254	-171.8	-248.0	+974.2	+320.3	0.69	0.69		-193.7	+0.06
8	203	-172.0	-163.2	-1556.9	-511.6	0.69	0.69		-189.6	+0.09
9	203	-172.0	-163.2	-1556.9	-511.6	0.69	0.69		-189.6	+0.09
10	254	-171.8	-247.5	+965.3	+320.3	0.69	0.69		-193.7	+0.06
11	203	-171.8	-249.2	+898.5	+293.6	0.69	0.69		-194.4	+0.06
12	526	-171.6	-178.1	-182.4	-62.3	0.51	0.51		-179.3	+0.15
13	2342	-171.5	-171.6	-89.0	-26.7	0.46	0.46		-193.1	+0.07
14	602	-162.2	-160.4	+680.6	-564.9	0.51	0.51	35.5	-197.9	+0.04
15	635	-11.0	-107.9	-115.7	-48.9	0.46	0.46	12.7	-126.9	+0.63

[1] BASED ON AN ALLOWABLE STRESS OF 206.8 MN/m^2

Table 3.3-2b: BOSOR3 Stress Analysis of Vacuum Jacket Design for OMS Fuel Tank

SEGMENT NO.	SEGMENT LENGTH (in.)	BOSOR3 ANALYSIS LOADS:				FACE SKIN GAGES AND CORE DEPTH:			MAXIMUM STRESS (ksi)	MINIMUM MARGIN-OF-SAFETY [1]
		N_{10} (lb/in.)	N_{20} (lb/in.)	M_{10} (lb)	M_{20} (lb)	t_i (in.)	t_o (in.)	t_c (in.)		
2	11.6	-274	-763	+537	+188	0.020	0.020	1.40	-26.1	+0.14
3	16.1	-988	-994	-46	0	0.020	0.020	1.40	-26.2	+0.14
4	92.2	-980	-973	-20	-7	0.018	0.018	1.40	-28.0	+0.07
5	20.7	-980	-1008	-31	-11	0.020	0.020	1.40	-27.8	+0.08
6	8.0	-981	-1427	+203	+67	0.027	0.027	1.40	-28.2	+0.06
7	10.0	-981	-1416	+219	+72	0.027	0.027	1.40	-28.1	+0.06
8	8.0	-982	-932	-350	-115	0.027	0.027	1.40	-27.5	+0.09
9	8.0	-982	-931	-350	-115	0.027	0.027	1.40	-27.5	+0.09
10	10.0	-981	-1413	+217	+72	0.027	0.027	1.40	-28.1	+0.06
11	8.0	-981	-1423	+201	+66	0.027	0.027	1.40	-28.2	+0.06
12	20.7	-980	-1017	-41	-14	0.020	0.020	1.40	-26.0	+0.15
13	12.2	-979	-980	-20	-6	0.018	0.018	1.40	-28.0	+0.07
14	23.7	-926	-916	+153	-127	0.020	0.020	1.40	-28.7	+0.04
15	25.0	-63	-616	-26	-11	0.018	0.018	0.500	-18.4	+0.63

[1] BASED ON AN ALLOWABLE STRESS OF 30 ksi

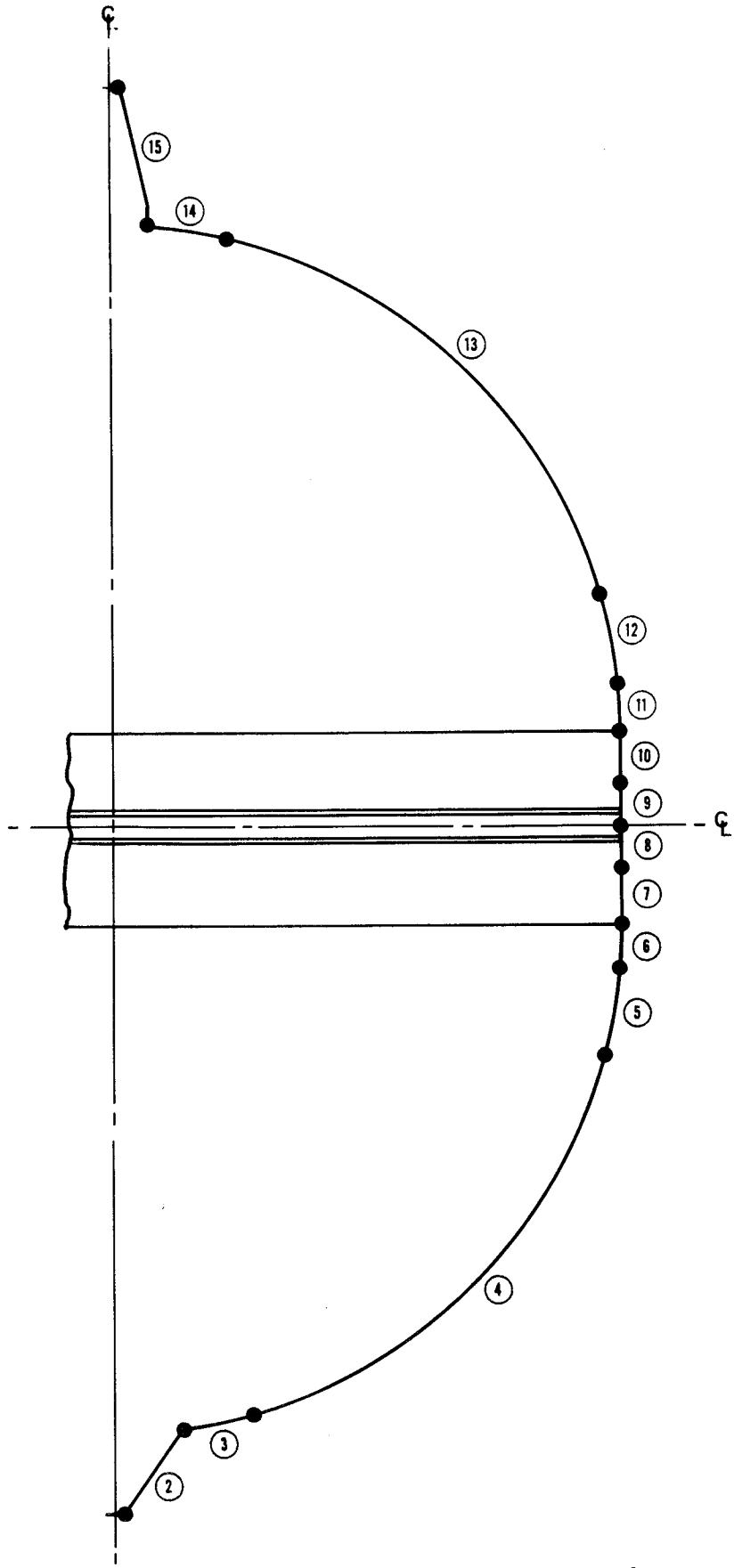

Figure 3.3-3: Segments for BOSOR 3 Analysis of Vacuum Jacket Design for OMS Fuel Tank

With

$k = 2$

$v = 0.3$

$t = 0.46$ mm (0.018 in)

$S = 0.300$

$\frac{F_{cr}}{E_t} = 0.0065$

Using this value with the aluminum alloy 2024-T81 stress-modulus curve shown in Figure 3.3-1, the critical intracell buckling stress, including material nonlinearity is 258.6 kN/m^2 (37.5 ksi). This provided a minimum margin of safety against intracell buckling at least,

$$M.S. = \frac{258.6}{193.1 \text{ (see Table 3.3-2)}} - 1 = +0.34$$

The 0.51 mm (0.020 in) and 0.69 mm (0.027 in.) face skin gages would have larger positive margins.

Face Wrinkling

The face wrinkling mode of failure is a possibility for the vacuum jacket; however, there are no representative data for this design. According to the Boeing Design Manual, Section 253.7,

> "Wrinkling is not considered a critical mode of failure for aluminum faced sandwich at room temperatures. The strength of adhesives available for these applications preclude this type of failure as does core strength for practical densities. When elevated temperature exposure is required, wrinkling becomes an important failure mode due to the lower strength

of the adhesive at elevated temperature. When high temperature adhesives are used they present a potential wrinkling problem at room temperature due to their usually lower strength and inherent brittleness.

If it appears likely that wrinkling will occur at or near the design load, the core density and/or the face gage should be increased."

The Boeing analysis method is based on a semi-empirical parametric analysis of representative test data. Since there are no data, an estimate of the face wrinkling potential for failure was made using the OPTRAN analysis equations. These equations are for a thick core sandwich with thin faces. They assumed that the wrinkling will be confined to a core depth of "w" where,

$$w = 0.72\ t\ (E_t E_c / G_c^2)^{1/3}$$

and

t = face skin gage

E_t = Face skin modulus in compression

E_c = Core modulus in compression

G_c = Core modulus in shear

for 33.64 kg/m^3 (2.1 lb/ft^3) Flex-Core at 450°K (350°F)

E_c = 224.1 MN/m^2 (32,500 psi)

and

G_c = 47.6 MN/m^2 (6900 psi)

With

t = 0.46 mm (0.018 in) and E_t = 6.55 GN/m^2 (9.5 x 10^6 psi)

w = 6.15 mm (0.242 in) which is less than half the core depth.

This indicated that only 6.1 mm (0.24 in) of core will be involved with the wrinkling mode. For th thicker face skins such as t = 0.69 mm (0.027 in), w = 9.5 mm (0.374 in). It was also less than half the core depth.

The equation for uniaxial compression, face wrinkling of this type was

$$F_{wr} = \frac{0.96\ (E_t E_c G_c/\lambda)^{1/3}}{1 + E_c A_o / (w \times F_c}$$

where

λ = 1 - v

A_o = 1.23 x F_c x w/E_c

F_c = The flatness strength of the core or core-to-face bond strength.

Assuming v = 0.3 and F_c = 889.4 kN/m^2 (129 psi) for 33.64 kg/m^3 (2.1 lb/ft^3) Flex-Core at 450°K (350°F) with 2024-T81 aluminum alloy faces

λ = 0.7

and

A_o = 0.001.

Using half of the uniaxial allowable stress as the biaxial allowable stress,

F_{wr} = 235.8 MN/m^2 (34.2 ksi)

which exceeds the 206.8 MN/m^2 (30 ksi) allowable stress assumed in the stress analysis. The allowable wrinkling stress for the 0.69 mm (0.027 in) sections was more than 234.4 MN/m^2 (34 ksi) and therefore, not critical. This analysis for wrinkling allowable stress is based on several assumptions and should be verified experimentally before the final OMS fuel tank design is released for fabrication.

Shear Crimping

The shear crimping mode of failure is a limiting case for general instability which is determined by the shear modulus of the core. The uniaxial allowable stress in the Boeing Design Manual, Section 253.8 was calculated by the equation,

$$F_{sc} = \frac{0.75d^2}{2t \times t_c} G_c$$

where d is the distance between the center of the face skins. For thin face skins on thick cores such as the vacuum jacket d is practically equal to t_c and the equation can be simplified to

$$F_{sc} = \frac{0.75\ t_c\ Gc}{2t}$$

For 33.64 kg/m^3 (2.1 lb/ft^3) Flex-Core, G_c = 47.MN/m^2 (6900 psi) and F_{sc} is much greater than the 206.8 MN/m^2 (30 ksi) allowable stress assumed in the stress analysis. Therefore, shear crimping was not critical.

Discussion of the Stress Analysis Results

Based on an allowable material stress of 206.8 MN/m^3 (30 ksi) "B-Basis" allowable proportional limit stress for aluminum alloy 2024-T81 at 450°K (350°F), the required core depth was increased to 35.56 mm (1.40 in) and some of the face skin gages were changed from the preliminary design used for the stability analysis. Since the thicker sandwich had more stiffness,

it can be assumed that the buckling strength is also increased and, therefore, adequate. The local modes of sandwich failure were checked and none were critical. There is a possibility of face wrinkling becoming a critical failure mode; however, there are no data to confirm this. Since the wrinkling allowables require test data, it is recommended that face wrinkling specimens be tested before the OMS fuel tank design is released for fabrication.

Vibration Analysis

The 27.94 mm (1.10 in) thick core preliminary vacuum jacket design was analyzed for minimum vibration frequency using the BOSOR 3 analysis method. The shell was prestressed by applying the external atmospheric pressure. Several mode shapes were investigated. The minimum frequency was 114 Hertz for 2 circumferential waves. This was about an order of magnitude better than the design requirement of 12 Hertz. Figure 3.3-4 is a plot of frequency versus wave number. Figure 3.3-5 is a plot of the minimum frequency mode shape normalized to a maximum displacement of 1 unit. Evidently the mass and the stiffness of the girth ring determine the minimum frequency.

An analysis of the vacuum jacket without the ring indicated that the vacuum jacket's minimum frequency was 130 Hertz. Therefore, increasing the core depth to 35.56 mm (1.40 in) should increase the minimum frequency but not significantly since the ring (a concentrated mass) determines the minimum vacuum jacket frequency.

Girth Ring Analysis

The girth ring assembly consisted of three sub-assembly rings bolted together with two structural cover plates. Vacuum sealing was accomplished by welding an outer sheet over the girth ring assembly. The material selected for the girth ring was aluminum alloy 2219-T62, heat treated and aged after welding. The vacuum sealing weld cannot be heat treated and aged. It was assumed to remain in the post weld condition. The integrity of the weld is necessary to maintain the strength of the girth ring. The material properties for 2219-T62 aluminum alloy are listed in Table 3.3-3. They were taken from the Boeing Design Manual.

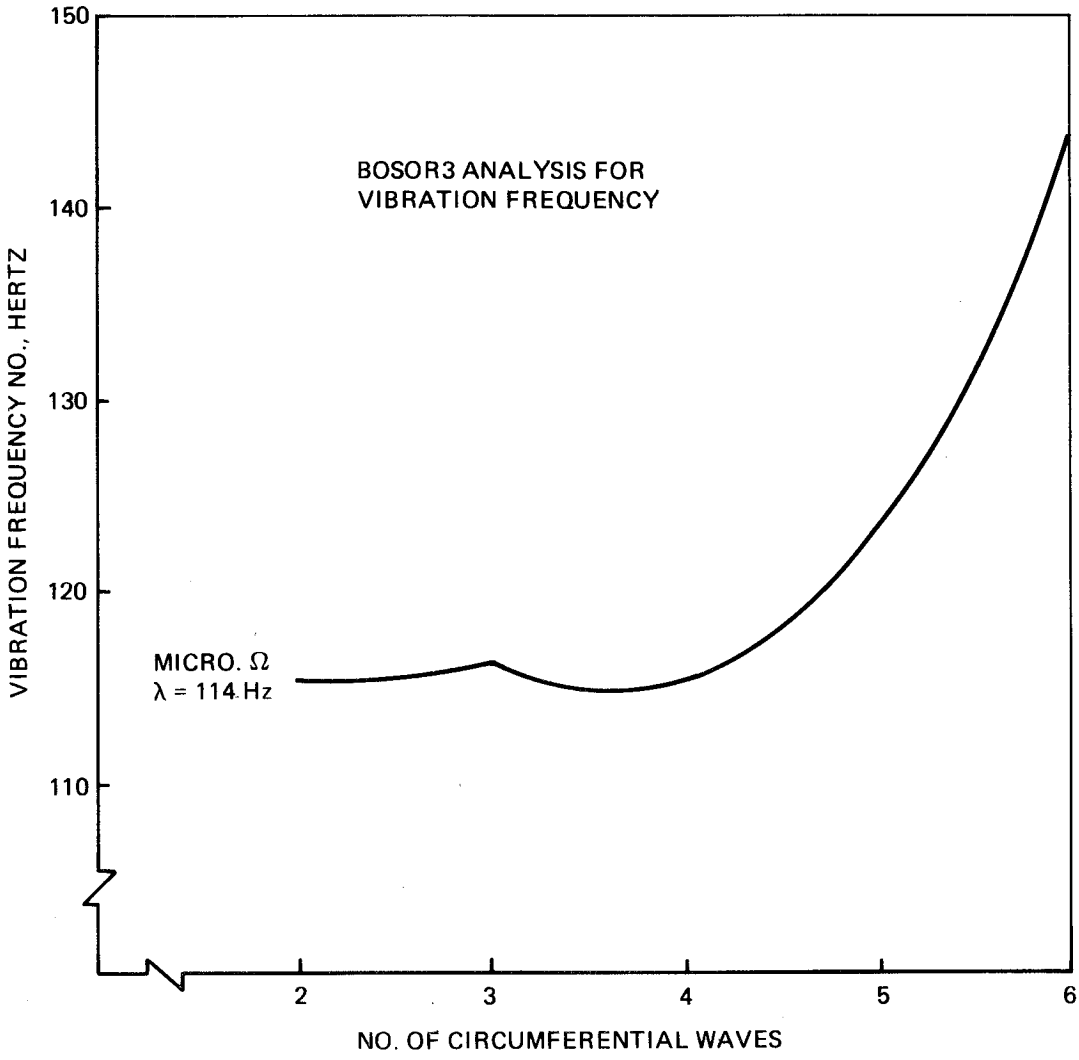

Figure 3.3-4: Vibration Frequency Versus Number of Circumferential Waves for OMS Fuel Tank Vacuum Jacket Design

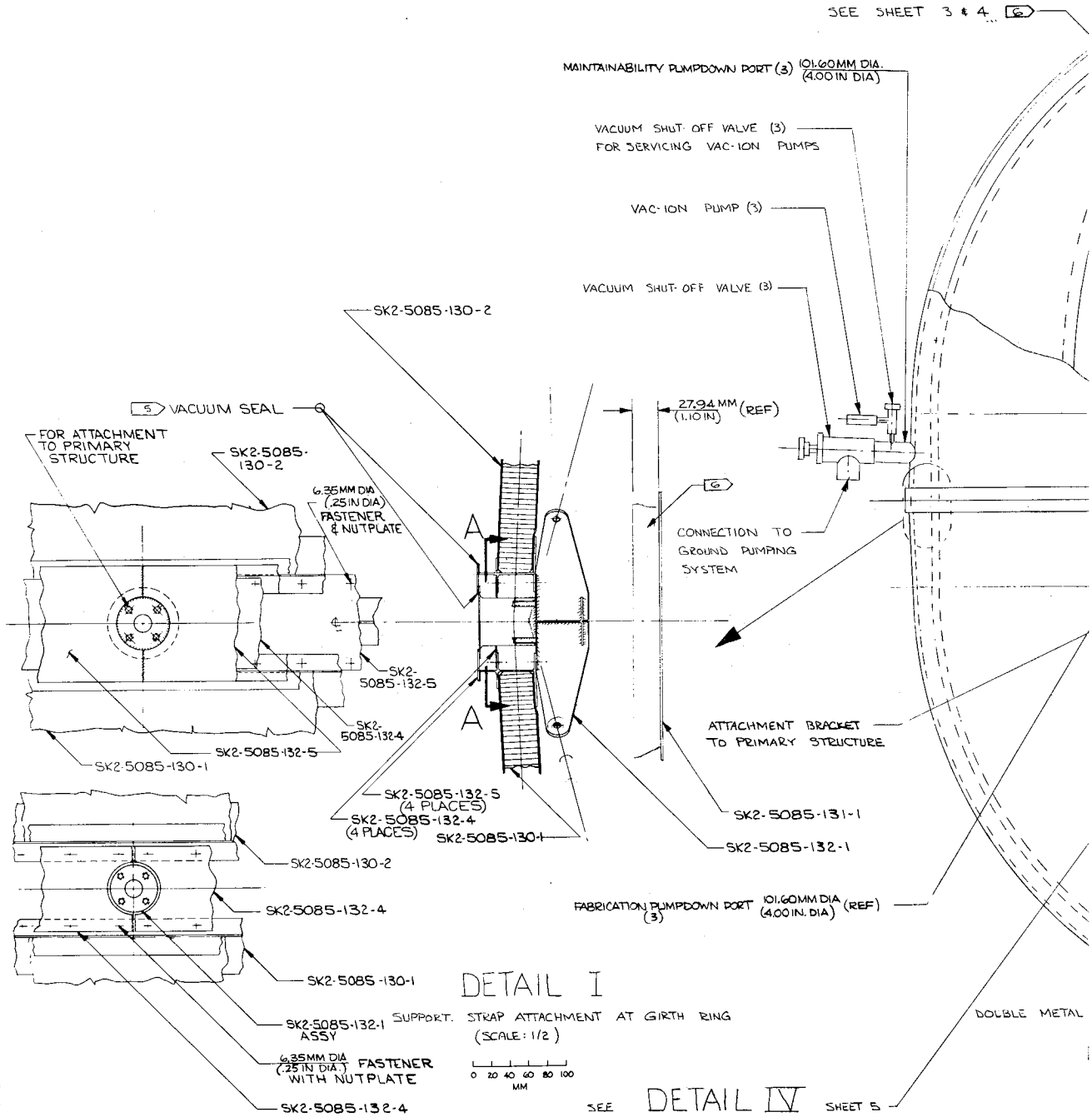
SEE SHEET 3 & 4 6
MAINTAINABILITY PUMPDOWN PORT (3) 101.60MM DIA. (4.00 IN DIA)
VACUUM SHUT-OFF VALVE (3) FOR SERVICING VAC-ION PUMPS
VAC-ION PUMP (3)
VACUUM SHUT-OFF VALVE (3)
SK2-5085-130-2
5 VACUUM SEAL
FOR ATTACHMENT TO PRIMARY STRUCTURE
SK2-5085-130-2
6.35MM DIA (.25 IN DIA) FASTENER & NUTPLATE
27.94 MM (1.10 IN) (REF)
6
CONNECTION TO GROUND PUMPING SYSTEM
A
A
SK2-5085-132-5
SK2-5085-132-4
SK2-5085-132-5
SK2-5085-130-1
SK2-5085-132-5 (4 PLACES)
SK2-5085-132-4 (4 PLACES)
SK2-5085-130-1
ATTACHMENT BRACKET TO PRIMARY STRUCTURE
SK2-5085-131-1
SK2-5085-132-1
SK2-5085-130-2
SK2-5085-132-4
SK2-5085-130-1
SK2-5085-132-1 ASSY
6.35MM DIA (.25 IN DIA.) FASTENER WITH NUTPLATE
SK2-5085-132-4
FABRICATION PUMPDOWN PORT (3) 101.60MM DIA (4.00 IN. DIA) (REF)
DETAIL I
SUPPORT. STRAP ATTACHMENT AT GIRTH RING
(SCALE: 1/2)
0 20 40 60 80 100
MM
SEE DETAIL IV SHEET 5
DOUBLE METAL
HELIUM LINE SHUT-OFF VALVE
SECTION A-A
(SCALE: 1/2)
0 20 40 60 80 100
MM

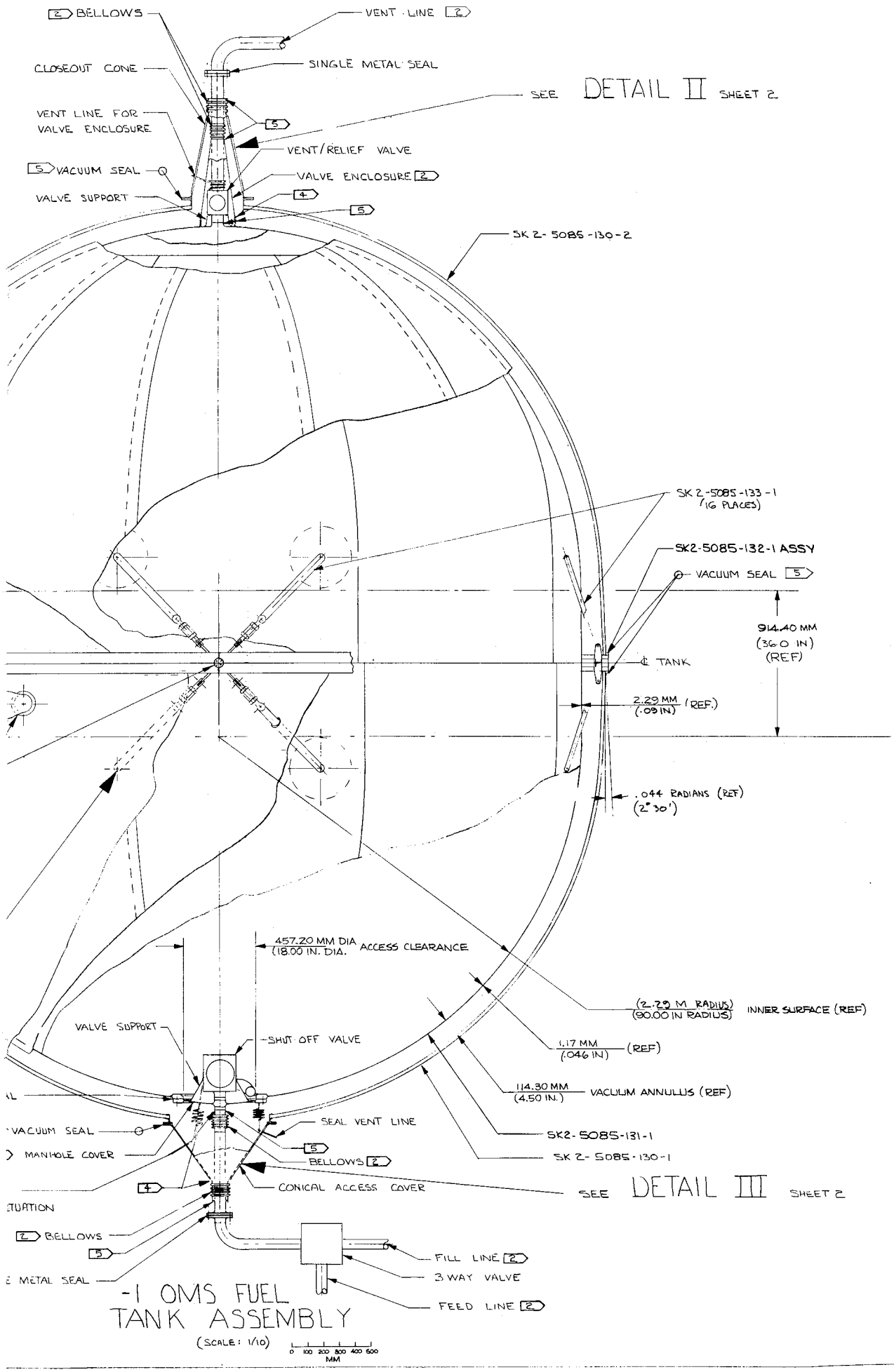

-1 OMS FUEL TANK ASSEMBLY

(SCALE: 1/10)

REVISIONS	
9/11/72	10/10/72
11/10/72	12/10/72
1/10/73	

ASSEMBLY AND QUALIFICATION PROCEDURES

1.0 DETAILS AND SUBASSEMBLIES
- a) PRESSURE VESSEL WELD ASSEMBLY. LN_2 COLD SHOCK, PROOF PRESSURE TEST AND HELIUM LEAK CHECK
- b) SUPPORT STRAP DETAILS
- c) GIRTH RING WELD ASSEMBLY AND MACHINING
- d) VACUUM JACKET SUBASSEMBLIES
- e) MLI BLANKET SUBASSEMBLIES
- f) MANHOLE COVER ASSEMBLY (COVER, SHUT-OFF VALVE, AND FEED LINE)

2.0 ASSEMBLE PRESSURE VESSEL, SUPPORT STRAPS, GIRTH RING, VENT LINE, AND VENT RELIEF VALVE.

3.0 INSTALL MLI BLANKET ON PRESSURE VESSEL. INSULATE SUPPORT STRAPS AND VENT LINE.

4.0 INSTALL VACUUM JACKET SUBASSEMBLIES. SEAL JOINTS AT GIRTH RING AND VENT LINE OUTLET FOR VACUUM.

5.0 INSTALL MANHOLE COVER, FEED LINE, AND SEAL VENT LINE. INSULATE THE AREA. INSTALL VACUUM JACKET COVER. SEAL JACKET COVER AND FEED LINE OUTLET FOR VACUUM.

6.0 HELIUM LEAK CHECK ASSEMBLY. REPAIR AS NECESSARY. PUMPDOWN VACUUM ANNULUS TO 5×10^{-5} TORR. CONDUCT VACUUM DECAY TEST. PRECONDITION WITH HEAT AND VACUUM PUMPING AS NECESSARY TO REACH REQUIRE DECAY RATE. PINCH OFF AND SEAL THE THREE FABRICATION · PUMPDOWN PORTS. CLOSE VACUUM VALVES ON THE MAINTAINABILITY PUMPDOWN PORTS.

7.0 CONDUCT BOIL-OFF TEST.

NOTES

[1] ALUMINUM ALLOY 2219 -T81

[2] STAINLESS STEEL

[4] DIFFUSION BOND

[5] WELD

[6] MULTI LAYER INSULATION (MLI)
- a) ALUMINIZED MYLAR (.15 MIL)/ DACRON NET (B4A) - 2.95 LAYERS/MM (75 LAYERS/INCH)
- b) OUTER 2.54 MM (.10 IN) LAYER - ALUMINIZED KAPTON (0.30 MIL)/DACRON NET (B4A) ~ 2.95 LAYERS/MM (75 LAYER/INCH)

[7] HOOK & PILE FASTENER - VELCRO OR EQUIVALENT

[8] DACRON THREAD

[9] ZYTEL 103 HS1-L NYLON RESIN

Figure 3.2-1

NAS 3-15848
DL TSRECLAY 7/25/72

OMS FUEL TANK ASSEMBLY
81205 SK 2-5085-129

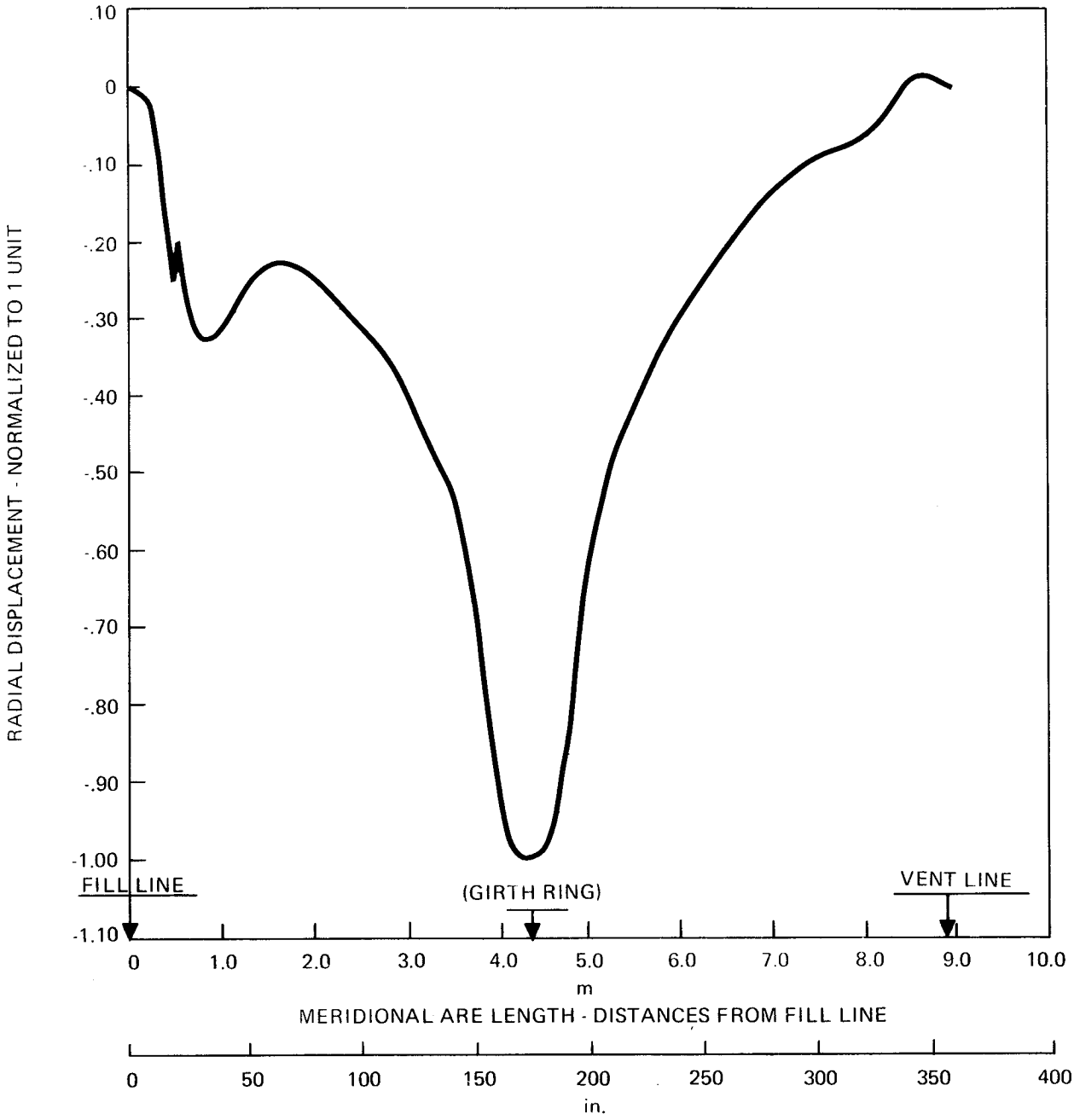

Figure 3.3-5: Vibration Mode Shape for 2 Circumferential Waves Vacuum Jacket Design - OMS Fuel Tank

The loads on the girth ring were calculated by the BOSOR 3 analysis method (Reference 4) to be:

P_{circ} = -93.4 kN (-20,840 lb)
N_{10} = -172 kN/m (-982 lb/in)
N_{20} = -160 kN/m (-931 lb/in)
M_{10} = -1560 N.m/m (-350 in-lb/in)
M_{20} = -512 N.m/m (-115 in-lb/in)

N_{10} and M_{10} are the meridional loads and P_{circ}, N_{20}, and M_{20} are the circumferential loads. The ring is biaxially stressed by these loads acting simultaneously.

The ring section properties used in the stress analysis were:

E_{ring} = 65.5 GN/m^2 (9.5 x 10^6 psi)

A_{ring} = 1626 mm^2 (2.52 in^2)

I_x = 3.07 μm^4 (7.38 in^4)

I_y = 1.36 μm^4 (3.27 in^4)

I_{xy} = 0 (o)

GJ = 55.8 GN/m^2 (8.09 x 10^6 psi)

e = +0.76 mm (0.03 in) inward from the elastic center of the sandwich shell at the girth

The 450°K (350°F) material properties were used since the critical stress condition occurs with ambient air pressure after the shuttle lands and the maximum structural temperature is assumed to be 450°K (350°F).

Table 3.3-3: Material Properties for Aluminum Alloy 2219-T62

PROPERTY	CONDITION				
	EXTRUSION 2219-T62 ALUMINUM ALLOY	BARE SHEET 2219-T62 ALUMINUM ALLOY		BUTT WELDS 2219 ALUMINUM ALLOY, SOLUTION TREATED AND AGED AFTER WELDING TO T62	
	294°K (70°F)	294°K (70°F)	450°K (350°F)	294°K (70°F)	450°K (350°F)
F_{tu}, MN/m^2 (ksi)	358.53 344.74 (52) (50)	372.32 (54)	264.76 (38.4)	282.69 (41)	193.05 (28)
F_{ty}, MN/m^2 (ksi)	220.63 206.84 (32) (30)	248.21 (36)	175.13 (25.4)	203.40 (29.5)	148.93 (21.6)
F_{cy}, MN/m^2 (ksi)	227.53 213.74 (33) (31)	262.00 (38)	186.16 (27)		
F_{su}, MN/m^2 (ksi)	206.84 (30)	220.63 (32)	156.51 (22.7)		
F_{bru}, MN/m^2 (ksi) 1.5 e/D	524.00 (76)	558.48 (81)	396.45 (57.5)		
F_{bry}, MN/m^2 (ksi) 1.5 e/D	344.74 (50)	399.90 (58)	283.38 (41.1)		
E, GN/m^2 (10^6 psi)		72.40 (10.5)	65.50 (9.5)		
E_c, GN/m^2 (10^6 psi)		74.46 (10.8)	67.43 (9.78)		
G, GN/m^2 (10^6 psi)		27.58 (4.0)	24.96 (3.62)		
u, ELASTIC		0.33	0.33		

Figure 3.3-6 is a sketch of the meridional loads acting on a half section of the girth ring. The combined N_{10} and M_{10} loads were resolved into equivalent line loads of 45.4 kN/m (259 lb/in) and 126.6 kN/m (723 lb/in). The 126.6 kN/m (723 lb/in) load was critical. The maximum stress at point ① in Figure 3.3-6 was

$$f = N/t - -126.6/.00069 = -184.9 \text{ MN/m}^2 \text{ (-26.800 ksi)}$$

The allowable stress in the sandwich skin was 206.8 MN/m^2 (30 ksi) and the minimum margin of safety was,

$$M.S. = \frac{206.8}{184.9} - 1 = +0.12$$

At point ② in Figure 3.3-6 the adhesive bonded lap joint must transfer 126.6 kN/m (723 lb/in). (The intended adhesive for this joint was XA3919 (3M Co.)). The Specimens with XA3919 adhesive tested at 450°K (360°F) carried in excess of 245.2 kN/m (1400 lb/in). This is nearly twice the required lap load at this joint and should be more than adequate.

The mechanically fastened joint at point ③ of Figure 3.3-6 must also carry 126.6 kN/m (723 lb/in). 6.35 mm (0.25 in) diameter A286 bolts at a pitch of 50.8 mm (2.0 in) were selected for this joint. The single shear load per fastener would be 0.0508 x 126.6 = 6.43 kN (1446 lb). The allowable single shear load at 450°K (350°F) was 8.9 kN (2007 lb) which is more than adequate. The minimum pitch of the fastners was determined by the bearing strength of the 2219-T62 at 450°K (350°F). With the allowable bearing strength equal to 396.6 MN/m^2 (57,500 psi), the required pitch was calculated as

$$p_{req'd} = \frac{F_{bru} \times Dxt}{N_i} = 50.29 \text{ mm (1.98 in)}$$

The maximum stress in the girth ring occurs at point ④ due to the eccentricity of the bolted joint. The maximum stress due to combined axial load and bending was calculated to be,

$$f_{max} = N_i/t + 6N_i/t = 7\ N_i/t = 349 \text{ MN/m}^2 \text{ (50,600 psi)}$$

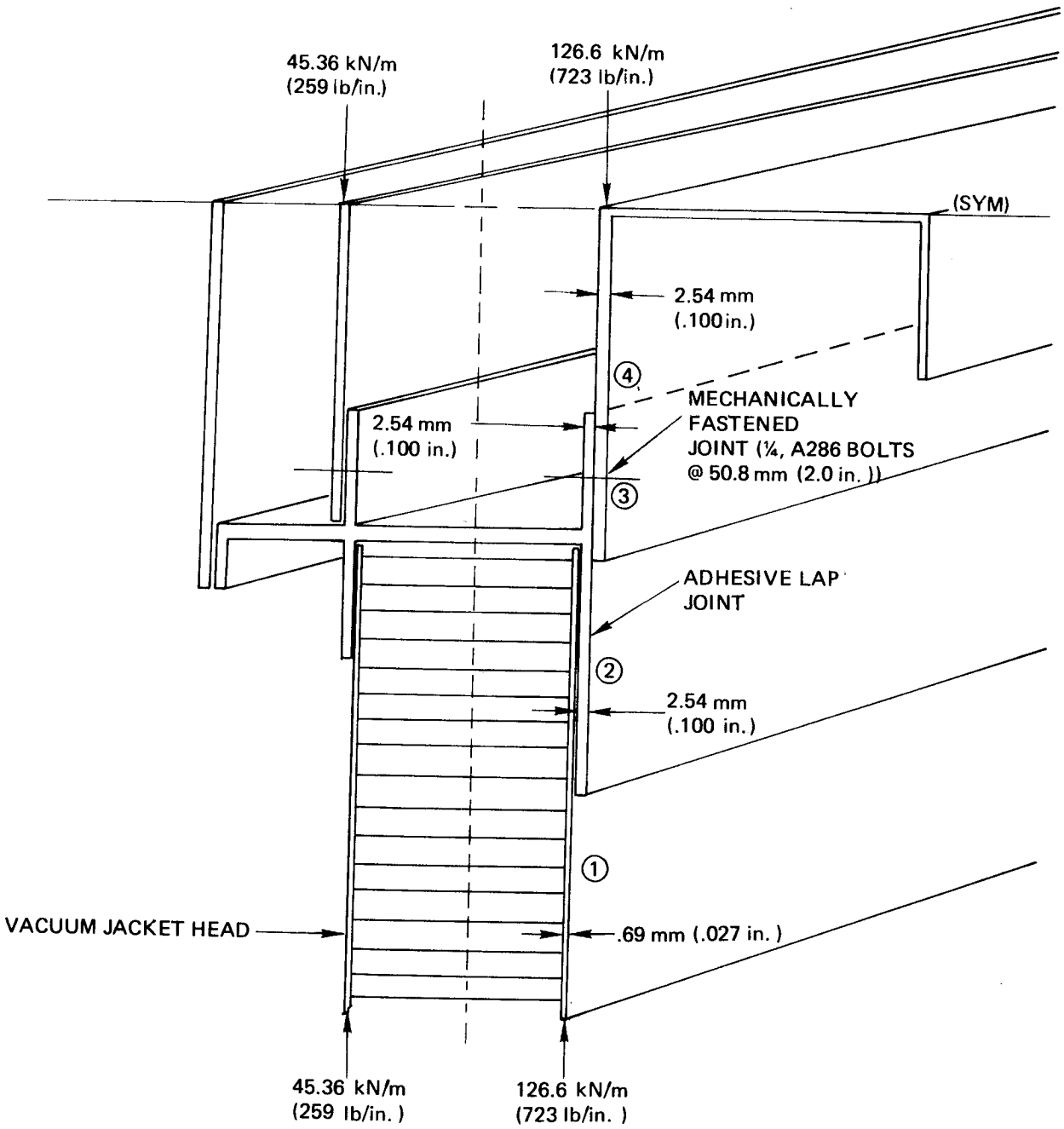

Figure 3.3-6: Meridional Loads on the Girth Ring for OMS Fuel Tank

where the $6N_i/t$ term is the bending stress due to the eccentricity of the single fastener lap joint.

The allowable plastic bending stress for 2219-T62 aluminum alloy at 450°K (350°F) from the Boeing Design Manual was an apparent fiber stress, F_b of 358.7 MN/m^2 (52,000 psi). Note that the actual material stress is much less than this but the linear bending theory indicates an apparent stress of 358.7 MN/m^2 (52 ksi). The minimum margin of safety at point ④ was calculated to be,

$$M.S. = 358.7/349 - 1 = +0.03$$

Figure 3.3-7 is a sketch of circumferential loads on the girth ring predicted by BOSOR 3. The total compression load on the ring was the sum of P_{circ} and the line loads N_{20} acting on the ring. Thus,

$$N_{circ} = P_{circ} + L_i \times N_{20} = -117.6 \text{ kN } (-26{,}440 \text{ lb})$$

The total moment was

$$M_{circ} = M_{20} \times L_i = 78 \text{ N.m } (-690 \text{ in-lb})$$

The maximum compression stress is the sum of the axial and bending stresses, and occurs at the tip of the free flange shown in Figure 3.3-7.

$$f_{max} = N_{circ}/A_{ring} + M_{circ}\, xc/I_y = -76.5 \text{ MN/m}^2 \text{ } (-11{,}090 \text{ psi})$$

The bending stress was only 4.1 kM/m^2 (590 psi) of f_{max}. The allowable buckling stress of the maximum stress point was 186.2 MN/m^2 (27 ksi) which was more than adequate.

The critically stressed point on the girth ring was the vacuum seal sheet. It had the largest b/t. The maximum stress on the sheet was

$$f_{max} = N_{circ}/A_{ring} - M_{circ}xc/I_y = -70.1 \text{ MN/m}^2 \text{ } (-10{,}160 \text{ psi}).$$

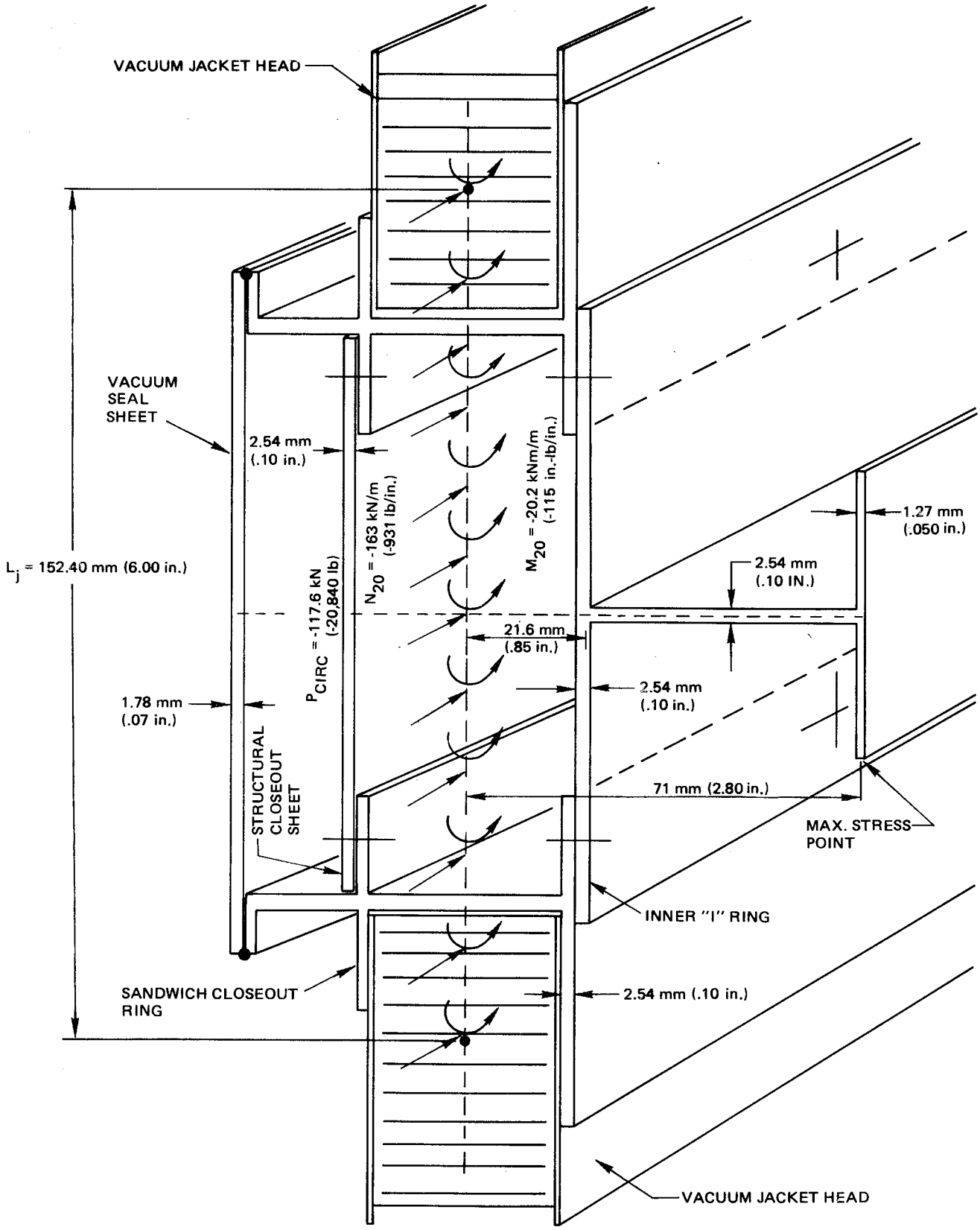

Figure 3.3-7: Circumferential Loads on the Girth Ring for OMS Fuel Tank

The allowable stress for initial buckling of the sheet was calculated as

$$F_{cr} = KE(t/b)^2 = 072.4 \text{ MN/m}^2 \text{ (-10,500 psi)}.$$

The minimum margin of safety was, M.S. = 72.4/70.1 -1 = +0.03.

The structural closeout sheet was stressed to about -72.4 MN/m^2 (-10,500 psi) in the circumferential direction plus about -17.9 MN/m^2 (-2590 psi) in the meriodional direction. The allowable stress for initial buckling of this sheet was -93.1 MN/m^2 (-13,500 psi) for biaxial compression. The minimum margin of safety was +0.28.

3.3.2 Pressure Vessel Analysis

The preliminary design for the LH_2 pressure vessel was analyzed using the BOSOR 3 analysis method, Reference 4. The design requirements specified in Section 3.1 were that the vessel be proof tested at room temperature to 241.3 kN/m^2 (35 psi) and at 20.5°K (-423°F) to 362.0 kN/m^2 (52.5 psi). The material stresses in both tests were not to exceed 95 percent of the allowable yield stresses.

The material selected was aluminum alloy 2219-T81. The welds will be left in the as-welded condition where the gores are welded together. Weld lands will be used throughout to compensate for the lower "as welded" properties. The A-Basis design allowables from Boeing Design Manual are listed in Table 3.3-4.

The results of the BOSOR 3 analysis are plotted in Figure 3.3-8 as the effective tension stress versus the meridional station measured from the centerline of the manhole located at the botton of the pressure vessel. Only half of the vessel was analysed since it was nearly symmetrical about the centerline located at station 160.

The effective stress, σ_e, is the von Mises "effective" stress computed from the inner and outer surface stresses in either the meridional or circumferential directions. There was no significant differences in the meridional and circumferential effective stresses. Referring to Figure 3.3-8, the low stresses at station 0.254 were due to the refinforcing ring at the edge of the manhole. At

Table 3.3-4: A-Basis Design Allowables for Aluminum Alloy 2219-T81

PROPERTY	CONDITION			
	2219-T81 ALUMINUM ALLOY AS RECEIVED		2219-T81 ALUMINUM ALLOY AS WELDED	
	AT 294°K (70°F)	AT 20.5°K (-423°F)	AT 294° (70°F)	AT 20.5°K (-423°F)
$F_{tu'}$ MN/m^2 (ksi)	413.69 (60)	579.16 (84)	179.26 (26)	255.11 (37)
$F_{ty'}$ MN/m^2 (ksi)	303.37 (44)	399.90 (58)	117.21 (17)	186.16 (27)
0.95 $E_{ty'}$ MN/m^2 (ksi)	289.58 (42)	379.21 (55)	110.32 (16)	172.37 (25)
$F_{su'}$ MN/m^2 (ksi)	241.32 (35)	337.84 (49)		
POISSON'S RATIO	0.33	0.33		
E, GN/m^2 (10^6 psi)	72.40 (10.5)	79.29 (11.5)		

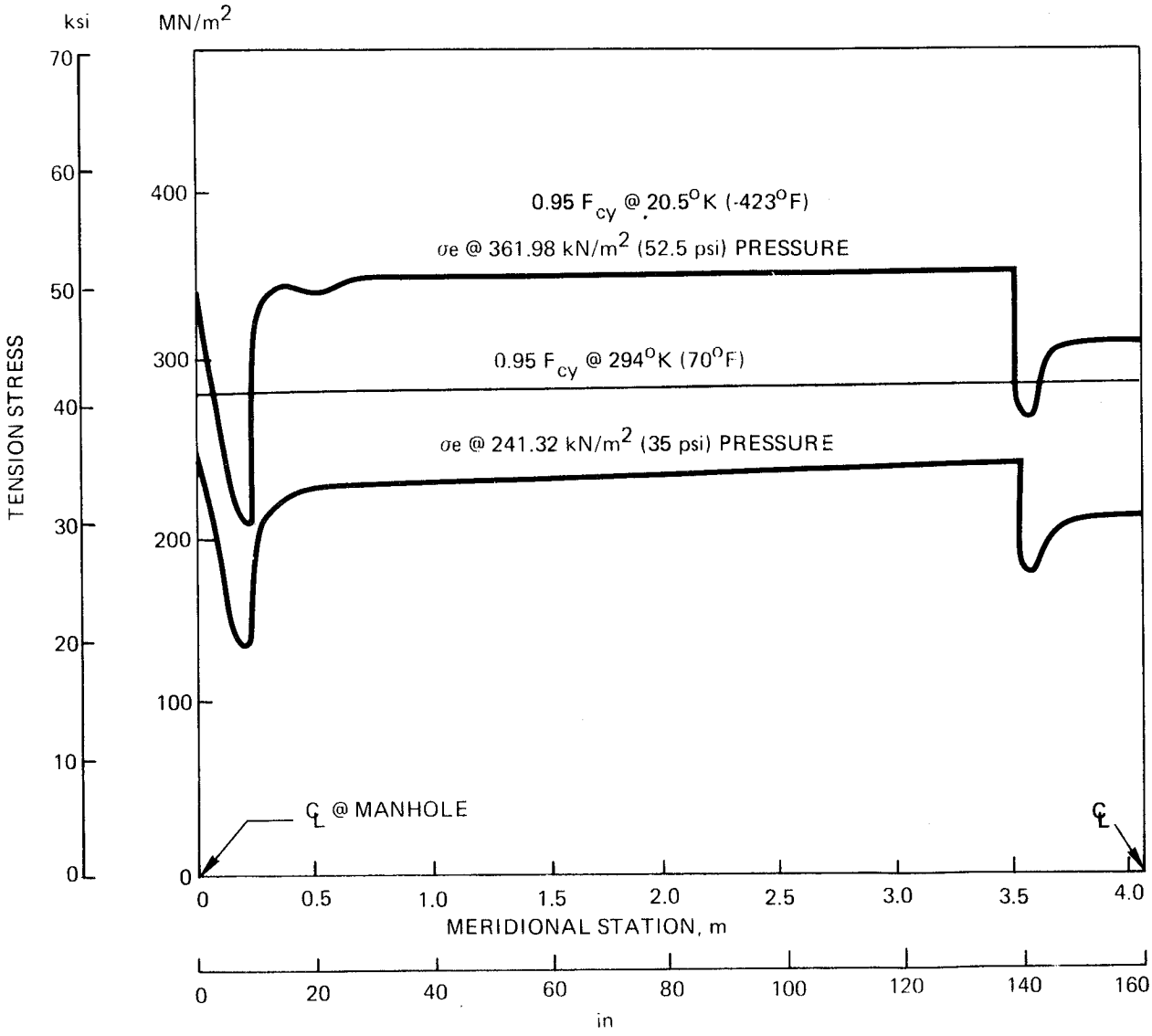

Figure 3.3-8: Effective Stress Vs Station for the Pressure Vessel - OMS Fuel Tank

station 3.556 a thick weld land was included in the BOSOR 3 analysis model. The effect was to locally lower the stresses.

Figure 3.3-9 is a plot of the radial displacements, W, at the meridional stations. At station 0.254 the manhole ring locally restricted the radial growth of the hemisphere. Near station 4.064 the cylinder section tended to grow more than the hemisphere. A separate analysis was made to determine the amount of thermal contraction due to loading the LH_2 and cooling the pressure vessel to 20.5°K (-423°F). The vessel would contract about 10.16 mm (0.4 in) inward. This would more than compensate for the growth due to the operating internal pressure of 241.3 kN/m^2 (35 psi).

Since the "as welded" allowable properties of the T81 condition material are less than the as-received material, the thickness of the weld lands would be more than double the nominal skin gages. At 294°K (70°F) the weld lands should be 2.6 times the nominal gage. At 20.5°K (-423"F) the land thickness should be 2.2 times the nominal gage. Using thinner weld lands would result in a lower margin of safety in the weld lands than the nominal gages.

3.3.3 Pressure Vessel Support System

The analysis of the pressure vessel support system discussed in this section was based on the use of fiberglass/epoxy tension straps. Subsequent investigation showed that the Kevlar 49/epoxy (PRD 49-3/epoxy) strap as described in Appendix A, Figure A-13 was structurally and thermally more efficient.

Loads and Deflection Analysis

Figure 3.3-10 is a schematic of the pressure vessel support system. The ultimate load components (F_x, F_y, F_z) were applied at the center-of-mass. The pressure vessel and the LH_2 were assumed to act as a rigid mass and transfer the loads to the attachment bosses. The tension straps transfer the loads to the support fittings which are rigidly attached to the vehicle primary structure.

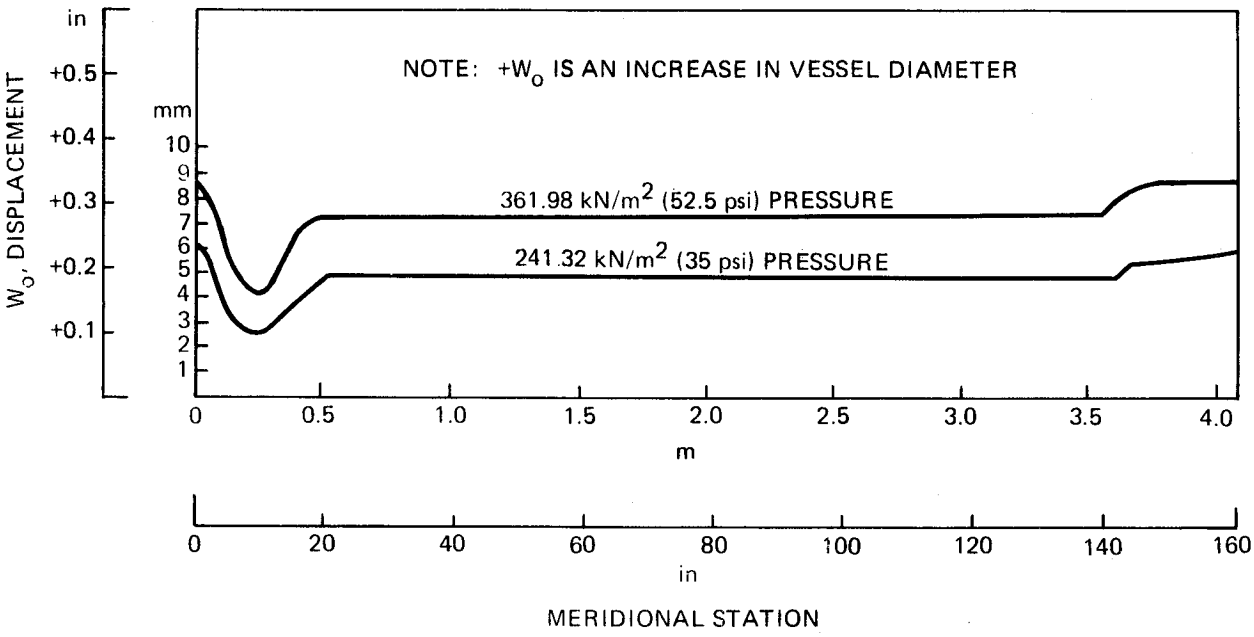

Figure 3.3-9: W_o Displacement Vs Station for the Pressure Vessel - OMS Fuel Tank

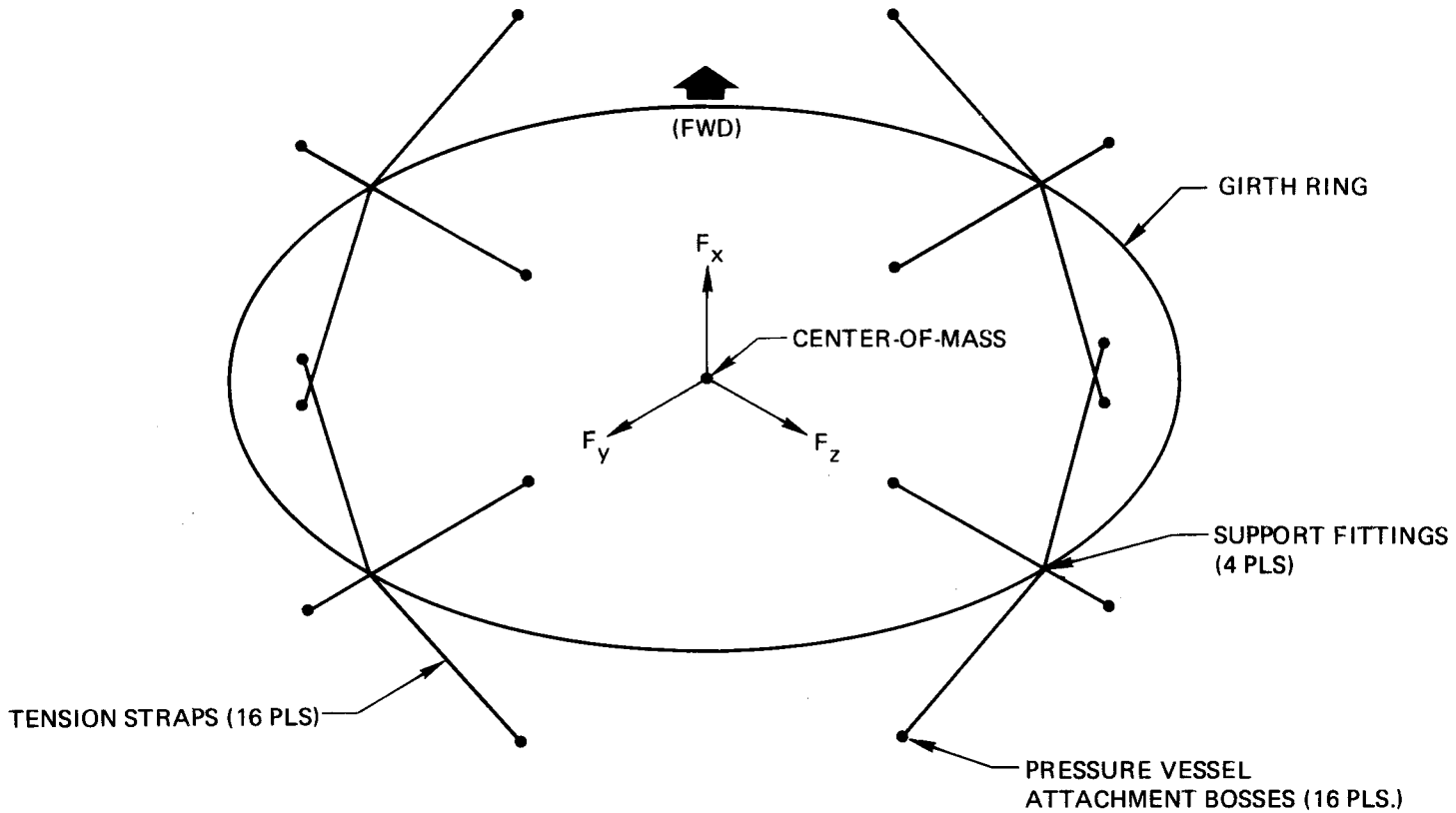

Figure 3.3-10: Structural Model for Pressure Vessel Support System for OMS Fuel Tank

The loads on the support system were due to the 4,559 kg (10,050 lb) weight of the LH_2 and an assumed total inert weight of the 826 kg (1821 lb) for the pressure vessel, support system and MLI. The limit-load factors applied to these weights are tabulated in Section 3.1. The 1.5 factor of safety was used to compute the ultimate loads. The ultimate load components for thirteen load conditions are listed in Table 3.3-5. Five of these were selected for the analysis to determine the maximum load in a tension strap.

The analysis for the five load cases were made in two steps since the tension straps cannot resist compression loads. The first step assumed that all sixteen straps were effective structural members. From this the compression members were assumed to be negligible and the analysis was rerun to determine the maximum tension load in the straps.

Figure 3.3-11 is a schematic of the first step analysis for load case 3, the maximum load case. All the lower support straps would be in compression; however, the straps cannot resist compression. The second step analysis "effectively" buckled these members by reducing their individual stiffnesses to one percent of a tension member. This redistributes the tension loads and determines the expected displacements for the ultimate loads. Figure 3.3-12 is a schematic of the second step loads for case 3. The maximum load 62.1 kN (14,000 lb) or 96.5 MN/m^2 (14 ksi) occurs in member (10) . Since the allowable tensile stress for these unidirectional fiberglass straps is at least 1205 MN/m^2 (175 ksi) the margin of safety is very large. The pin and clevis strap fittings should be designed for and proof tested to more than this ultimate load.

The maximum support fitting loads at the girth ring are shown in Figure 3.3-13. There are no loads on the lower two supports, since those straps were buckled in the analysis. More data on the shuttle structure interface will be required to complete the design and analysis of the support fittings.

Table 3.3-5: Ultimate Load Components for OMS Fuel Tank Support System Analysis

	LOAD CONDITION	TOTAL WEIGHT kg	TOTAL WEIGHT (lb)	FACTOR OF SAFETY	ULTIMATE LOAD COMPONENTS 1 F_X kN	F_X (lb)	F_Y kN	F_Y (lb)	F_Z kN	F_Z (lb)	ANALYSIS CASE
1.	LAUNCH	5,385	(11,871)	1.5	-110.31	(-24,800)	+79.17	(+17,800)	±79.17	(±17,800)	1
2.	LAUNCH				±126.77	(±28,500)	0	(0)	0	(0)	
3.	HI-Q BOOST				-150.34	(-33,800)	+63.16	(+14,200)	±79.17	(±17,800)	2
4.	HI-Q BOOST				±23.75	(±5,340)	±15.84	(±3560)	0	(0)	
5.	END BOOST				-251.31	(-56,500)	±47.37	(±10,650)	±47.37	(±10,650)	3
6.	END BURN	5.385	(11,871)		-251.31	(-56,500)	±39.59	(±8900)	±39.59	(±8,900)	
7.	ORBITER RE-ENTRY	2.194	(4,836)		+16.15	(+3630)	-96.97	(-21,800)	±32.25	(±7,250)	
8.	ORBITER RE-ENTRY				0	(0)	±32.25	(±7250)	0	(0)	4
9.	FLYBACK				+16.15	(+3630)	±32.25	(±7250)	±32.25	(±7250)	
10.	FLYBACK				0	(0)	-80.51	(-18,100)	0	(0)	
11.	FLYBACK				0	(0)	±32.25	(±7250)	0	(0)	
12.	LANDING				+41.99	(+9440)	-87.18	(-19,600)	±16.15	(±3630)	5
13.	LANDING	2,194	(4,836)	1.5	0	(0)	±16.15	(±3630)	0	(0)	

1 A. COORDINATE SYSTEM

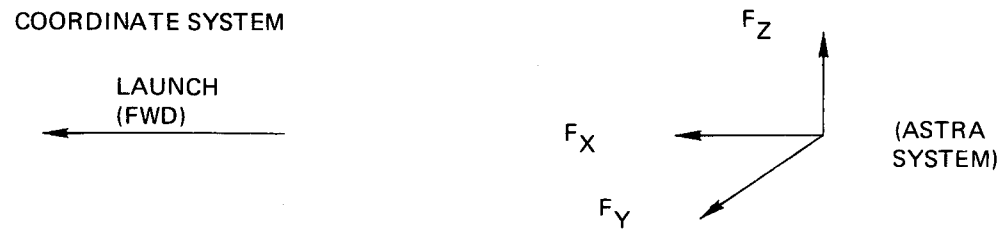

B. ULTIMATE LOAD = WT X LOAD FACTOR X FACTOR-OF-SAFETY.

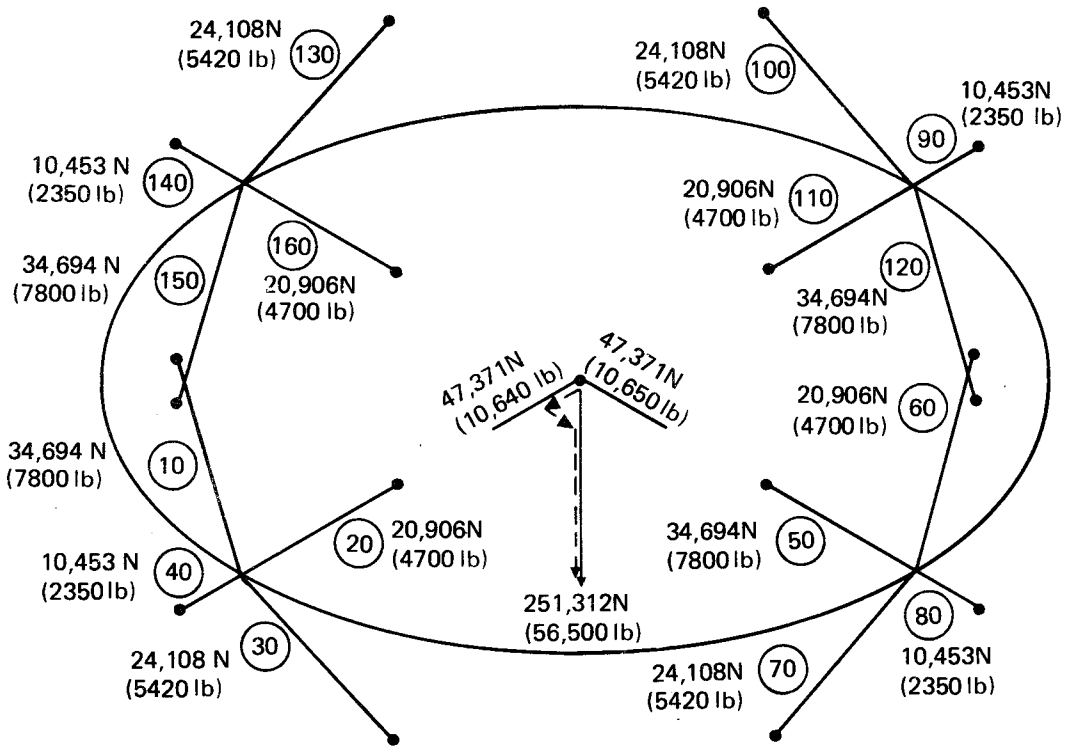

Figure 3.3-11: Case 3 - End Boost Ultimate Loads (Step 1) for OMS Fuel Tank

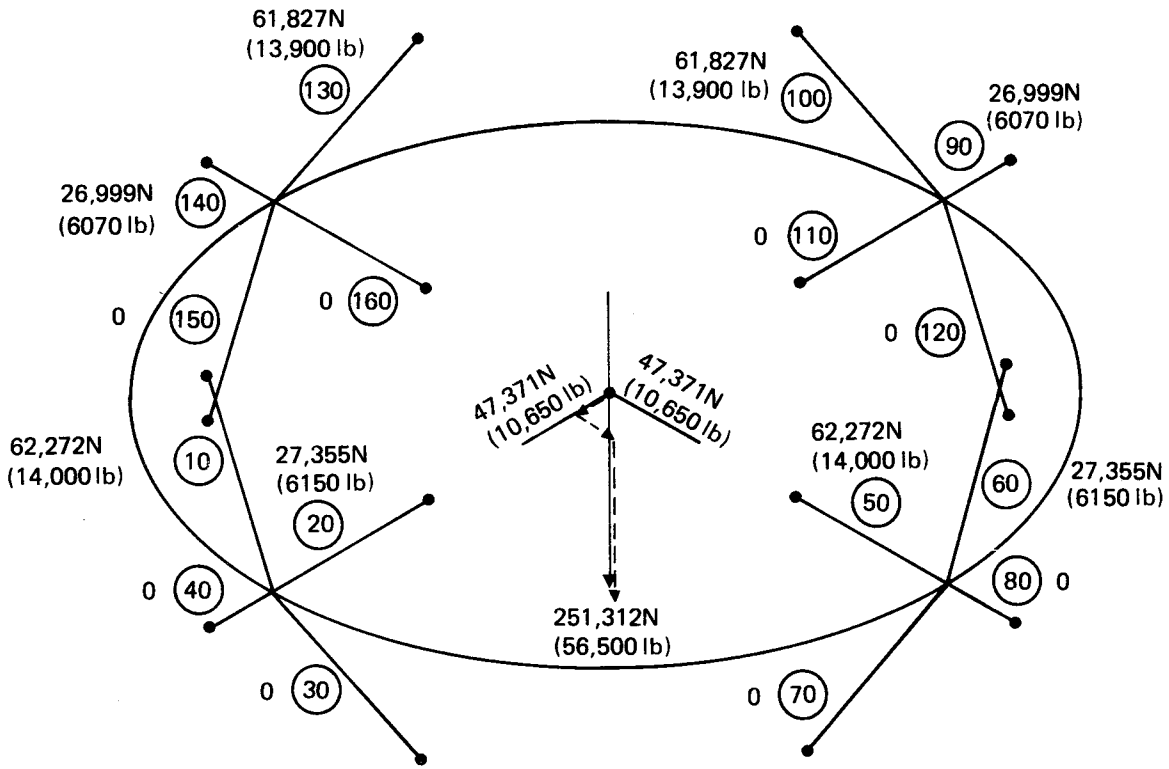

Figure 3.3-12: Case 3 - End Boost Ultimate Loads (Step 2) for OMS Fuel Tank

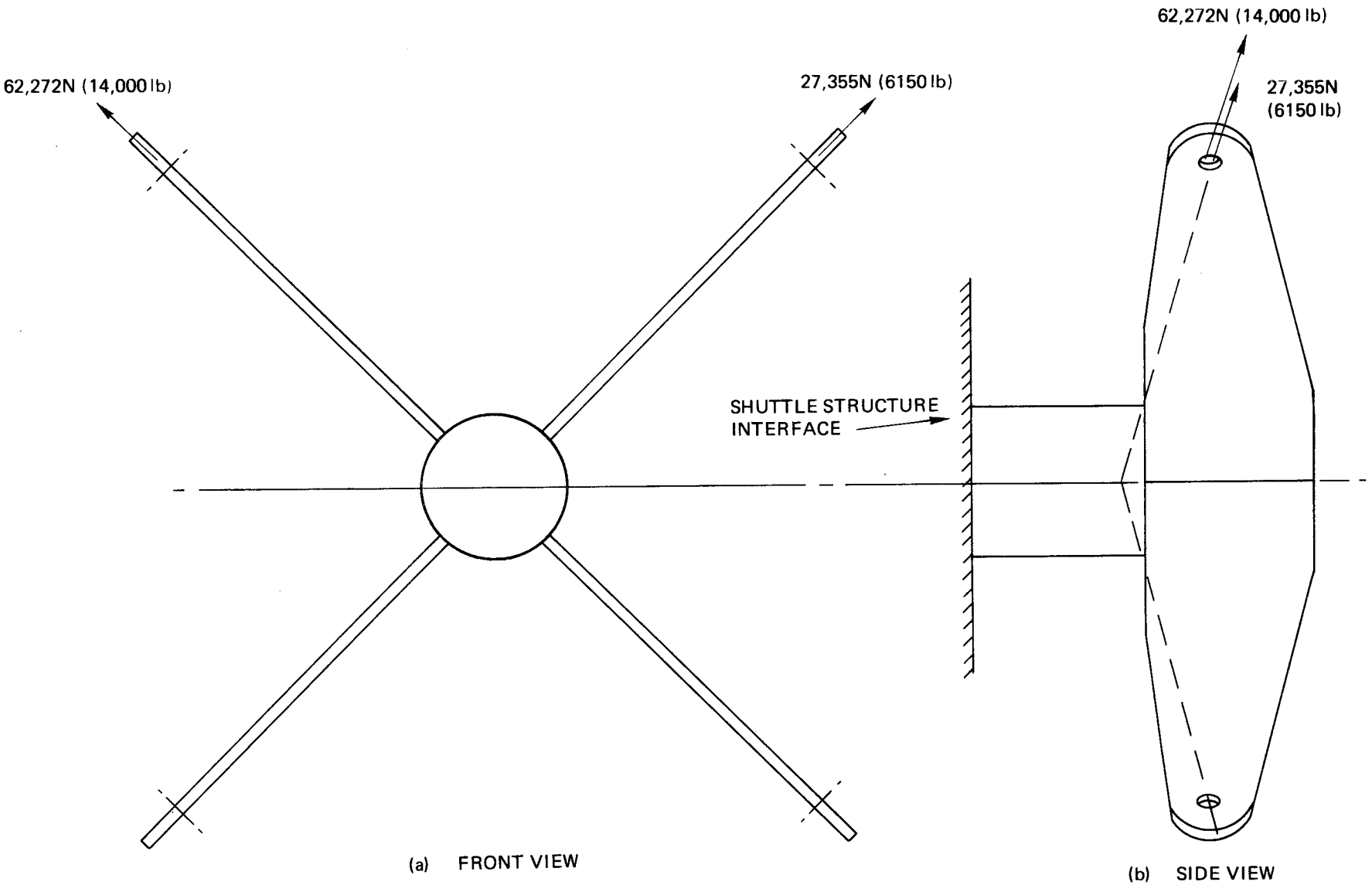

Figure 3.3-13: Support Fitting Ultimate Loads (Case 3) for OMS Fuel Tank

The maximum lateral clearance between the pressure vessel and the vacuum jacket is 114.3 mm (4.50 in), the space of the vacuum annulus. About 25.4 mm (1.0 in) of this will be occupied by the MLI. At the bosses where the support straps attach to the pressure vessel another 19.05 - 25.4 mm (3/4- 1 in) clearance will be required for the stud and clevis fitting. Another 12.7 mm (0.5 in) space will be required for the inward displacement of the vacuum jacket when the vacuum is acquired. The pressurized vessel will expand about another 12.7 mm (0.5 in) outward. This leaves about 38.1 mm (1.5 in) of space for displacements of the pressure vessel within the vacuum jacket.

The predicted displacement for ultimate load in Case 3 is considerably less than this; about 2.54 mm (0.1 in) maximum. Considering the assumption of a rigid mass for the pressure vessel and its LH_2 load, some of this space will be required for local bulging of the vessel during ascent. The 114.3 mm (4.50 in) vacuum annulus appears adequate for the calculated and anticipated displacements of the pressure vessel support system.

Vibration Analysis

The critical design condition for the pressure vessel support system was the 12 Hertz minimum design requirement. The minimum frequency depends on the strap stiffness and the mass of the LH_2 and the inert weights. A preliminary ASTRA analysis of the strap configuration and mass indicated that the minimum frequency was about 7 Hertz for lateral displacements in the plane of the girth ring. The area of the fiberglass straps was increased to 645.16 mm^2 (1.0 in^2) to correct this. Only about half of the straps are considered effective since the straps will buckle when loaded in compression.

The final analysis was based on the ultimate loads for Case 3. Only the tension members were included for stiffness and those were prestressed with the ultimate loads. The predicted minimum frequency was 13.9 Hertz in a lateral displacement mode which exceeds the design requirement.

Attachment Boss Analysis

The attachment bosses should distribute the concentrated loads of the tension straps to the pressure vessel. Locally around the boss there may be very high bending stresses due to the eccentricity of the strap to the surface of the pressure vessel. The attachment bosses are located on the hemispherical shell near the junction of the hemisphere with the cylindrical center section. As a result, the state of stress is very complex. There are no known solutions for the combined shear and moment loads coupled with the discontinuity stresses in the pressure vessel; however, an approximate analysis was made to estimate the magnitude and location of the maximum stresses.

The analysis method of P. P. Bijlaard (Reference 5) was selected as a first approach to the analysis of the attachment bosses. It was developed for the effect of local loads acting upon attachments to spherical shells. Direct solutions were determined by Bijlaard for the case of an external moment acting on a rigid cylindrical insert using the theory of shallow spherical shells. His results were used to calculate the stresses on the attachment bosses.

Figure 3.3-14 is a partial section of an attachment boss. The external moment is caused by the eccentricity, e, of the strap fitting to the reacting load in the attachment. Assuming an eccentricity of 8.255 mm (0.325 in) and a maximum strap load of 62.3 kN (14,000 lb) the ultimate external moment will be 514 m.N (4560 in-lb). This external moment, M, was used with Bijlaard's numerical results to determine the deflection and stress resultants in the attachment boss. The moment was applied along the axis of the tension strap.

Figure 3.3-15 is a plan view schematic of the attachment boss with the external moment applied at the lug bolt. The stresses vary with the angle theta around the boss. The maximum tensile stresses occur at theta equal to 3.14 radians (180 degrees).

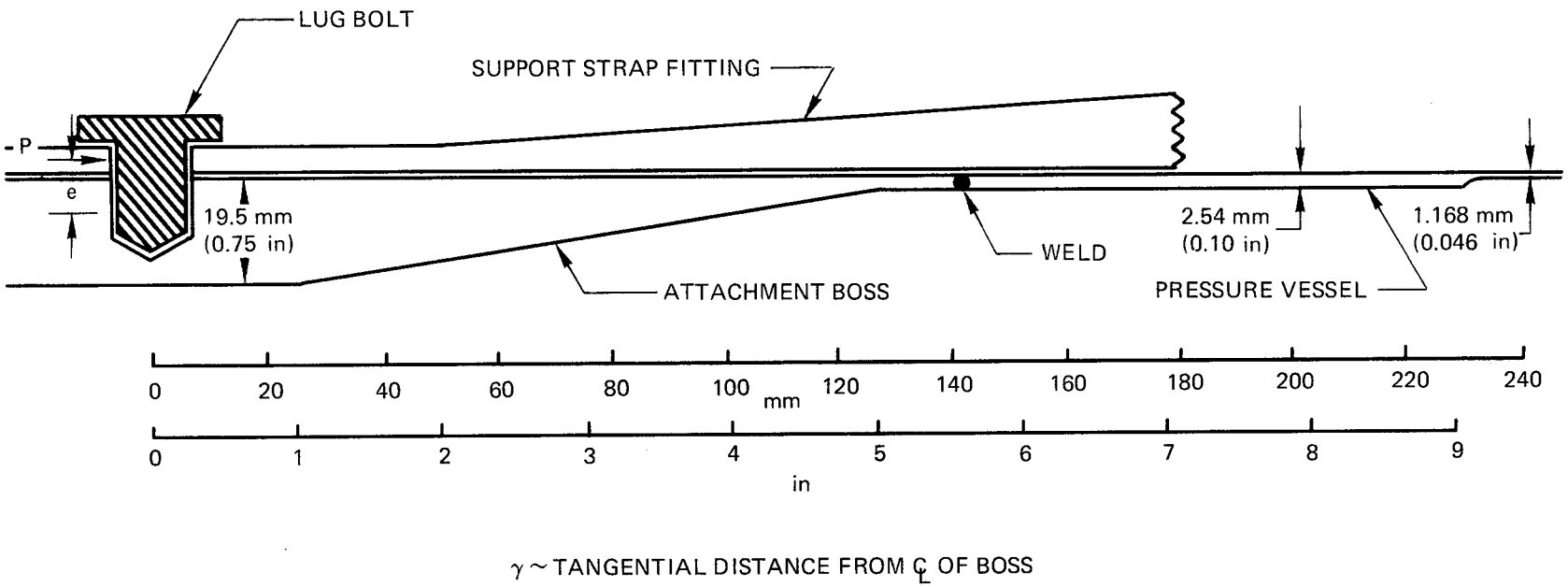

Figure 3.3-14: Partial Section of Pressure Vessel Attachment Boss - OMS Fuel Tank

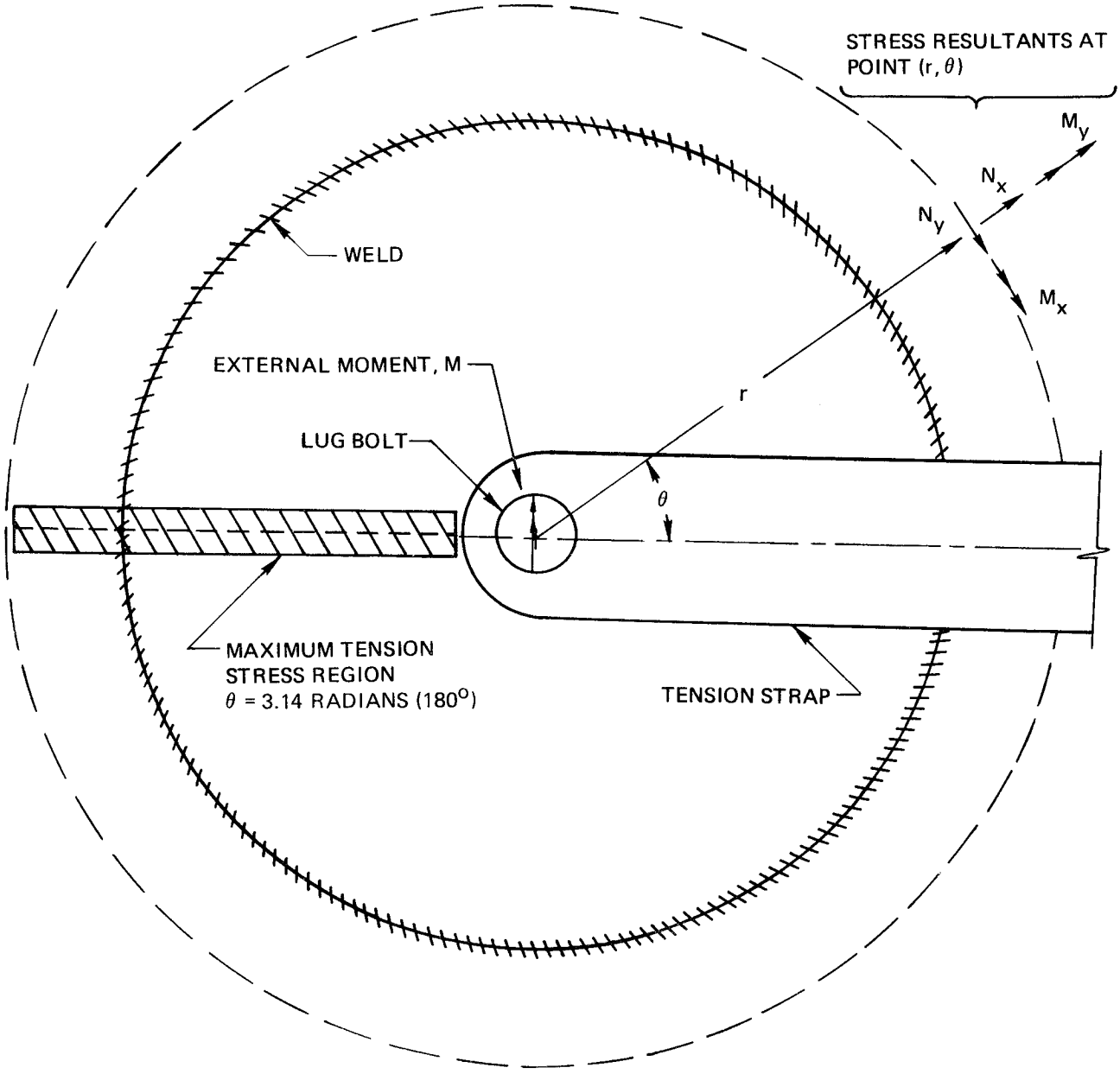

Figure 3.3-15: Plan View of OMS Fuel Tank Pressure Vessel Attachment Boss for Stress Analysis

The equations used for the deflection and the stress resultants were:

$$w = k_1 \frac{M}{Et^2} \sqrt{\frac{R}{t}} \cos\theta$$

$$M_x = k_2 \frac{M}{R} \sqrt{\frac{R}{t}} \cos\theta$$

$$M_y = k_3 \frac{M}{R} \sqrt{\frac{R}{t}} \cos\theta$$

$$N_x = k_4 \frac{M}{Rt} \sqrt{\frac{R}{t}} \cos\theta$$

$$N_y = k_5 \frac{M}{Rt} \sqrt{\frac{R}{t}} \cos\theta$$

where

- M is the external applied moment
- E is the modulus of elasticity
- t is the pressure vessel thickness
- R is the pressure vessel radius
- $k_{1,2..}$ are the coefficients calculated by Bijlaard for different r's. See Figures 8-12 in Reference 5.

Table 3.3-6 lists the calculated values for the deflection, w, and the stress resultants M_x, M_y, N_x, and N_y at various radii from the lug bolt. When theta equals 3.14 rad (180 degrees) the cos θ = -1 and the signs of all the values are reversed.

The critical stresses in the boss will be the combined effect of the bending moments, the axial loads, and the internal pressure. For a thickness, t,

$$f_x = \pm \frac{6M_x}{t^2} + \frac{N_x}{t} + \frac{pR}{2t} \quad \text{(radial stress)}$$

$$f_y = \pm \frac{6M_y}{t^2} + \frac{N_y}{t} + \frac{pR}{2t} \quad \text{(tangential stress)}$$

Table 3.3-6: Deflections and Stress Resultants for the Pressure Vessel Attachment Boss - OMS Fuel Tank

For u = 0.2, M = 512.21 N. m (4560 IN-LB) at θ = 0 radius (0^o)

r		w		Mx		My		Nx		Ny	
mm	in	mm	in	N.m/m	in-lb/in	N.m/m	in-lb/in	kN/m	lb/in	kN/in	lb/in
12.7	0.5	-0.864	-0.034	+10142	+2280	+2829	+636	-346.75	-1980	-92.99	-531
25.4	1.0	-1.092	-0.043	+4048	+910	+2713	+610	-239.92	-1370	-478.10	-2730
50.8	2.0	-1.676	-0.066	+1351	+304	+1219	+274	-292.46	-1670	-598.93	-3420
76.2	3.0	-1.626	-0.064	+676	+152	+676	+152	-292.46	-1670	-558.66	-3190
101.6	4.0	-1.524	-0.060	+338	+76	+476	+107	-266.19	-1520	-465.84	-2660
127.0	5.0	-0.432	-0.017	0	0	+67	+15	-159.37	-910	-79.68	-455
152.4	6.0	-0.279	-0.011	0	0	0	0	-106.48	-608	0	0
177.8	7.0	-0.102	0.004	0	0	0	0	-79.68	-455	0	0
203.2	8.0	0	0	0	0	0	0	0	0	0	0

The maximum tensile stresses occur when θ = 3.14 rad (180°) and N_x and N_y are positive. The moments cause the maximum tensile stresses on the outer surface when θ = 3.14 rad (180°) and on the inner surface when θ = 0 rad (0°).

Figure 3.3-16 is a plot of the maximum fiber stresses along the radial θ = 3.14 rad (180°). The maximum material stresses will be 235 MN/m^2 (34.1 ksi) outside the boss due to the internal pressure of 241 kN/m^2 (35 psi). Within the boss the maximum stresses will occur at r = 12.7 mm (0.5 in) and 127 mm (5.0) from the lug bolt. The critical stress area will be at r = 127 mm (5.0 in) for the f_x stress which will stress the transverse butt weld across the weld. The f_y stress will be parallel to the weld.

The allowable transverse butt weld strengths for 2219-T81 aluminum alloy, as-welded were:

F_{tu} = 179 MN/m^2 (26 ksi) at RT

= 255 MN/m^2 at 20.3°K

(37 ksi at -423°F)

F_{ty} = 117 MN/m^2 (17 ksi) or RT

= 186 MN/m^2 at 20.3°K

(27 ksi at -423°F)

The margin of safety at the weld will be

M.S. = +0.48

Near the lug bolt the margin is less

M.S. = 0.27

Although these margins of safety are rather large, there is considerable uncertainty in the prediction of the maximum stresses since the effects of the discontinuity stresses were not included. A more detailed analysis would be required to predict the discontinuity stresses due to the range in gage and the hemisphere to cylinder transition zone.

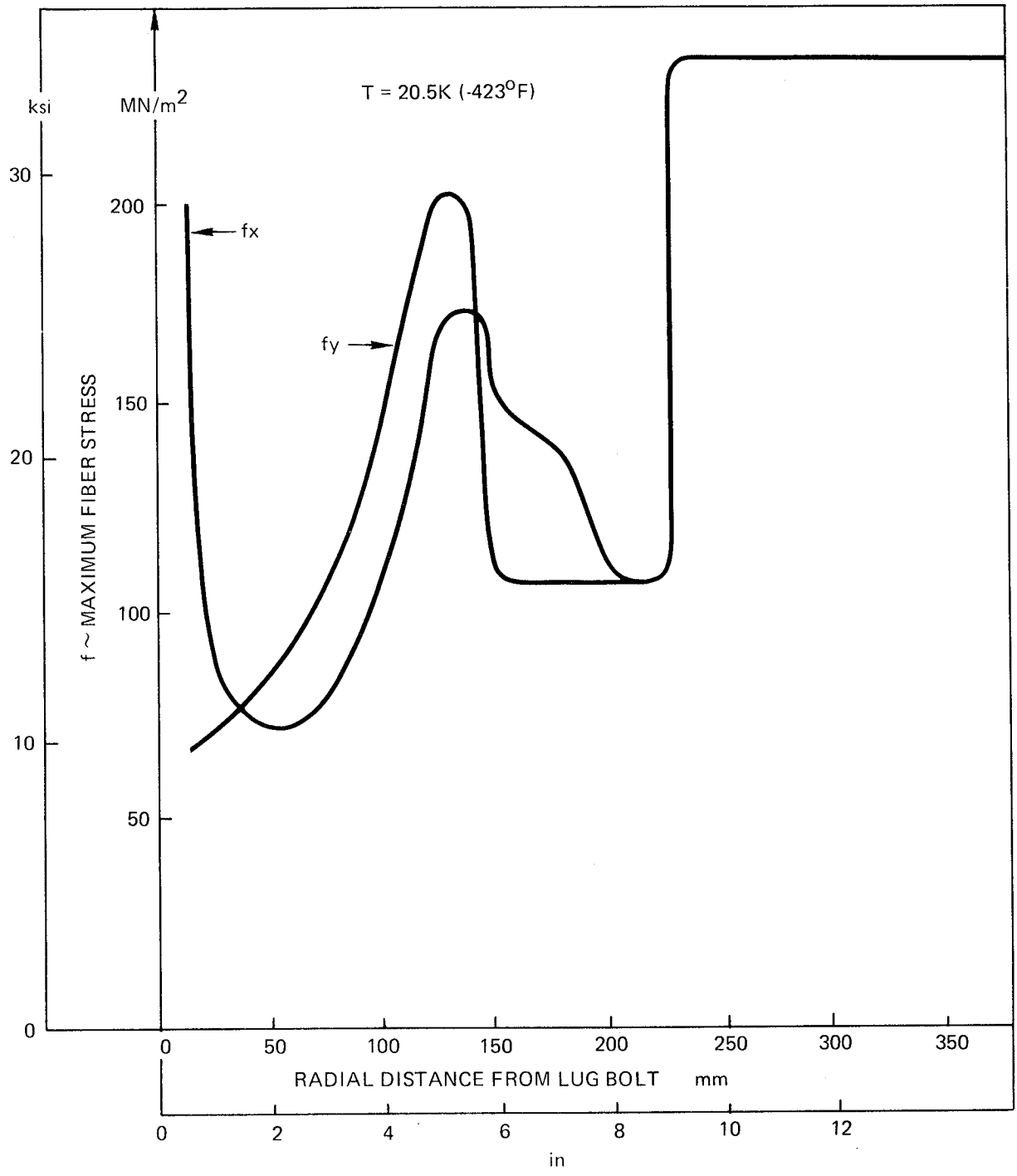

Figure 3.3-16: Maximum Fiber Stresses in Pressure Vessel Attachment Boss - OMS Fuel Tank

3.4 THERMAL ANALYSES

3.4.1 Heat Flow Predictions

Detailed heat flow predictions were developed for use in the detailed MLI thickness, hydrogen boil-off, tank gage trade study discussed in Section 3.4.4.

The heat flow analysis provided data on the total heat flow into the tank interior as a function of MLI thickness. This total heat flow was predicted as a sum of the heat flow through the basic idealized MLI (no discontinuities or penetrations) and the additional heat flow contributions associated with each particular penetration or discontinuity feature.

The heat flow predictions were computed with the aid of the BETA (Boeing Engineering Thermal Analyzer) program, operated in a steady-state thermal diffusion mode. The BETA program provides for three-dimensional simulation of heat flow and can include conduction, convection and radiation heat transfer. Material properties may vary with temperature in accordance with input tables or functional expression. The material properties used in the thermal analyses are shown in Table 3.4-1.

The effects of H_2 and air leakage in the MLI is taken into account in the effective thermal conductivity expression shown in Table 3.4-1. The investigation which led to this expression is described in Appendix B.

Analytical models of the various tank system features, which were analyzed by means of the BETA program to yield the component terms of the total heat flow are described in Appendix C. The selected MLI fastener arrangements are shown in Appendix A. The models for thermal analysis of these fasteners were the same as those illustrated in Appendix C, except for changes to the appropriate dimensions. Outer (warm surface) boundary temperatures used in the analyses are given in conjunction with each model description. Inner (cold surface) boundary temperatures were all taken as 20.5°K (37°F). Although the saturated liquid temperature actually varies with tank pressure, which was treated as a variable in the trade study, preliminary computations showed that the change in the hydrogen saturated liquid temperature over the pressure range considered affected the total heat flow by less than 1%. Therefore, the tank interior boundary temperature was assumed constant.

TABLE 3.4-1

MATERIAL PROPERTIES

1. MLI Blanket Configuration: Aluminized Mylar/Dacron Net with aluminized Kapton/Dacron Net in outer 2.54 mm (0.10 in) of outer blanket; layer density = 2.95 layers/mm (75.0 layers/inch)

2. Aluminized Mylar/Dacron Net mass density = 35.08 kg/m^3 92.84 lb/ft^3)

3. Aluminized Kapton/Dacron Net mass density = 45.49 kg/m^3 (2.84 lb/ft^3)

4. MLI effective thermal conductivity normal to the thickness of the double aluminized Mylar/Dacron net of 2.95 layers/mm (75 layers/inch) is:

$$k = 1.73 \times 10^{-1} \left[.371 \times 10^{-6} \left(\frac{T_1 + T_2}{2} \right) + 3.805 \times 10^{-4} \left(\frac{T_1 4.67 - T_2 4.67}{T_1 - T_2} \right) \right]$$

$$+ 2.34 \times 10^{-2} P_{N1} T_1^{-.48} + 9.92 \times 10^{-2} P_{H1} T_1^{-.7} \quad \frac{watt - m}{m^2 - K}$$

T in K

P_N = partial pressure of N_2 (or Air), N/M^2

P_H = partial pressure of H_2, N/m^2

Subscript 1: Hot surface of MLI
Subscript 2: Cold surface of MLI

$$k = 1.2 \left[.206 \times 10^{-6} \left(\frac{T_1 + T_2}{2} \right) + 4.4 \times 10^{-15} \left(\frac{T_1^{4.67} - T_2^{4.67}}{T_1 - T_2} \right) \right]$$

$$+ 28.7 P_{N1} T_1^{-.48} + 122 P_{H1} T_1^{-.7} \quad \frac{Btu - In}{ft^2 - hr - °R}$$

T in R
P in Torr

TABLE 3.4-1 (Cont.)

5. Aluminum conductivity:

$$k = .2405 \times 10^{-2} + 1.18 \times 10^{-5} \left(\frac{T_1 + T_2}{2}\right) \quad \frac{\text{watt-cm}}{\text{cm}^2\text{K}} \text{ ; T in K}$$

$$= .139 + 3.79 \times 10^{-4} \left(\frac{T_1 + T_2}{2}\right) \quad \frac{\text{Btu-in}}{\text{ft}^2\text{-sec-R}} \text{ ; T in R}$$

6. Corrosion Resistant Steel conductivity:

$$k = 1.32 \times 10^{-3} + 2.17 \times 10^{-7} \left(\frac{T_1 + T_2}{2}\right) - .534 \times 10^{-9} \left(\frac{T_1 + T_2}{2}\right)^2$$

$$\frac{\text{watt-cm}}{\text{cm}^2\text{ K}} \text{ ; T in K}$$

$$= .077 + 6.99 \times 10^{-6} \left(\frac{T_1 + T_2}{2}\right) - 9.54 \times 10^{-9} \left(\frac{T_1 + T_2}{2}\right)^2$$

$$\frac{\text{Btu-in}}{\text{ft}^2\text{-sec-R}} \text{ ; T in R}$$

7. Fiberglass/Epoxy (non-structural) conductivity:

$$K = 2.89 \times 10^{-6} + 8.18 \times 10^{-9} \left(\frac{T_1 + T_2}{2}\right) \quad \frac{\text{watt-cm}}{\text{cm}^2\text{ K}} \text{ ; T in K}$$

$$= 1.67 \times 10^{-4} + 2.63 \times 10^{-7} \left(\frac{T_1 + T_2}{2}\right) \frac{\text{Btu-in}}{\text{ft}^2\text{-sec-R}} \text{ ; T in R}$$

TABLE 3.4-1 (Cont.)

8. PRD/Epoxy strap 3716 mm^2 (0.576 in^2) cross-sectional area
Unidirectional 54% fiber composite conductivity parallel to filaments

Temperature		Conductivity	
°K	(°R)	W/m-K	(Btu/ft-hr-R)
50	(90)	.0606	.035
100	(180)	.0762	.044
200	(360)	.104	.060
300	(540)	.1315	.076
400	(720)	.163	.094

9. Nylon conductivity:

$$K = .281 \times 10^{-2} - 1.097 \times 10^{-2} \left(\frac{T_1 + T_2}{2}\right)^{-0.6} \frac{\text{watt-cm}}{\text{cm}^2\ \text{K}} \text{ ; T in K}$$

$$= .1624 - .903 \left(\frac{T_1 + T_2}{2}\right)^{-0.6} \frac{\text{Btu-ft}}{\text{ft}^2\text{-hr-R}} \text{ ; T in R}$$

10. MLI surface emittance:

$$\varepsilon = 4.25 \times 10^{-3}\ T^{.667}, \text{ T in K}$$

$$= 2.87 \times 10^{-3}\ T^{.667}, \text{ T in K}$$

11. Aluminum emittance:

$\varepsilon = 0.2$

12. Corrosion Resistant Steel emittance:

$\varepsilon = 0.2$

13. Fiberglass/Epoxy emittance:

$\varepsilon = 0.8$

TABLE 3.4-1 (Cont.)

14. PRD/Epoxy emittance:
    $\varepsilon = 0.8$

15. Nylon emittance:
    $\varepsilon = 0.4$

16. Pressure Vessel Minimum Gage = 0.762 mm (0.030 in)

17. Pressure Vessel Weld Land Factor:
    $Wt_{tank} = 1.0465\ Wt_{tank\ membrane}$

The results of the heat flow analysis are given in Table 3.4-2. It is pointed out that the various component heat flow values are the incremental values associated with those components. Thus, they were added directly to the total basic heat flow rather than replacing any part of it. Each component incremental heat flow was assumed independent of the other component flows. In reality, some interaction would undoubtedly occur but the resulting effects were not expected to be significant. The lack of dependence of some of the component incremental heat flows upon MLI thickness reflects the observation that, for those components, the additional heat flow results almost entirely from conduction and radiation through added heat paths rather than disturbance of the flow through the main MLI. Therefore, for those components it was assumed that the incremental heat flow was indepedent of MLI thickness for the range of thickness important to the trade study.

Prior to the detailed BETA-program analysis of the manhole and feed valve penetration and the vent valve penetration, simplified estimates of heat flow for these two components were computed. These preliminary analyses considered only the additional direct conduction heat paths, plus the radiation inside the feed and main vent lines. Other radiant heat exchanges and increases or decreases in heat flow across the main MLI in the vicinity of the penetration were ignored. Upon completion of the full, detailed analysis of the manhole and feed valve assembly it was found that the preliminary heat flow estimate

Table 3.4-2. Heat Flow Results

COMPONENT		HEAT FLOW MLI THICKNESS				
		12.7 mm (0.50 in.)	25.4 mm (1.00 in.)	38.1 mm (1.50 in.)	50.8 mm (2.00 in.)	76.2 mm (3.00 in.)
BASIC MLI						
UNIT HEAT FLOW	Watt/m^2 (Btu/ft^2-hr)	.655 (.208)	.3276 (.104)	.2196 (.0697)	.1647 (.0523)	.1099 (.0349)
COMPONENT TOTAL HEAT FLOW FOR AREA 78.67 m^2 (846.8 ft^2)	Watt (Btu/hr)	51.57 (176.0	25.84 (88.2)	17.29 (59.0)	12.98 (44.3)	8.67 (29.6)
SINGLE-STEP LAP JOINT						
UNIT HEAT FLOW	Watt/m Btu/ft-hr	.01115 (.0116)	.01644 (.0171)	.01865 (.0194)	.01990 (.0207)	.02134 (.0222)
COMPONENT TOTAL INCREMENTAL HEAT FLOW FOR 100m (360.8 ft) JOINT LENGTH	Watt (Btu/hr)	1.225 (4.18)	1.805 (6.16)	2.051 (7.00)	2.189 (7.47)	2.346 (8.01)
SMALL NYLON PIN-TYPE FASTENERS (0.762 mm)						
UNIT HEAT FLOW	M Watt (Btu/hr)	.08145 ($.278 \times 10^{-3}$)	.06226 ($.2125 \times 10^{-3}$)	.04820 ($.1645 \times 10^{-3}$)	.03633 ($.124 \times 10^{-3}$)	.01758 ($.060 \times 10^{-3}$)
COMPONENT TOTAL HEAT FLOW FOR 1956 FASTENERS (SMALL NYLON PIN-TYPE FASTENERS, 0.762 mm)	Watt (Btu/hr)	.1594 (.544)	.1217 (.4155)	.09435 (.322)	.07105 (.2425)	.03437 (.1173)
LARGE NYLON PIN-TYPE FASTENERS (1.60 mm PIN)						
UNIT HEAT FLOW	Watt (Btu/hr)	.7105 (.002425)	.4726 (.001613)	.3662 (.00125)	.3173 (.001083)	.2784 (.00095)
COMPONENT TOTAL HEAT FLOW FOR 204 FASTENERS	Watt (Btu/hr)	.1450 (.495)	.0964 (.329)	.0747 (.255)	.0648 (.221)	.0568 (.194)
NYLON PIN AND GROMMET TYPE FASTENERS (6.35 mm PIN)						
UNIT HEAT FLOW	Watt (Btu/hr)	.01193 (.0407)	.00888 (.0303)	.00757 (.0258)	.00659 (.0225)	.00498 (.0170)
COMPONENT TOTAL HEAT FLOW FOR 84 FASTENERS	Watt (Btu/hr)	1.002 (3.42)	.7457 (2.545)	.6358 (2.17)	.5538 (1.89)	.4190 (1.43)
STRUCTURAL SUPPORT STRAP PENETRATION						
UNIT HEAT FLOW	Watt (Btu/hr)	.0677 (.2312)	.05614 (.1916)	.05035 (.1716)	.04642 (.1584)	.04066 (.1388)
COMPONENT TOTAL INCREMENTAL HEAT FLOW FOR 16 STRAPS	Watt (Btu/hr)	1.083 (3.696)	.8983 (3.066)	.8056 (2.746)	.7428 (2.535)	.6505 (2.220)
MANHOLE ACCESS & SHUT-OFF VALVE ASSEMBLY						
COMPONENT TOTAL INCREMENTAL HEAT FLOW	Watt (Btu/hr)	2.266 (7.734)	2.266 (7.734)	2.266 (7.734)	2.266 (7.734)	2.266 (7.734)
VENT VALVE ASSEMBLY						
COMPONENT TOTAL INCREMENTAL HEAT FLOW	Watt (Btu/hr)	3.052 (10.418)	3.052 (10.418)	3.052 (10.418)	3.052 (10.418)	3.052 (10.418)
TOTAL HEAT FLOW	Watt (Btu/hr)	60.50 (206.48)	34.83 (118.87)	26.27 (89.668)	21.92 (74.805)	17.50 (59.72)
TOTAL HEAT TO TANK INTERIOR FOR 720 hr MISSION	M Watt/sec (Btu)	156.8 (148655)	90.29 (85584)	68.12 (64561)	56.82 (53859.6)	45.36 (42998)

agreed with the detailed results to within 3.5%. Since this difference was well within the expected accuracy of the detailed analyses and since the preliminary estimate erred on the high side, it was decided to use the corresponding simplified analysis results for the vent valve assembly as the final prediction for that component. The more effective direct conduction heat paths and the less extensive disruption of the basic main MLI in the case of the vent valve assembly should result in a similar accuracy for the simplified analysis of that assembly.

3.4.2 Thermodynamic Analysis

The thermodynamic analysis provided data on the relation between heat flow to the tank interior and pressure rise in a closed tank. This data was used in the Section 3.4.4 Trade Study. For each combination of MLI thickness and vent pressure, the difference between total heat absorbed and heat required to produce the pressure rise was heat available to vaporize (boil-off) hydrogen. For all cases, the initial pressure was assumed to be 110.3 kN/m^2 (16.0 psia).

The thermodynamic analysis assumed isothermal conditions within the tank and liquid-vapor equilibrium throughout the pressure rise. The analysis considered the heat absorbed by both the liquid and the ullage space vapor. Variations in internal energy and heat of vaporization with pressure were included.

3.4.3 Pressure Vessel Sizing

The preliminary sizing of the pressure vessel wall thickness was a function of pressure. A simple membrane stress computation was employed and the 20.5°K (-423°F) proof test design condition of Section 3.1 was determined to be the critical conditions. The weight of structural attachments and plumbing details was assumed to be independent of pressure. The incremental weight of tank segment weld lands was included by means of constant factor on the tank weight based on membrane thicknesses.

The tank wall thickness was sized as a function of ullage pressure plus 34.5 kN/m^2 (5.0 psia). This excess pressure was the assumed additional pressure determined by propulsion system requirements prior to engine start. (See Table 3.4-3.)

3.4.4 Trade Study

A trade study was conducted on the OMS fuel tank to optimize MLI thickness, hydrogen boil-off and pressure vessel gage. The trade study incorporated results of the heat flow analysis, Section 3.4.1; the thermodynamic analysis, Section 3.4.2; and pressure vessel sizing, Section 3.4.3.

The trade study used the tank dimensions and MLI definition shown in Figure 3.2-1. The sandwich configuration for the vacuum jacket was 5056 aluminum Flex-Core, 33.64 kg/m^3 (2.1 lb/ft^3), 35.6 mm (1.40 in) thick; 2024 T3 aluminum alloy face skins 1.17 mm (0.024 in) thick on the inner surface and 0.31 mm (0.012 in) thick on the outer surface. The pressure vessel was sized for the 20.5°K (37°R) proof test condition except that the proof pressure was varied rather than considered fixed at 241.3 kN/m^2 (35.0 psia). The mass of hydrogen liquid and gas in the tank were based on the requirements of Section 3.1. Other assumptions and ground rules for the trade study are listed in Table 3.4-3.

The BETA (Boeing Engineering Thermal Analyzer) program was used in a one-dimensional simulation of steady state heat flow through the system. The analytical model included coupled radiation and conduction through the vacuum jacket honeycomb core, radiation across the vacuum annulus, effective conduction through the multilayer, and conduction through each solid material layer. Boundary conditions were 311°K (100°F) at the outer surface of the vacuum jacket and $T_{sat.\ liq.}$ varies with tank pressure, which was treated as a variable in the trade study, preliminary computations showed that the change in $T_{sat.\ liq.}$ over the pressure range considered affected the total heat flow less than 1%. Therefore, for this study the internal boundary temperature was taken as a constant 20.4°K (-423°F).

TABLE 3.4-3
TRADE STUDY GROUND RULES

1. Tank Area = 78.670 m^2 (846.8 ft^2)
2. Tank Total Volume = 65.129 m^3 (2300 ft^3)
3. Initial Liquid Hydrogen Mass = 3896.3 kg (8590 lb)
4. Mission Duration = 720 hr

TABLE 3.4-3 (Cont.)

5. No Intermediate Burn
6. Steady-state Heat Flow During Mission
7. Initial Tank Internal Pressure = 110.3 kN/m^2 (16.0 psia)
8. Pressure in Vacuum Annulus (at outer surface of main MLI) = 6.65 N/m^2 (5.0×10^{-5} torr)
9. NPSP (at engine pump inlet) 13.8 kN/m^2 (2.0 psia)
   Feed line pressure drop 20.7 kN/m^2 (3.0 psia)
   Additional Pressure, above saturated vapor pressure, dictated by propulsion system requirements. 34.5 kN/m^2 (5.0 psia)

Trade study results are shown in Figures 3.4-1 and 3.4-2. Figure 3.4-1 gives the sum of insulation weight and boil-off weight as a function of insulation thickness and vent pressure. Figure 3.4-2 shows the variation of insulation, boil-off, and tank weight with vent or final pressure, permitting identification of the minimum total weight or optimum design point. Table 3.4-4 gives details of the design represented by that point. The tank gages and weights shown in Table 3.4-4 do not include a constant additional thickness included in the actual design to allow for acceleration loads. This omission has no effect on the pressure or MLI thickness results from the trade study.

TABLE 3.4-4
TRADE STUDY RESULT SUMMARY
Optimum Design Point

Vent or Final Pressure	193.1 kN/m^2	(28.0 psia)
Tank Design Pressure	227.6 kN/m^2	(33.0 psia)
Insulation Thickness	2.769 cm	(1.09 in.)
Insulation Weight	78.47 kg	(173 lb)
Hydrogen Boil-off	0	
Tank Weight*	304 kg	(670 lb)
Tank Head Gage	1.04 mm	(0.041 in.)
Tank Cylinder Gage	2.08 mm	(0.082 in.)
Total Weight (Tank Walls + Insulation)	382 kg	(843 lb)

*Includes 1.15 factor for increased thickness at weld lands.

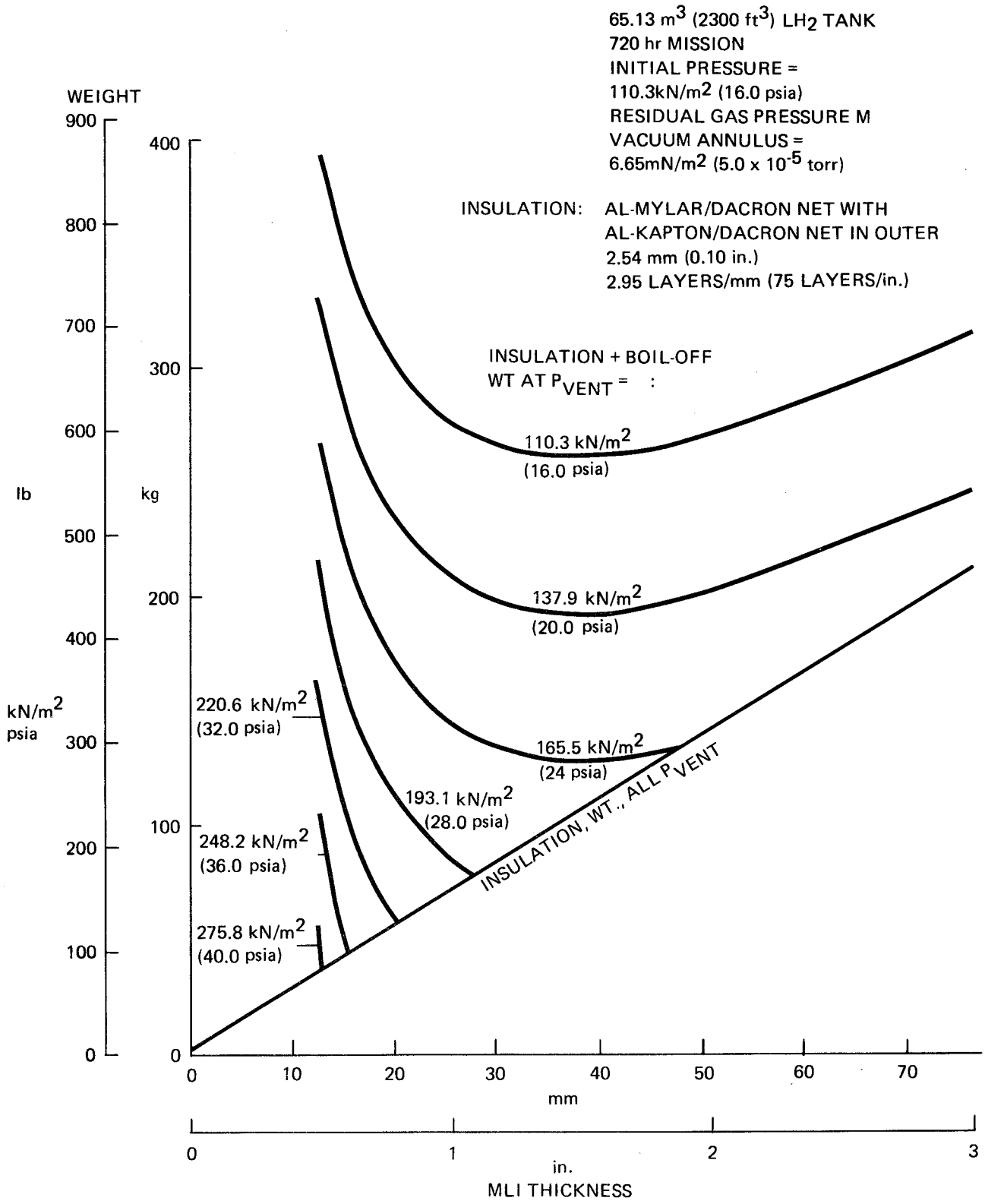

Figure 3.4-1. Insulation + Boil-Off Weight vs Pressure and MLI Thickness

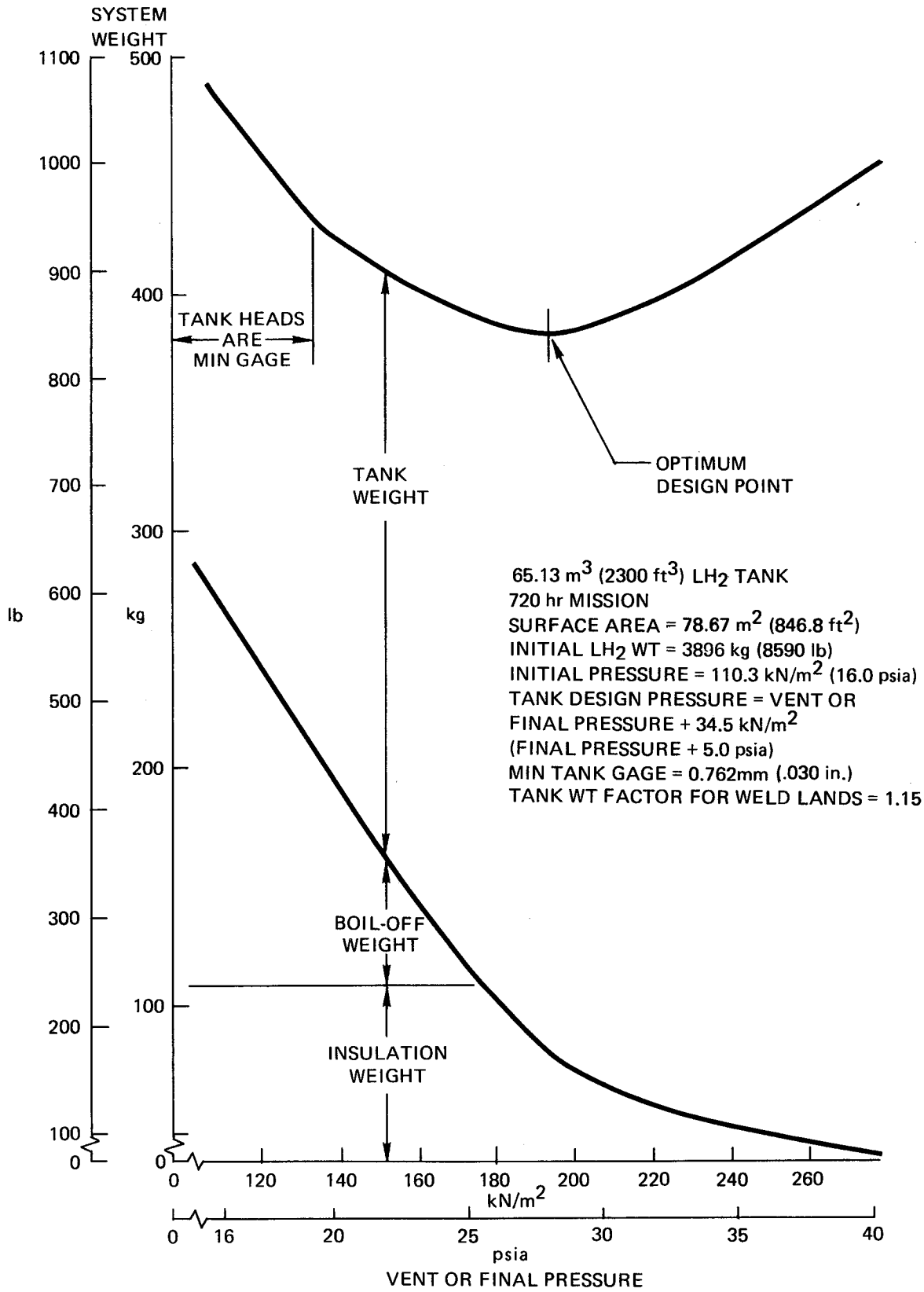

Figure 3.4-2: System Weight vs LH_2 Tank Pressure

3.4.5 Detail Investigations

Detail investigations of the OMS fuel tank thermal protection system were conducted to (1) define the maximum MLI temperature, (2) study the effects of lateral conductivity in the MLI blanket at joints and fasteners, and (3) compare effects on fuel tank design optimization for three pressure vessel support strap materials.

Maximum MLI Temperatures

Design requirements for the OMS fuel tank stipulate a 450°K (350°F) maximum temperature on the vacuum jacket external surface, occurring during orbiter reentry. A maximum allowable temperature of 394°K (250°F) was assumed for the aluminized Mylar layers. Aluminized Kapton was selected for the outer layers of the outer MLI blanket to insure the system's ability to withstand the high temperature design condition. An investigation was conducted to determine the temperatures through the MLI blanket with the vacuum annulus at the design pressure of 6.649 mN/m^2 (5.0×10^{-5} torr). The data from this analysis was used to verify the adequacy of the 2.54 mm (0.10 in.) depth of aluminized Kapton layers to prevent overheating of the aluminized Mylar.

A realistic reentry thermal environment was defined which was consistent with the baseline orbiter design and the environment therein. A point was found on the lower surface of the orbiter, near the aft end of the body, where the heat transfer from the internal surfaces of the structure would produce a 450°K (350°F) maximum temperature on the outer surface of the OMS tank vacuum shell. The heat transfer from this point during the course of the entire reentry from 122,000 m (400,000 ft) was used as the driving condition for the transient analysis. The tank itself was assumed empty but with an initial tank wall temperature of 20.5°K (37°R).

The one-dimensional model of Appendix C, Figure C-1 was employed for the reentry transient thermal analysis.

Results of the transient analysis are shown in Figure 3.4-3. The outer surface of the MLI reached a maximum temperature just below the 450°K (350°F) peak on the vacuum jacket. The temperature at the 2.54 mm (0.10 in) depth, where

the first aluminized Mylar layer is encountered, reached a peak of 372°K (209°F). Thus, the adequacy of the design was verified, at least for the basic insulation system.

It is possible that MLI temperatures will be higher during reentry than those shown in Figure 3.4-3 for some areas where local heat leaks occur. Only a small percentage of the vacuum shell, however, will be adjacent to the high temperature structure of the orbiter lower surface taken as the basis for the present analysis. Also, precautions will be taken at the support and plumbing penetrations to assure that the MLI is capable of surviving localized higher temperatures without degradation. For these reasons the 2.54 mm (0.10 in) thickness of aluminized Kapton layers was judged as adequate.

MLI Lateral Conductivity Investigation

During the course of the thermal analyses of MLI joints and fasteners, it was observed that the total additional heat flow associated with the particular penetration often exceeded that arising from the added conductance of the fastener or the radiation through the joint gaps. The additional heat flow arose from the interaction between the fasteners or joint gaps and the MLI, wherein additional heat diffused laterally into the MLI, leading to extra heat transfer to the cold wall over an area much larger than that of the heat leak feature alone.

The use of a MLI design employing an opaque spacer rather than the Dacron net to reduce the radiation component of the effective lateral conductivity, possibly reducing the penetration MLI interaction, was considered. In order to investigate the value of such a substitution, a thermal analysis of the MLI joint, as illustrated in Appendix C, Figure C-2, was conducted with the MLI lateral conductivity taken as that for an aluminized Mylar/Tissuglas system. In order to isolate the effect of the lateral conductivity change, the normal conductivity for aluminized Mylar/Dacron net was retained. In reality, a design advantage arising from reduction in heat flow due to the lower effective lateral conductivity of the Tissuglas system would be at least partially lost due to the greater weight of the Tissuglas system for the same basic heat flow.

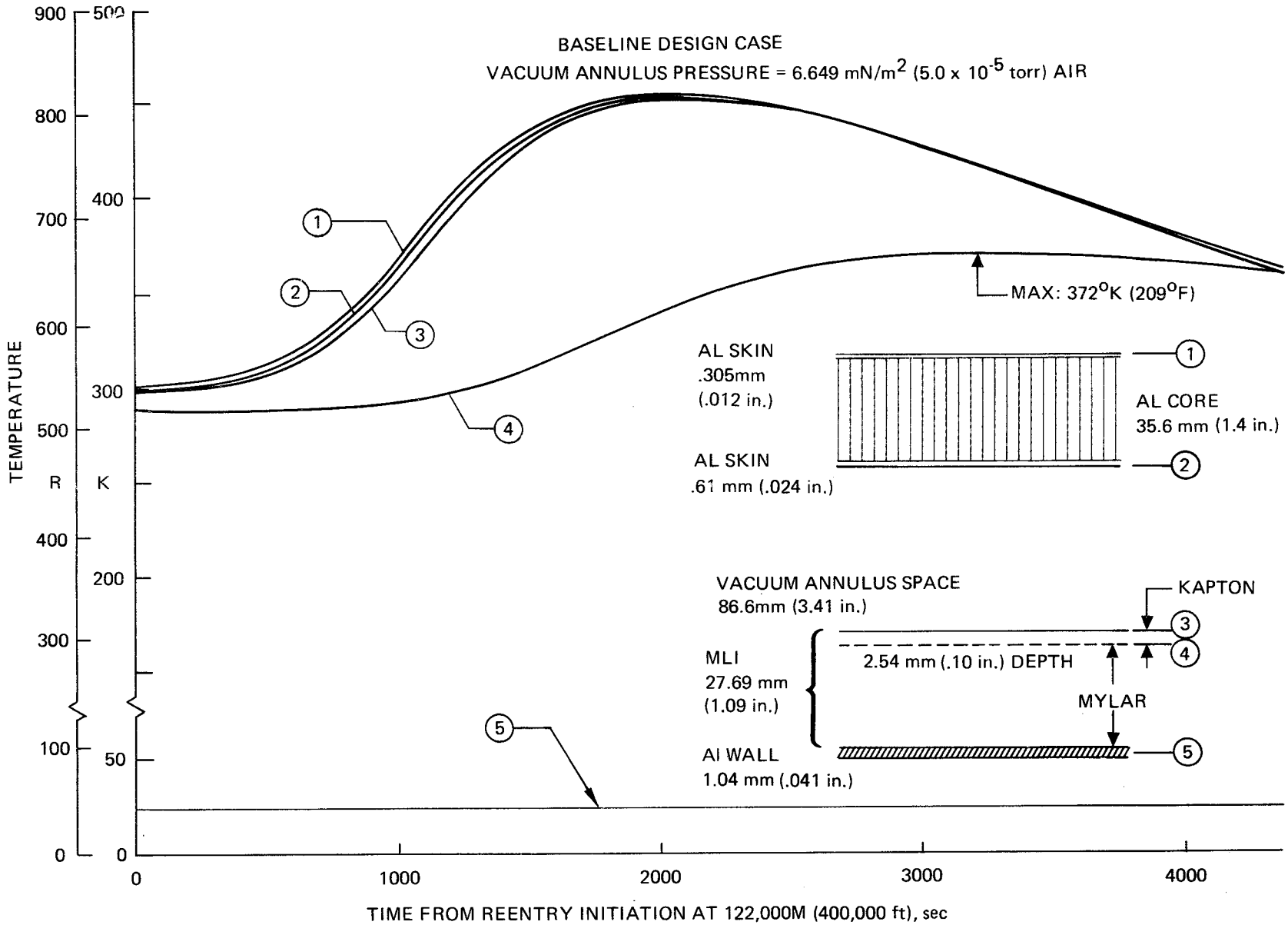

Figure 3.4-3. Temperatures During Orbiter Reentry

The results of the analysis described above showed that the Tissuglas system lateral conductivity afforded only a 5% reduction in the incremental heat leak. It was concluded that this heat flow reduction was not sufficient to warrant the substitution of Tissuglas spacers for the Dacron net locally at the penetrations.

Support Strap Design Comparisons

Heat flow values and the resulting impacts on insulation-boil-off-tank weight optimization were computed for pressure vessel support strap designs employing three materials: fiberglass/epoxy, Kevlar/epoxy (PRD/epoxy) and titanium. The analytical model for thermal analysis of the strap and the procedure for optimization are described in Appendix C. Optimization results included the effects of the selected MLI fastener designs and the tank weld land factors as described in Section 3.4-1 and thus are consistent with thermal analysis results for the baseline full scale design. A summary of the results of the comparative study is given in Table 3.4-5.

The heat flow values in Table 3.4-5 pertain to direct conduction through the strap only. In assessing the effects of strap material upon the optimized design, it was assumed that changes in material had no influence on heat flow through the surrounding MLI beyond the effects computed earlier. (As described in Section 3.4 these effects were those resulting only from the locally reduced MLI thickness at the strap attachment bolt). As a check on this assumption, the temperature distributions in the three strap designs were examined. As can be seen in Figure 3.4-4 the distributions differ little between the three materials. Thus, thermal interactions between the strap and MLI, if any, should not differ significantly from one material to another and the principal effect of strap material changes on total heat flow will be through the strap's direct conduction.

3.4.6 Gas Leakage Studies

The effects of air and hydrogen leakage and vacuum pump capability upon vacuum annulus pressure, heat flow, boil-off and MIL temperatures for the OMS fuel tanks were investigated in the gas leakage studies.

Table 3.4-5. Support Strap Thermal Comparisons

ANALYSIS CONDITIONS: PRESSURE VESSEL: 20.5°K (-423°F)
VACUUM JACKET: 311°K (100°F)
STRUCT ATTACH PT: 339°K (150°F)

STRAP MATERIAL	STRAP CROSS SECTION	HEAT FLOW ONE STRAP	OPTIMIZED DESIGN SUMMARY MLI THK	VENT PRESS	H_2 BOILOFF	TANK WT
	mm^2 ($in.^2$)	Watts (btu/hr)	mm (in.)	kN/m^2 (psi)	kg (lb)	kg (lb)
FIBERGLASS/EPOXY	645.2	.237	29.2	200.0	0	313
	(1.0)	(.809)	(1.15)	(29.0)		(690)
* KEVLAR/EPOXY	371.6	.02007	27.69	193.1	0	304
(PRD/EPOXY)	(.576)	(.0685)	(1.09)	(28.0)		(670)
(GAL-4Y)	283.9	.8274	30.98	221	0	346
	(.44)	(2.824)	(1.22)	(32.5)		(762)

*PRESENT DESIGN CHOICE

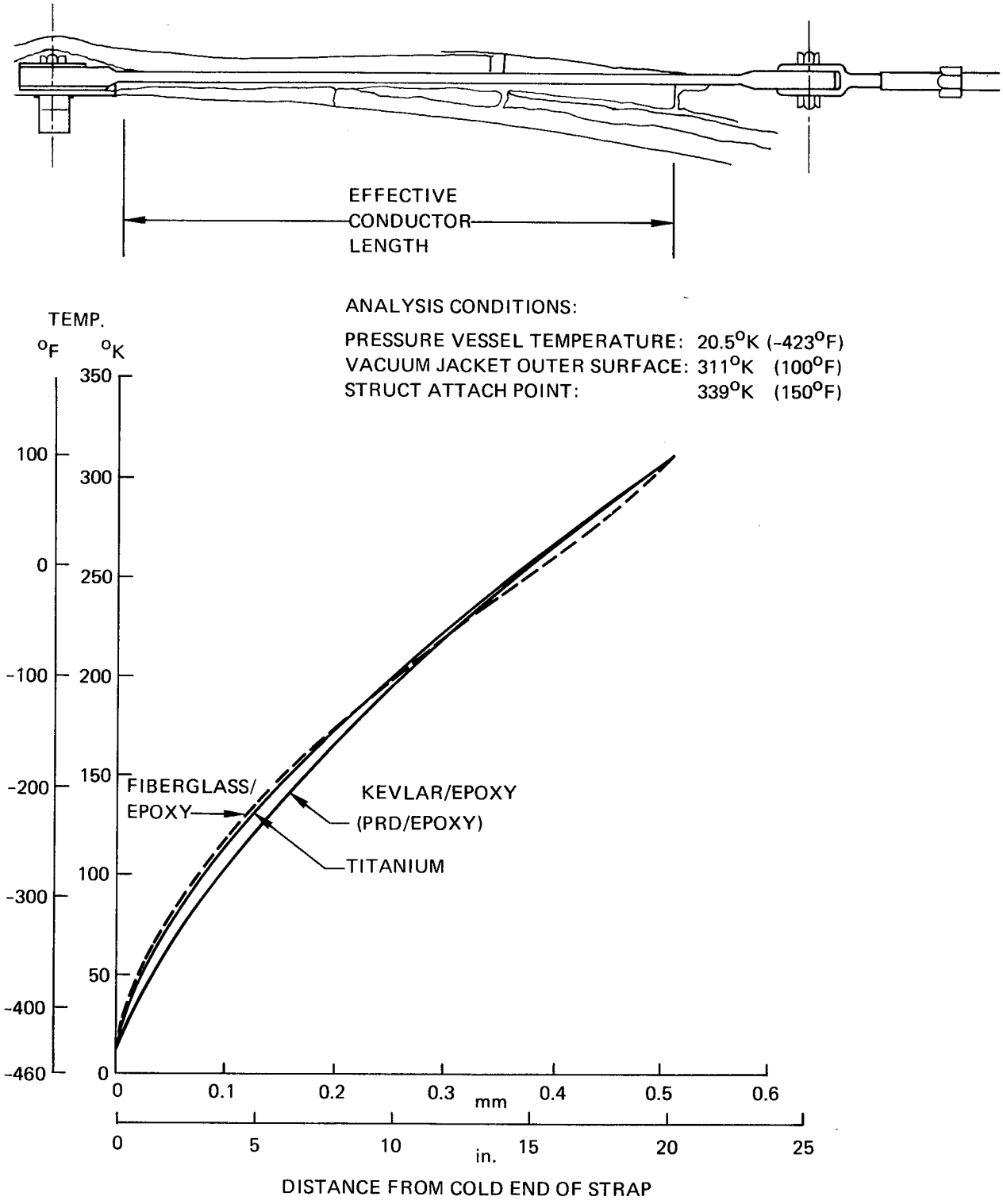

Figure 3.4-4. Temperature Distributions – Support Strap

Assumptions

All predictions for the cases of air as the assumed gas in the annulus must be regarded only as approximations for two reasons. First, it is unlikely that the gas in the annulus will be pure air but rather an unknown mixture of residual air plus water vapor and volatile hydrocarbons arising from various organic materials within or communicating with the annulus space. Second, the air and other contaminants (other than hydrogen) will be subject to cryopumping and thus will not behave as fixed quantities as was assumed for the calculations.

All leakage calculations were made under the assumption of free molecule diffusion. Initial steady-state leakage and pressure calculations were made assuming the gas temperature in the annulus was that of the annulus walls for the baseline 6.649 mN/m^2 (5.0×10^{-5} torr) pressure case. In later calculations for heat flow versus pressure, these temperatures were found to deviate very little from the baseline values. In the reentry thermal analysis, the effects of varying temperatures in the annulus upon gas pressures and conductivities were accounted for.

For the nominal leak rate case a total leak rate of 3.0×10^{-8} ml/sec (He at standard temperature and pressure) was selected, on the basis of vendor data on metallic seals, assuming the use of three seals. This value converts to 3.690×10^{-12} g/sec (2.929×10^{-11} lbm/hr) of H_2.

Vacuum Pump Characteristics

A 5 L/S D-1 (5.0 liters/second differentiation) Ultek pump was selected for application in these studies. Data on the capabilities and characteristics of these pumps were taken from Reference 6. A single ion pump rated at 5.0 liter/sec (air at .6649 mN/m^2 or 5.0×10^{-6} torr) will at the basline conditions in the vacuum annulus pump 3.049×10^{-8} g/sec (2.42×10^{-7} lbm/hr) of H_2. A single pump thus has capability far in excess of that needed to accommodate the nominal leak.

Pump rates required to balance a range of leak rates over a range of steady state vacuum annulus pressures are shown in Figure 3.4-5. The curves reflect that, for a given volumetric leak rate, the mass flow varies strongly with pressure.

Effect of Vacuum Annulus Pressure on Heat Flux

The effects of varying quantities of air and H_2 in the vacuum annulus upon heat flux through the MLI are shown in Figure 3.4-6. The data of the figure were computed using the analytical model of APPENDIX C, Figure C1, and effective conductivity developed for the respective gases by the method of APPENDIX B. The heat flux values of Figure 3.4-6 are the incremental values above that associated with the baseline pressure of 6.649 mN/m^2 (5.0×10^{-5} torr) of air.

The curves of Figure 3.4-6 apply only for steady state pressures and pressure-temperature equilibrium within the MLI. The heat flux-pressure relationships may be represented, to a close approximation, by the following expressions:

Air, $\Delta p < .133\ N/m^2$ (1.0×10^{-3} torr):

$$\Delta q_p = 18.67\ \Delta p\ watt/m^2,\ \Delta p \text{ in } N/m^2$$
$$= 7.88 \times 10^{-2}\ \Delta p\ Btu/ft^2\text{-hr},\ \Delta p \text{ in torr}$$

H_2, $\Delta p < .133\ N/m^2$ (1.0×10^{-3} torr):

$$\Delta q_p = 18.429\ \Delta p\ watt/m^2,\ \Delta p \text{ in } N/m^2$$
$$= 7.78 \times 10^{-2}\ \Delta p\ Btu/ft^2\text{-hr},\ \Delta p \text{ in torr}$$

The data of Figure 3.4-6 provided the basis for examining the effects of several potential leakage conditions upon the tank system performance. In the ensuing calculations, the effects of various gas pressures in the annulus were assumed to be only those represented by Figure 3.4-6 i.e., the effects on the basic one-dimensional heat flow only. Actually, the presence of gas at pressures other than the baseline value would have a second-order effect on the total heat flow through its influence on incremental heat flow associated with MLI joints, fasteners and other penetrations. These effects were judged to be negligible, however.

Evaluation of System Performance

The results of evaluations of the selected leakage or residual pressure conditions' effects on system performance are presented in Table 3.4-6. All of the situations investigated are allowable conditions in that the 10% boil-off limit is not exceeded.

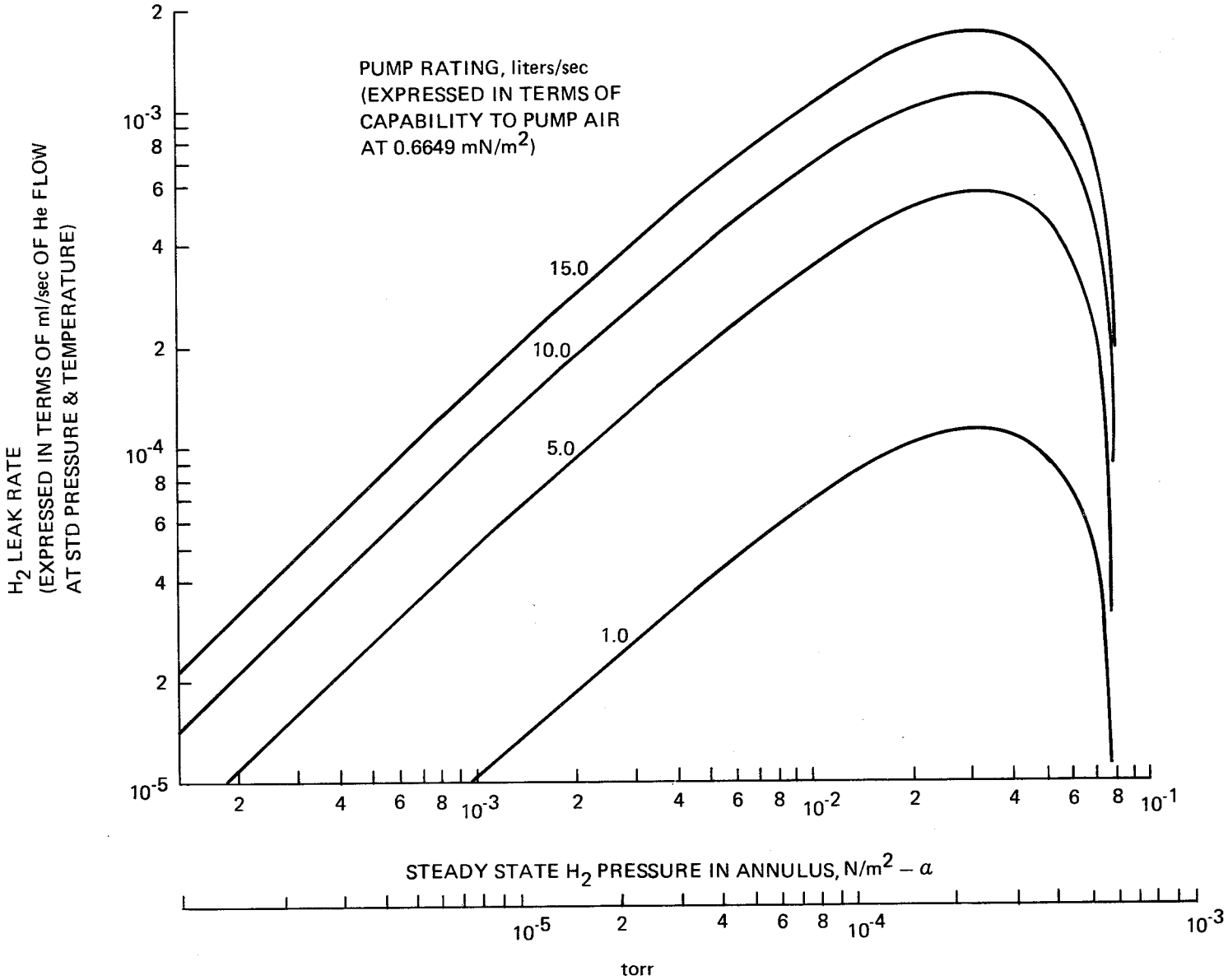

Figure 3.4-5. Equilibrium H_2 Gas Leak Rates vs Pump Rates

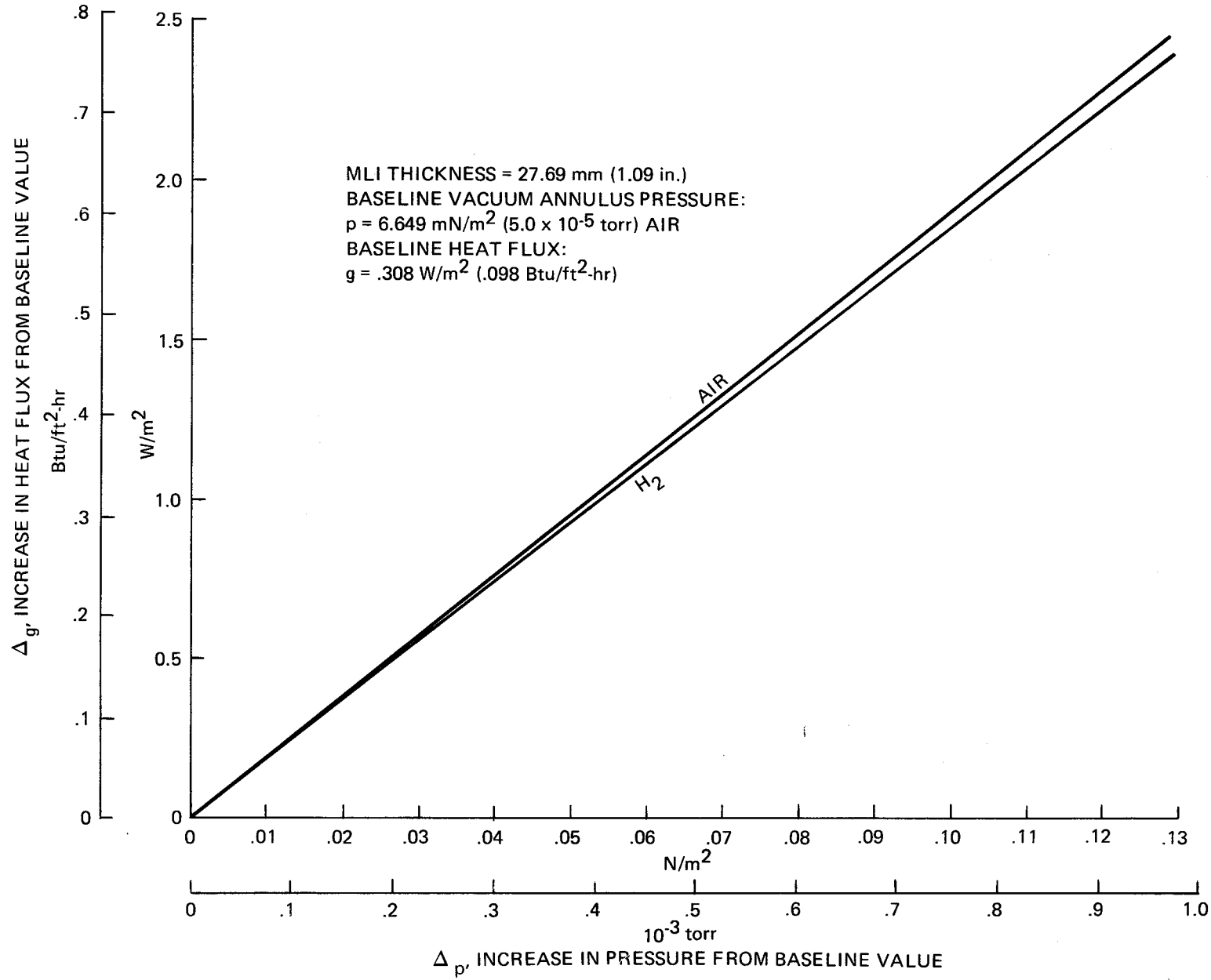

Figure 3.4-6. Heat Flux vs Vacuum Annulus Pressure

Cases 1, 3 and 4 in Table 3.4-6 are constant vacuum annulus pressure cases and may be viewed as static conditions or as conditions where constant pumping rates balance constant leakage or outgassing rates at the particular pressures. Examination of the curves of Figure 3.4-5, however, discloses that H_2 pressures above 31.92 mN/m^2 (2.4×10^{-4} torr) fall on the "back side" of the pump capability curves, indicating an unstable and probably unrealistic condition. Thus, case number 4 realistically applies only to a fixed quantity of H_2 in the annulus and no pumping or leakage in progress.

Reentry Thermal Analyses

The discussion in Section 3.4.5 showed that the basic insulation system could survive the high temperature reentry environment with the outer 2.54 mm (0.10 in) of MLI made up of aluminized Kapton/Dacron net layers.

However, the design ground rules allow up to 10% H_2 boil-off and since such H_2 loss can result from leakage gas in the vacuum annulus, it was necessary to examine MLI reentry temperatures under conditions of vacuum annulus pressures corresponding to the 10% boil-off limit. The conditions analyzed are cases 3, 4 and 5 in Table 3.4-6.

The gas effective conductivity expression, as described in Appendix B for MLI application, was modified for the reentry thermal analysis for application to a single space between parallel surfaces. The resulting formula, for the two gases of interest is

$$k_g = .0616\, S\, P_{air}\, T_m^{-.48} + .244\, S\, p_{H_2}\, T_m^{-.7}, \quad \frac{\text{watt-m}}{m^2\text{-K}}$$

$$= 1920\, S\, P_{air}\, T_m^{-.48} + 7610\, S\, p_{H_2}\, T_m^{-.7}, \quad \frac{\text{Btu-in.}}{ft^2\text{-hr-R}}$$

S = annulus space, mm (in)

P = partial pressure, N/m^2 (torr)

T_m = mean temperature of gas in annulus, K (R)

An evaluation of the Knudsen Numbers for the gas in the vacuum annulus, as shown below, disclosed that Table 3.4-6 cases 3, 4 and 5 may lie near or just

Table 3.4-6. Effects of Vacuum Annulus Leakage or Pressure on System Performance

CASE	DESCRIPTION	H_2 NET LEAK RATE; ml/sec (EXPRESSED IN TERMS OF STD He	AT END OF 30 DAY MISSION				
			VACUUM ANNULUS PARTIAL PRESSURES; mN/m^2 (torr)		PRESSURE VESSEL PRESSURE; kN/m^2 (psia)	SYSTEM HEAT LOAD; Mw-sec (Btu)	H_2 BOIL-OFF kg (lb)
			AIR	H_2			
1.	BASELINE	0	6.649 (5.0×10^{-5})	0	193.1 (28.0)	87.52 (82960)	0
2.	NOMINAL H_2 LEAK (NO PUMPING)	3.0×10^{-8}	6.649 (5.0×10^{-5})	1.291 ($.971 \times 10^{-5}$)	196.5 (28.58)	89.93 85240	0
3.	CONST AIR PRESSURE YIELDING 10% BOIL-OFF	0	60.21 (4.528×10^{-4})	0	241.3* (35.0)	163.85 (155307)	389.6 (859)
4.	CONST H_2 PARTIAL PRESSURE YIELDING 10% BOIL-OFF	0	6.649 (5.0×10^{-5})	54.25 (4.080×10^{-4})	241.3* (35.0)	163.85 (155300)	389.6 (859)
5.	CONST H_2 LEAK RATE YIELDING 10% BOIL-OFF (NO PUMPING)	2.591×10^{-6}	6.649 (5.0×10^{-5})	108.50 (8.159×10^{-4})	241.3* (35.0)	163.85 (155300)	389.6 (859)

*ASSUMED VENT VALVE SETTING

outside the boundary of the free-molecule regime, depending upon the free-molecule-transition criterion employed.*

Case (Table 3.4-6)	Kn
1	12.01
3	1.245
4	2.736
5	1.318

$$Kn = \frac{\lambda}{S} = \frac{\text{molecule mean free path}}{\text{characteristic dimension (annulus space)}}$$

It was concluded, however, that any error resulting from the use of a gas conductivity expression derived for free-molecule conditions would not be important to the predicted temperature histories. The basis for this conclusion was the observation that in all the cases analyzed, radiation remained the dominant mode of heat transfer across the annulus.

Figure 3.4-7 is a typical curve plotted from the results of the reentry thermal analysis. This figure shows the results from the Table 3.4-6 case 51.e. constant 2.591×10^{-6} H_2 leak rate into the annulus yielding after 30 days vacuum annulus partial pressures of 6.649 mN/m^2 (5.0×10^{-5} torr) an + 108.5 mN/m^2 (8.16×10^{-4}) H_2. The maximum Mylar shield temperature in this case is 386°K (235°F) and cases 3 and 4 were 380°K (225°F) and 386°K (235°F) respectively. Thus, the 2.54 mm (0.10 in) layer of Kapton shield is adequate.

Conclusions

The several significant conclusions reached on the basis of the gas leakage calculation were:

*Some authors recommend Kn > 1.0 as defining the free-molecule regime; others specify Kn > 10.0 as the criterion.

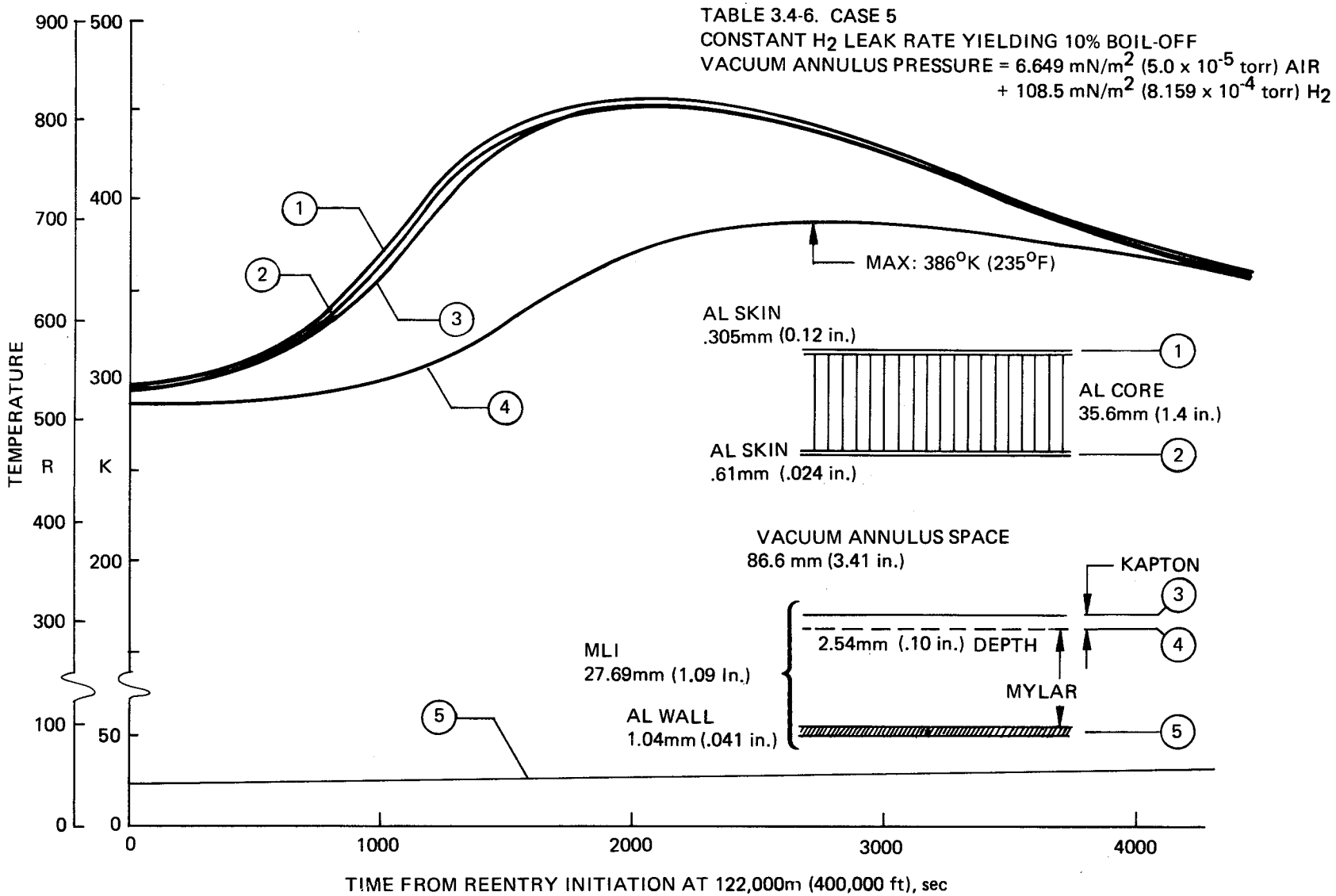

Figure 3.4-7. Temperatures During Orbiter Reentry

1) That a small ion pump could easily accommodate a reasonable assumed nominal H_2 leak rate;
2) That three small ion pumps could handle rather large leak rates, provided the annulus pressure was not allowed to rise above a particular level (this critical pressure is high enough so as not to place a difficult requirement on vacuum maintenance);
3) That some increase in heat flow due to leakage or residual annulus pressure beyond the baseline design values could be tolerated with no boil-off or other penalty;
4) That rather large leak rates (approximately 100 times the nominal) or rather large residual annulus pressures (almost 10 times the baseline design value) can be tolerated before the 30 day, 10% H_2 boil-off limit is reached; and finally,
5) That the 2.54 mm (0.10 in) Kapton outer layers in the outer MLI blankets is adequate to prevent high temperature MLI damage even in the high MLI conductivity case resulting in 10% boil-off.

4.0 HALF SCALE LH_2 TEST MODEL DESIGN & ANALYSIS

4.1 DESIGN REQUIREMENTS

The half scale LH_2 test model was controlled by the criteria outlined below. These criteria were based on the contract work statement and test and transportation safety considerations.

4.1.1 Life

Equivalent to one hundred operational flight cycles (pressure and thermal).

4.1.2 Thermal Protection System

The thermal protection system will be designed to provide the same heat flow per unit of tank surface area as in the OMS fuel tank design.

4.1.3 Loading Conditions

Load factors critical to tank and support structure design will be as specified in the following table. These limit load factors are recommended in Reference 1.

Transportation Limit-load Factors

Mode	Longitudinal (g)	Lateral (g)	Vertical (g)
Truck	±3.5	±2.0	±6.0

4.1.4 Pressure Vessel Supports

Factors of Safety

Yield	1.1
Ultimate	1.5

Thermal Conditions

Maximum	450°K (+350°F)
Minimum	20.3°K (-423°F)

4.1.5 Vacuum Jacket

Minimum weight design using materials selected for the OMS fuel tank design. Limit design external pressure = 101.4 kN/m^2 (14.7 psia)

Factors of Safety

Yield	1.1
Ultimate	1.4

Temperature Conditions

Maximum	450°K (+350°F)
Minimum	R.T.

4.1.6 Pressure Vessel

Design to minimize cost and ease of fabrication

operating pressure = 117.2 kN/m^2 (17 psia)

Configuration

2.29m (7.5 ft) inside diameter x 2.75 m (9.0 ft)

Design Conditions

Room temperature proof test = 279.4 kN/m^2 (40 psia)

Design burst pressure = 482.6 kN/m^2 (70 psia)

4.1.7 Plumbing Lines

Factor of Safety

Proof	1.5
Ultimate	2.5

4.2 DESIGN

The LH_2 test model was essentially a half scale simulation of the OMS fuel tank design. With the exception of the "boiler plate" pressure vessel all major components on the LH_2 test model were initially designed using the same configuration but scaled down and manufacturing processes proposed for the OMS fuel tank. Design improvements were made to the component details of the LH_2 test model as manufacturing planning and hardware fabrication progressed. Most of these LH_2 test model design changes would be reflected in the OMS fuel tank design before it was released for manufacture.

Appendix D contains the complete set of released drawings for the fabrication of the LH_2 test model. Figure 4.2-1 is the LH_2 test model assembly drawing. The assembly and the major component design features are discussed in the following paragraphs.

4.2.1 Assembly (Figure 4.2-1)

The major differences between the LH_2 test model assembly and the OMS fuel tank assembly occur at the two apex fitting locations. The vent line and vent relief valve arrangement was replaced with a fill and vent tube arrangement, without a valve located in the vacuum anulus. The fill and feed line, the manhole cover and the submerged shut off valve arrangement were replaced with a simulated plumbing line arrangement which did not penetrate the pressure and vacuum jacket walls nor contain a manhold cover. Rather the simulated plumbing line provided the heat leak to the cryogen which represented the total scaled heat leak of the OMS fuel tank vent line plus the fill and feed line.

The vacuum pump down and maintenance arrangement was simplified on the LH_2 test model. The vacuum pumpdown experience discussed in Section 4.7.5 suggests that a similar arrangement would satisfy the OMS fuel tank requirements and thereby eliminate a potential vacuum seal problem in the vacuum pumpdown line adhesive bond joint to the vacuum jacket.

SK2-2082-13VS

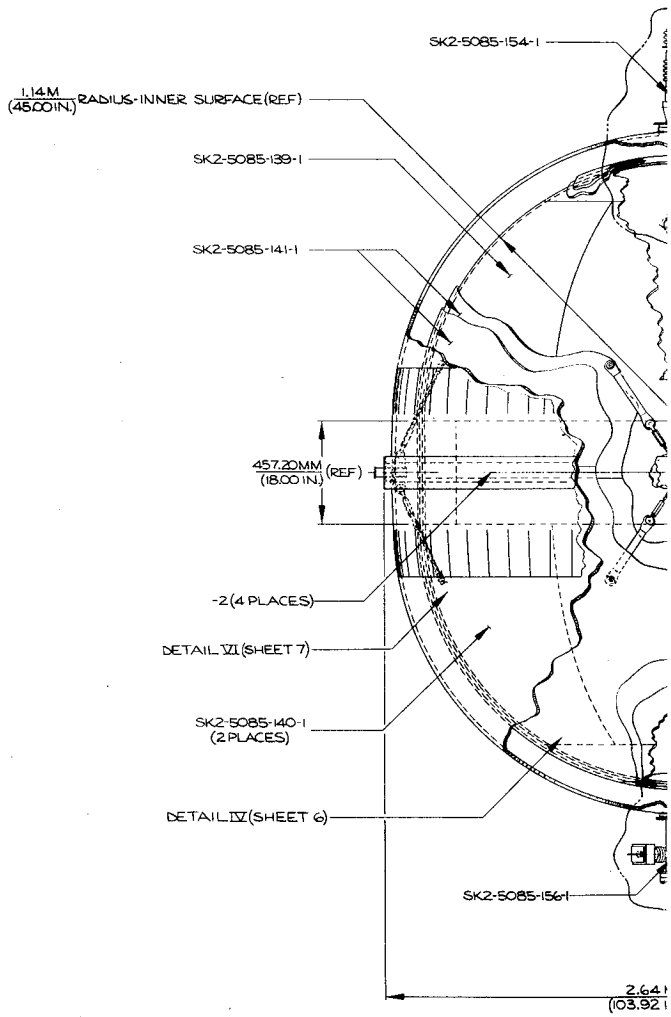

-1 HAL

LH_2 TES

ASSE

REVISIONS			
ZONE LTR	DESCRIPTION	DATE	APPROVED
A	RE-DRAWN	8/30/74	

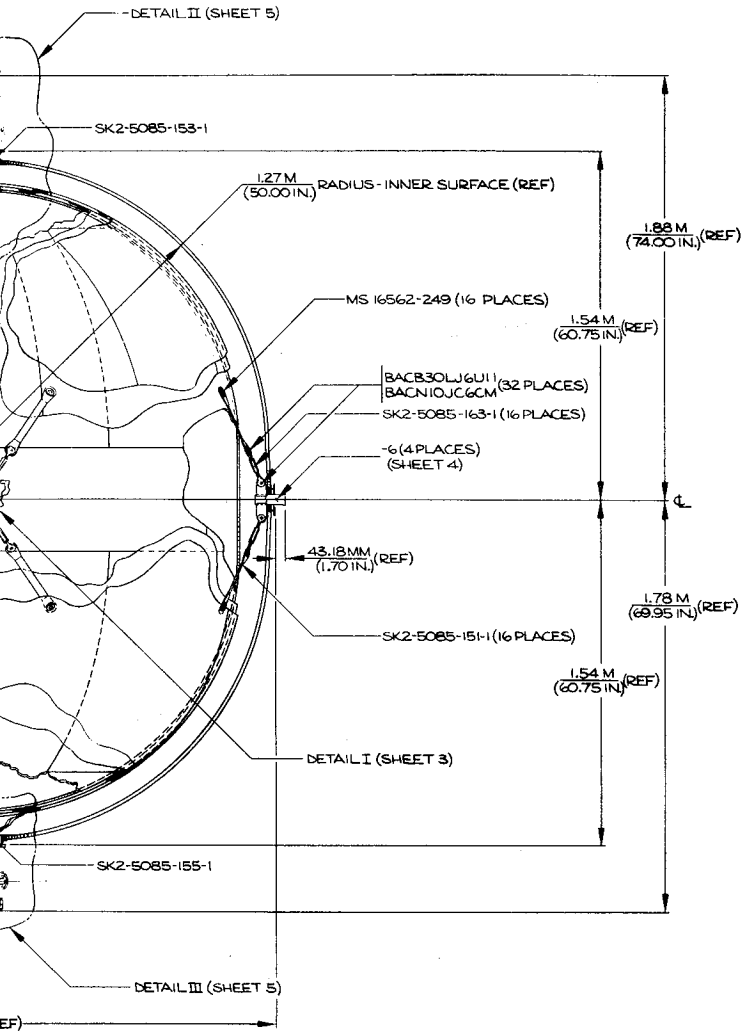

SCALE
MODEL
MBLY

Figure 4.2-1

SEE SHEET 1 FOR PARTS LIST AND NOTES

DATA REVIEW		CONTRACT NUMBER	THE BOEING COMPANY
DWG QUAL		NAS3-15848	CORPORATE OFFICES SEATTLE, WASHINGTON 98124
STRUCT		DWN D.M.DUNNING 8/30/74	HALF SCALE
MATL & PRCS		CHK	LH_2 TEST MODEL
		ENGR	ASSEMBLY
		ORG	
		PROJECT APPROVAL	SIZE J CODE IDENT NO 81205 SK2-5085-137
CHANGE/ITEM NUMBER			SCALE 1/10 SH 2 OF 4

DRAWING RECORDS CLERK

DWG ORIG BY (ORG) 2-5520

SK2-5085-137 REV A2

SK2-2082-1315 REV

4.2.2 Vacuum Jacket (Figures 4.2-2 and D-9 through D-12)

Two significant design improvements developed as the detail drawings and the manufacturing planning were being prepared. The first, mentioned in the discussion on the assembly, was the relocating of the vacuum pumpdown port and the three vac-ion pumps to the simulated plumbing vacuum jacket apex closeout fitting. Since this was a monocoque aluminum fitting, the pumpdown port and vac-ion pump lines were welded to the fitting. The weld joint provided a more reliable vacuum seal than the bonded joint necessary on the OMS fuel tank. The second design improvement was the use of welded stretch formed sections for the girth ring. This approach was more cost effective with better weight control than the machined ring proposed in the OMS fuel tank design.

Head Construction

The vacuum jacket heads for the LH_2 test model comprised the machined apex fitting and the welded stretch formed girth ring bonded to the honeycomb sandwich shell.

Twelve 0.305 mm (0.012 in) gage, 2024-T81 aluminum stretched-formed gores were used for both inner and outer face skins. At the more highly stressed girth area, a doubler of the same gage was bonded to both inner and outer face skins. The joint of the inner face skin gores consisted of an inner 0.076 mm (0.003 in) thick 1100-H18 aluminum vacuum sealing strip and an outer 0.305 mm (0.012 in) thick 2024-T81 aluminum structural joining strip. XA 3919 (3 M Co) adhesive was used to bond this joint and the doubler to the inner face skin. An outer 0.305 mm (0.012 in) thick 2024-T81 aluminum structural strip bonded with XA 3919 adhesive was used to join the outer skin gore. The outer skin doubler was bonded with XA 3919 adhesive. The 5056/F40 - 0.0014, 33.64 kg/m^3 (2.1 lb/ft^3), 15.37 mm (6.05 in) thick, aluminum Flex-Core was bonded to the face skins with Metlbond 329 adhesive.

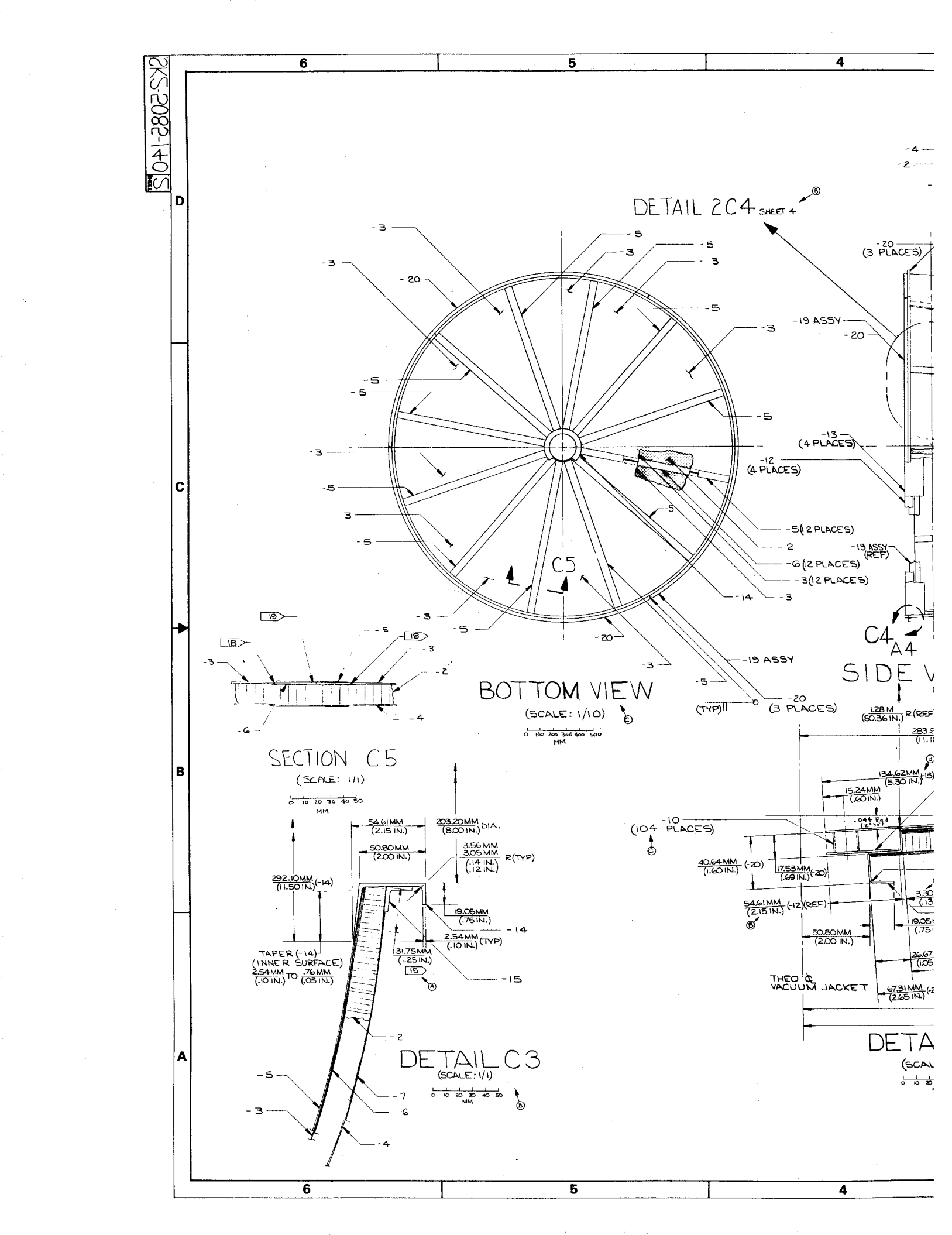
DETAIL 2C4 SHEET 4
C5
BOTTOM VIEW
(SCALE: 1/10)
SECTION C5
(SCALE: 1/1)
DETAIL C3
(SCALE: 1/1)
C4
A4
SIDE V
-20 (3 PLACES)
-19 ASSY
-13 (4 PLACES)
-12 (4 PLACES)
-5 (2 PLACES)
-6 (2 PLACES)
-3 (12 PLACES)
-19 ASSY (REF)
-10 (104 PLACES)
THEO @ VACUUM JACKET
TAPER (-14) (INNER SURFACE)
2.54MM (.10 IN.) TO .76MM (.03 IN.)
54.61MM (2.15 IN.)
203.20MM (8.00 IN.) DIA.
50.80MM (2.00 IN.)
3.56 MM 3.05 MM (.14 IN.) (.12 IN.) R(TYP)
292.10MM (11.50 IN.) (-14)
19.05MM (.75 IN.)
2.54MM (.10 IN.) (TYP)
31.75MM (1.25 IN.)
134.62MM (5.30 IN.)
15.24MM (.60 IN.)
40.64MM (1.60 IN.) (-20)
17.53MM (.69 IN.) (-20)
54.61MM (2.15 IN.) (-12) (REF)
67.31MM (2.65 IN.)

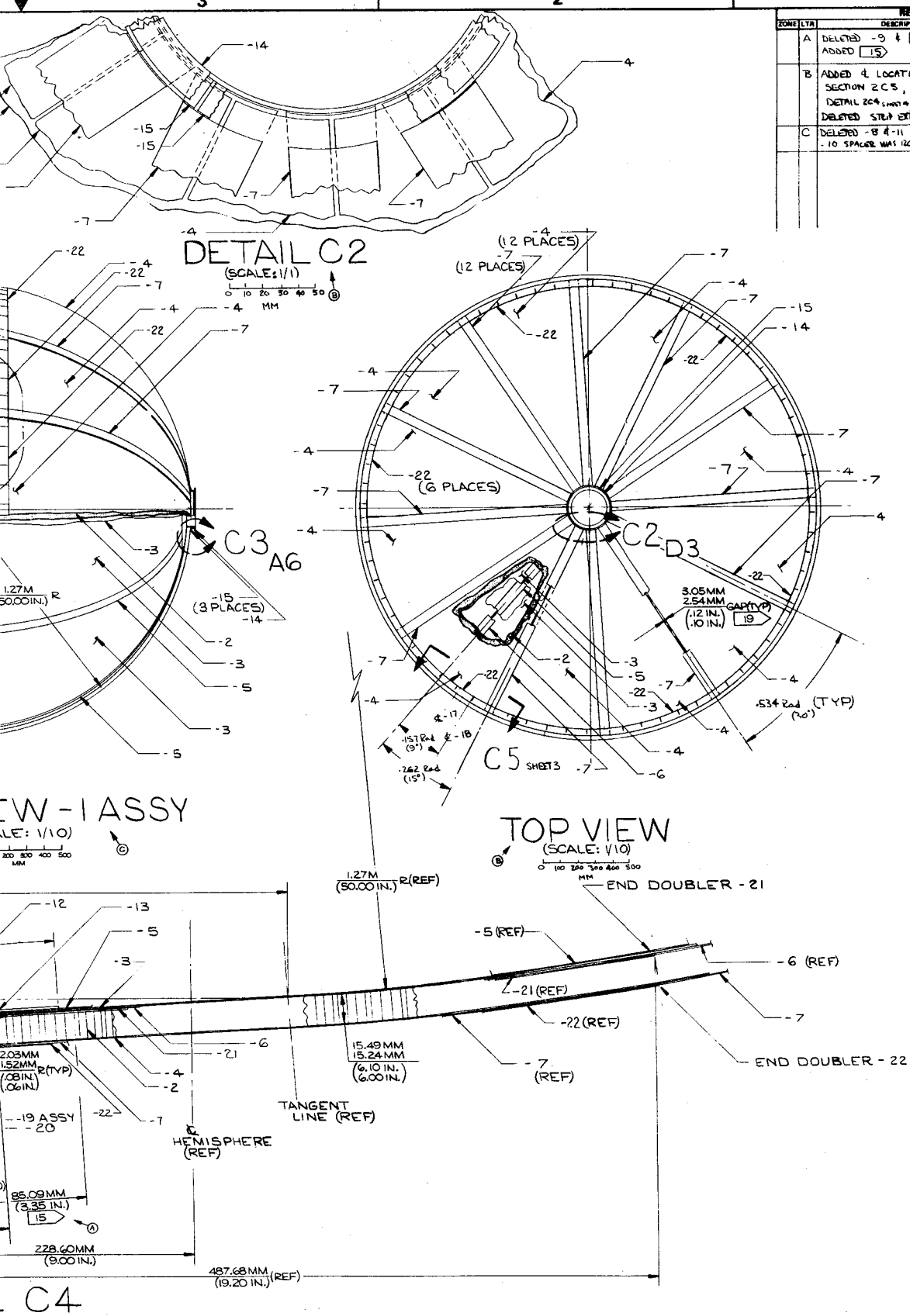

REVISIONS				
ZONE	LTR	DESCRIPTION	DATE	APPROVED
	A	DELETED -9 & 5 ADDED 15	4/16/73	BMB
	B	ADDED & LOCATING -17 & -18, SECTION 2C5, DETAIL C5 (MAY) DETAIL 2C4 SHEET 4, & 12 DELETED STRIP EXT -16.	7/6/73	BMB
	C	DELETED -8 & -11 FILLERS -10 SPACER WAS 120 PLACES	7/26/73	BMB

Figure 4.2-2

SEE SHEET 1 FOR PARTS LIST AND NOTES

DATA REVIEW	
DWG QUAL	
STRUCT	
MATL & PRCS	
CHANGE/ITEM NUMBER	

CONTRACT NUMBER NAS3-15848

DWN	K.W. OSBORNE	12-19-72
CHK		
ENGR	D.L. BARCLAY	3-26-73
ORG		
PROJECT APPROVAL		

THE BOEING COMPANY
CORPORATE OFFICES SEATTLE, WASHINGTON 98124

VACUUM JACKET HEAD ASSEMBLY-HALF SCALE LH2 TEST MODEL

SIZE	CODE IDENT NO	SK2-5085-140
J	81205	

SCALE NOTED SH 2 of

DRAWING RECORDS CLERK

DWG ORIG BY (ORG) 2-5520

SK2-5085-140 C2

2KS-2082-140S

TOTAL WEIGHT OF VACUUM JACKET ASSEMBLY

	Item	kg	lb.
1)	Two vacuum jacket heads with joining plates bolted in place, and vacuum seal strip welded in place	144.81	319.24
2)	Inlet closeout fitting	4.19	9.23
3)	Simulated Plumbing Closeout Fitting	3.16	6.97
4)	Closeout Fitting Cover Plate with Connector	1.62	3.58
5)	Trunnions	3.59	7.88
	TOTAL	157.35	346.90

4.2.3 MLI (Figures D-13 through D-27)

The major design improvement made to the LH_2 test model MLI panel assemblies was the use of one type (Figure D-27) of Nylon pin and washer assembly for assembling the MLI panel. A single pin and a multiple (3) pin arrangement was used. The experience gained in fabrication of the MLI panels for the LH_2 test model suggests that this same assembly arrangement can be used for the OMS fuel tank.

The total weight of the 28 MLI panel assemblies was 23.59 kg (52.0 lb).

4.2.4 Pressure Vessel (Figure D-8)

The "boiler plate" pressure vessel was a simplified design for ease of manufacture. The total weight of the pressure vessel assembly including the inlet tube and the simulated plumbing line was 525.74 kg (1159.06 lb).

4.2.5 Support Strap (Figure D-30)

The lighter loading on the LH_2 test model pressure vessel support system made it possible to simplify the titanium end fitting to Kevlar/epoxy (PRD/epoxy) adhesive bond joint.

The total weight of the support straps with turnbuckles was 10.30 kg (22.70 lb).

4.3 STRUCTURAL ANALYSIS

Structural analysis was made for the vacuum jacket, the girth ring and the pressure vessel support system to assure that the LH_2 test model met the design requirements of Section 4.1.

"Point" designs for three different core thicknesses were made to determine the optimum core depth and vacuum jacket weight for the LH_2 test model. Materials and method of fabrication were selected from the OMS fuel tank study Section 3.0. Both stress and stability analyses were used to size the "point" designs. From these data the optimum core depth and skin gages were selected for the final stress and stability analysis. The structural analysis of the support system concentrated on loads, deflections, and stresses for the LH_2 test model transportation and test conditions.

4.3.1 Vacuum Jacket

Structural Optimization

The three different "Point" designs were made for the LH_2 test model vacuum jacket at the maximum design temperature (Reference Section 4.1) of 450°K (350°F). Core thicknesses of 12.7 mm (0.5 in), 17.8 mm (0.7 in) and 22.8 mm (0.9 in) were assumed to bracket the optimum vacuum jacket weight. The BOSOR 3 (Reference 4) analysis method was used to determine the aluminum face skin thicknesses required for each core thickness. The materials used were:

Core: 5056 Aluminum Flex-Core, 33.64 kg/m^3 (2.1 lb/ft^3) density,

Face Skins: Aluminum 2024-T81, bare

An allowable compression stress of 207 MN/m^2 (30 ksi) was used for the aluminum 2024-T81, consistent with the material allowables used in the OMS fuel tank design. The OMS fuel tank girth ring properties were used in the optimization since a girth ring of this size appeared to be a practical minimum also for the LH_2 test model. A knockdown factor of 0.28 was used for the stability critical designs.

The BOSOR 3 structural model is shown in Figure 4.3-1. Thirteen segments were used to accommodate possible changes in cross section or a more detailed analysis model. Segments ① through ⑪ were sandwich construction. Segments ⑫ and ⑬ were monocoque to simulate the bellows and closeout at the top of the vacuum jacket. A constant core thickness was used for all the sandwich segments. The required face skin gages calculated for each core thickness are listed in Table 4.3-1 for a "stress critical" design and a "stability critical" design.

The weights for each core thickness and critical case were calculated. An adhesive weight of 0.346 kg/m^2 (0.0006 lb/in^2) was included for the core to face bond of each face. The weights versus core thickness are plotted in Figure 4.3-2. The optimum weight 62.6 kg (168 lb) was achieved at a core thickness of about 15.2 mm (0.6 in). For that optimum design the vacuum jacket had an equal chance of exceeding the allowable stress of 207 MN/m^2 (30 ksi) or failing in general instability. Thinner core designs than the optimum would be heavier and be stability critical. Thicker core designs than the optimum would be heavier and stress critical.

The optimum weight core thickness of 15.7 mm (0.6 in) was selected for the LH_2 test model vacuum jacket. Standard skin gages of 0.302 mm (0.012 in) thick 2024-T81 alclad were selected for this design. Segments ① - ④ and ⑨ - ⑪ used single gages of this material for each face skin. Segments ⑤ - ⑧ used two gages of the 0.302 mm (0.012 in) material adhesively bonded together for each face skin. The following sections describe the analyses of this design.

Stress Analysis

The 2024-T81, alclad aluminum sheet purchased in the 0.302 mm (0.012 in) thickness has slightly lower properties than the bare material due to the cladding. Table 4.3-2 lists the analysis properties for aluminum 2024-T81 alclad at several temperatures. The 5056 aluminum Flex-Core properties at 294°K (70°F) and 450°K (350°F) are listed in Table 4.3-3.

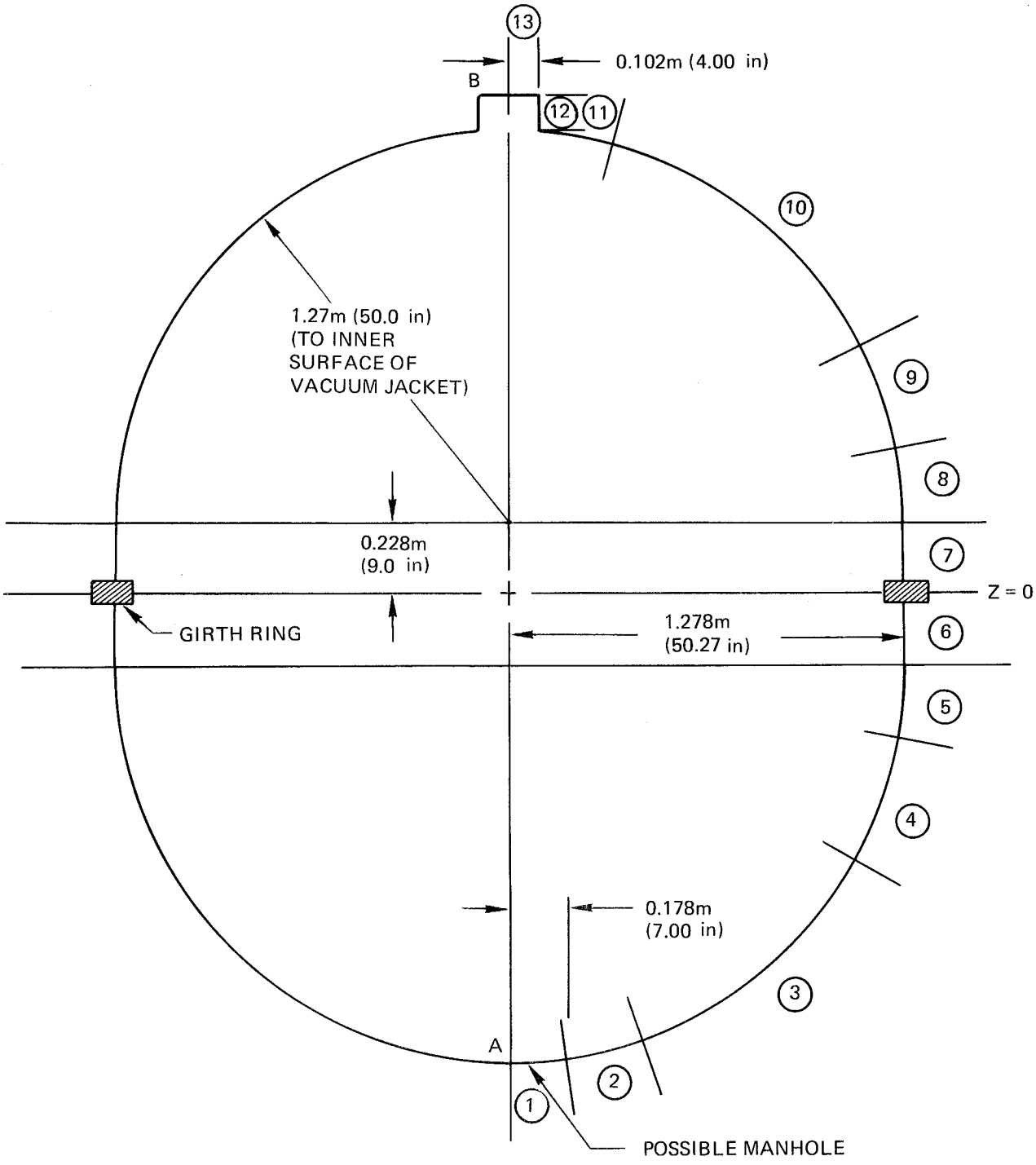

Figure 4.3-1: BOSOR3 Structural Model for the Vacuum Jacket - LH_2 Test Model

Table 4.3-1: Required Face Skin Gages for Different Core Thicknesses on the Vacuum Jacket Head - LH_2 Test Model

Critical Load Condition: -142 kN/m^2 (-20.6 psi) at 450°K (350°F)

Materials: Face Skins - Aluminum alloy 2024-T81, bare
Core - 5056 aluminum - Flex-Core 33.64 ka/m^3 (2.1 lb/ft^3)

Core Thickness	Critical Case	Segments (1) - (4), (9) - (11) [1]	Segments (5) - (8) [1]
12.7 mm (0.5 in)	1. Stress	.254/12.7/.254, (.010/.5/.0150)	.457/12.7/.457 (.018/.5/.018)
12.7 mm (0.5 in)	2. Stability	.254/12.7/.254, (.010/.5/.010)	.558/12.7/.558 (.022/.5/.022)
17.8 mm (0.7 in)	3. Stress	.254/17.8/.254, (.010/.7/.010)	.406/17.8/.406 (.016/.7/.016)
17.8 mm (0.7 in)	4. Stability	.254/17.8/.254, (.010/.7/.010)	.356/17.8/.356 (.014/.7/.014)
22.8 mm (0.9 in)	5. Stress	.254/22.8/.254, (.010/.9/.010)	.356/22.8/.356 (.014/.9/.014)
22.8 mm (0.9 in)	6. Stability	.254/22.8/.254, (.010/.9/.010)	.254/22.81.254 (.010/.9/.010)

[1] Numbers shown are gages and core thickness of sandwich in the order - $t_i/t_c/t_o$ where,

t_i - inner skin gage - mm (in)

t_c - core thickness - mm (in)

t_o - outer skin gage - mm (in)

The minimum gage thickness was .254 mm (.010 in)

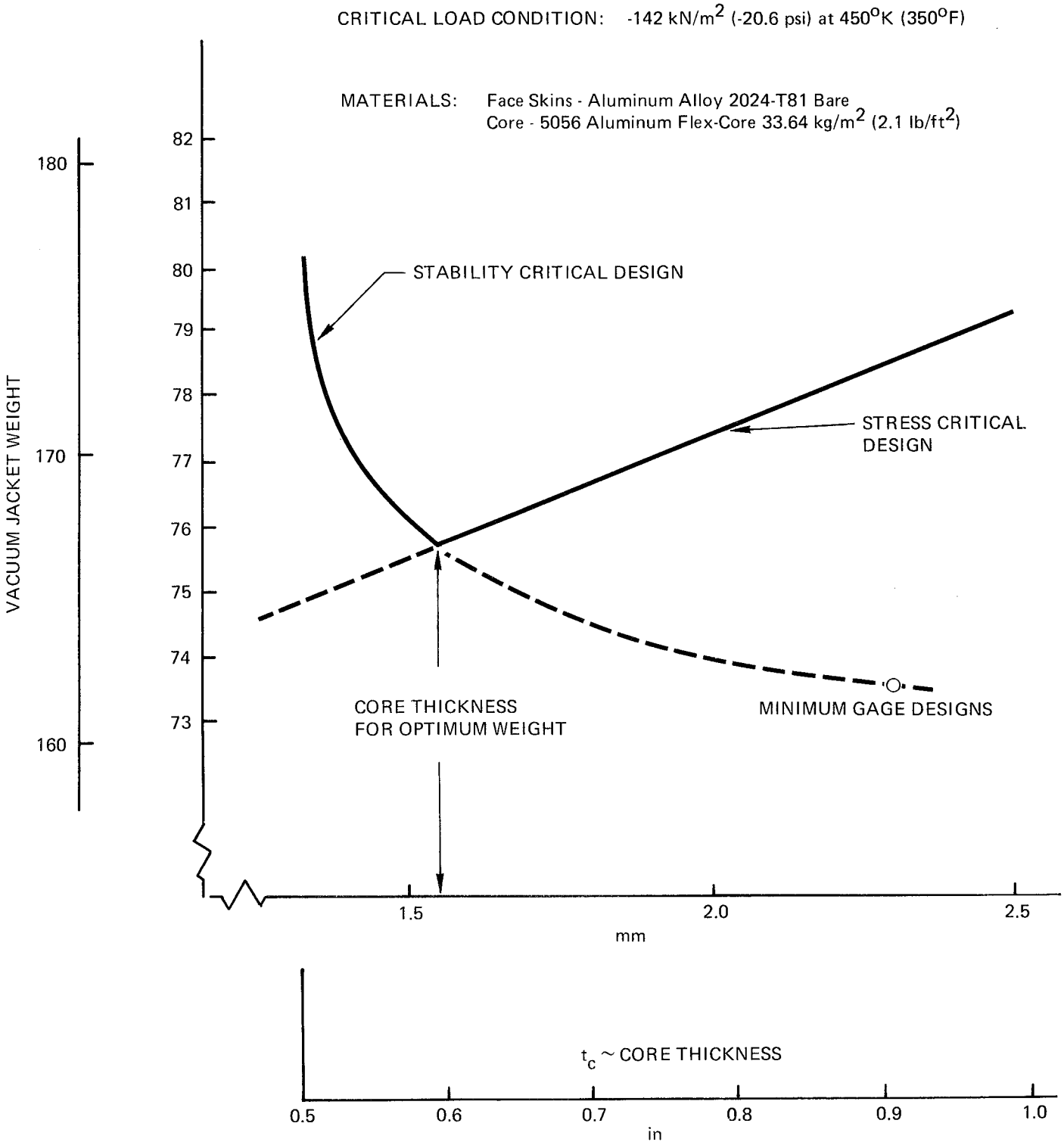

Figure 4.3-2: Vacuum Jacket Weight Vs Core Thickness - LH_2 Test Model

Table 4.3-2: Analysis Properties - Aluminum Alloy 2024-T81, Alcad 0.302 mm (.012 in) Thick
B - Basis Allowables

TEMPERATURE		E		v	G		Fcy		Fp.l.	
^oK	^oF	GN/m^2	psi x 10^6		GN/m^2	psi x 10^6	MN/m^2	ksi	MN/m^2	ksi
294	70	66.9	9.7	0.33	24.8	3.6	393.0	57	290.0	42
395	250	64.8	9.4	0.33	24.1	3.5	351.6	51	255.1	37
450	350	62.1	9.0	0.33	23.4	3.4	296.4	43	206.8	30
478	400	60.0	8.7	0.33	22.8	3.3	234.4	34	137.9	20

Table 4.3-3: Analysis Properties - 5056 Aluminum Flex-Core, 33.64 kg/m^3 (2.1 lb/ft) Density, 15.2 mm (0.6 in) Thick

TEMPERATURE		APPROX. HONEY COMB ALL SIZE		E_c		G_l		G_w		F_t		F_c	
^oK	^oF	mm	in.	MN/m^2	ksi	MN/m^2	ksi	MN/m^2	ksi	kN/m^2	psi	kN/m^2	psi
294	70	76.2	.300	359	52	100	14.4	55	8.0	1440	208	1440	208
450	350	76.2	.300	222.7	32.3	61.4	8.92	34.2	4.96	889.3	129	889.3	129

The BOSOR 3 model shown in Figure 4.3-3 was used for the stress and deflection analysis. Following the optimization study it was decided to make both halves of the vacuum jacket identical. This simplified the analysis model. Since the girth ring is a plane of symmetry, only half the vacuum jacket was analyzed.

Face Stresses

Two sandwich constructions were used for the vacuum jacket head. Segments 2 and 3 were constructed of a nominal face skin thickness of 0.302 mm (0.012 in) gage on a 15.2 mm (0.6 in) thick core. Segments 4 and 5 were constructed using two sheets of 0.302 mm (0.012 in) gage on each side of a 15.2 mm (0.6 in) thick core.

The vacuum jacket head was analyzed for the two temperatures, 294°K (70°F) and 450°K (350°F); and the two external pressures, 101 kN/m^2 (14.7 psi) and 142 kN/m^2 (20.6 psi) specified in the design requirements, Section 4.1. The limit load was 101 kN/m^2 (14.7 psi) external pressure at 450°K (350°F). The critical design condition was the ultimate load 142 kN/m^2 (20.6 psi) external pressure at 450°K (350°F). It was assumed that all the face skins would be thinner than the nominal gage, but within the tolerance permitted by the sheet specification.

The results of the BOSOR 3 deflection analysis for -142 kN/m^2 (-20.6 psi) at 450°K (350°F) are plotted in Figures 4.3-4 through 4.3-7 for Segments 2 through 5 . The maximum radial deflection, W_o, was 2.13 mm (0.085 in.) inward at arc length 0.38 m (15 in.). The maximum membrane loads were N_{10} = -92 kN/m (-525 lb/in.) and N_{20} = -122 kN/m (-700 lb/in.). The maximum M_{10} bending moment was -843 N. m/m (-190 in-lb/in) and occurred at the girth ring, arc length 85. The critical stresses were calculated with the equations described in Section 3.3.1 . The allowable compression stress was assumed to be the proportional limit stress, Fpl listed in Table 4.3-2. At 450°K (350°F) it is 206 MN/m^2 (30 ksi) for the aluminum alloy 2024-T81, alclad material using B-Basis allowables. B-Basis allowables were selected because a proof test was required for the vacuum jacket head. The -165 MN/m^2 (-24.4 ksi) maximum stress in the 0.302 mm (0.012 in.) face skins occurred at arc length 1.75 m (68.8 in.). Using the allowable stress, the margin-of-safety was,

M.S. = 206/165-1 = +0.23

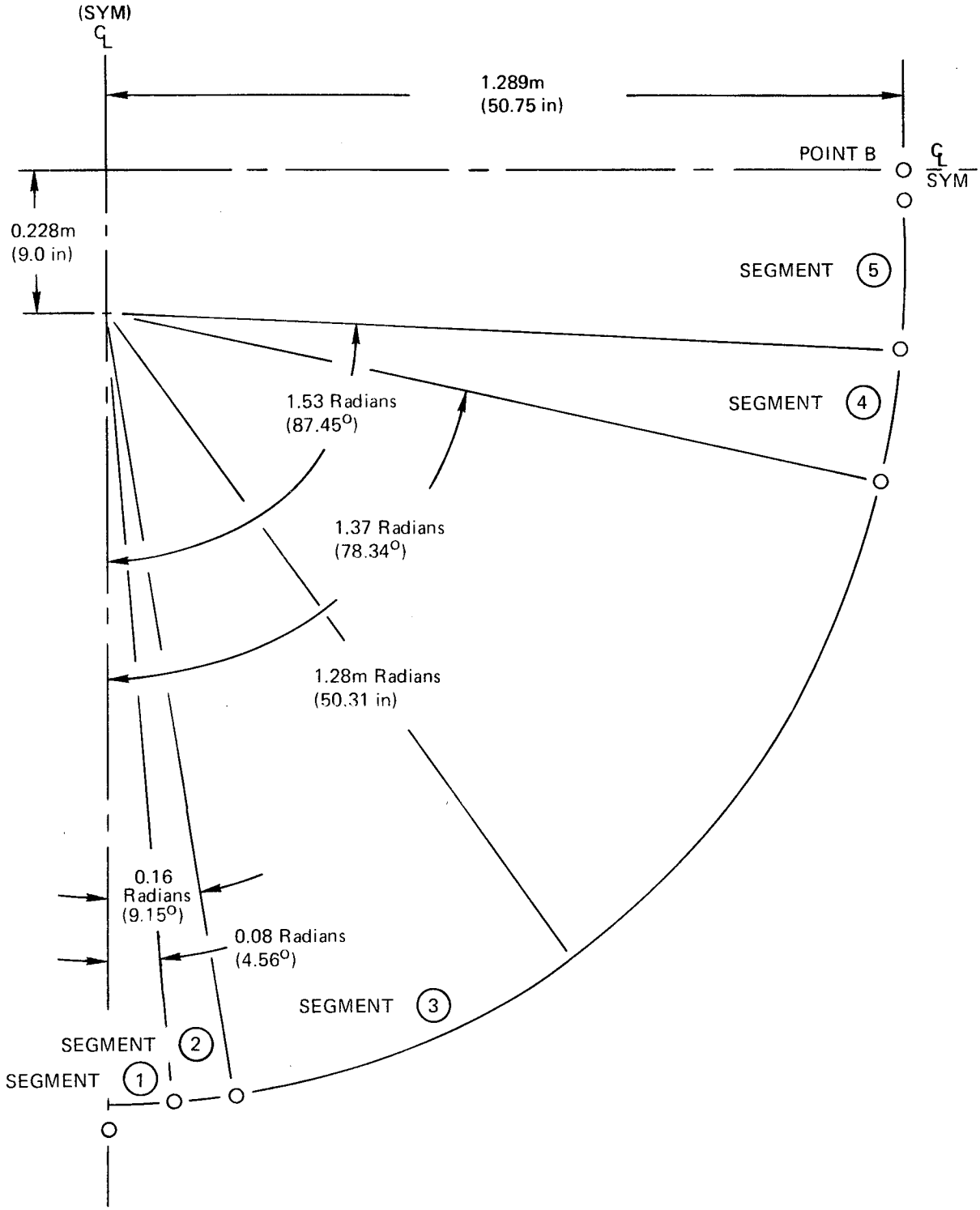

Figure 4.3-3: Vacuum Jacket Head Reference Surface for BOSOR3 Analysis - LH_2 Test Model

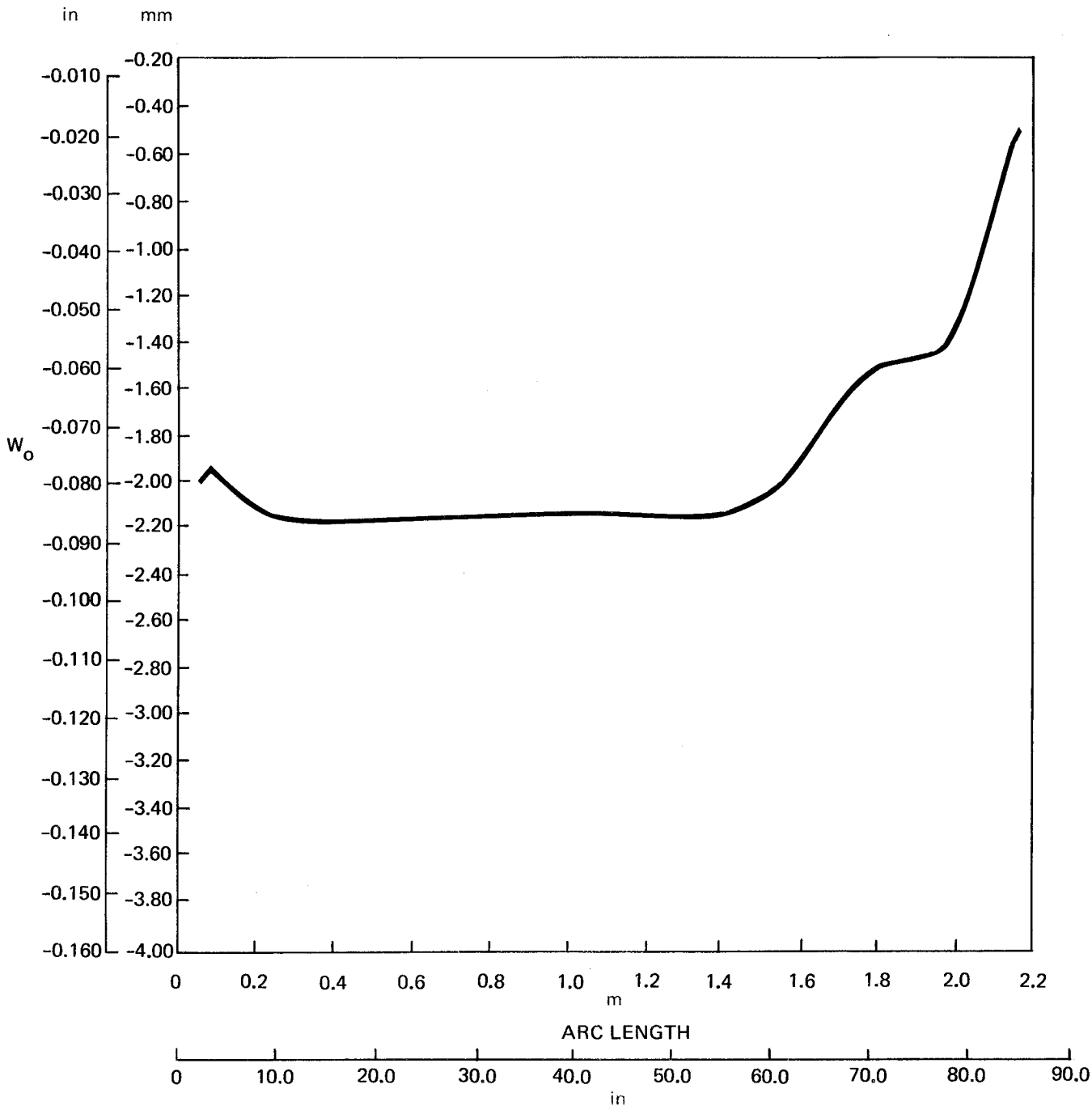

Figure 4.3-4. Wo Versus ARC Length at 450°K (350°F) for Vacuum Jacket LH_2 Test Model

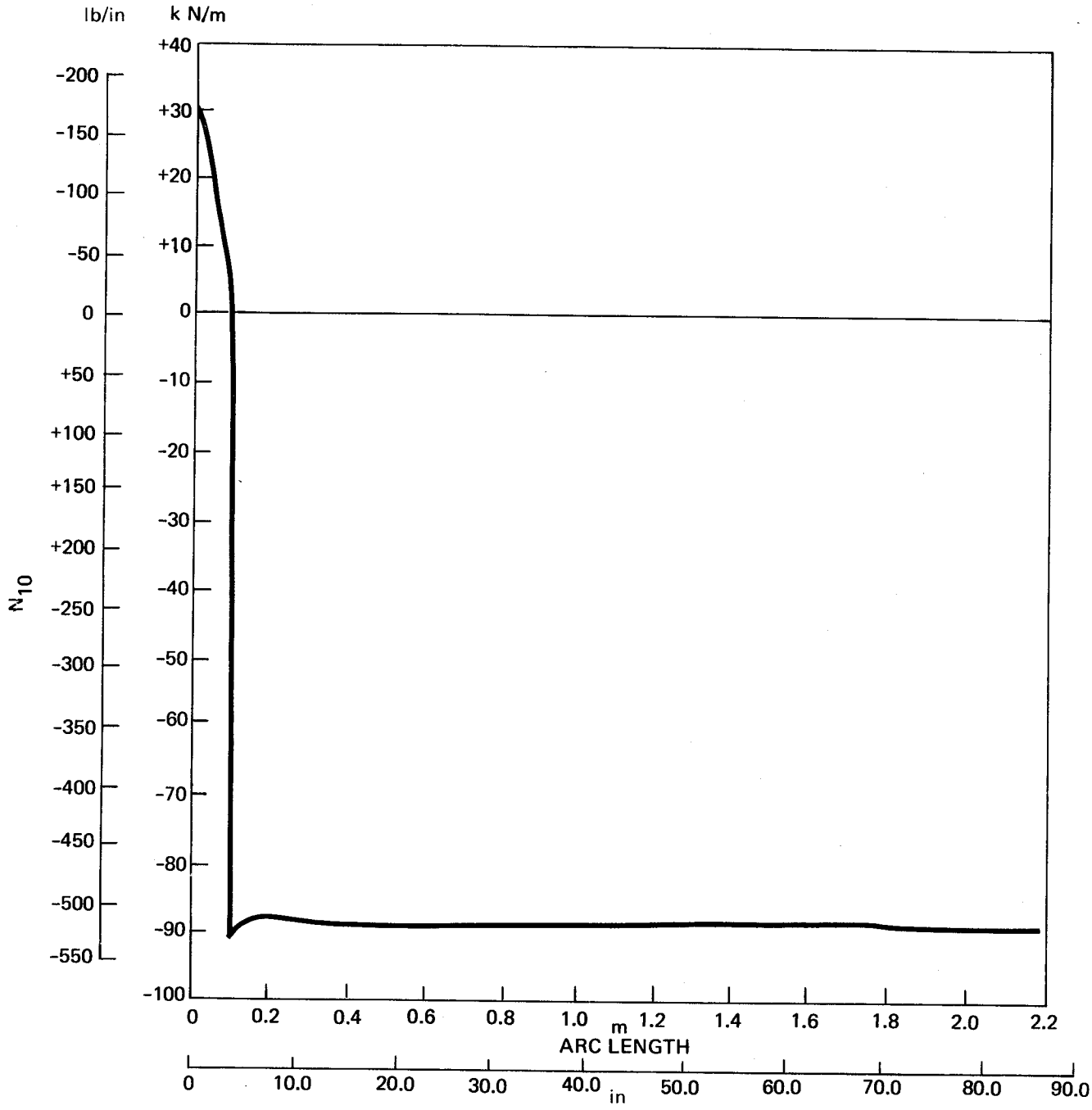

Figure 4.3-5. N_{10} Versus ARC Length at 450°K (350°F) for Vacuum Jacket - LH_2 Test Model

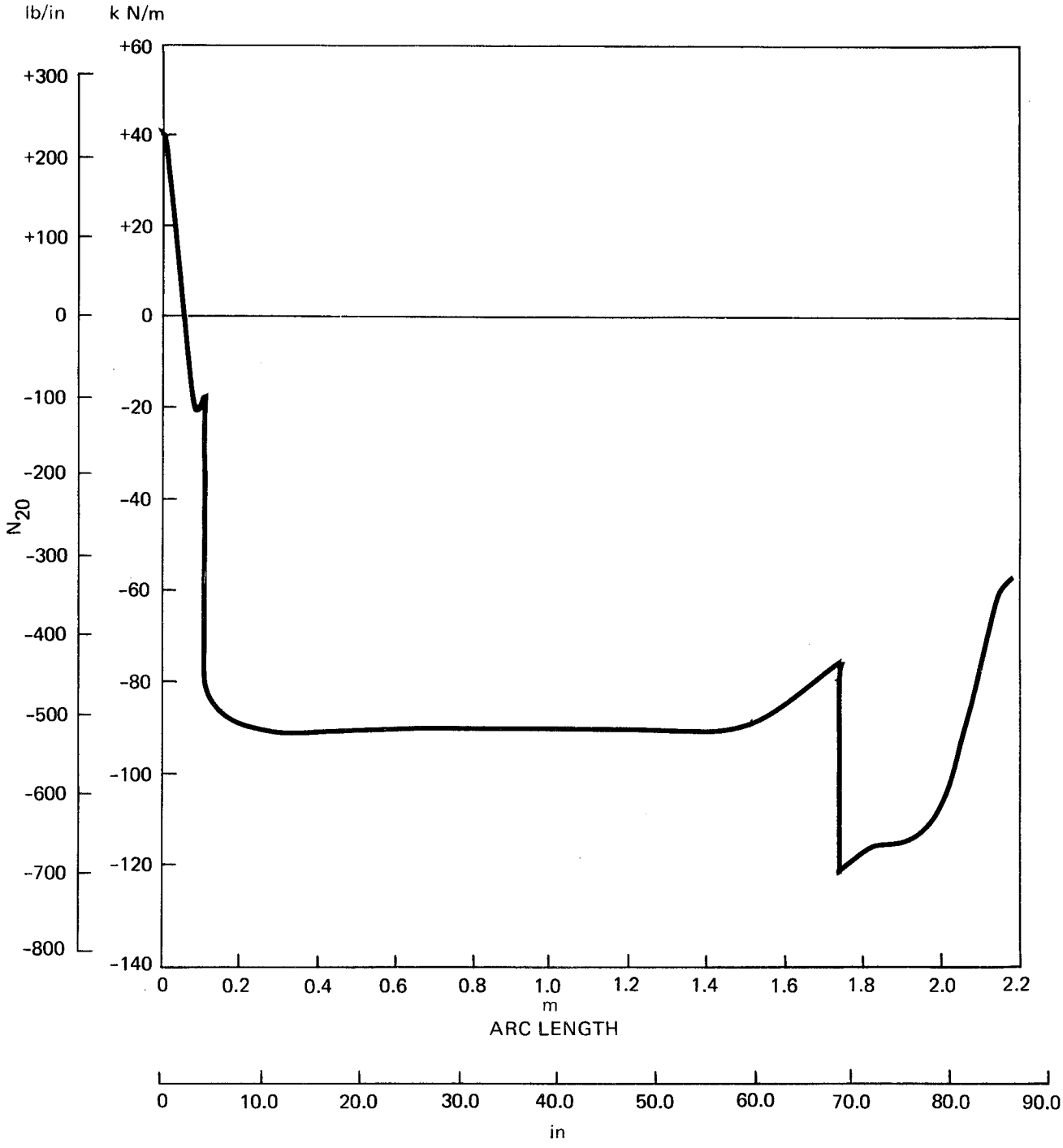

Figure 4.3-6. N_{20} Versus ARC Length at 450°K (350° F) for Vacuum Jacket - LH_2 Test Model

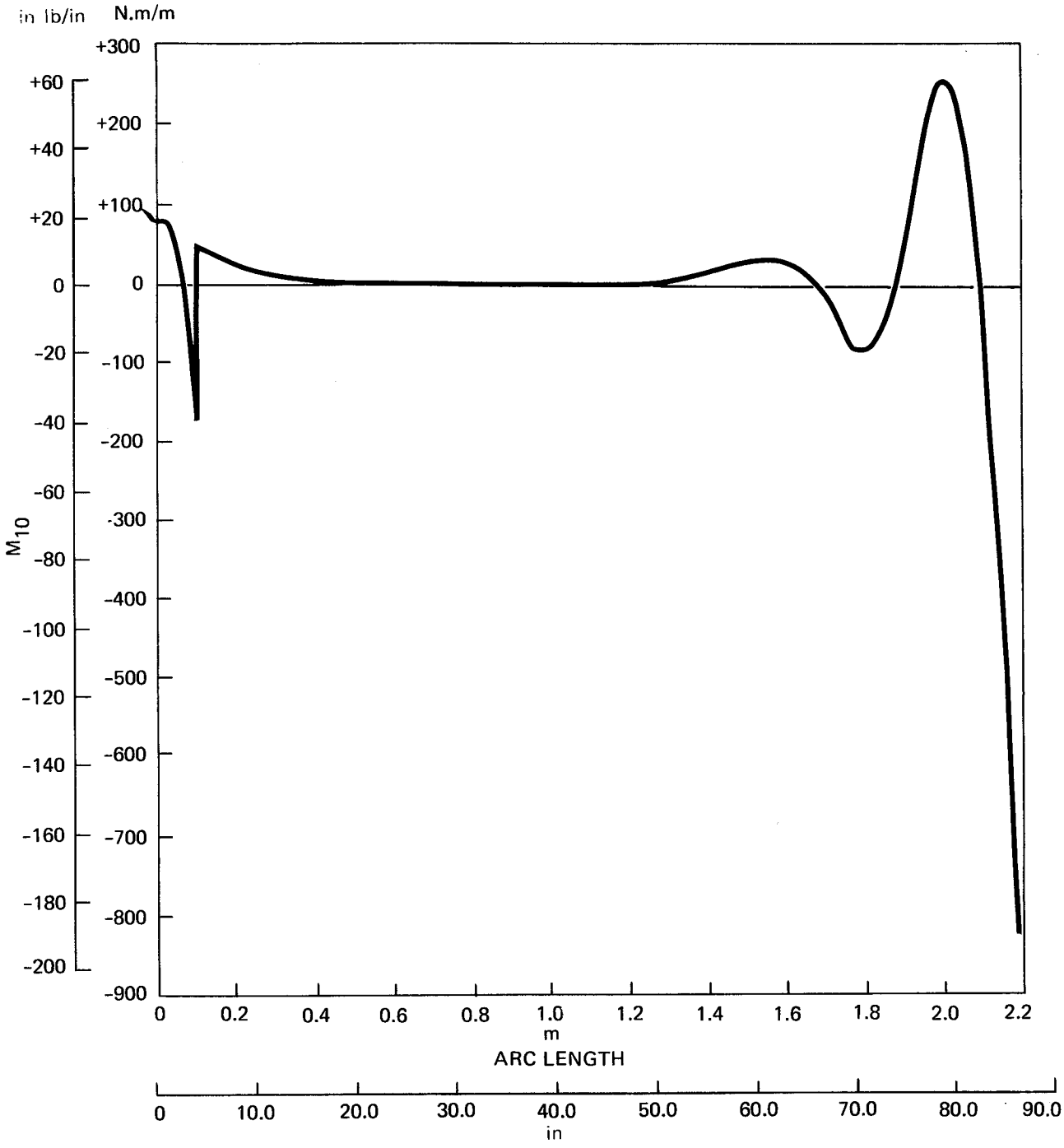

Figure 4.3-7. M_{10} Versus ARC Length at 450°K (350°F) for Vacuum Jacket - LH_2 Test Model

The -135 MN/m^2 (-19.6 ksi) maximum stress in the 0.604 mm (0.024 in.), face skins occurred at arc length 2.16 m (85.1 in.). The margin-of-safety there was

M.S. = 206/135-1 = +0.53

Both of these margins were for the nominal face skin gages. Assuming that the minimum gage of the 0.302 mm (0.012 in.) nominal sheet was 0.267 mm (0.0105 in.) and that stretch-forming reduced the thickness by 2.5 percent, the minimum gage would be 0.259 mm (0.0102 in.). This would result in locally higher stresses since the loads were the same. At arc length 1.75 m (68.8 in.), the maximum local face skin stress would be -191 MN/m^2 (-27.7 ksi) resulting in a margin-of-safety of

M.S. = 206/191 -1 = +0.80

At arc length 2.16 m (85.1 in.) the minimum face skin gage would be two 0.259 mm (0.0102 in.) sheets bonded together. The maximum stress would be -158 MN/m^2 (-23.0 ksi) resulting in a margin-of-safety of

M.S. = 206/158 -1 = +0.30

Intracell Buckling

The allowable intracell buckling stresses were computed using the equations described in Section 3.3.1. However, the 45-inch diameter head test data from Reference 3 were analyzed to determine new values of k and s which were representative of the LH_2 test model vacuum jacket head construction and loading. The values used were k = 7.4 and s = 0.4.

For the 0.302 mm (0.012 in.) nominal face skin gage the allowables stresses were determined by an F/E_t ratio of 0.0050. The allowable stresses were read from Figure 4.3-8, the stress-modulus plot for aluminum 2024-T81 alclad. The allowable stress at 450°K (350°F) was 240 MN/m^2 (35 ksi); at 294°K (70°F) the allowable stress was 310 MN/m^2 (45 ksi). The nominal face skin gage margin-of-safety at 450°K (350°F) and 142 kN/m^2 (20.6 psi) was

M.S. = 35/24.4 -1 = +0.43

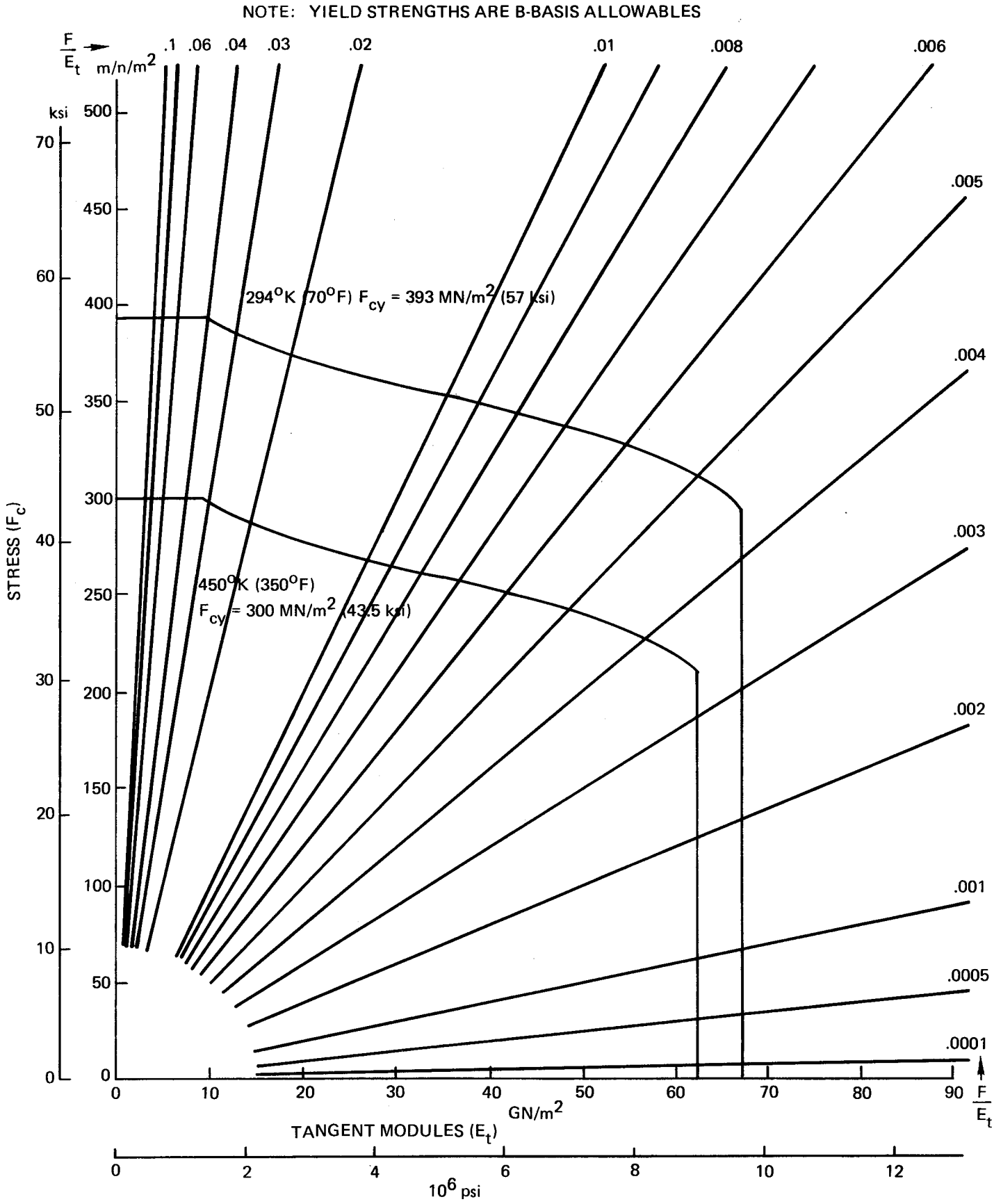

Figure 4.3-8. Stress Modulus Curve for Clad 2024-T81 Aluminun Alloy

The minimum gage thickness allowable stress was based on a face skin gage of 0.259 mm (0.0102 in.). Locally the maximum stress on this minimum gage could be -191 MN/m^2 (-27.7 ksi). The allowable intracell buckling stress for this minimum gage would be 217 MN/m^2 (31.5 ksi) resulting in a minimum gage margin-of-safety of

$$M.S. = 217/191 - 1 = +0.13$$

Face Wrinkling

The allowable aluminum stress for the minimum face skin gage 0.259 mm (0.0102 in.) at 450°K (350°F) was calculated using the equations described in Section 3.3. With t = 0.259 mm (0.0102 in.) and E = 62 GN/m^2 (9.0 x 10^6 psi), the effective depth of the face wrinkling into the core was calculated as 3.4 mm (0.134 in.) Since this was less than half the core thickness the allowable face wrinkling stress, F_{wr}, would be at least 255 MN/m^2 (37 ksi). The minimum margin-of-safety would be at least

$$M.S. = 255/191 - 1 = +0.34$$

Shear Crimping

The shear crimping allowable calculated using the equation described in Section 3.3 for the 0.604 mm (0.024 in.) thickness would be at least 255 MN/m^2 (37 ksi). The minimum margin-of-safety would be at least

$$M.S. = 255/191 - 1 = +0.34$$

Stability Analysis

The LH_2 test model vacuum jacket with 15.2 mm (0.6 in.) thick core was analyzed for stability using the same structural model described in Section 3.3. The eigenvalue analysis with linear bending prebuckling deformations was made for both the 294°K (70°F) and 450°K (350°F) conditions and the nominal and minimum face skin gage sandwich constructions. The minimum eigenvalue loads occurred at a circumferential wave number of 6 in all cases. The allowable buckling load was determined by multiplying the eigenvalues by a knockdown factor of 0.28 which was determined in Reference 3.

Figure 4.3-9 is a plot of the critical external pressure versus the circumferential wave number, n, for each of the four cases. The mode for n = 6 of each case are plotted in Figures 4.3-10 and 4.3-11 as W versus arc length. "W" is the radial deflection normalized to 1.00 unit at the point of maximum deflection. For practical purposes these mode shapes are identical. This was desirable since the proof test would be conducted at 294°K (70°F). Also typical variations in the face skin gages would not change the buckling mode. Thus, the 294°K (70°F) proof test including the F/S prediction method would produce a high level of confidence in the structural stability of the vacuum jacket when loaded at 450°K (350°F) during the system evaluation tests.

Girth Ring Analysis

Figure 4.3-12 is a sketch of half the girth ring assembly. Ring No. 1 was permanently bonded to the vacuum jacket head. Ring No. 2 consisted of two joining plates which fastened the two heads together at the girth. The vacuum sealing sheet was not included in the analysis since it would buckle at a low circumferential load and be ineffective to carry structural loads.

The condition analyzed was the F/S proof test where a maximum external pressure of 172 kN/m^2 (25 psi) at 294°K (70°F) would be applied hydrostatically to the vacuum jacket head.

The maximum loads on the girth ring assembly were calculated with a BOSOR 3 analysis using the vacuum jacket heat construction specified above. The ring properties used in the analysis are listed in Table 4.3-4. The girth ring assembly carried a meridional moment and circumferential and meridional loads. These loads and moment on the girth ring assembly for an external pressure of 172 kN/m^2 (25 psi) at 294°K (70°F) shown in Figure 4.3-13 are:

Circumferential Load	=	13.9 kN (3126 lb)
Meridional Load, N_{10}	=	111 kN/m (630 lb/in)
Meridional Moment, M_{10}	=	11.3 kN.m/m (211 in-lb/in)

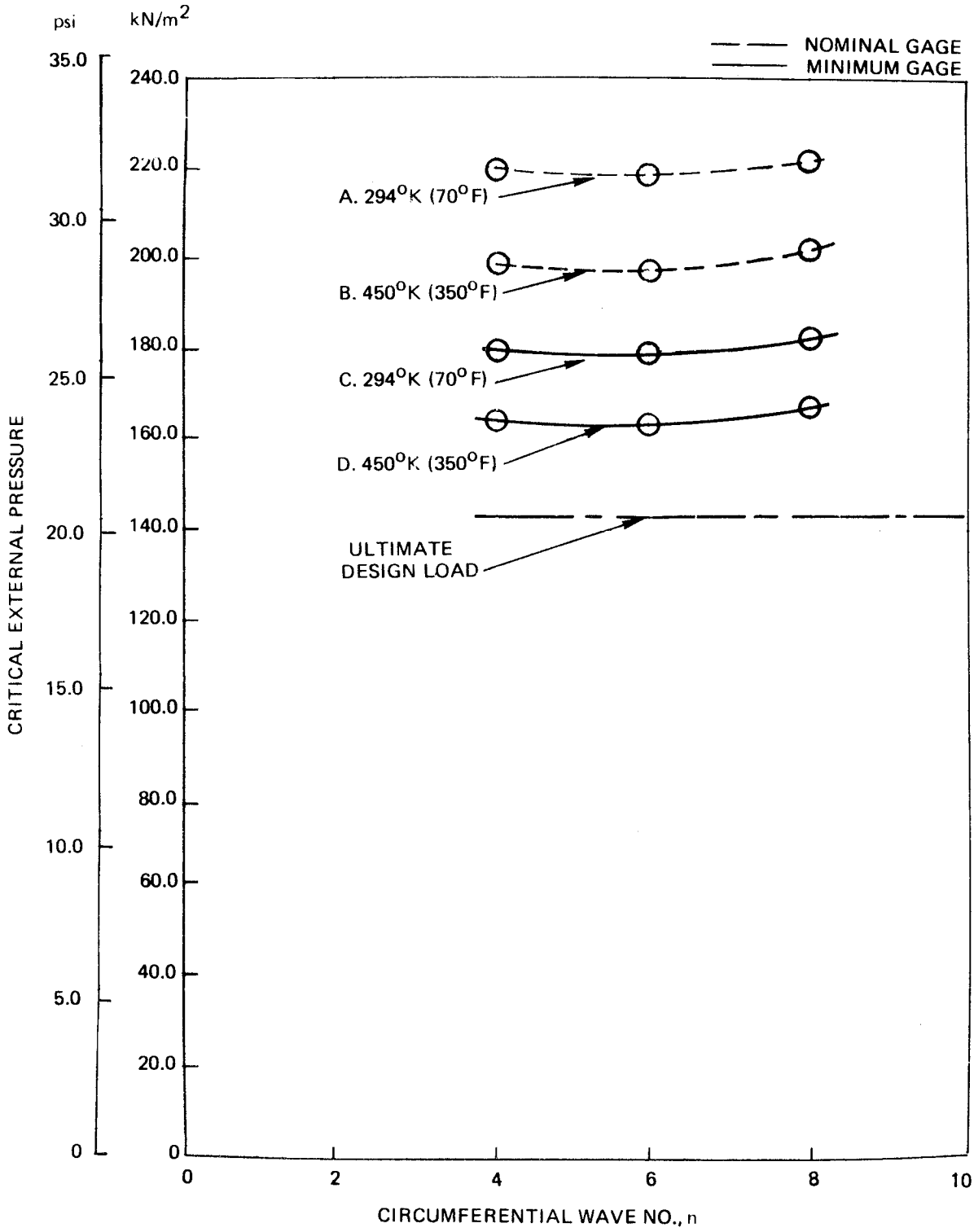

Figure 4.3-9. Critical External Pressure Versus Circumferential Wave No for Vacuum Jacket - LH_2 Test Model

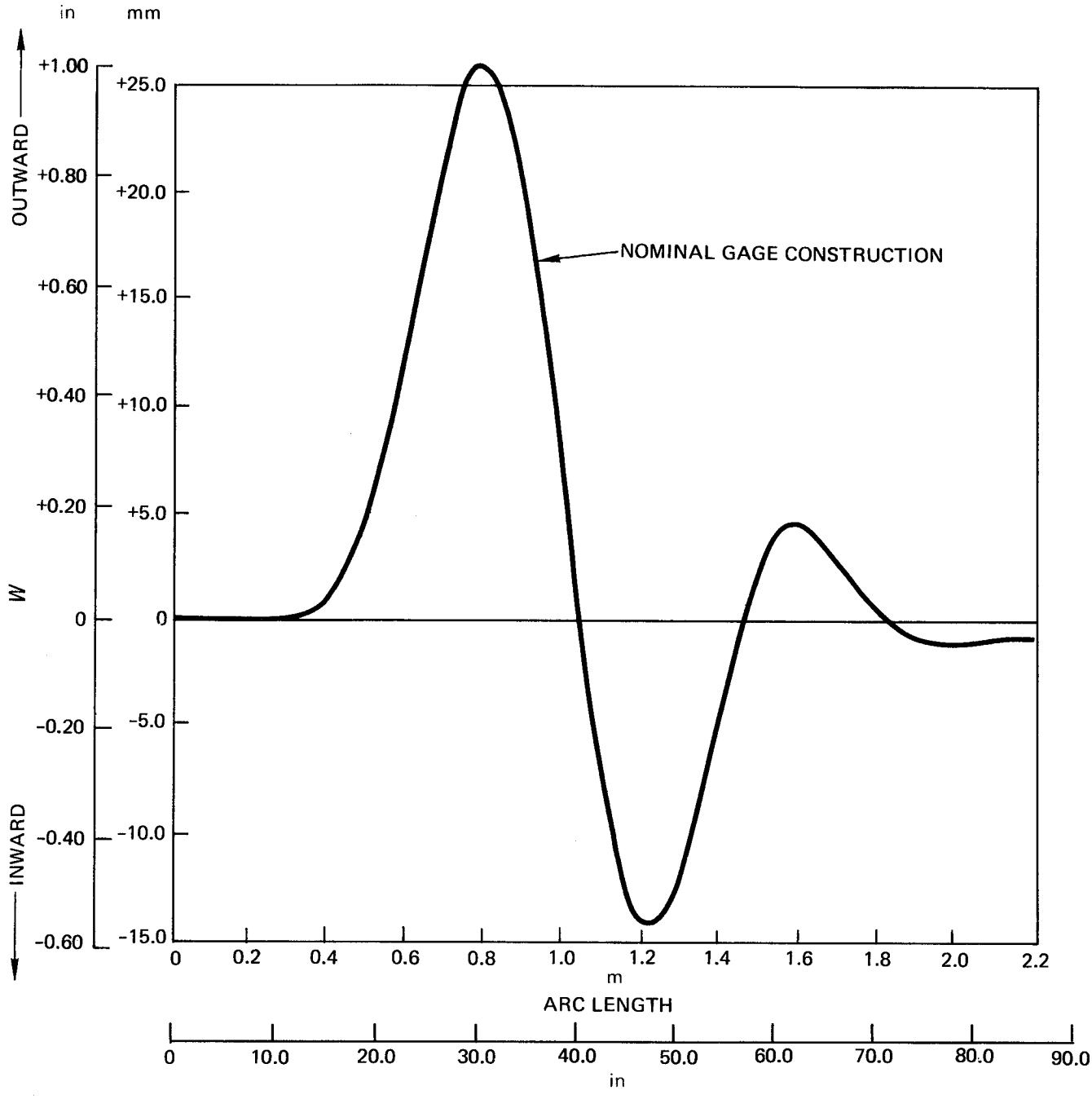

Figure 4.3-10. W Versus ARC Length at 294°K (70°F) for Vacuum Jacket - LH_2 Test Model

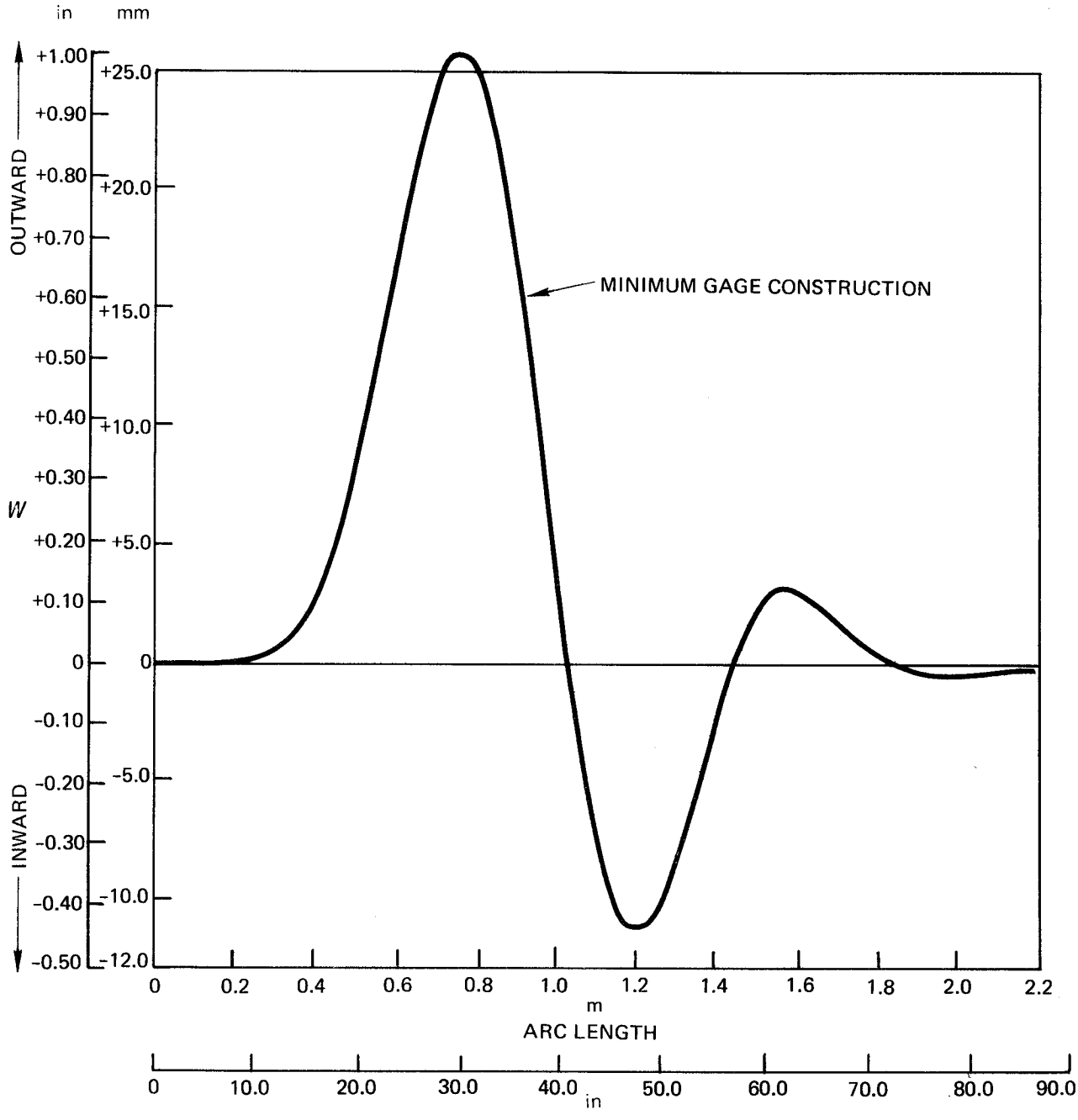

Figure 4.3-11. W Versus ARC Length at 450°K (350°F) for Vacuum Jacket - LH_2 Test Model

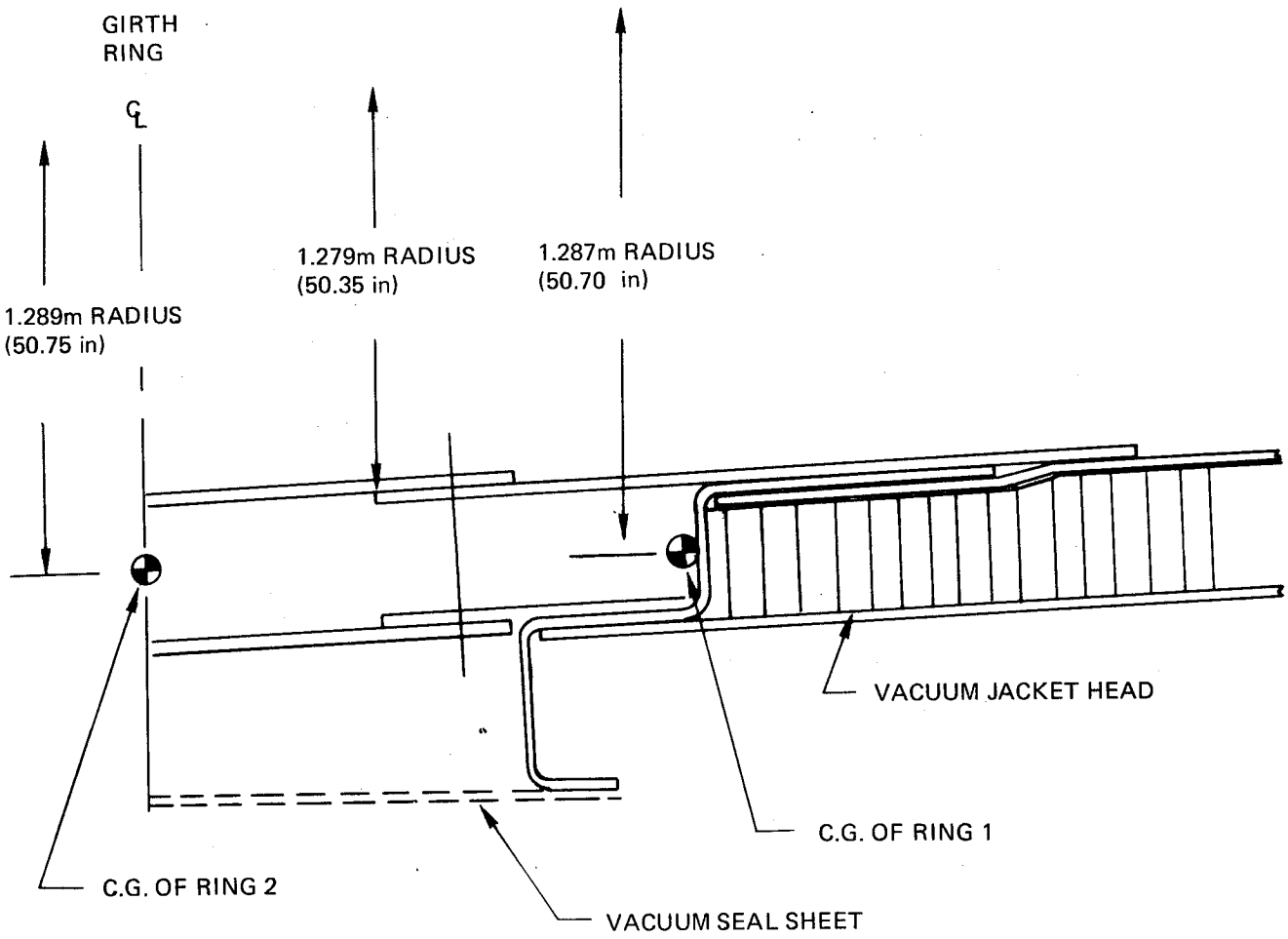

Figure 4.3-12 Details of Girth Ring Assembly for Analysis - LH_2 Test Model

Table 4.3-4. Analysis Properties of 6061-T6 Aluminum Alloy Girth Ring for LH_2 Test Model

RING	E at 294°K (70°F)		E at 450°K (350°F)		A		^1Y		^1X		^1XY		$^e1$		$^e2$		GJ AT 294°K (70°F)		GJ AT 450°K (350°F)	
	G N/m^2	10^6 psi	G N/m^2	10^6 psi	μ m^2	$in.^2$	nm^4	$in.^4$	nm^4	$in.^4$	nm^4	$in.^4$	mm	in.	mm	in.	MN/m^2	psi	MN/m^2	psi
1	69.6	10.1	64.8	9.4	336	0.52	45.8	0.11	200	0.48	0	0	0	0	0	0	11.4	1653	10.5	1525
2	69.6	10.1	64.8	9.4	206	0.32	20.4	0.049	150	0.36	0	0	0	0	+73.5	+2.9	68,250	0.99×10^6	64,100	0.93×10^6

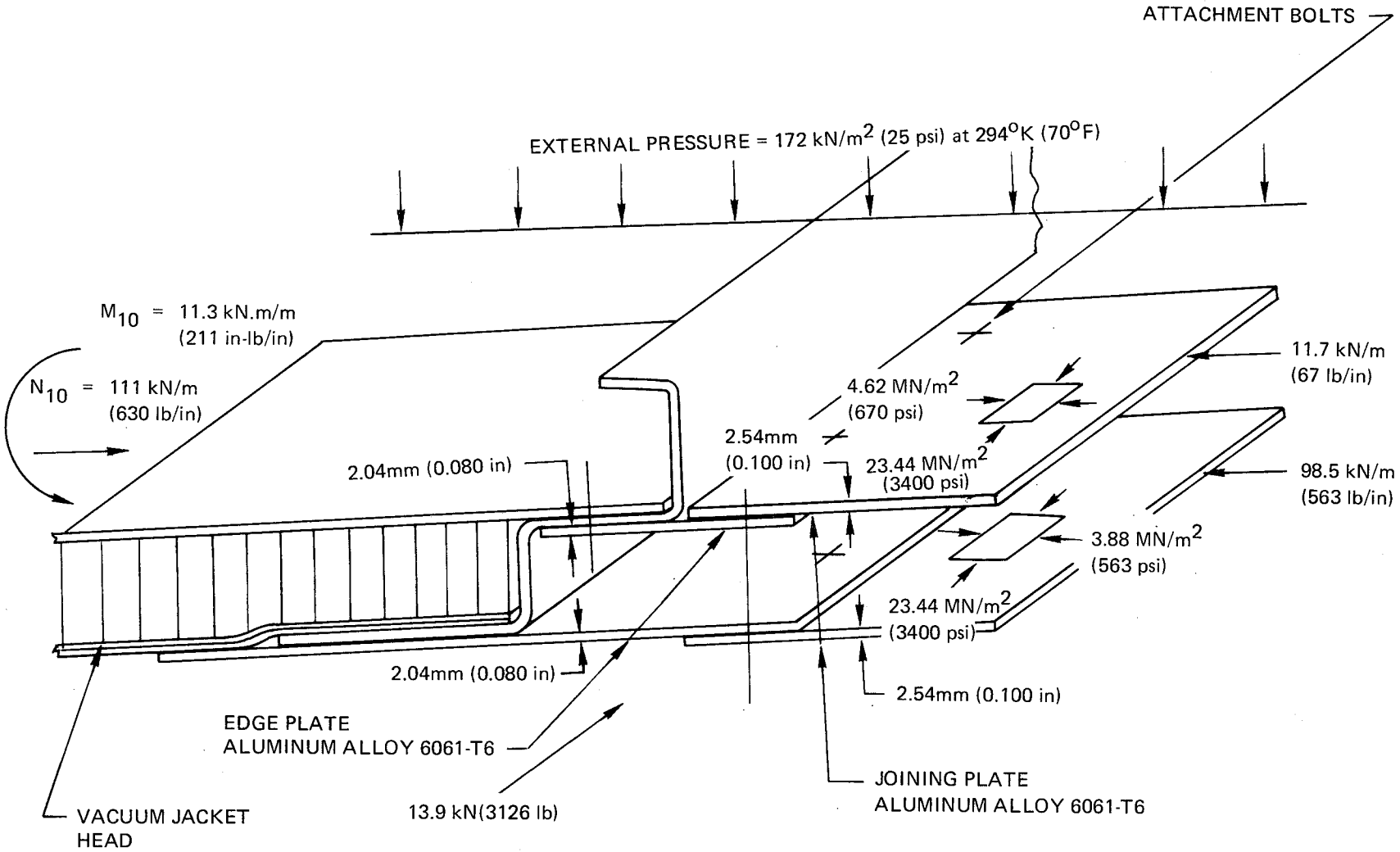

Figure 4.3-13: Biaxial Loads and Stresses on the Girth Ring Assembly - LH_2 Test Model

Joining Plate Stresses

The meridional loads are resolved into static equivalent line loads on the right hand side of the figure. The maximum load 98.5 kN/m (563 lb/in) occurred on the inner joining plate. Both inner and outer joining plates were biaxially stressed as shown on the insets in Figure 4.3-13.

The critical section of the assembly was the inner joining plate with biaxial compressing stresses of,

$$f_x = 98.5 \times 10^3/2.54 \times 10^{-3} = 38.7 \text{ MN/m}^2 \text{ (5630 psi)}$$

$$f_t = 13.9 \times 10^3/(3.34 \times 10^{-4} + 4(6.45 \times 10^{-5}) = 23.5 \text{ MN/m}^2 \text{ (3420 psi)}$$

The allowable compression stress for a very wide sheet is

$$F_x = KE\ (t/a)^2$$

where k = 0.9 and a = the length of the unsupported sheet in the x direction = 81.4 mm (3.20 in). With E = 6.95 GN/m^2 (10.1 x 10^6 psi) and t = 2.54 mm (0.100 in)

$$F_x = 60.5 \text{ MN/m}^2 \text{ (8800 psi)}$$

The allowable stress in the circumferential direction is

$$F_y = KE\ (t/b)^2$$

where K - 3.62, E = 6.95 GN/m^2 (10.1 x 10^6 psi) t = 2.54 mm (0.100 in.)
and b = 81.4 mm (3.20 in.)

F_y = 197.5 MN/m^2 (28,700 psi) for 6061-T6 aluminum when the inelasticity of the material is considered.

The buckling criteria for the biaxially compressed inner joining plate was

$$\frac{f_x}{F_x} + \frac{f_y}{F_y} = 1$$

and

$$\frac{38.7}{60.5} + \frac{23.5}{197.5} = 0.64 + 0.12 = 0.76$$

The margin-of-safety was at least,

M.S. = 1/0.76 -1 = +0.31

Attachment Bolts

The number and size of bolts were selected to use as few as possible without exceeding the bearing strength of the 2.04 mm (0.080 in.) thick aluminum 6061-T6 edge plates. The allowable single shear loads for the stainless steel bolts assumed in the analysis are listed in Table 4.3-5.

Table 4.3-5: Allowable Single Shear Loads for NAS 1217CR

Nom. Size		Allowable Ultimate Single Shear Load	
mm	(in.)	kN	(lb)
6.35	1/4	14.6	3285
7.94	5/16	22.8	5135
9.53	3/8	32.9	7400

A comparison of the numbers required for three different diameter NAS 1217 CR bolts to join the vacuum jacket heads at the girth ring is shown in Table 4.3-6.

Table 4.3-6: Number of NAS 1217CR Bolts Required to Join Vacuum Jacket Heads at Girth Ring

Nominal Size		Allowable Bearing Yield Load [1] for t = 2.04 mm (0.080 in.)		Maximum Pitch for 98.5 kN/m (563 lb/in)		Required Number of Bolts at Each Vacuum Jacket Head Joint
mm	(in.)	kN	(lb.)	mm	(in.)	(n)
6.35	1/4	5.42	1220	54.86	2.16	148
7.94	5/16	6.76	1525	68.83	2.71	118
9.53	3/8	8.13	1830	82.55	3.25	99

[1] F_{bry} @ e/D = 2.0, B-Basis allowable = 420 MN/m^2 (61 ksi) @ 294°K (70°F)

The 9.53 mm (3/8 in.) bolts were selected. This provided about a 0^+ margin-of-safety against bearing yield of the girth ring assembly during the proof test. The margin-of-safety for the system evaluation test at 450°K (350°F) for a bearing ultimate strength of 420 MN/m^2 (63,000 psi) would be at least +0.25. Due to the joint configuration at the four trunnion fittings, 104.9.53 mm (3/8 in.) bolts were actually used to join each vacuum jacket heat to the girth ring.

Proof Test Requirements

The objective of the proof test was to verify the structural integrity of the vacuum jacket for the critical design loads. Specifically, the vacuum jacket was to be capable of withstanding a 142 kN/m^2 (20.6 psi) external pressure at 450°K (350°F) after 100 thermal cycles to a maximum external temperature of 450°K (350°F).

It was planned to proof test the vacuum jacket heat at 294°K (70°F) to 172 kN/m^2 (25 psi) external pressure. This pressure was the minimum value required to assure the necessary strength. It included a 10 percent factor for the thermal cycle degradation and a 10 percent factor for the general instability strength. The latter value was determined by the stability analysis. The thermal cycle factor was determined by the sandwich beam tests of Section 4.5.1.

Table 4.3-7 summarizes the vacuum jacket analysis for the (A) Critical Design Load, and (B) Proof Load Cases. The critical external pressures were computed for each failure mode to identify the probable mode of failure for the nominal gage and the minimum gage constructions. The proportional limit stress does not cause failure per se. It does signal the probable onset of inelastic behavior in the aluminum face skins. The expected failure mode for both load cases was general instability. The vacuum jacket design had a 50 percent probability of meeting or exceeding the 172 kN/m^2 (25 psi) proof load with a +0.03 margin-of-safety.

Table 4.3-7. Vacuum Jacket Analysis Summary - LH_2 Test Model

LOAD CASE OR FAILURE MODE	CRITICAL EXTERNAL PRESSURE WITH				COMMENTS
	Nominal Gage 0.305 mm (.012 in)		Minimum Gage 0.259 mm (.0102 in)		
	MN/m^2	psi	MN/m^2	psi	
A. Critical Design Load at 450°K (350°F) with F.S. = 1.4	142	20.6	142	20.6	
1. Proportional Limit Stress 207 MN/m^2 (30 ksi)	174	25.3	153	22.2	Non-linear behavior starts, no failure.
2. Intracell Buckling	230	33.4	176	25.5	
3. Face Wrinkling	225	32.6	190	27.5	
4. Shear Crimping	225	32.6	190	27.5	
5. General Instability (n = 6)	195	28.3	163	23.6	Critical Mode M. S. = +0.14
B. Proof Test Load at 294°K (70°K) with F.S. = 1.0	172	25.0	172	25.0	
1. Proportional Limit Stress 240 MN/m^2 (42 ksi)	244	35.4	214	31.0	Non-linear behavior starts, no failure.
2. Intracell Buckling	296	43.0	196	28.4	
3. Face Wrinkling	349	50.6	294	42.6	
4. Shear Crimping	349	50.6	294	42.6	
5. General Instability (n = 6)	217	31.5	178	25.8	Critical Mode M.S. = +0.03

4.3.2 Pressure Vessel Support System

The pressure vessel support system is shown in Figure 4.2-1. It consisted of four sets of four straps connecting the pressure vessel to the attachment brackets. The attachment brackets connected the LH_2 test model assembly to the test stand. Figure 4.3-14 is a schematic of the model used for the support system loads analysis. The pressure vessel (and liquid) was treated as a rigid body mass concentrated at the centroid. The end of the support straps were constrained to move with the same rigid body motion as the tank mass. The pressure vessel and liquid loads were transferred to the sixteen straps at the strap to pressure vessel attachment points. The strap loads were transferred through the four attachment brackets to the test stand ring. The ring was supported at two places, nodes 10 and 580.

The structural properties used in the analysis were:

Support Straps Kevlar 49/epoxy (PRD 49/epoxy)

area	=	232.26 mm^2 (0.36 in^2)
E	=	82.05 GN/m^2 (11.9 $x10^6$ psi)
G	=	6.90 GN/m^2 (1.0 x 10^6 psi)
v	=	0.3
density	=	1300.96 kg/m^3 (0.047 lb/in^3)
		(-1.67 x 10^6 in/in/°F)
Tref	=	294°K (70°F)
Allowable stress in tension, ST	=	930.79 MN/m^2 (135 ksi)
Allowable stress in compression, SC	=	344.74 MN/m^2 (50 ksi)
Allowable stress in shear, SS	=	34.47 MN/m^2 (5 ksi)

Test Stand Ring and Attachment Brackets (Standard Weight Steel Pipe)

area	=	1470.97 mm^2 (2.28 in^2)
weight	=	(7.58 lb/ft)

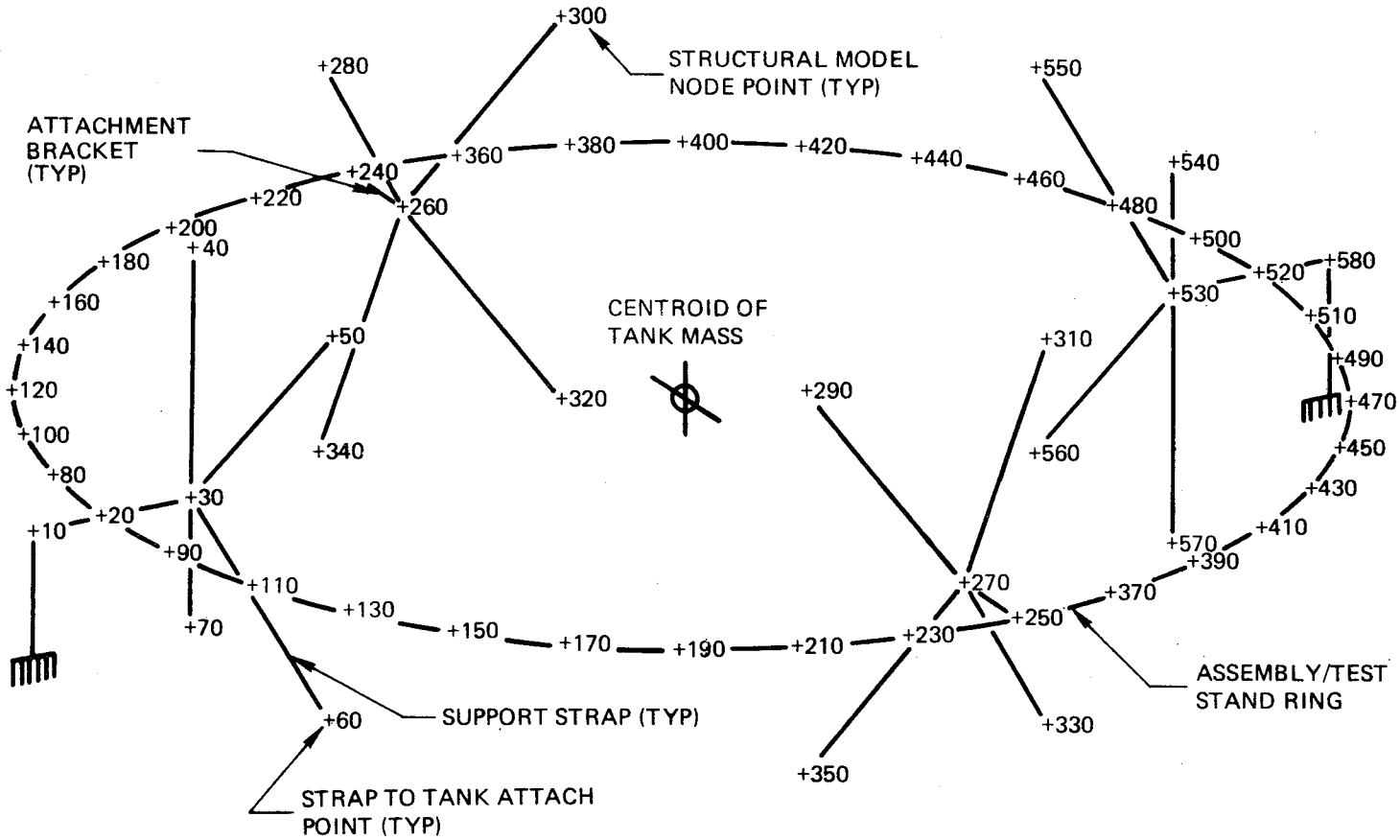

Figure 4.3-14. Loads Analysis Model For Support System — LH_2 Test Model

Nominal
Diameter = 76.2 mm (3.0 in.)
t = 5.49 mm (0.216 in.)
I = ($3.017\ in^4$)
E = 206.84 GN/m^2 (30×10^6 psi)
G = 124.11 GN/m^2 (18.0×10^6 psi)
v = 0.25
= (6.0×10^{-6} in/in/RF)

Allowable stress in tension, ST = 137.90 MN/m^2 (20 ksi)
Allowable stress in compression, SC = 137.90 MN/m^2 (20 ksi)
Allowable stress in shear, SS = 82.74 MN/m^2 (12 ksi)

The design criteria for the loading conditions are specified in Section 4.1. Four loading conditions were analyzed to select the critical loads for support system. The load sets were:

Load Set 1 - Transportation Limit Load Factors X = ±3.5, Y = ±2.0, Z = +6.0
Load Set 2 - Transportation Limit Load Factors X = ±3.5, Y = ±2.0, Z = +1.0
Load Set 3 - Static load case in the test stand
Load Set 4 - Static load case for a 1.57 Radians (90 degree) rotation of the test stand ring.

All of these load cases assumed the pressure vessel was empty with the MLI installed. The weight of the vacuum jacket was carried by the girth ring to the attachment brackets.

The estimated weight of the pressure vessel was 419.6 kg (925 lb) plus 34 kg (75 lb) for MLI for a total estimated weight of 453.6 kg (1,000 lb). This was multiplied by the load factors for Sets 1 and 2 and applied to the centroid of the tank mass shown in Figure 4.3-14. Note that all these loads are limit loads. The pressure vessel support had a 1.1 factor of safety for yield and an ultimate factor of safety of 1.5. The allowable stresses used for the standard weight steel pipe are safe working stresses and have a material factor of safety of at least 1.5.

The structural model was analyzed for the four load cases using the NASTRAN method. The primary objective was to identify the maximum load case for strength design of the support strap fittings. The secondary objective was to strength check the test stand ring and attachment brackets. It was expected that they were conservatively sized for the design loads.

Because the support straps could not resist compression loads, the analysis was conducted in two steps. The first step treated all the straps as rigid and stable members to identify which straps were in compression. Those straps were effectively "buckled" by reducing their stiffness to one percent of the effection stiffness in tension. The second analysis computed the correct tension loads (and the displacements).

The critical load case for the straps and the brackets was load Set 1. Figure 4.3-15 is a plot of the deflected shape of the support system, and shows also the strap loads. The deflection scale is magnified to show the deflected shape. The maximum limit load in a strap is 14.3 kN (3215 lb) tension. The net displacement of the strap to pressure vessel attachment point is approximately,

$$r = \sqrt{T_1^2 + T_2^2 + T_3^2} = 6.86 \text{ mm } (0.27 \text{ in.})$$

There was ample room within the vacuum annulus to accommodate this size deflection without compacting the MLI or rubbing the jacket against the pressure vessel. The maximum tension load of the support straps at room temperature was,

$$P_{ult} = \text{F.S.} \times P_{lim} = 1.5 \times 14.3 = 21.45 \text{ kN } (4825 \text{ lb})$$

The proof load requirement should not exceed the yield strength of the materials. The proof load of the strap at room temperature was set at the allowable yield load

$$P_{proof} = P_{yield} = \text{F.S.} \times P_{lim} = 1.1 \times 14.3 - 15.73 \text{ kN } (3530 \text{ lb})$$

Each of the support straps were proof tested to (3600 lb) (Reference Section 4.5-2) prior to use, which insured that the straps had at least a 1:1 factor of safety for the limit load condition and a good bonded joint.

The stress analysis of the standard weight steel pipe revealed that the stresses in the test stand ring were very low and not critical.

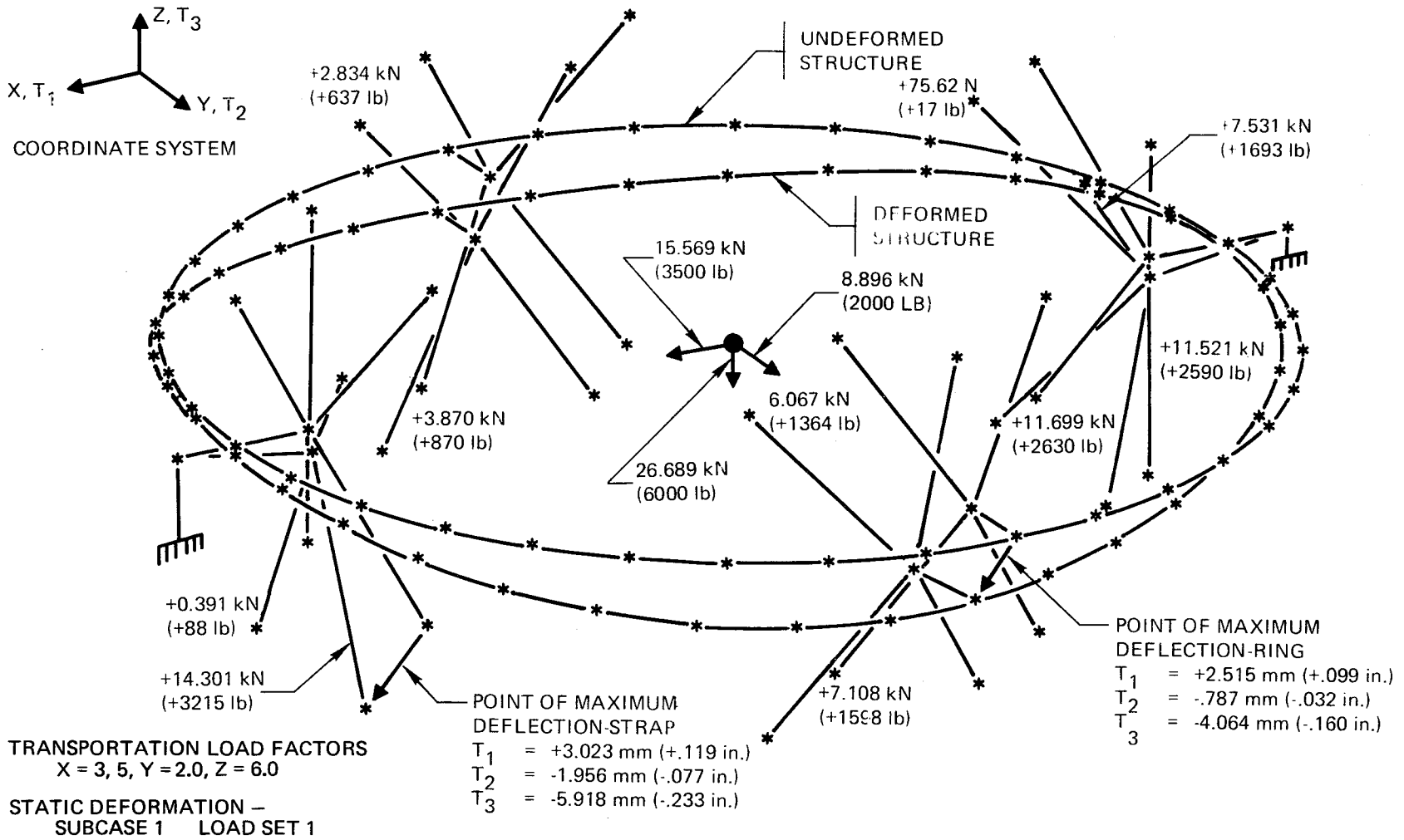

Figure 4.3-15: Maximum Deflection and Loads on Support System - LH_2 Test Model

4.4 THERMAL ANALYSIS

4.4.1 Vent Assembly Analysis

Analyses were conducted to determine 1) the adequacy of the vent line design for test safety purposes and 2) to estimate the probable heat leak into the cryogen from the vent assembly arrangement during testing.

Vent Line Sizing and Safety Requirements

Analyses of boil-off rates and vent line size requirements for the cases of the normal boil-off tests and a possible catastrophic insulation failure during thermal cycling test were made. These were followed by an analysis to provide data for establishing safety requirements in the event of catastrophic insulation failure during boil-off tests.

Vent Line Sizing

The adequacy of the 19.05 mm (0.75 in.) diameter vent line was evaluated for safety purposes. Velocities of boiled-off hydrogen were estimated for nominal heat flow test conditions and for an assumed catastrophic insulation failure at the high temperature thermal cycle test condition.

The estimate of hydrogen boil-off rate at the nominal heat flow test condition was made prior to completion of the heat flow predictions of Section 4.4.2. Therefore, the total heat flow to the cryogen was estimated on the basis of program objectives rather than on computed or measured values. If the LH_2 test model experiences the same basic MLI heat flux as the OMS fuel tank design, the total heat flow to the LH_2 test model would be 8.49 watts (28.99 Btu/hr). For the purpose of boil-off estimation this value was increased by 50% to account for unavoidable departures from the desired thermal scaling, possible excessive heat leaks, and the additional heat leak at the fill-vent-instrumentation penetration. The resulting heat flow of 12.73 watts (43.4 Btu/hr) yields, at an ambient pressure of 101.3 kN/m^2 (14.7 psia), a boil-off rate of 0.0285 g/sec (0.226 lb/hr). This rate, in turn, flowing through a 19.05 mm (0.75 in) diameter tube produces a velocity of only 0.0664 m/sec (0.2175 ft/sec), obviously an acceptable value.

The adequacy of the vent line was further assessed for the case of a catastrophic failure of the insulation system (by loss of vacuum in the annulus) during the thermal cycling tests. During this time only a small residual amount of LH_2 would be present in the tank. It was assumed for the present purpose that 10% of the tank interior area would be wetted with the cryogen. Then, assuming the highest possible LH_2 nucleate boiling heat transfer of 69.4 K watt/m^2 (22000 Btu/ft^2 -hr) (Reference 7) a velocity of 386 m/sec (1265 ft/sec) will be produced by the boil-off. Although this rate is just above the choked flow velocity of 355 m/sec (1163 ft/sec), the occurrence of the maximum nucleate boiling heat transfer rate is extremely unlikely. Therefore, the 19.05 mm (0.75 in.) diameter vent line was concluded to provide adequate pressure relief in the case of sudden loss of vacuum during the thermal cycling tests.

Safety Requirements

An analysis was performed to provide data for establishing safety requirements in the event of catastrophic insulation failure during boil-off tests.

The condition investigated was the worst-case situation foreseeable during the entire series of tests for this program. The pressure vessel was assumed full of LH_2 and the outside surface of the vacuum jacket was at a uniform 311°K (100°F). This case would result in greater boil-off in the event of insulation failure than the case of the high temperature test, where the vacuum jacket outer surface will be 450°K (350°F) but the pressure vessel will be only partly ($\approx$5%) full. It was assumed that the loss of vacuum was caused by leakage of H_2 gas into the annulus and the MLI, resulting in a pressure of 1358 MN/m^2 (19.7 psia) in the annulus.

The rate of heat transfer to the LH_2 was computed considering natural convection through the H_2 gas in the annulus and nucleate boiling within the pressure vessel. The vacuum jacket skins and core, the MLI, and the pressure vessel wall were assumed to offer no thermal resistance. Convective heat transfer coefficients across the annulus were derived by the formula for vertical enclosed spaces from Reference 8, incorporating the appropriate properties for gaseous H_2 at the pressure assumed. The effective boiling heat transfer coefficient was derived from data from Reference 9. The simultaneous equations shown below were solved by an iterative procedure.

$$h'_c (T_a - T_w) = \dot{q}_{boil}$$

$$\dot{q}_{boil} = f(T_w - T_{H_2}), \text{ from curve of Reference}$$

h'_c = effective convective heat transfer coefficient, from Reference 8, watt/m^2 -°K (But/ft^2 -sec-°R)

$\dot{q}_{boil}$ = nucleate boiling rate, watt/m^2 -°K (Btu/ft^2 -sec)

T_a = temperature of vacuum jacket 311°K (560°R)

T_w = temperature of pressure vessel wall, °K (°R)

T_{H_2} = temperature of LH_2 in pressure vessel, 24°K (42.3°R) at initially assumed 0.2413 MN/m^2 (35 psia) saturated liquid condition.

The following results were obtained:

Additional heat flow per unit of tank area due to 0.1358 MN/m^2 (19.7 psia) H_2 in annulus	= 3.935 Kw/m^2 = (0.347 Btu/ft^2 -sec)
Total heat flow to tank interior (includes 1.2 times normal predicted heat flow	= 77.496 Kw (73.47 Btu/sec)
Resulting boil-off mass rate	= 0.1843 kg/sec = (0.4064 lb/sec)
Resulting boil-off volumetric rate, at atmospheric pressure	= 154.15 liter/sec = (5.444 ft^3/sec)

Assuming the existence of simple chocked flow at some point in the vent system, with no crictional or other losses, a minimum vent area of 434.8 mm^2 (0.674 in^2) would be required. Thus, a minimum burst disc diameter of approximately 23.6 mm (0.93 in.) was indicated. The pressure in the pressure vessel consistent with choked vent flow and discharge to 0.1014 MN/m^2 (14.7 psia) ambient is 0.2206 MN/m^2 (32 psia).

The assumptions of all vertical surfaces for convective heat transfer calculations and the neglect of vacuum jacket thermal resistance tended to result in boil-off predictions in excess of what might actually occur. Also, depletion of LH_2 in the pressure vessel resulting from the boil-off would rapidly lower the liquid level, reducing the wetted area, and reducing the boil-off rate as venting progressed. On the other hand, frictional losses in the vent stack, vent line, relief valve, or burst disc orifice may result in greater resistance to boil-off flow and a greater pressure within the pressure vessel. It is possible also that transients may result in momentary boil-off rates exceeding the predicted value. From these considerations it was recommended that some reasonable margin, e.g., 50%, be added to the predicted boil-off rate or area requirement for vent system design.

A severe H_2 leak into the annulus, without adequate pressure relief to limit the annulus pressure to the assumed 19.7 psia, would produce greater heat transfer and boil-off rates than presently predicted. It was therefore decided that an appropriate relief valve be located in the vacuum pump line. The presence of air in the annulus at the same pressure assumed for the H_2 case investigated would result in lower heat transfer and boil-off.

Vent Assembly Analysis

The vent assembly and the LH_2 fill preconditioner attached to it received special attention in the course of the heat flow review. This assembly was to extend outside the thermal shroud and thus would experience boundary temperatures not fully controlled in the course of the boil-off tests. The preconditioner would act somewhat as a guard and was expected to strongly influence these boundary temperatures. It did not appear practical to unequivocally predict the extent of this influence, however, because of the complexity of the many heat paths involved (vent line, instrumentation wires and conduits, fill and control lines, mechanical supports) and the unpredictable influence of the ambient environment (air temperature and currents, moisutre or air condensation, ambient radiation). The fact that the heat flow through this assembly depends upon the boil-off mass flow rate further prevented final prediction of heat leak contribution at that time. The thermal analysis of this assembly was, therefore, treated parametrically, and it was planned to instrument the assembly (Reference Section 4.4.3) so that the actual key boundary temperature would be measured, thereby permitting prediction of the net heat leak.

Model

Figure 4.4-1 illustrates the vent assembly and fill preconditioner for the purpose of describing the thermal analysis model. Actually, the assembly was somewhat more complex than shown, with thermocouple and liquid level sensor leads passing through the vent tube and out through ports in the vent plenum. A burst disk and other ports were planned to be installed in the plenum. Support for the preconditioner and the thermal shroud have also been omitted in the model.

For analysis the vent tube was divided into a number of elements and a steady state heat balance assumed for each element, i.e.,

$$Q_{k,i} = Q_{k,i+1} + Q_{c,i}$$

where Q_k = heat conducted across element boundary
Q_c = heat convected across element inner surface

The Q_k's satisfied the usual Fourier law, which in this case may be expressed

$$Q_{k,i} = k \frac{A_{c,i}}{(x_i - x_{i-1})} \left[\frac{(T_{i-1} + T_i)}{2} - \frac{(T_i + T_{i+1})}{2}\right]$$

where k = vent tube material conductivity
A_c = vent tube cross-section area
x = distance along vent tube length
T = vent tube temperature

The Q_c's were evaluated by

$$Q_{c,i} = h_i A_{s,i} \left[\frac{(T_i + T_{i+1})}{2} - \frac{(T_{b,i} - T_{b,i+1})}{2}\right]$$

where A_s = vent tube element inner surface area
T_b = vent gas bulk temperature

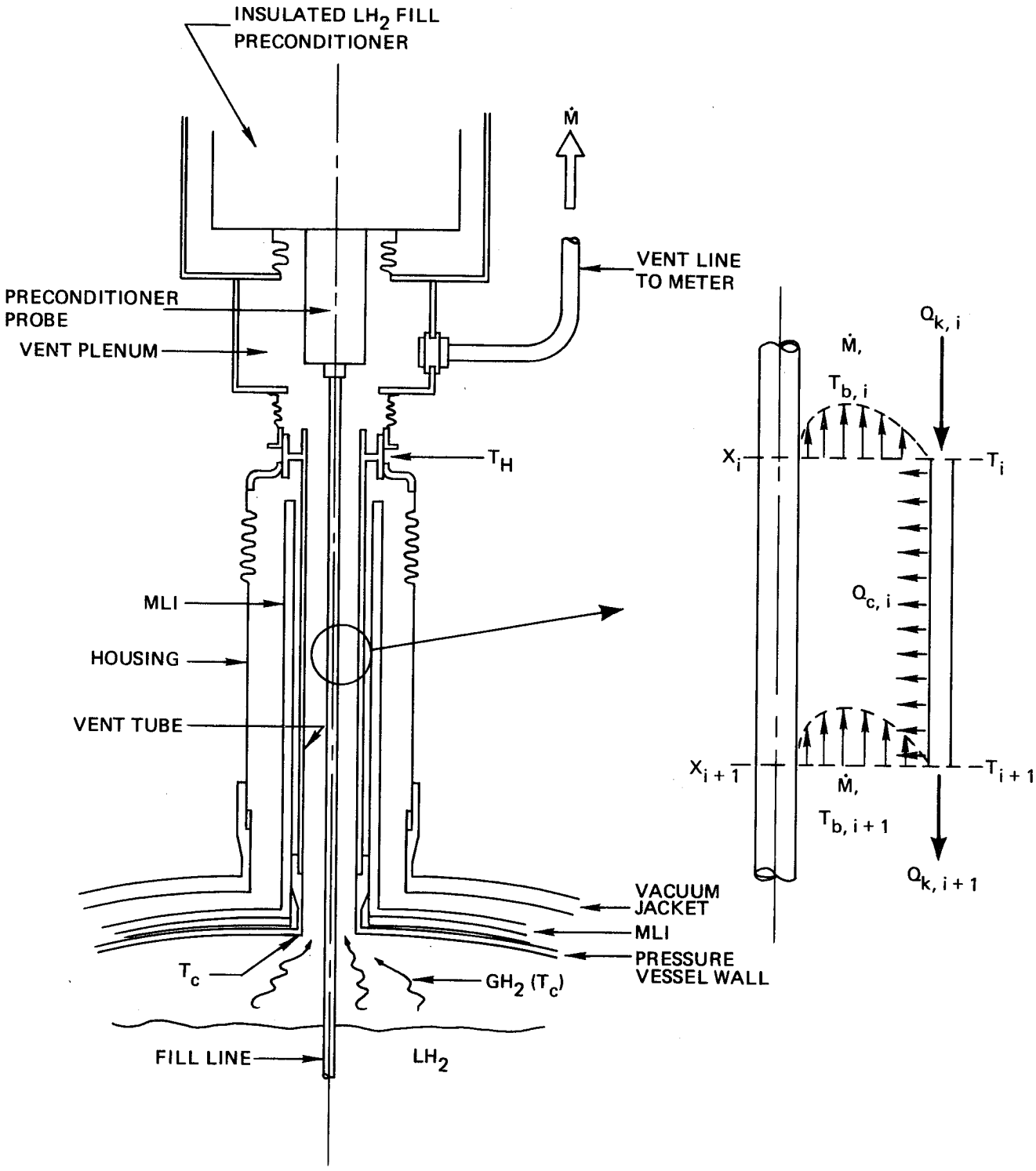

Figure 4.4-1: Fill & Vent Assembly Schematic LH_2 Test Model

The vent gas convective heat transfer coefficient, h, was evaluated by the method of Kays (Reference 10), for flow of a gas near the entrance of a circular tube with approximately constant heat transfer. Finally, a simultaneous condition,

$$T_{b,i} = T_{b,i+1} + Q_{c,i}/(\dot{M}C_p)$$

where $\dot{M}$ = vent (boiloff) mass flow rate

C_p = vent gas specific heat

must be satisfied.

Relations represented by all of the preceding equations were programmed for digital computer. Geometric and material properties appropriate to the vent assembly were incorporated and provisions made to input the hot boundary temperature (T_H), the cold boundary temperature (T_c), and the boiloff mass flow rate ($\dot{M}$).

Several simplifying assumptions were implied in the formulation of the analytical model. The influence of the coaxial fill line was ignored. Initially, the line will be filled with LH_2. As the boiloff test progresses, with the fill valve closed, the liquid in the line may vaporize but its temperature should never exceed that of the surrounding vent gas. In all probability, the fill line would be very near 20.5K (-423°F) since each end was immersed in LH_2.

The effect of the fill line distorting the velocity and temperature profiles and influencing the values of wall heat transfer coefficients was assumed negligible and was ignored. The chilling effect of the fill line would reduce the T_b values to less than those computed in the analysis, tending to increase the cooling effect of the vent gas, increasing the heat intercepted from the vent tube.

Heat interchange between the vent tube and the MLI insulation assembly surrounding it was ignored since earlier detailed thermal analysis of a similar configuration on the OMS fuel tank design (Section 3.4) indicated this heat interchnage

to have negligible effect on the component heat leak. The heat flow by effective lateral conduction in the MLI and conduction in the fiberglass support tube was found, in previous similar analyses, to be significant and would be computed as one of the components in the total heat flow to the tank.

Radiation through the interior of the vent tube was not included in the analysis. Figure 4.4-1 does not show a copper sleeve which was to be installed to slip loosely over the upper end of the vent tube and the lower end of the preconditioner probe. Although this sleeve must incorporate holes for vent flow and the passage of instrumentation wires, its presence would result in the vent tube interior essentially viewing only surfaces at or very near LH_2 temperatures. Thus, no significant net radiant heat transfer through the vent tube was expected.

Thermocouple and liquid level sensor wires passing through the vent tube were a potential heat leak. It was planned, however, that all such leads would be wrapped several turns around the preconditioner probe before being routed through the instrumentation part in the vent plenum. Thus, the probe would act as a guard in intercepting heat entering the assembly through these wires.

Results

The analysis of the vent assembly described in the preceding section was carried out for a range of boiloff mass flow rates from 0.0126 gm/sec (0.10 lb_m/hr) to 0.126 gm/sec (1.0 lb_m/hr). The preliminary nominal rate predicted earlier was 0.01701 gm/sec (0.135 lb_m/hr). For most of the assumed boiloff rates, the hot boundary temperature (T_H) was varied from 89K (-300°F) to 273K (32°F). For all calculations the cold boundary temperature (T_C), which applied to both the cold end of the vent tube and the boiloff gas entering the lower ends of the tube, was set at 20.5K (-423°F).

Thermal analysis results in terms of net heat flow reaching the tank are shown in Figure 4.4-2. The preliminary nominal total heat flow to the test model was predicted as 9.9W (34.7 Btu/hr). It is thus seen that, except at combinations of very low boiloff rate and very high hot boundary temperatures, the vent tube net heat leak will probably be a very small part of the total heat flow. The heat conducted by the tube insulation assembly, which is not included in the figure, will raise the numbers slightly. This additional heat flow will be dependent upon T_H, but not significantly upon the boiloff rate.

It is seen that the heat balance in the vent assembly is self-stabilizing. That is, an increase in boiloff rate will tend to reduce the net heat flow to the tank, which, in turn, will reduce the boiloff rate. It is also noted that low values of T_H result in very low net heat flow rates. The test estimates of test lab personnel place this temperature in the liquid air range.

Justification for an estimate of T_H in the neighborhood of liquid air can be seen in the results shown in Figure 4.4-3. The heat flow in the figure is the heat being absorbed from the ambient environment at the location of T_H, i.e., the heat conducted through the flange at the upper end of the vent tube. It is equal to the sum of the net heat conducted to the tank and the net heat being removed in the form of vent gas enthalpy. The heat being absorbed at the T_H location is very large for all except the very lowest assumed boiloff rates and T_H values. It is difficult to postulate that natural convection and ambient radiation could supply heat at most of the levels indicated. The conclusion, then, is that equilibrium with the external environment would be reached only at very low values of T_H and thus, that the probable net heat flow to the tank is quite low.

The dependence of the vent assembly heat leak upon the boiloff rate and the hot boundary temperature made firm prediction of the contribution of this assembly to the total heat load impossible at the time. An estimate of the most probable heat leak value was made to permit computation of a pre-test prediction, but for the purpose of final program analytical-experimental-comparisons, a value was planned to be read from Figure 4.4-2 using the actual M and T_H. For this purpose a thermocouple was planned for the T_H

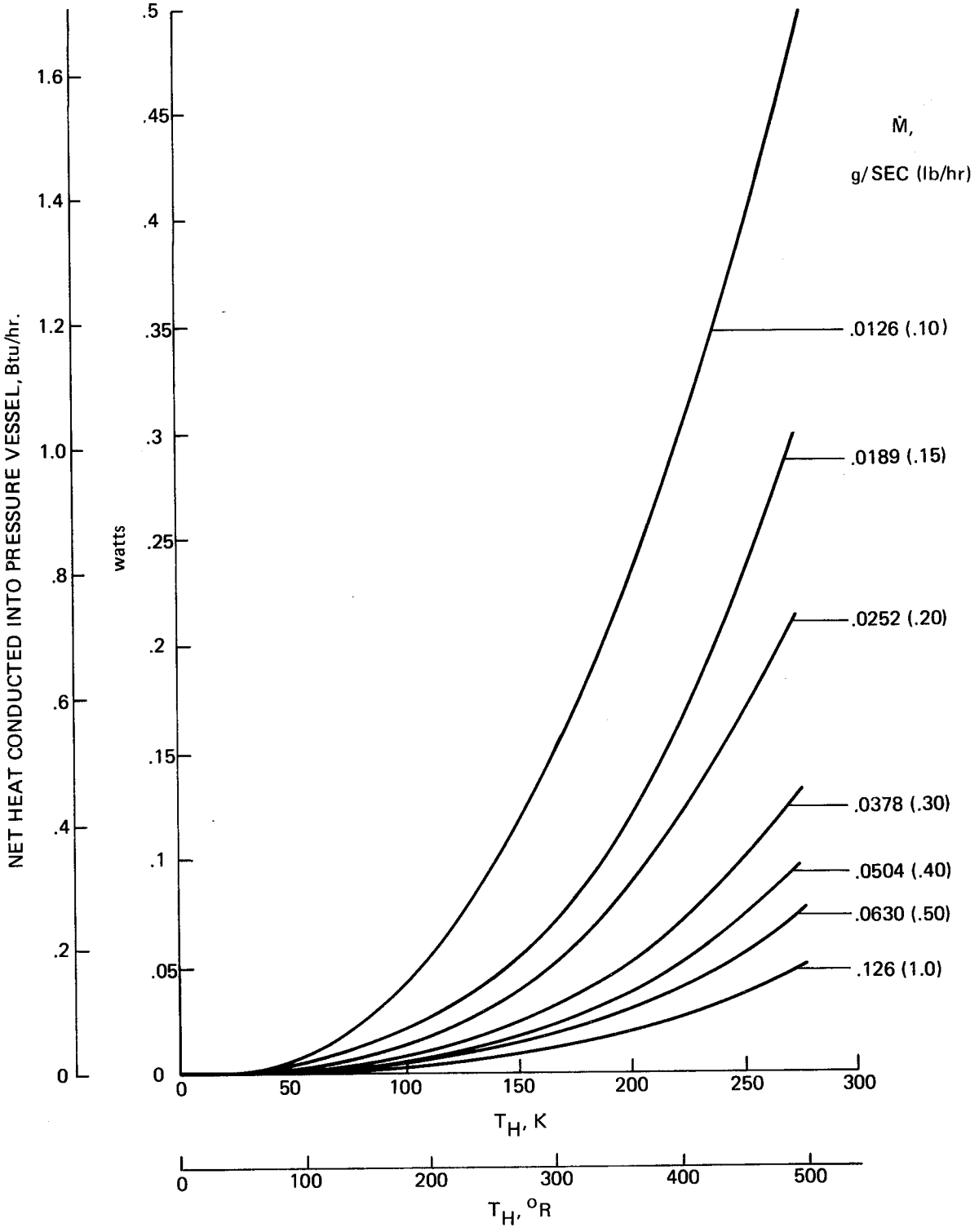

Figure 4.4-2: Vent Tube Net Heat Leak, LH_2 Test Model

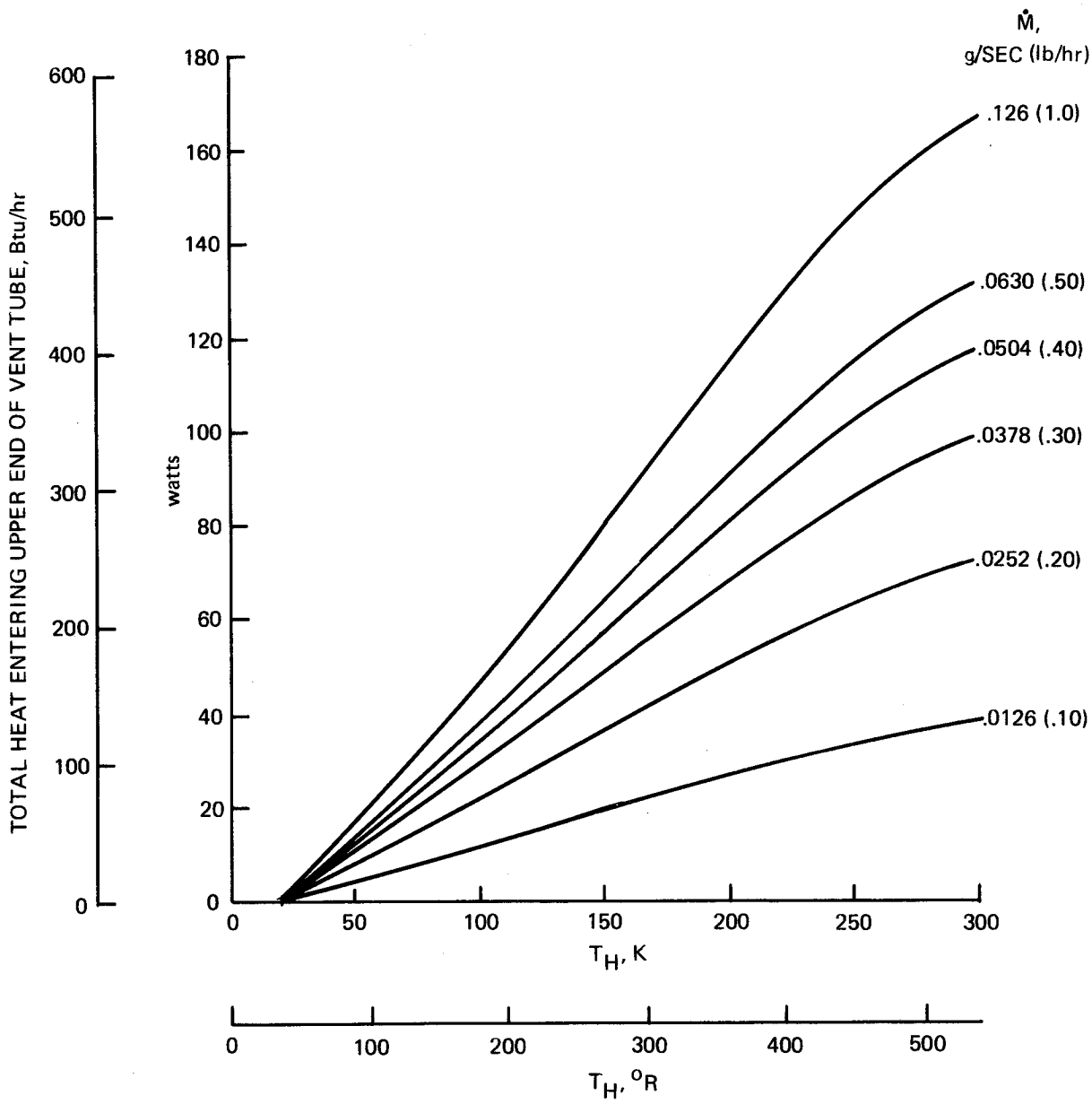

Figure 4.4-3: Vent Tube Total Heat Input LH_2 Test Model

location. In order to further assess the analysis validity, other thermocouples were planned for location on the vent tube and fill line, and suspended in the vent gas in the tube annular space.

4.4.2 Heat Flow Predictions

Heat flow predictions were made for the half-scale LH_2 test model design as it was constructed. These predictions are shown in Table 4.4-1 along with the ideal heat flow values, based on program thermal scaling objectives. The failure to achieve exact thermal scaling for each of the components resulted from compromises that were necessary in designing the LH_2 test model.

Heat flow values in Table 4.4-1 are applicable to the 311K (100°F) vacuum jacket outer surface test condition and an assumed 6.5 mN/m^2 (5.0×10^{-5} Torr) vacuum annulus air pressure. With the exception of the fill, vent, and instrumentation line assembly, the thermal analysis of each component followed the same procedure and employed similar analytical models as the analysis of the OMS fuel tank design, as discussed in Section 3.4. The heat flow value for the actual fill and vent assembly was taken from results of the parametric thermal analysis of that component discussed in 4.4.1. For the purpose of the present tabulations, a vent flow of 0.0126 g/sec (0.10 lb/hr) and a hot boundary temperature (T_H) of 88.9K (-300°F) were assumed. It is seen from Table 4.4-1 that the resulting predicted vent flow, i.e., boil-off rate, differs from the assumed value. The actual vent flow, as well as the actual hot boundary temperature, was planned to be measured during the test and the fill and vent line heat flow prediction re-evaluated at that time. Therefore, there appeared to be little value in iterating the present predictions to reconcile this discrepancy, whose effect is relatively minor.

For the basic MLI the unit heat flow (heat flux) scales exactly, i.e., equals the OMS fuel tank design value, assuming achievement on the LH_2 test model design of the expected thickness, layer density, and boundary temperatures. The total heat flow for the LH_2 test model design deports slightly from the ideal value because of a small discrepancy in area scaling. This discrepancy exists because of the use of pressure vessel inside diameter as the characteristic scaling dimension and the relatively thick wall of the LH_2 test model pressure vessel.

Component	Ideal - Based on OMS Fuel Tank Design Prediction and Thermal Scaling Objectives			Actual - Based on Final Pre-Test LH_2 Test Model Design Predictions		
	Unit Q Watt/Unit (Btu/unit-hr)	n Units of Area, Length, or No.	Component Total Q Watts (Btu/hr)	Unit Q Watt/Unit (Btu/unit-hr)	n Units of Area, Length, or No.	Component Total Q Watts (Btu/hr)
Basic MLI	.3428 (.10894)	19.7 m^2 (211.7 ft^2)	6.76 (23.063)	.3428 (.10894)	20.1 (216.38 ft^2)	6.90 (23.572)
Single Step Lap Joint	.01664 (.01734)	27.5 m (90.2 ft)	.458 (1.565)	.01664 (.01734)	36.2 (118.8 ft)	.603 (2.06)
Fasteners: .0762 mm (.030 in) Pin Single Fastener	$.608 \times 10^{-4}$ ($.2077 \times 10^{-3}$)	490	.0298 (.1018)	$.594 \times 10^{-4}$ ($.2029 \times 10^{-3}$	280	.0166 (.0568)
.0762 mm (.030 in) Pin Groups of 3 Fasteners		0	0	$.841 \times 10^{-4}$ ($.2875 \times 10^{-3}$	912	.0767 (.2622)
.160 mm (.063 in) Pin	$.461 \times 10^{-3}$ (.001577)	51	.0235 (.0804)		0	0
.635 mm (.25 in) Pin & Grommet	.00875 (.02988)	21	.1837 (.6269)		0	0
Structural Supp. Strap	.00501 (.0171)		.222	.01227 (.04189)		.515
Attach Ftg. Penetration	.00887 (.0303)			.01994 (.0681)		
Total	.01388 (.0474)	16	(.7584)	.03221 (.10999)	16	(1.760)
Access and Shut-Off Valve, or Sim. Plumbing Penetration	.5661 (1.9335)	1	.5661 (1.9335)	1.5419 (5.266)	1	1.5419 (5.266)
Vent, Fill, & Inst. Line Penetration	.7626 (2.6045)	1	.7626 (2.6045)	.0449 (.15349)	1	.0449 (.15349)
Total Heat Flow			8.998 (30.73)			9.700 (33.13)
H_2 Boil-Off g/sec (lb/hr)			.0201 (.160)			.02167 (.1722)

Table 4.4-1: LH_2 TEST MODEL DESIGN THERMAL ANALYSIS RESULTS

The heat flow for MLI joints, like that for the basic MLI, scales axactly on the basis of heat flow per unit of joint length. The proper total length of joint to provide the desired total joint incremental heat flow could not be provided because of MLI standard material width limitations.

The MLI fastener arrangement on the actual LH_2 test model differs considerably from that shown for the OMS fuel tank design, resulting in differences between the predicted heat flow contributions for the actual test model and those indicated as ideal scaled values. The changes in fastener design are results of simplification in the fastener concept and experience in fabricating actual MLI panels. Similar changes would be incorporated in the OMS fuel tank design if it were revised. Thus, the tabulated differences are a result of design evolution and exist only because the OMS fuel tank design was treated as frozen.

The incremental heat leak associated with the pressure vessel support strap penetration, like that for the OMS fuel tank design, was predicted by considering independently the conduction through the strap and the additional heat flow through the MLI resulting from the removal of MLI to accommodate the attachment fitting on the pressure vessel. The Kevlar/epoxy (PRD/epoxy) strap for the LH_2 test model design was sized to provide the desired heat flow, meeting the scaling objective. For a 254 mm (10.0 in.) effective thermal resistance length the cross-section area of the strap is .465 mm^2 (0.72 in^2). The contribution of the attachment fitting penetration to the heat flow exceeds the ideal scaled value and even exceeds the value for the OMS fuel tank design because of the size of the cut-out in the inner MLI panel to accommodate the attachment fitting and clevis.

The simulated plumbing penetration, intended to represent, by means of one assembly on the LH_2 test model, the two plumbing penetration assemblies of the OMS fuel tank design, was analyzed in a manner analogous to the analysis of the vent valve assembly on the OMS fuel tank design (See Section 3.4). For the simulated plumbing penetration on the LH_2 test model design, the main tube, the simulated seal vent and valve actuator lines, the fiberglass insulation support tube, and the MLI wrap around the main tube (Appendix D, Figure D-13) were each sized to yield, to a practical approximation, the desired heat flow contribution. The use of standard material gages where appropriate is one reason for

the lack of exact thermal simulation, as seen in Table 4.4-1. Another reason for the discrepancy was the necessity to make compromises in modelling the plumbing penetration configuration in order to meet test functional and instrumentation requirements and facility clearance restrictions.

4.5 MATERIAL EVALUATION TESTS

4.5.1 Sandwich Beam and Edgewise Compression Specimens

The test panel was fabricated per Figure D-21, Appendix D, to provide eight beam specimens 68.58 mm (2.70 in) wide by 558.8 mm (22.0 in) long. Figure 4.5-1 is a cutting diagram of the panel specifying beam identification. Some of the beams were cut into edgewise compression specimens designated A, B, or C as shown in Figure 4.5-1.

The test plan for these specimens is summarized in Table 4.5-1. Two load directions were used, A and B. The A load direction put the outer skin (Detail II of Figure D-30 Appendix D) lap joint in compression. The B load direction put the Detail 1 lap joint in compression.

Figures 4.5-2a and b are photographs of the test apparatus used for the beam flexure and load cycle tests. Figure 4.5-2a shows the loading apparatus for the beam fexure tests and the transite environmental conditioning box used for the 450°K (350°F) temperature tests. For the load and temperature cycle work four beams (11-14) were loaded together as shown in Figure 4.5-2b. The beams were shimmed to assure an even distribution of load to each beam.

The test results are summarized in Table 4.5-2. Beams 9, 10, 11, and 13 were tested to failure. Beams 15 and 16 were cut up for edgewise compression specimens.

Beams 9 and 10 were tested in flexure with a single concentrated load at midspan. The first test (Type A) was conducted at 294°K (70°F) to the limit load of 275.79 N (62 lb) which produced a stress of 10549 MN/m^2 (15.3 ksi) 2024-T81 in the aluminum face skins. This test confirmed that the sandwich beam would carry the design limit load stress as a simple beam and also provided a measure of the beams' bending stiffness, P/Y. The design value for P/Y was 71.28 kN/m (407 lb/in) at 294°K (70°F). The test values agreed very

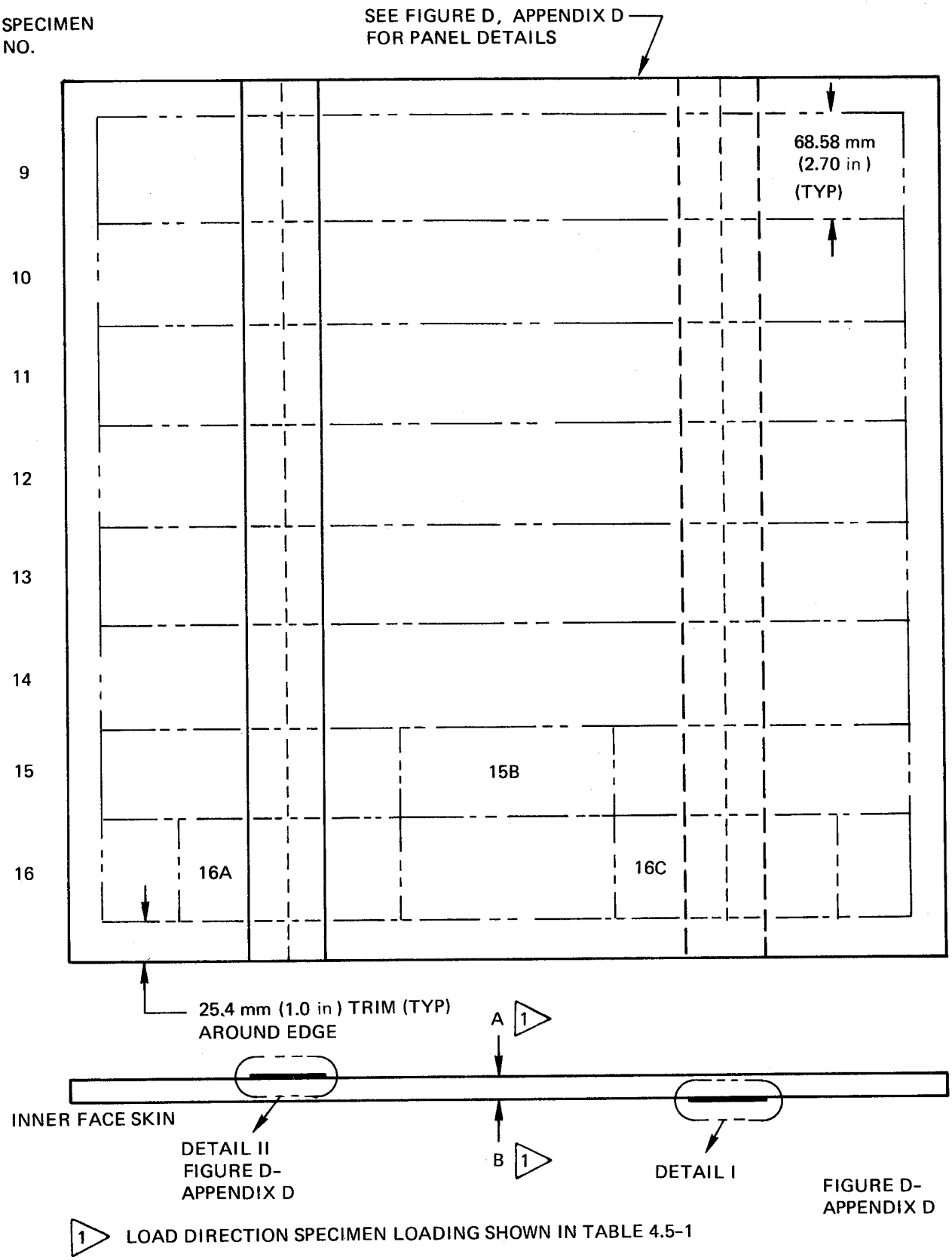

Figure 4.5-1. Sandwich Beam and Edgewise Compression Specimens

Table 4.5-1. Test Plan for Sandwich Beam and Edgewise Compression Members

NO. [1]	SIZE 68.58 mm (2.70IN.) x mm	lb	LOAD DIRECTION	CYCLE BEFORE TEST 4	TEST
9	558.8	22	A	0	1. LONG BEAM FLEXURE AT 294°K (70°F) [2] TO LIMIT LOAD. 2. LONG BEAM FLEXURE TO FAILURE AT 450°K (350°F) [3]
10	558.8	22	B	0	1. LONG BEAM FLEXURE AT 294°K (70°F) [2] TO LIMIT LOAD. 2. LONG BEAM FLEXURE TO FAILURE AT 450°K (350°F) [3]
11	558.8	22	A	100	1. LONG BEAM FLEXURE AT 294°K (70°F) [2] 2, LONG BEAM FLEXURE TO FAILURE AT 450°K (350°F) [3]
12	558.8	22	A	100	NONE
13	558.8	22	B	100	1. LONG BEAM FLEXURE AT 294°K (70°F) [2] 2. LONG BEAM FLEXURE TO FAILURE AT 450° (350°F) [3]
14	558.8	22	B	100	NONE
15B	152.4	6	–	0	EDGEWISE COMPRESSION AT R.T. AND 450°K (350°F)
16A & C	152.4	6	–	0	EDGEWISE COMPRESSION AT R.T. AND 450°K (350°F)

[1] FIGURE 4.5-1

[2] LIMIT LOAD = 275.79 N (62 lb) RECORD LOAD MIDSPAN DEFLECTION DATA

[3] RECORD LOAD MIDSPAN DEFLECTION DATA AND FAILURE LOAD

[4] RECYCLE EQUALS
HEATING SPECIMENS FROM 294°K (70°F) TO 450°K (350°F), LOADING TO FACE SKIN LIMIT STRESS, UNLOADING, THEN COOLING TO 294°K (70°F)

DESIGN LIMIT LOAD EQUALS 275.79 N (62 lb) OR 2/3 OF [3] FAILURE LOAD WHICHEVER IS LOWER. LOAD APPLIED AT MIDSPAN OF EACH BEAM.

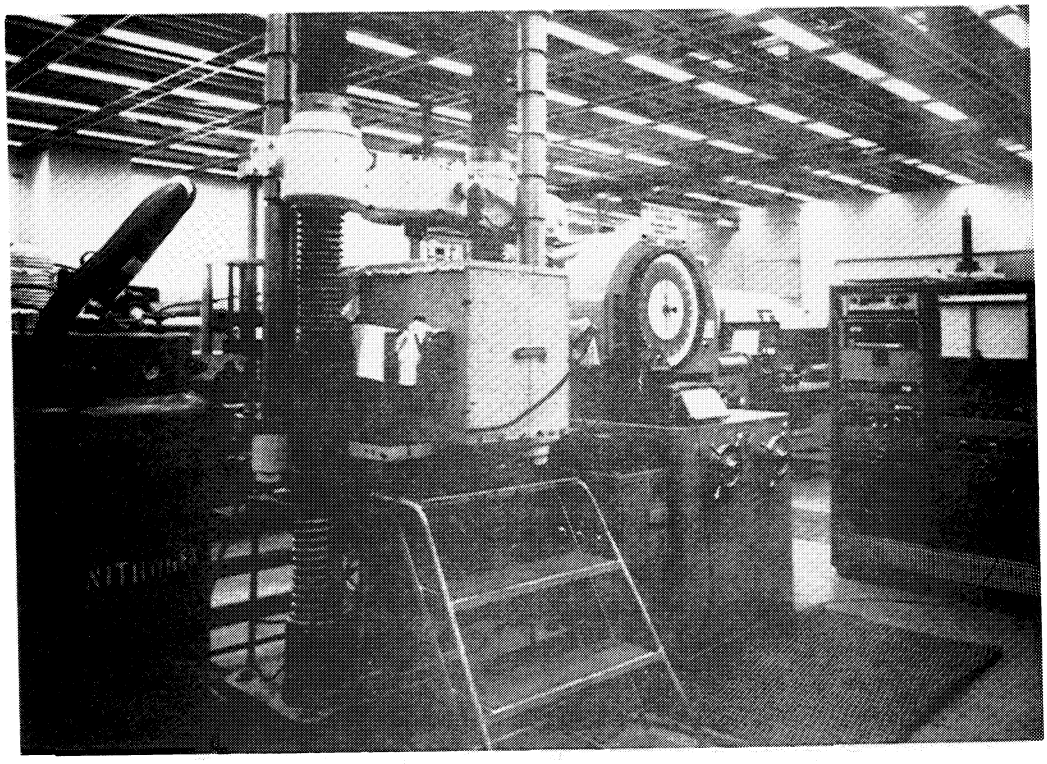

a: BEAM FLEXURE TEST APPARATUS WITH ENVIRONMENTAL CONDITIONING BOX

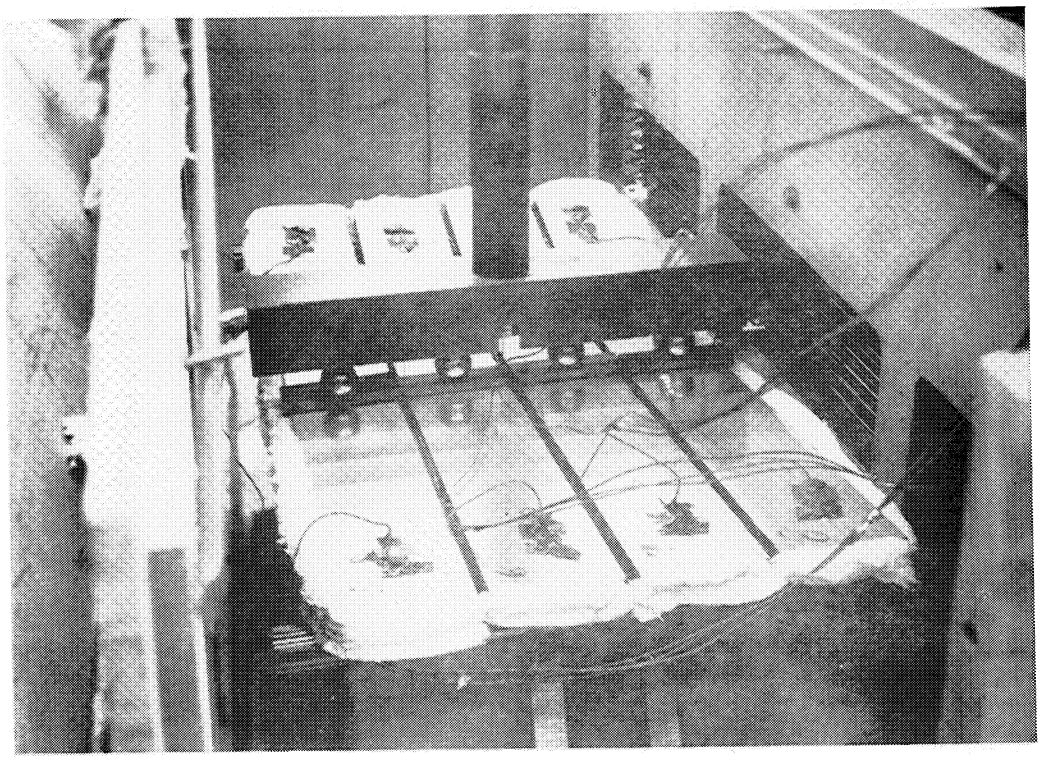

b: INTERIOR OF ENVIRONMENTAL BOX

Figure 4.5-2. Sandwich Beam Specimens Vacuum Jacket—LH_2 Test Model

Table 4.5-2. Summary of Sandwich Test Data

SPEC NO.	LOAD DIR.	CYCLES BEFORE TEST	TEST TYPE	TEST TEMPERATURE		TEST RESULTS							
						LIMIT LOAD		P/Y		ULTIMATE LOAD			
				°K	°F	N	lb	N/m	lb/in	N	lb	COMMENTS	F_{cu} AT BREAK
9	A	0	A.FLEX B.FLEX	294 450	70 350	275.79 275.79	62 62	73.03 66.37	417 379	809.58	182	NO FAILURE F_{cu} = 308.89 M N/m^2(44.8 ksi) F_{su} = 372.32 k N/m^2 (54 psi)	154.44 M N/m^2 (22.4 ksi)
10	B	0	A.FLEX B.FLEX	294 450	70 350	275.79 275.79	62 62	68.65 64.80	392 370	800.68	180	NO FAILURE F_{cu} = 305.44 M N/m^2(44.3 ksi) F_{su} = 365.42 k N/m^2 (53 psi)	305.44 M N/m^2 (44.3 ksi)
11	A	100	A.FLEX B.FLEX	294 450	70 350	275.79 275.79	62 62	77.76 60.07	444 343	676.13	152	NO FAILURE F_{cu} = 257.86 M N/m^2(37.4 ksi) F_{su} = 310.26 k N/m^2 (45 psi)	193.74 M N/m^2 (28.1 ksi)
13	B	100	A.FLEX	294 450	70 350	275.79 275.79	62 62	76.36 63.75	436 364	747.30	168	NO FAILURE F_{cu} = 284.75 M N/m^2(41.3 ksi) F_{su} = 344.74 k N/m^2 (50 psi)	242.0 M N/m^2 935.1 ksi)
15B		0	A.COMP B.COMP C.COMP	294 450 294	70 350 70	7562.0 6227.5	1700 1400			15,591	3505	NO FAILURE NO FAILURE F_{cu} = 373.0 M N/m^2 (54.1 ksi)	
16A		0	A.COMP B.COMP C.COMP	294 450 294	70 350 70	7562.0 6227.5	1700 1400			18,972	4265	NO FAILURE NO FAILURE F_{cu} = 454.37 M N/m^2(65.9 ksi)	
16C		0	A.COMP B.COMP C.COMP	294 450 294	70 350 70	7562.0 6227.5	1700 1400			12,811	2880	NO FAILURE NO FAILURE F_{cu} = 306.8 M N/m^2 (44.5 ksi)	

closely with the calculated value. The second test (Type B) on beams 9 and 10 was conducted at 450°K (350°F). The beams were loaded to failure to measure the P/Y up to 275.79 N (62 lb) load and to determine the ultimate beam load. The ultimate beam load was measured to assure that there was at least a 1.5 factor-of-safety for the load and thermal cycle tests. The ultimate beam loads were approximately 800.68 N(180 lb). The comments column of Table 4.5-2 summarizes the ultimate load stress in the aluminum face skin (f_{cu}) and the ultimate load core shear stress (f_{su}). Figure 4.5-3a shows the location and type of failure for beams 9 and 10. Beam 9 did not fail at the point of maximum face stress. The f_{cu} calculated for the location of the failure is shown to the right of the comments column in Table 4.5-2.

Beam 10 broke at the point of maximum stress. The calculated value of P/Y at 450°K (350°F) was 372 for tests 9B and 10B which agree very closely with the measured values.

Beams 11 and 13 were loaded to 275.79 N (62 lb) and 450°K (350°F) one hundred times to simulate 100 space shuttle flights. The beams were then tested at 294°K (70°F) to 275.79N (62 lb) to measure P/Y. The beams were then tested at 450°K (350°F) and loaded to failure to measure P/Y and the residual ultimate strength. These data showed an apparent increase in P/Y at 294°K (70°F), a small decrease in P/Y at 450°K (350°F), and a small decrease in ultimate strength after 100 thermal and load cycles. The apparent increase in P/Y at 294°K (70°F) was about 9 percent. The decrease in P/Y at 450°K (350°F) was about 6 percent after 100 cycles. The decrease in beam strength was about 12 percent.

Since the design of the vacuum jacket was based on buckling of the sandwich shell, the stiffness parameter, P/Y, was the critical degradation factor. Beam strength was important but not as critical as the stiffness. The maximum decrease in bending stiffness at 450°K (350°F) was measured on Beams 9

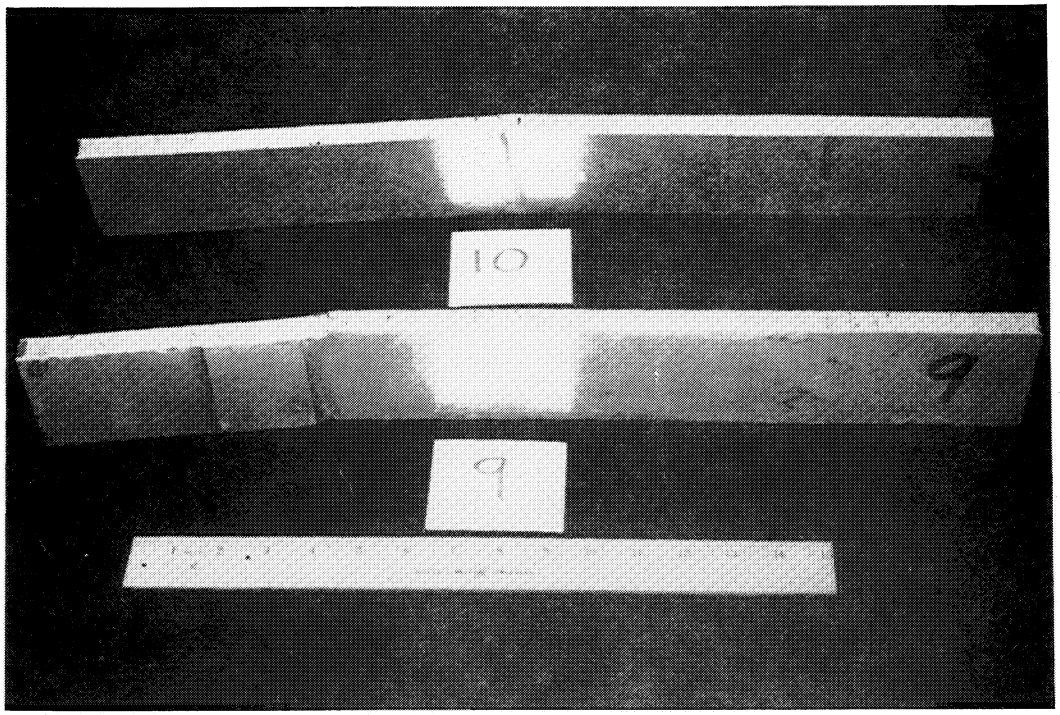

a: FAILED SPECIMENS 9 AND 10

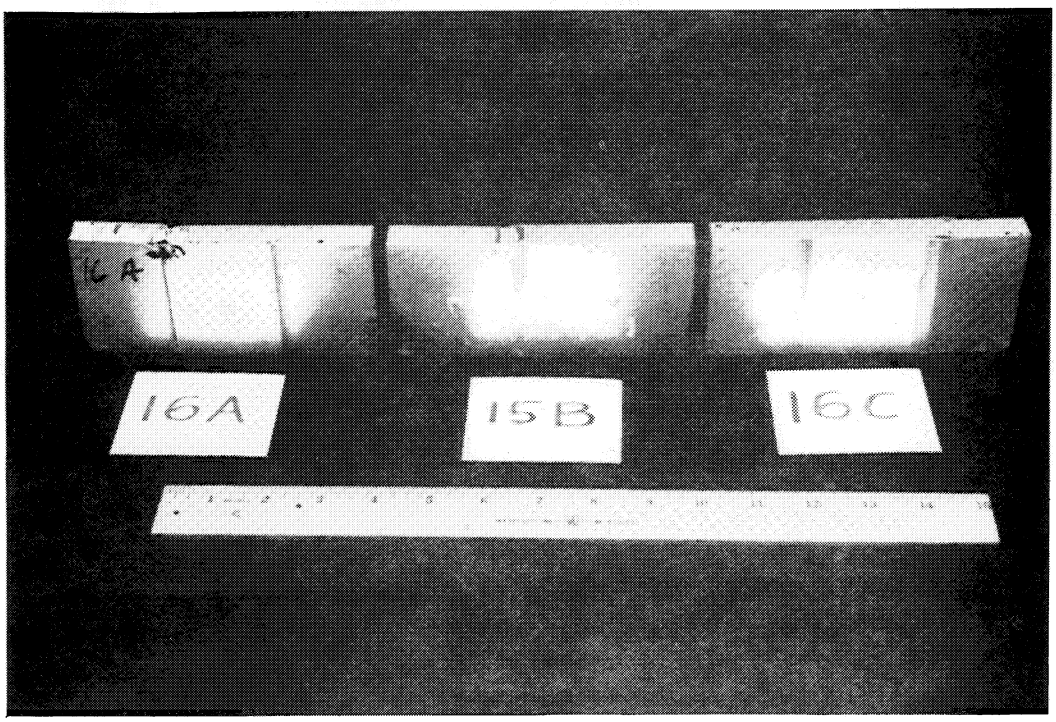

b: FAILED SPECIMENS 16A, 16B, AND 16C

Figure 4.5-3. Sandwich Beam Specimens Vacuum Jacket—LH_2 Test Model

and 11. The stiffness was 90.5 percent of the original stiffness after 100 cycles. It would be expected from this, that the vacuum jacket stiffness would decrease by this amount for the 100 simulated flight cycles scheduled for the system evalation tests. It was necessary to increase the proof load requirements (see Section 4.3.1) by this factor to assure that the proof load vacuum jacket would withstand the effects of a 450°K (350°F) temperature and 100 flights. The effect of 450°K (350°F) was estimated from the data for beams 9 and 10. The maximum decrease in stiffness was measured on beam 9. The effect of 450°K (350°F) was 379/417ths of the 294°K (70°F) stiffness or 90.9 percent. This was almost exactly the predicted effect for aluminum 2024-T81 sheet. Therefore, the required proof load at 294°K (70°F) for the vacuum jacket was calculated to be,

$$\text{Proof Load Pressure at 294°K (70°F)} = 142.03\ \text{kN/m}^2 \times \frac{1}{.905} \times \frac{1}{.909}$$

Ultimate Design Pressure (20.6 psi)	Effect of Temperature Factor	Effect of 100 Cycles Factor

$$= 172.37\ \text{kN/m}^2\ (25.0\ \text{psi})\ \text{external pressure}$$

The three edgewise compression specimens 15B, 16A, and 16C were tested to check the design of the interior and exterior skin splices. Figure 4.5-3b is a photograph of the failure modes. Specimen 15B represented the basic sandwich material without any joints. Specimen 16A contained a lap joint in one skin which represented the external skin splice for the vacuum jacket. Specimen 16C contained a joint representative of the interior skin splice. All three specimens failed by the face wrinkling mode with the face skin buckling into the lightweight 33.64 kg/m^2 (2.1 lb/ft^3) aluminum 5056 Flexcore. The allowable compression yield stress for aluminum 2024-T81 sheet at 450°K (350°F) is 310.26 MN/m^2 (45 ksi). Comparing this value with the data for specimens 15B and 16A, it can be seen that both the basic sandwich and the external splice joint developed strength in excess of the allowable

compression yield stress. However, specimen 16C, the internal skin splice joint, did not develop the allowable compression yield strength. The cause for this was the joggle put in the outer skin by the uniform core thickness being joggled over the 0.305 mm (0.012 in) and 0.076 mm (0.003 in) doublers used for the inner skin splice. The estimated allowable strength for this joint was 253.04 MN/m^2 (36.7 ksi) at 450°K (350°F). This still provided a reasonably large margin-of-safety for the vacuum jacket.

The basic sandwich design for the vacuum jacket for the limit load of -101.35 kN/m^2 (-14.7 psi) external pressure resulted in an aluminum face skin stress of 105.49 kN/m^2 (15.3 ksi) compression in both the longitudinal and meridional directions of the hemispherical end domes. The ultimate joint strength was 1.4 times this at 450°K (350°F) or 147.55 kN/m^2 (21.4 ksi). This requirement can be compared to the f_{cu} data in Table 4.5-2. Beam test 9B failed at an f_{cu} = 154.44 kN/m^2 (22.4 ksi). All other beams exceeded this value as did the edgewise compression specimens. In fact, the edgewise compression strength of the joint design in beam 9 was 454.37 kN/m^2 (65.9 ksi) in pure compression. This indicated that the effect of core shear stress greatly reduced the allowable beam compression stress. Note that the ultimate core shear stresses (f_{su}) for beams 9, 10, 11, and 13 in Table 4.5-2 ranged from 310.26 to 372.32 kN/m^2 (45 to 54 psi). The typical ultimate shear strength for this core is 551.58 kN/m^2 (80 psi) at 450°K (350°F). Figure 4.5-4 is an interaction plot of beam compression stress versus core shear stress. The edgewise compression specimen data corresponding to the failure mode of the beam specimens are connected by dashed lines to the core shear strength. All the specimens were assumed to have the same core shear strength, 551.58 kN/m^2 (80 psi). The end points of the allowable interaction curve were taken as the compression yield strength of the 2024-T81 aluminum face skins and the 5056 aluminum Flex-Core. The $R_c^2 + R_s^2 = 1$ interaction curve appears to fit the assumptions without violating any of the test data. The effect of core shear stress on the beam compression strength was expected to have very little impact on the

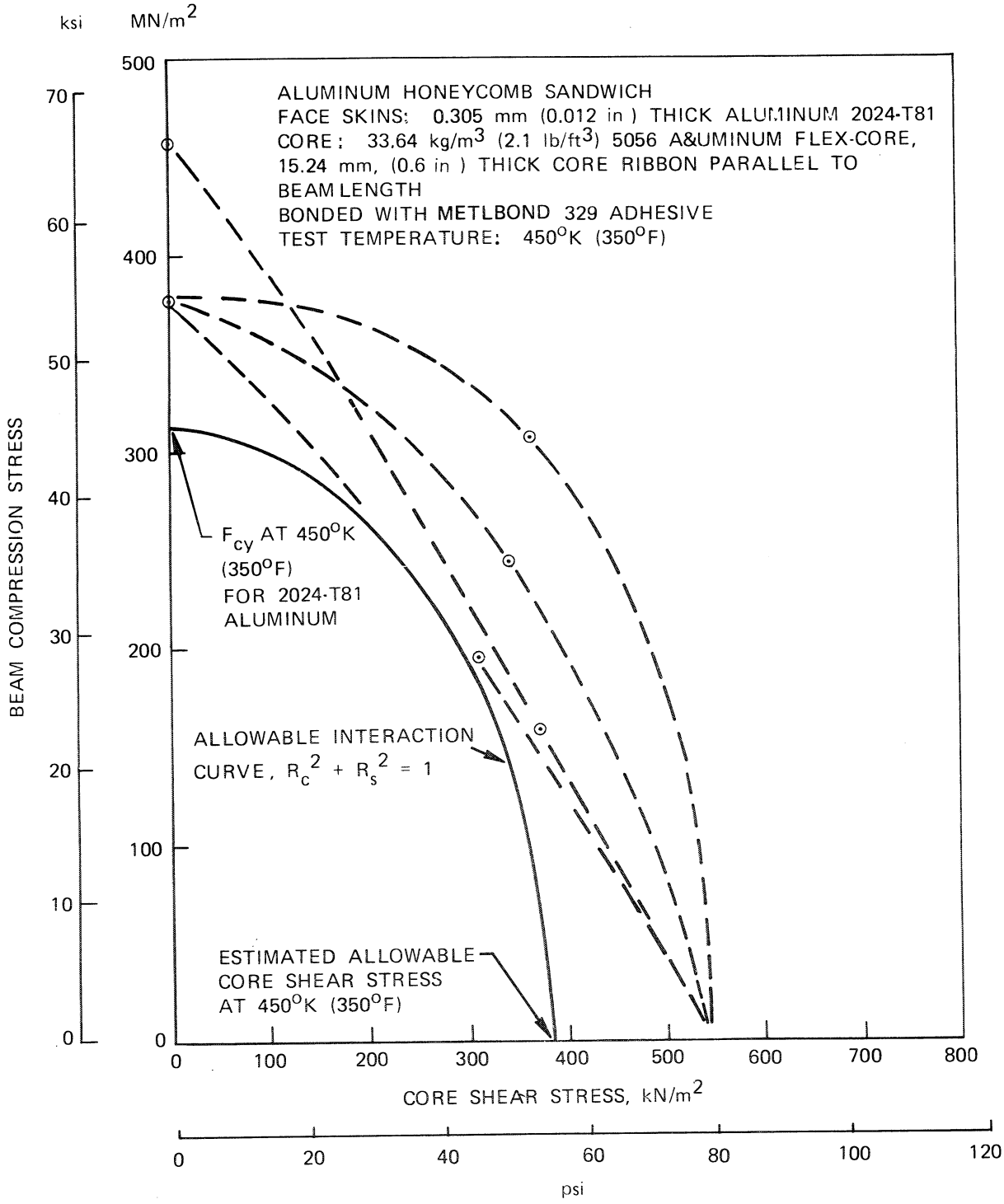

Figure 4-5-4. Interaction Curve for Face Compression and Core Shear Stress

vacuum jacket strength because of its very low core shear stress. There was low core shear stresses in the transition area from the hemisphere to cylinder sections and near the girth ring, but practically no core shear stresses in the hemispherical heads.

In summary, these sandwich beam and edgewise compression tests indicated that:

1) The effects of temperature and the degradation due to 100 thermal and load cycles was approximately 9 percent each. The 172.37 kN/m^2 (25 psi) external pressure proof load for the vacuum jacket was sufficient to account for both of these effects combined.

2) The lap joint design for the outer face skin had sufficient strength to develop the compression yield strength of the 2024-T81 aluminum.

3) The lap joint design for the inner face skin was weaker than the basic sandwich and the outer skin lap joint. It would not develop the compression yield strength of the 2024-T81 aluminum. The weakness was caused by joggle in the outer skin. The joggle was caused by the core lapping 0.305 mm (0.012 in.) skin doubler of the joint. The estimated allowable joint strength was 253.04 MN/m^2 936.7 ksi) in the aluminum face skin. This still provided a large margin of safety for the vacuum jacket design.

4.5.2 Support Strap Tests

Kevlar/Epoxy (PRD/epoxy) was selected in the design studies (Section 3.2) as the most efficient state-of-the-art material for the OMS fuel tank pressure vessel support straps. EA 934 (Hysol Division, the Dexter Corp.) appeared to be the most promising adhesive for bonding the GAL-4V titanium end fittings to the PRD/epoxy strap. Hysol catalogue data shows that 12.7 mm (0.5 in) overlap bonds with 2024 T3 alclad aluminum tested at 21.37 kN (3100 psi) at

R.T. and ≃ 5.52 kN (800 psi) at 450°K (350°F) shear stress. It was assumed for design purposes that equivalent shear stresses at the respective temperatures could be developed with an EA 934 bond between the titanium end fittings and the Kelvar/Epoxy (PRD/epoxy) strap. There was, however, no catalogue data for allowable shear stresses at 20.5K (-423°F). In order to obtain this data a preliminary test strap assembly was fabricated and tested at 20.5 (-423°F). Results from this test, along with the Hysol catalogue data were used to design the support strap assembly for the LH_2 test model. This support strap assembly was tested to verify its structural adequacy for the load and temperature requirements. The results of this test along with other design developments occurring at the time, suggested some minor modifications to the support strap design. A second support strap assembly was fabricated incorporating these modifications and then tested.

Preliminary Test

Figure 4.5-5a is a photograph of the preliminary strap assembly which was tested to obtain adhesive shear values at 20.5°K (-423°F) for EA 934. Bonding 6A-4V titanium to Kevlar/epoxy laminate, Figure D-29, Appendix D, describes the details of this assembly. Figure 4.5-5b shows the specimen mounted in the LH_2 cryostat. The strap failed at 5.34 kN (1200 lb) at 20.5°K (-423°F) developing an average shear stress of $\frac{5.34}{2 \times 0.019 \times 0.0254}$ = 5.52 MN/m^2 (800 psi).

Support Strap Assembly Specimen 1

The Hysol catalogue data and the results from the preliminary test were used to design support strap assembly speciman 1 which was similar to the one shown in Figure 4.5-6. Specimen geometry and test results are shown in Table 4.5-3. Drawing details were similar to those shown in Figure D-30, Appendix D. The differences were 24 ply, Kevlar/epoxy tape in place of 10 ply and a 360.68 mm (14.20 in) length between end fitting $\mathcal{L}$'s in place of 335.28 mm (13.20 in).

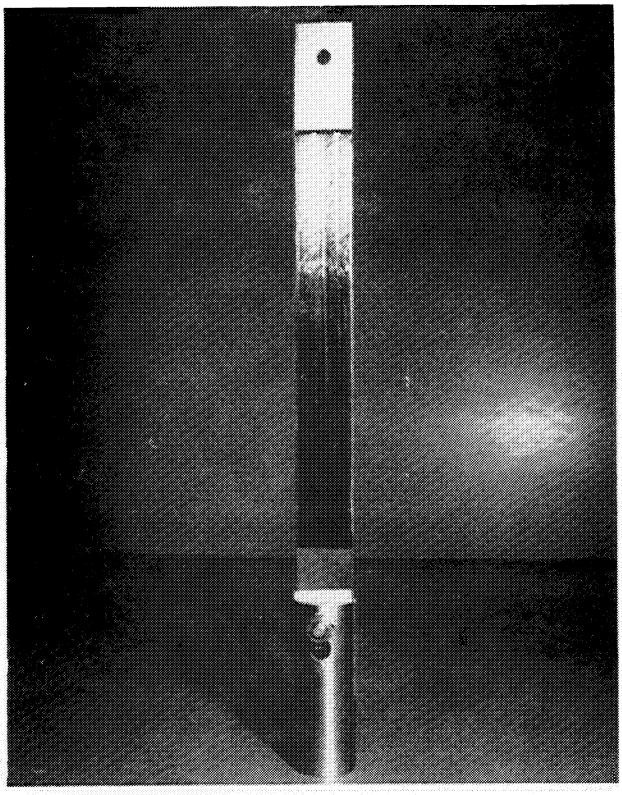

A. TEST SPECIMEN

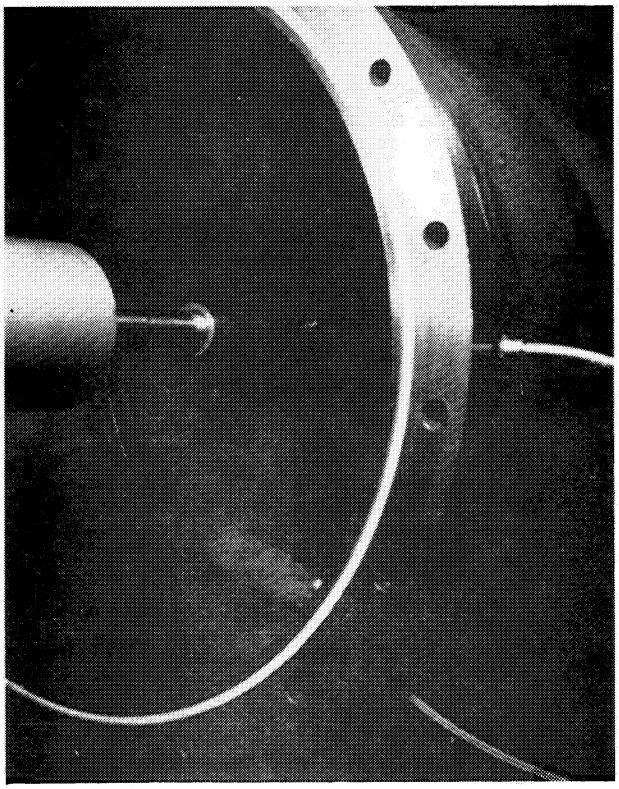

B. SPECIMEN MOUNTED IN LH_2 CRYOSTAL

Figure 4.5-5. Support Strap Preliminary Test

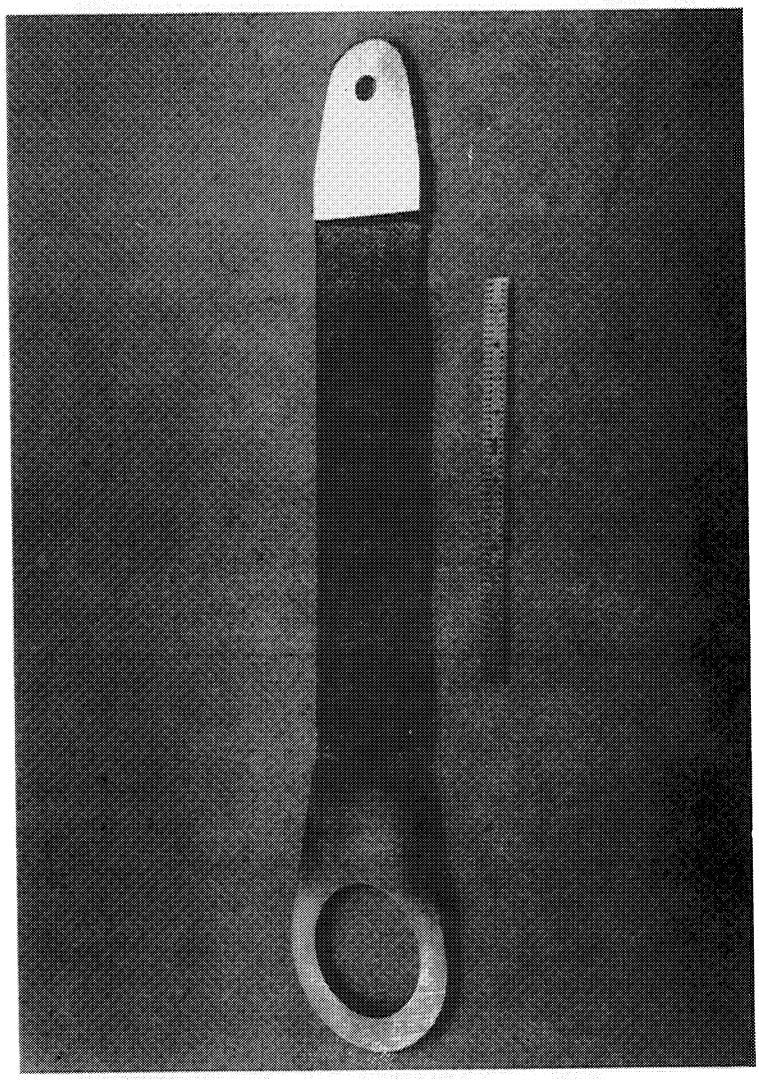

Figure 4.5-6. Pressure Vessel Support Strap Assembly Test Specimen 2–LH_2 Test Model

Table 4.5-3. Geometry and Test Results for Pressure Vessel Support Strap Assembly Specimens - LH_2 Test Model

SPECIMEN	GEOMETRY						TEST RESULTS				
	LENGTH BETWEEN ENG FTG. c's		KEVLAR (PRD) 49-3/EPOXY STRAP				ULTIMATE RT TENSION LOAD		TYPE OF FAILURE	ELONGATION AT PROOF LOAD & RT 16.01 kN (3600 in)	
			WIDTH		THICKNESS						
	mm	in	mm	in	mm	in	kN	lb		mm	in
1	360.68	14.20	50.4	2.00	4.572	0.18	(1) 17.57 (2) 19.02	(1) 3950 (2) 4275	SMALL END FITTING DEBOND	0.7239	0.0285
2	335.28	13.20	50.4	2.00	1.524	0.06	(3) 21.57	(3) 4850	LARGE END FITTING DEBOND SEE FIGURE 4.5-	(3) 1.0338	(3) 0.0407

(1) TESTED AFTER:

1) LARGE END FITTING JOINT AREA CYCLED WITHOUT LOAD FROM 450°K (350°F) TO 77.4°K (320°F-) FOR 100 CYCLES
2) SMALL END FITTING JOINT AREA HEATED TO 450°K (350°F AND THE SPECIMAN CYCLED FROM 111.21 TO 2224.11N (25 TO 500 lb) TENSION FOR 92 CYCLES. (100 CYCLES NOT COMPLETED DUE TO TEST MACHINE MALFUNCTION CAUSING PARTIAL DEBONDING OF SMALL END FITTING TO PRD 49-3/EPXOY STRAP)
3) SPECIMAN (WITHOUT REPAIR) COOLED TO 20.5°K (-42°F) IN A CRYOSTAT AND CYCLED FROM 111.21 TO 2224.11N (25 TO 500 lb) TENSION FOR 100 CYCLES
4) SPECIMAN (WITHOUR REPAIR) FAILED AT RT AT 17.57 K kN (3950LB). FAILURE BY DEBONDING OF SMALL END FITTING FROM PRD 49-3/EPOXY STRAP

(2) TESTED AFTER REBONDING SMALL END FITTING TO PRD 49-3/EPOXY STRAP

(3) TESTED AFTER BOTH END FITTING JOINT AREAS WERE COLD SHOCKED TO 77.4°K (-320°F)

The design criteria for the LH_2 test model pressure vessel support straps was:

Tension Loads

Proof:	16.01 kN (3600 lb)	based on transportation load factors
Ultimate:	21.49 kN (4830 lb)	

Temperature

At pressure vessel boss:	20.5 K (-423°F)	minimum
	RT	maximum
At vacuum jacket trunnion:	RT	minimum
	450°K (350°F)	maximum

Cycles

100 load and thermal cycles.

The test plan called for

1) Proof load to 16.01 kN (3600 lb) tension at room temperature (RT). Record strap extension at load.

2) Conduct 100 thermal cycles on the large end fitting to Kelvar strap adhesive joint. Each thermalcycle shall consist of a) heat to 450°K (350°F $^{+0}_{-25°F}$) (1 min), b) cool to RT (2 min), c) cool to 77.4°K (320°F) (1 min), d) heat to RT (2 min).

3) After cycles 1, 5, 10, 20, 30, 40, 50, 60, 70, 80, 90, 100 inspect bond joint for cracks.

4) Cycle at 500 lb tension 100 times at 450°K (350°F $^{+0}_{-25°F}$).

5) Cycle at 500 lb tension 100 times at 20.5°K (-423°F).

6) Load to 21.49 kN (4830 lb) tension at RT.

During the thermal cycle tests, a hairline crack appeared in the adhesive fillet on one side after three cycles. No change was observed until the 30th cycle when a hairline crack appeared in adhesive fillet on the other side. Then on the 50th cycle, another hairline crack appeared in the fillet on the first side. No change was observed for the remainder of the thermal cycle tests.

Test machine malfunction caused partial debonding of the small end fitting to the strap, and prevented completing more than 92 tension load cycles at 450°K (350°F). This strap without repair completed the tension load cycles at 20.5 K (-423°F) then was failed at RT at 17.57 kN (3950 lb). The failure load was inadequate to meet the design requirements. The small end fitting was rebonded and the strap retested. It failed at a RT tension load of 19.02 kN (4275 lb).

Support Strap Assembly Specimen 2

Several items contributed to support strap design modification:

1) It was concluded that a greater pressure vessel movement could be tolerated than that allowed by the 0.7239 mm (0.0285 in) elongation measured on Specimen 1 at RT proof load,

2) It was found that a shorter support strap was needed in order to provide adequate turnbuckle adjustment during assembly,

3) Specimen 1 was judged as being too stiff for a purely tension carrying support strap, and

4) A decrease in strap cross sectional area would decrease the support strap thermal scaling inaccuracy.

Specimen 2, a shorter, thinner support strap, was fabricated and tested. Figure 4.5-6 is a photograph of this specimen after testing. Figure D-30, Appendix D, is the assembly drawing for this specimen, as well as for the sixteen pressure vessel support straps used on the LH_2 test model. Table 4.5-3 shows the strap geometry and test results.

The EA 934 adhesive bond had been verified at 20.5 K (-423°F) and 450°K (350°F) on Specimen 1, and further testing at these temperatures was not considered necessary. Both end fitting joint areas on Specimen 2 were cold shocked to 77.4°K (-320°F) then proof tested to 16.01 kN (3600 lb) at RT, at which point the strap elongation was measured. Specimen 2 was then failed at 21.59 kN (4850 lb) tension.

It was concluded from these tests that the Specimen 2 design was structurally adequate for the loads and temperature environment requirements for the LH_2 test model pressure vessel support straps.

4.5.3 MLI Thermal Tests IR&D

Insulation Assembly Elevated Temperature Test

In order to observe the response of the insulation system materials at temperatures expected during shuttle reentry, an elevated temperature test was run on an assembled sample of insulation design components. In the case of adhesive tapes for securing folds in the MLI shield materials and for attaching thermocouple junctions and leads, two candidate types were tested.

The test specimen design is shown in Figure D-38, Appendix D. The 0.152 m (6 inch) square specimen consisted of inner and outer MLI blankets incorporating the full scale number of Mylar and Kapton shields and Dacron spacers. The specimen also included a lap joint, representing the insulation girth joint, and Nylon pin fasteners and their associated X850 laminate

or aluminum foil reinforcing patches. Also included were Velcro hook and pile patches for joining outer to inner blanket, and for attaching the inner blanket to the aluminum base plate, which simulated the pressure vessel wall. Kapton shields at 2 levels and Mylar shields at 3 levels incorporated folds simulating those required on the full and half-scale insulation panel designs to produce blankets conforming to the double curvature. Each fold in the test specimen was secured with one 25.4 mm by 3.81 mm (1 inch by 0.15 inch) strip of Mystic 7402 aluminum foil tape and one similar sized Permacel EE6600 aluminized Mylar tape. The outer double layers of Dacron net were loosely sewn or laced together along the joint lines, as planned for the actual insulation blankets. It was intended that Dacron thread be used for these seams but Nylon thread was inadvertently used instead.

Thermocouples were installed in the test sample on the aluminum base plate, on the outer surface of the inner blanket, at the Mylar-Kapton interface in the outer blanket, on the outer surface of the outer blanket, and on the outer surface of an aluminum plate suspended just above the insulation assembly. All thermocouples attached to insulation shields were held by the Permacel EE6600 tape. Those attached to the aluminum plates were secured with a high-temperature Teflon tape.

The assembled test specimen is shown in Figure 4.5-7a. The photograph was taken after the test runs and after the specimen had been disturbed for examination of some of the internal layers. The test specimen incorporated a greater number of Velcro patches and thermocouples per unit area of MLI than the actual panels had. This fact resulted in a lower layer density and greater blanket thickness than expected for the actual panels.

The specimen was tested in a one-atmosphere air environment in a conventional radiant heat lamp oven. No forced air cirulation was used. Radiant lamp power was automatically controlled to drive temperatures measured on the

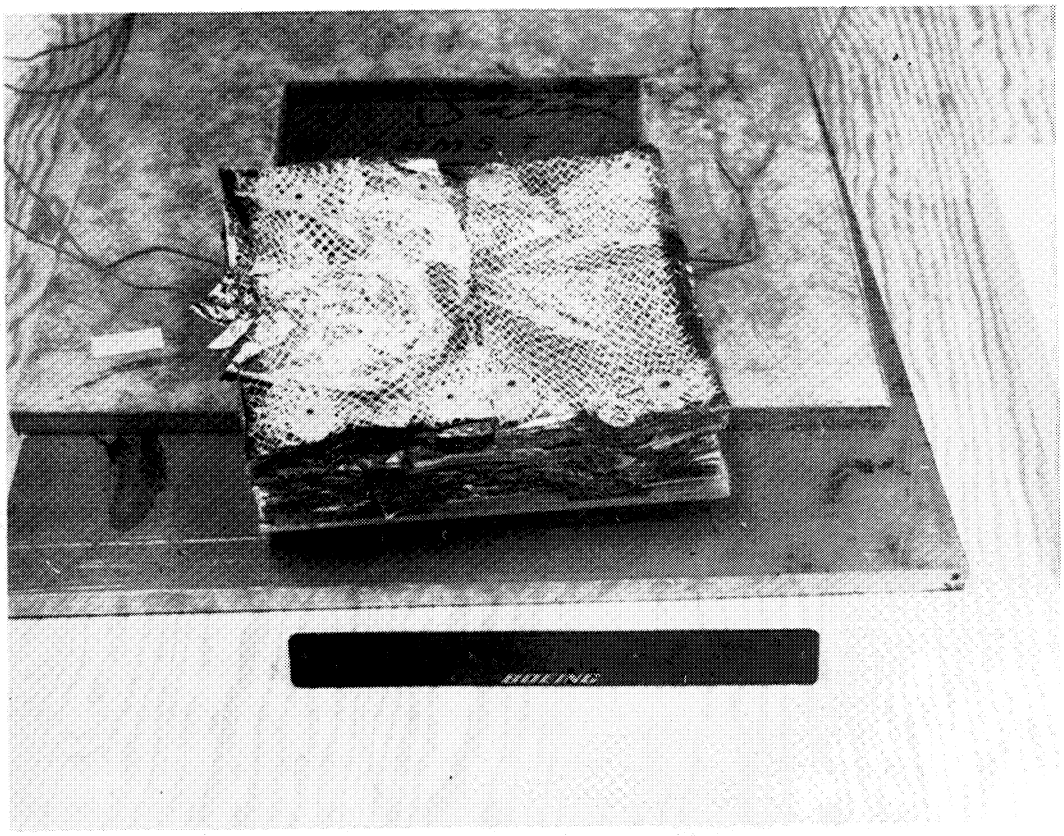

A: TEST SPECIMEN ASSEMBLY

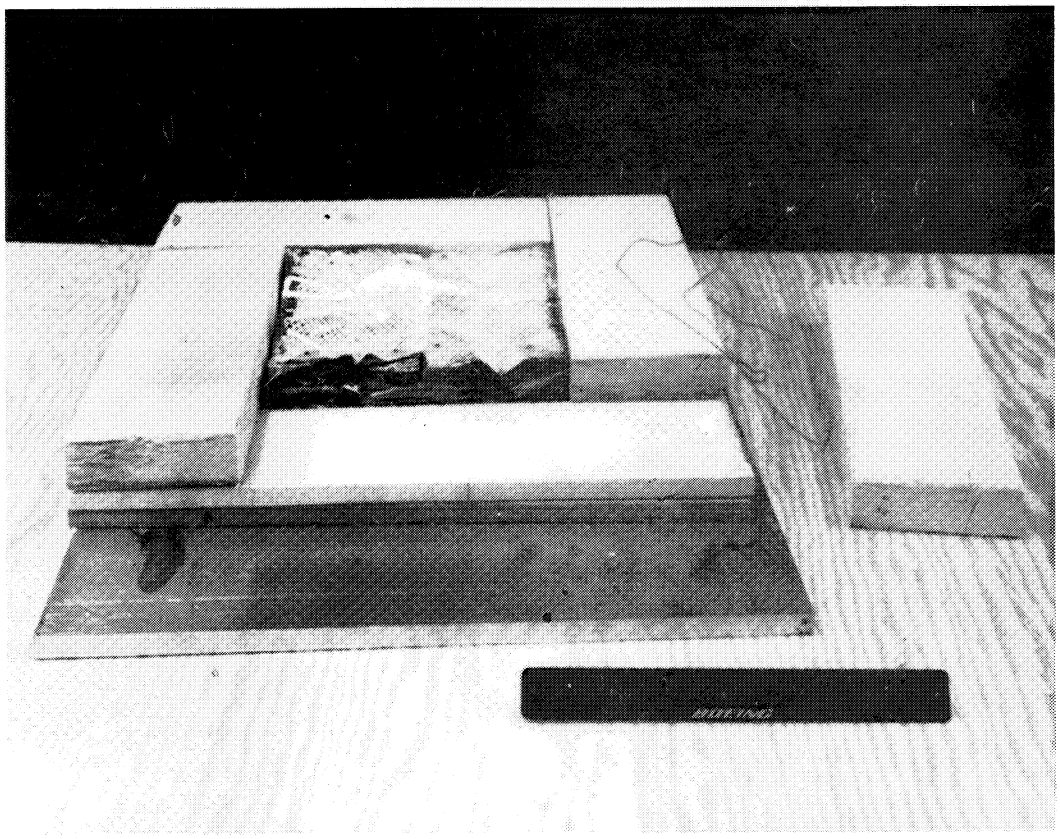

B: TEST SPECIMEN PARTIALLY ENCLOSED FOR TEST

Figure 4.5-7. MLI Assembly Thermal Test

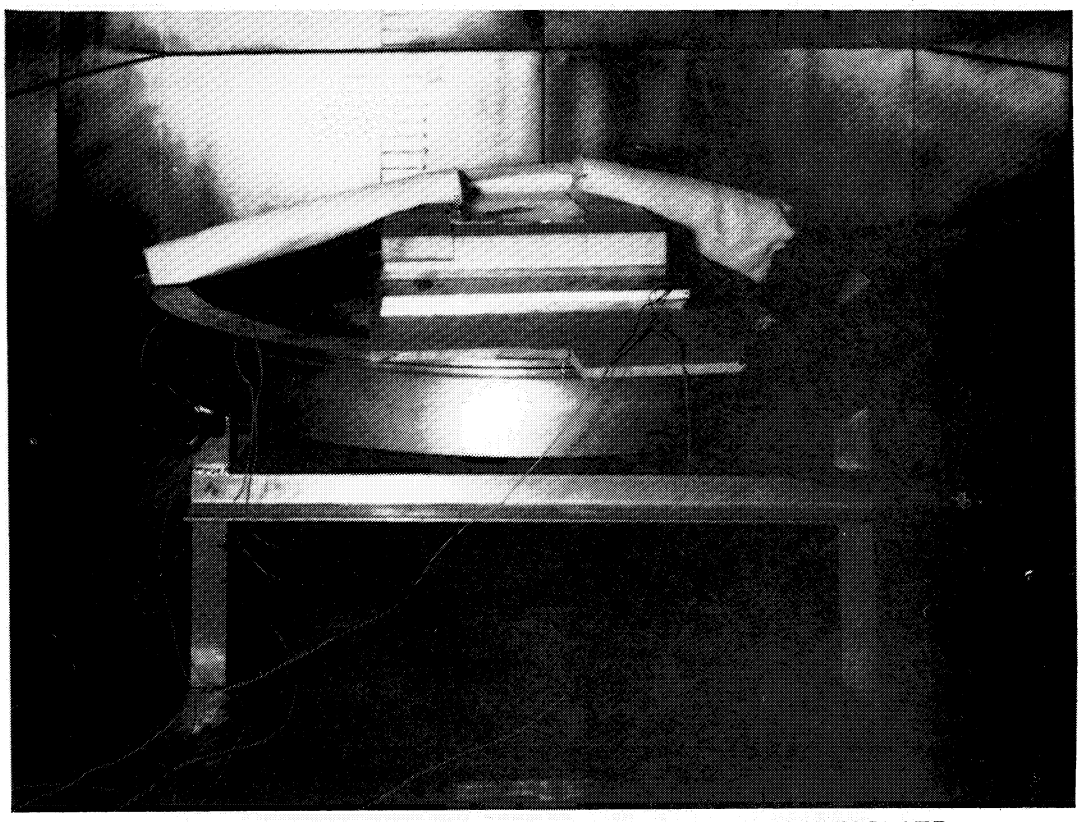

A: TEST SPECIMEN ARRANGEMENT WITH ALUMINUM PLATE FOR UNIFORM HEADING

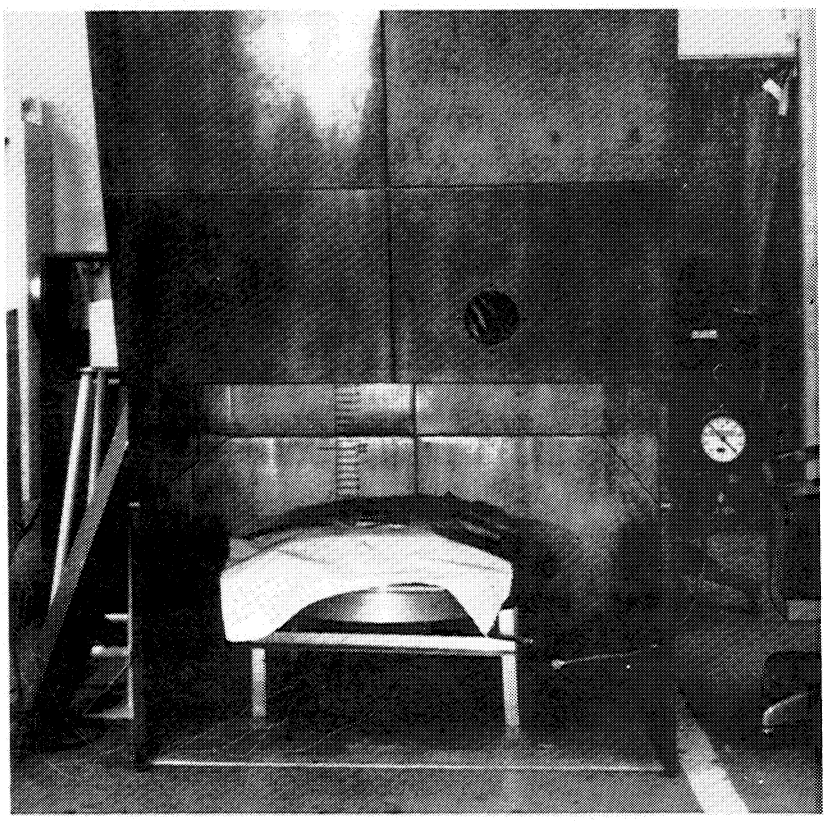

B: TEST SETUP IN RADIANT OVEN

Figure 4.5-8. MLI Assembly Thermal Test

outer surface of the aluminum plate suspended immediately above the test specimen to manually set values.

Preparation and installation of the test specimen in the furnace is shown in Figures 4.5-7b, and 4.5-8. The MLI assembly, on its 2.54 mm (0.10 inch) aluminum base plate was placed on a 0.3048 m (1.0 ft) square by 12.7 mm (0.50 inch) thick aluminum heat sink. The specimen was then enclosed by blocks of rigid insulation to minimize heating of the exposed edges of MLI. (See Fig. 4.5-7b). The rigid insulation blocks were built up to a level approximately 2.54 mm (0.10 inch) above the highest points on the specimen. A 2.54 mm (0.10 inch) aluminum plate, slightly larger than the test specimen, and with tabs to rest upon the rigid insulation blocks, was placed over the specimen in order to provide a uniform, controlled heating environment. (See Fig. 4.5-8a). Finally, a fiberglass cloth with a 0.152 m (6 inch) square cutout was draped over the test assembly to further shield the test specimen edges from radiated heat. (See Fig. 4.5-8b).

Two test runs were made. In the first run the test specimen was gradually heated to a maximum of 394°K (250°F) to check out procedures and instrumentation. The original plan was to set the automatic heat lamp controller to the maximum desired temperature, as measured on the surface of the upper aluminum plate, and wait until radiation and convection raised the MLI surface to the same temperature. Early during run No. 1, it became evident that such temperature equalization would require an extremely long time, if it was to occur at all. Therefore, the programmed temperature at the aluminum plate surface was set to higher values, cautiously at first. It was feared that the lag in the MLI response and the heat stored in the aluminum plate might result in the MLI surface temperature overshooting the desired 394°K (250°F) even after lamp shutoff, if the aluminum plate was allowed to reach a temperature much higher than 394°K (250°F).

The concern of overshooting the desired MLI maximum surface temperature was allayed, however, after observing that the MLI surface temperature tended to reach a steady-state value substantially lower than each aluminum plate value. It was concluded that because of the different absorptivities of

the aluminum plate and the Teflon tape over the plate's thermocouple, the temperature registered by that thermocouple did not accurately represent the average temperature of the plate. It is also possible that a significant amount of heat was being conducted away from the plate into the rigid insulation blocks surrounding the test specimen.

A temperature of 394°K (250°F) was reached on the MLI surface, with the controller (aluminum plate temperature) set at 444°K (340°F), after 32 minutes of run No. 1. Heating was then terminated and the specimen allowed to cool gradually prior to removal for inspection. Examination revealed that one of the Mystic aluminum foil tapes on the MLI outer surface had developed a dull appearance and a roughened surface texture, and had begun to separate from the Kapton shield surface. No other degradation of any other specimen components was observed after run No. 1.

The objective in run No. 2, the principal test of the specimen, was to raise the outer surface of the MLI to 450°K (350°F), the maximum expected during orbiter reentry. It was recognized that this condition would probably result in exceeding the 394°K (250°F) Mylar shield design allowable for the upper layers of Mylar, but since post-test examination of Mylar shields at some greater depth in the assembly would permit assessment of their response to 394°K (250°F), this result was acceptable.

Heat was applied rapidly in run No.2 in an attempt to develop a temperature gradient across the specimen resembling that expected during orbiter reentry. Of course, the test inner boundary temperature 303°K (85°F), did not simulate the tank wall cryogenic temperature expected in flight. Heating was initiated with a controller (aluminum plate temperature of 478°K (400°F) and was increased in successive steps to 500, 506, 533, 553°K (440, 450, 500, 535°F), and finally, 561°K (550°F). The MLI surface reached 454°K (357°F) 38 minutes after heating initiation. Heating was then terminated and the specimen allowed to cool for inspection.

Figure 4.5-9 shows the temperatures recorded during run No. 2, plotted along with the theoretically predicted MLI temperatures for orbiter reentry. These predicted values are the same as those shown in Section 3.4, Figure 3.4-3. The test was not planned to yield MLI temperature histories approximating those expected during reentry but fortuitously the test values showed a resemblance to the predictions; hence the inclusion of the predicted curves in the figure. The measured temperatures show fluctuations near the end of the run due to step increases in controller settings in attempt to achieve the desired 450°K (350°F) MLI surface maximum. As in run No. 1, no overshoot in MLI surface temperature occurred after heating termination.

The post-test examination of the specimen revealed no serious effects from the heat cycle but several minor changes were observed. The deterioration of the Mystic aluminum foil tape on the outer surface, observed after run No. 1 had not progressed any further. Other samples of this tape within the specimen showed similar surface degradation, the degree of which diminished with successively deeper (cooler) samples. Only one sample in addition to the surface strip showed any loss of adhesion. The Permacel aluminized Mylar tape showed no degradation at all. The aluminum foil patches used under some of the Velcro installations showed no degradation, nor did the X850 laminate patches.

Dacron net layers on the outer surface of each blanket, which had been laced along the joint lines, showed shrinkage of 3.175 mm to 6.35 mm (1/8 to 1/4 inch) along each edge. Since no other Dacron net layers exhibited any shrinkage at all, however, it was felt that this shrinkage was due to response of the Nylon thread that was erroneously used for the lacing. No other effects of the heat on the Dacron net was seen.

One Nylon pin fastener had failed at the exposed stem-washer fusion. None of the other seven fasteners similarly exposed showed any deterioration. It was concluded that the failed fastener was probably poorly formed on assembly.

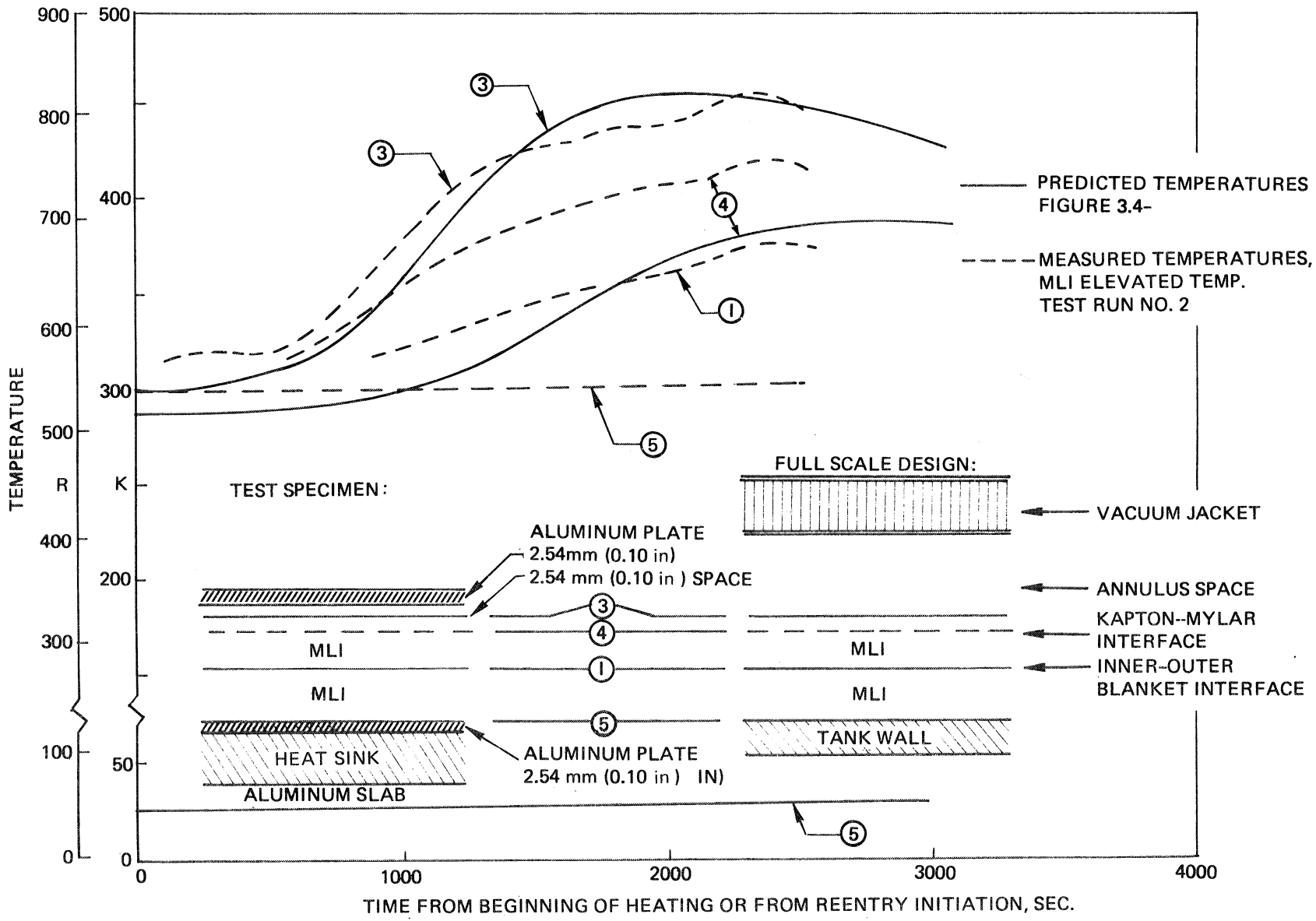

Figure 4.5-9. MLI Reentry Temperatures - Analysis & Test

The Velcro patches showed no effects of the elevated temperatures.

The layers of Mylar shields that experienced the highest temperature (417°K, 290°F) were closely examined. The first 3 or 5 layers of Mylar appeared to have acquired a wrinkled texture distinguishable from the normal wrinkles seen in the cooler layers or in virgin samples. The fact that only the first few shields exhibited this effect indicates that 417°K (290°F) may be near the threshold for thermal deterioration of the aluminized Mylar shields. No shrinkage of the high temperature Mylar shields could be detected nor could any loss of strength be detected by tearing the tested samples and virgin samples with the fingers.

It was concluded from the test that the Permacel EE6600 aluminized Mylar tape was definitely superior to the Mystic 7402 aluminum foil tape for securing shield folds and attaching thermocuples for the LH_2 test model. It was furthermore concluded that all other components of the MLI system design would adequately meet the elevated temperature requirements of the program. Concern remained, however, regarding the possible tendency of the Dacron net to shrink upon exposure to elevated temperatures.

Insulation Net and Shield Elevated Temperature Test

In the Insulation Assembly Elevated Temperature Test there was no way of accurately measuring changes in reflective shield or net spacer dimensions resulting from the heat cycle. The apparent shrinkage of the Dacron net layers on the outer surface of both blankets and the possibility of undetected shrinkage or growth of shield layers led to the decision to test each of these components separately for dimensional change.

A single layer of Dacron net and a single layer of double aluminized Kapton shield were cut as accurately as possible to 0.3048 m (1.0 ft) square dimensions. These samples were laid on a 2.54 mm (0.10 in) thick aluminum sheet with their edges accurately coinciding with scribed lines marking 0.3048 m (1.0 ft) squares on the aluminum. No restraint was used to secure the samples on the aluminum sheet. The Kapton sample had on its upper surface

three strips of the Permacel EE6600 aluminized Mylar tape, included as a further test of this tape. Three thermocouples were provided to monitor the test environment; one on the Kapton shield and two on the aluminum base sheet.

The aluminum sheet carrying the test specimens was supported on a slab of rigid insulation in the same radiant oven as used for the insulation assembly test and was subjected to a thermal cycle similar to that of run No. 2 of the assembly test. The samples were held at approximately 450°K (350°F) for 8 minutes and then allowed to cool for examination. Care was taken in moving the aluminum sheet into and out of the furnace so as not to disturb the samples.

No dimensional change of the Kapton shield relative to the scribe marks could be measured. There was no change in the appearance of adhesion of the aluminized Mylar tape.

The Dacron net appeared to have pulled away from the scribe marks in the neighborhood of two of the corners. This displacement ranged from 1.78 mm to 2.54 mm (0.07 in to 0.10 in) and tapered to zero away from corners. Elsewhere, the net edges conformed precisely to the scribe marks. When the net was lifted off the aluminum sheet, it was found to weakly adhere to the sheet at several points. This adherence appeared to be due to minute burrs on the sheet surface or adhesion due to contaminants on the sheet. Even though very weak, these points of adherence were strong enough to have prevented uniform relative movement of the net and sheet through a thermal expansion and contraction cycle. Thus the observed local edge displacement of the net could have resulted from a "crawling" action of the net during thermal expansion and contraction of the sheet. It is also possible that an irreversible working of the knots in some areas of the net caused the displacement.

The absence of any overall shrinkage of the Dacron net sample and the much smaller percentage edge displacement as compared with the shrinkage observed on the MLI assembly specimen tends to confirm the conclusion that the Nylon lacing thread was responsible for the apparent shrinkage on the latter specimen. There appears to be no basis for concern over serious heat-shrinkage of the Dacron net. A reasonable amount of looseness in the enclosing layers of the net on the assembled LH_2 test model insulation should be adequate to prevent overstressing net seams or compressing the MLI.

4.6 LH_2 TEST MODEL FABRICATION

The LH_2 test model assembly consisted of two (2) vacuum jacket heads, twenty-eight (28) MLI panels, sixteen (16) support straps with turnbuckles and one (1) pressure vessel. All components except for the pressure vessel were manufactured at the Boeing Company facilities in Seattle, Washington. The pressure vessel was manufactured by Cosmodyne Corporation, Torrance, California.

4.6.1 Vacuum Jacket Heads

The details of the vacuum jacket head assembly are discussed in Section 4.2, and are shown in Figure 4.2-2. The vacuum jacket head drawings are shown in Figures D-9 through D-12 in Appendix D. The girth ring details and adhesive bond attachment to the sandwich shell are shown in Detail C4 of Figure 4.2- . The basic sandwich shell construction is described in the Figure 4.6-1 photograph.

Girth Ring

The 6061 aluminum girth ring was made in three segments. Each segment was made by (1) brake forming the cross section from a blank sheet, (2) solution heat treating, (3) stretch forming to the required radius and then, (4) artificially aging to T6.

The three segments were fusion welded together into a ring with the welds remaining in the as-welded condition. The welds were helium leaked checked with a vacuum cup arrangement.

Prior to head assembly, the ring was chemical cleaned and the surface faying with the inner face skin was coated with XA 3919 adhesive which was air dryed and protected with plastic until installation on the mandrel. The surface faying with the outer face skin was sanded with 400 grit paper, solvent cleaned, then primed with metlbond 329 Type 2, prior to assembling the outer face skin gores.

Face Skin Gores

The face skin gores were made from 0.305 mm (0.012 in.) thick 2024 aluminum alclad. The gore fabrication process called for (1) solution heat treating the sheet stock blanks, (2) stretch forming to contour as shown in Figure 4.6-2a,

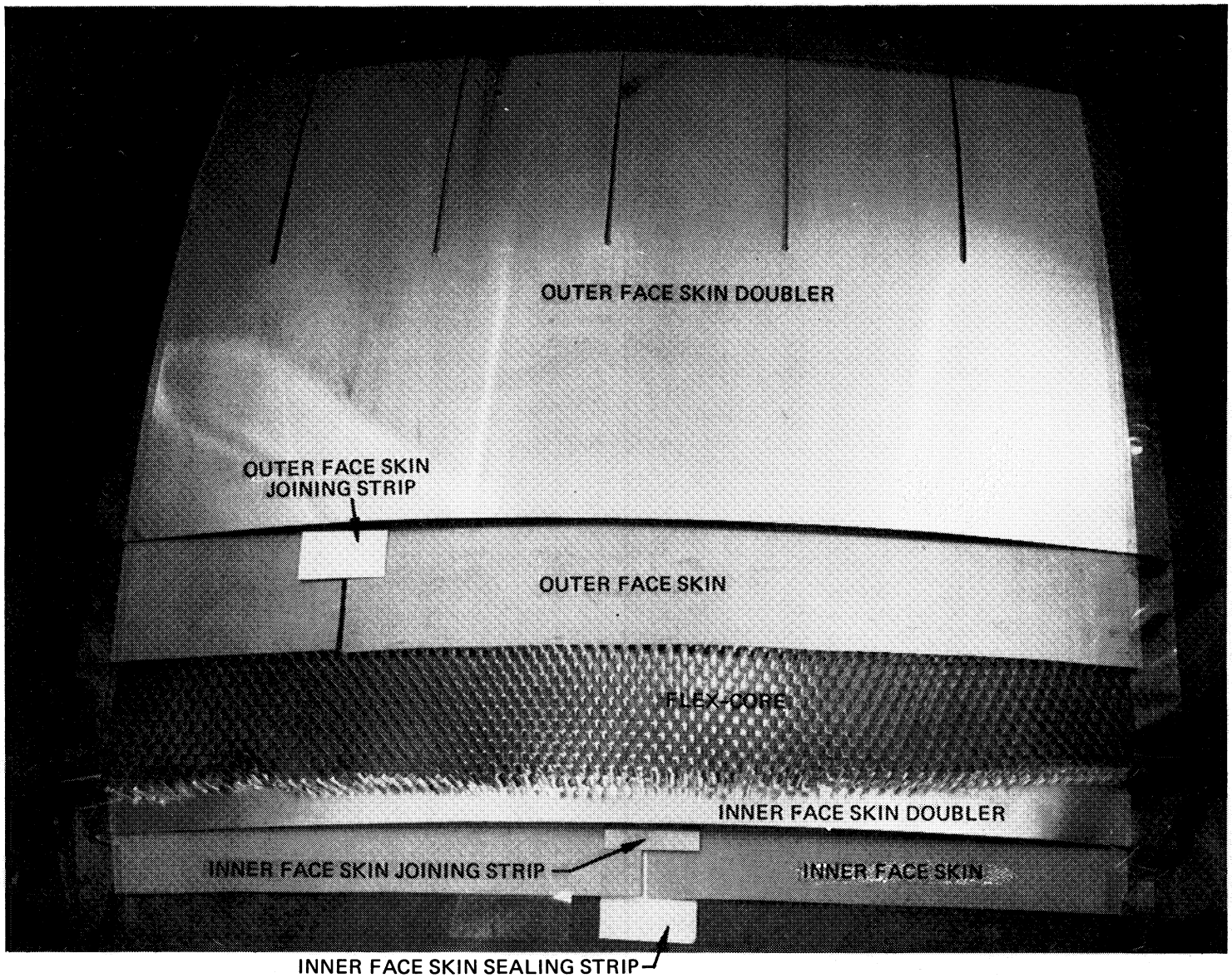

Figure 4.6-1. Vacuum Jacket Head Sandwich Construction Arrangement LH_2 Test Model

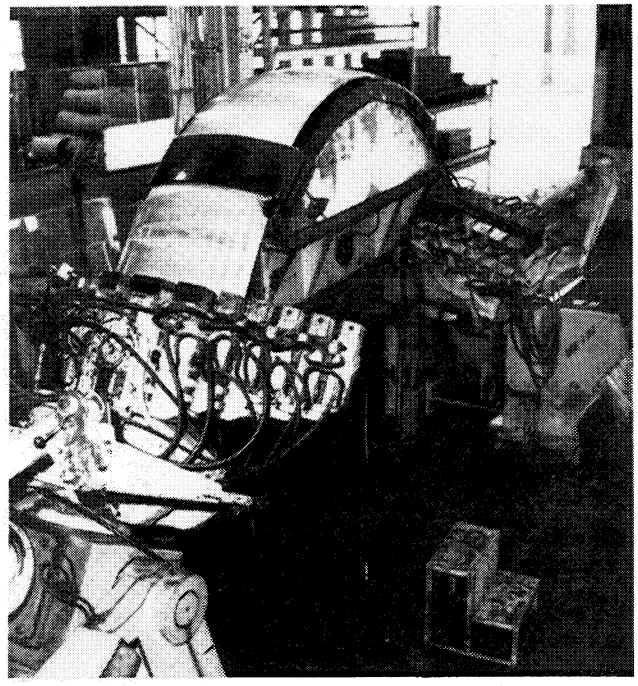

a: STRETCH FORMING GORE

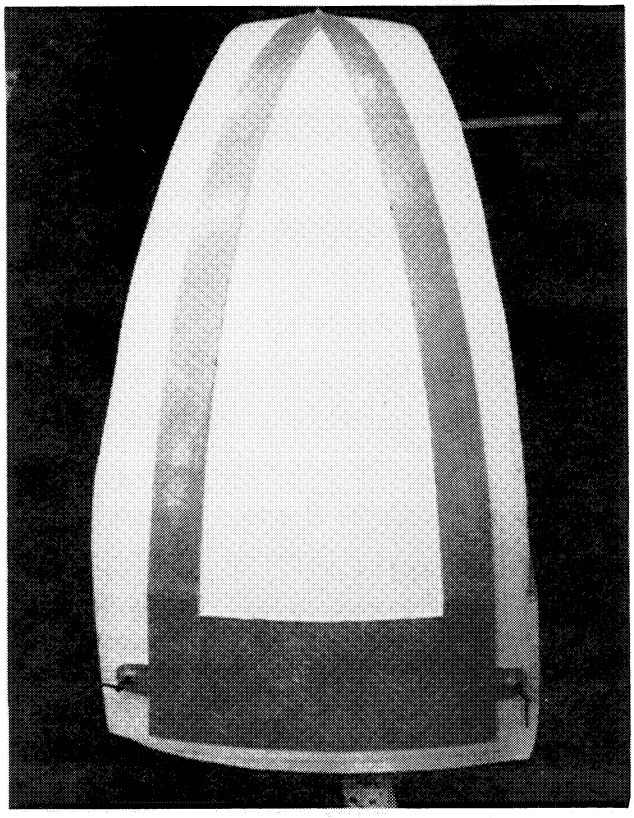

b: GORE TRIM TEMPLATE

Figure 4.6-2. Face Skin Gore Fabrication—Vacuum Jacket Head, LH_2 Test Model

(3) artificially aging to T81 then (4) trimming the gore to size on the trim template shown in Figure 4.6-2b. The finished gores were then stored on a handling fixture until assembly.

Prior to head assembly, the gores were chemical cleaned. After cleaning, the inner surface edges of the inner face skin gores faying with the sealing strips, the apex fitting and the girth ring were coated with XA 3919 adhesive and air dried. Later on in the head assembly process, prior to installing the 0.305 mm (0.012 in.) gore joining strips and priming for the core adhesive, the outer surface of the inner face skin was sanded with 400 grit paper and solvent cleaned. The outer face skin gores were primed with metlbond 329 type 2 immediately following the chem-cleaning.

Flex Core

After cutting the Flex-Core to fit, it was vapor degreased, dried and assembled to the inner face skin assembly.

Head Assembly

The same male fiberglass/epoxy mandrel was used throughout the assembly and autoclave curing of both vacuum jacket heads. Two layers of AF 3306 (3M Co.) Dacron positioning cloth were laid up on the mandrel prior to installing vacuum jacket head details. This cloth was used to provide an annulus between the inner face skin and the mandrel which could be evacuated for helium leak checking the inner face skin assembly. The machined apex fitting and the welded girth ring were accurately located on the mandrel. Then the inner face skin gores and the 0.076 mm (0.003 in.) vacuum sealing strips which had been pre-coated with XA 3919 adhesive were positioned on the mandrel. This assembly was covered with an FEP Teflon layer, a glass cloth layer and the vacuum bag. The assembly was cured in the autoclave at vacuum pressure.

It was difficult in the autoclave, to maintain identical temperatures in the mandrel and the assembled parts being cured. The rate of temperature rise in the autoclave was controlled to (2°F/min.) but a differential thermal growth was still experienced between the mandrel and the inner face skin assembly. This occurred on both heads and resulted in some of the 0.076 mm (0.003 in.)

vacuum sealing strips cracking during this cure cycle. The repair was to fill the gap between gores with XA 3919 adhesive then to bond the 0.305 mm (0.012 in.) aluminum structural joining strips in place.

After completing this curing operation, the inner face skin assembly was vacuum leak checked as shown in Figure 4.6-3a photograph. The girth ring was sealed off at the mandrel with Zeroperm and a vacuum sealing compound. A vacuum sealed plate with a hose connection to the leak detector vacuum pump was installed on the apex fitting. The annulus between the inner face skin assembly and the mandrel was pumped down and the gore joints sprayed with helium. Vacuum leaks were repaired by applying additional coats of XA 3919 adhesive, and curing in the autoclave as shown in Figure 4.6-3b.

It should be noted that the vacuum level obtained during this leak check was on the order of (1 x 10 torr). It was not possible to obtain a better vacuum due to the large epoxy surface area of the mandrel, as well as the geometry of the vacuum system. The resulting leak detecting sensitivity was less than desired but was judged adequate at this stage of manufacture.

As a final check on vacuum leak tightness, the complete inner face skin assembly with doublers was bagged as shown in Figure 4.6-4a. The bag was filled with helium. There was no indication of helium leakage.

The Flex-Core was assembled to the inner face skin with Metlbond 329 adhesive. A structural foaming adhesive BAC 5-90, Type 2, Class 350, Grade 50 was used to splice the Flex-Core seams. The caul plates shown in Figure 4.6-4b were used to prevent damage to the outer Flex-Core edges during the cure cycle of the inner face skin to core bond. Figure 4.6-5a is a photograph of the assembled Flex-Core after curing. The potting to reinforce the core at the girth ring joint can be seen in the figure.

The outer face skin gores were bonded to the core and the girth ring with metlbond 329 adhesive. The joining strips and the doubler were bonded to the outer face skin gores with XA 3919 adhesive. After completion of all the autoclave bond curing operations, the head was removed from the mandrel.

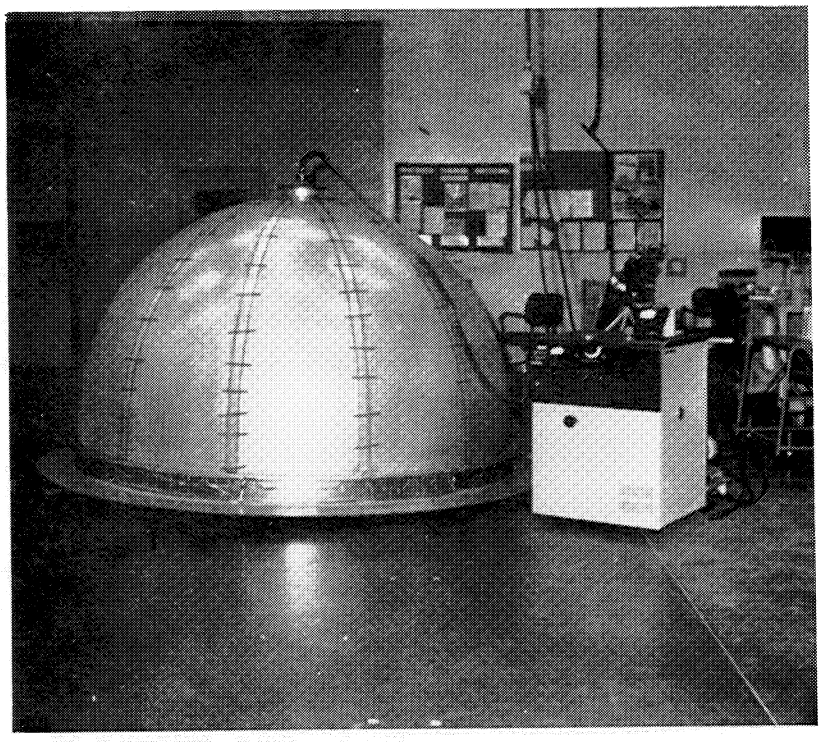

a: VACUUM LEAK CHECKING INNER FACE SKIN ASSEMBLY JOINTS

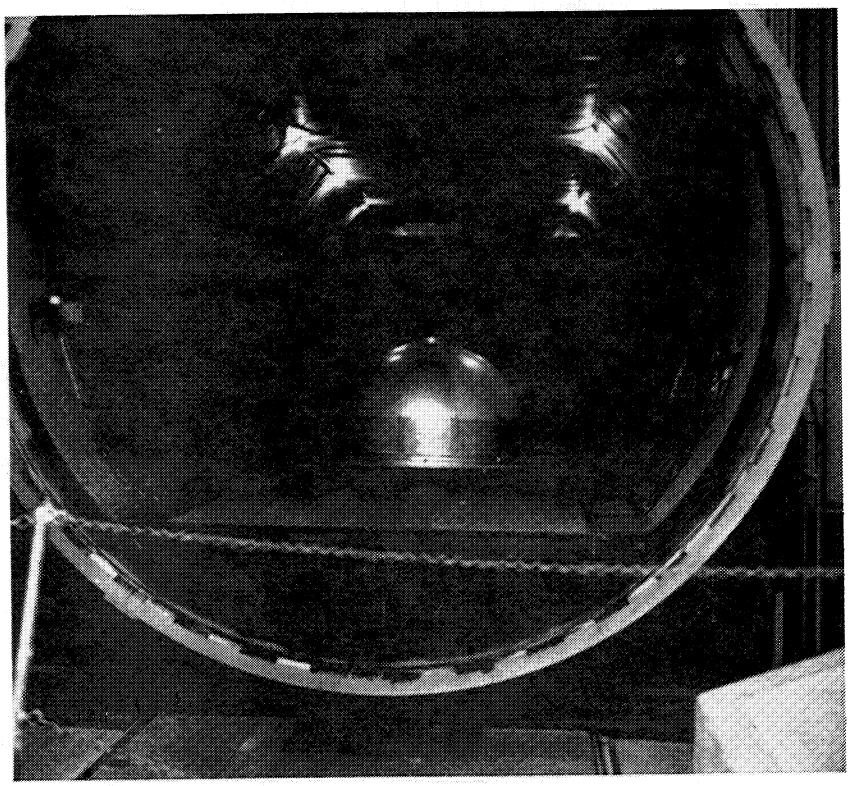

b: AUTOCLAVE CURING INNER FACE SKIN REPAIR BONDS

Figure 4.6-3. Vacuum Jacket Head Assembly—LH_2 Test Model

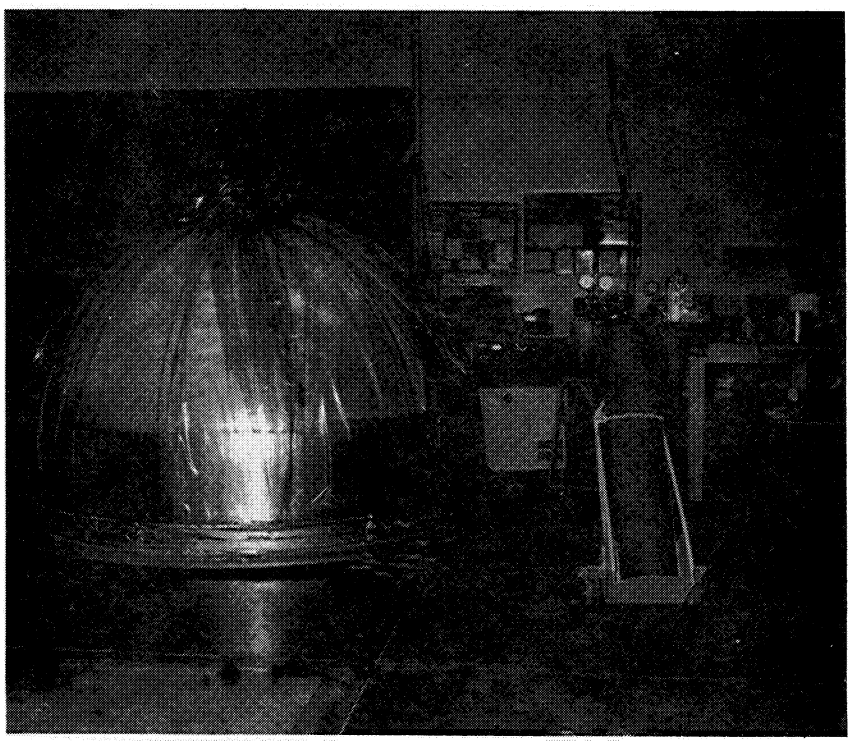

a: HELIUM LEAK CHECK OF COMPLETE INNER FACE SKIN ASSEMBLY

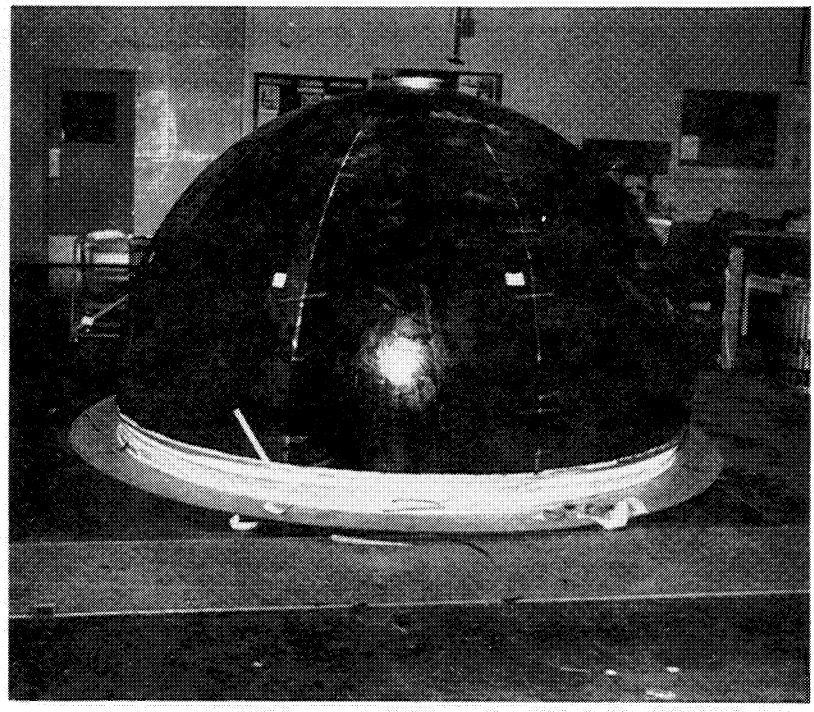

b: CAUL PLATES PROTECTING FLEX-CORE EDGES

Figure 4.6-4. Vacuum Jacket Head Assembly—LH_2 Test Model

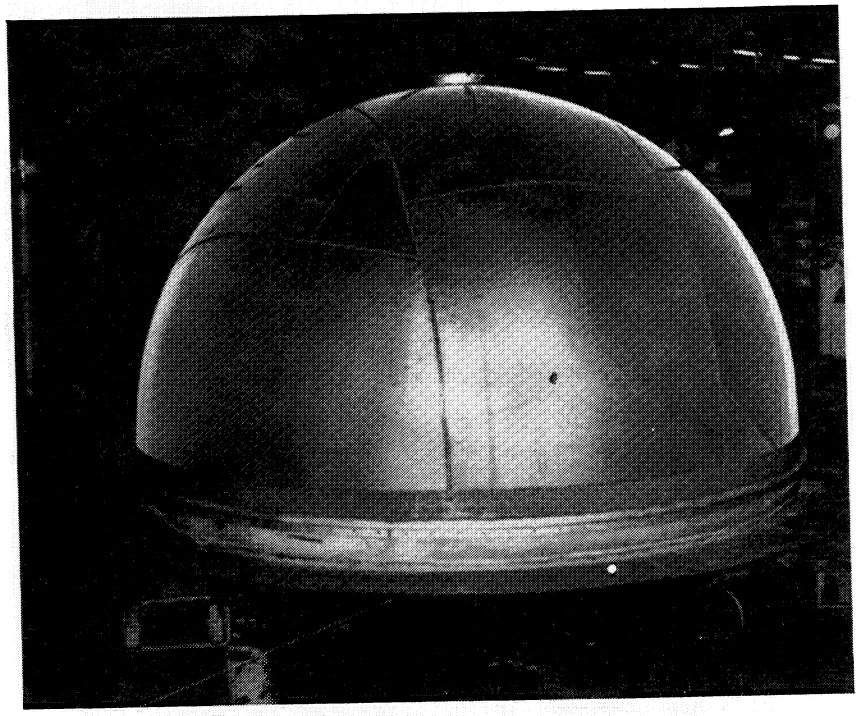

a: FLEX-CORE ASSEMBLED TO INNER FARE SKIN

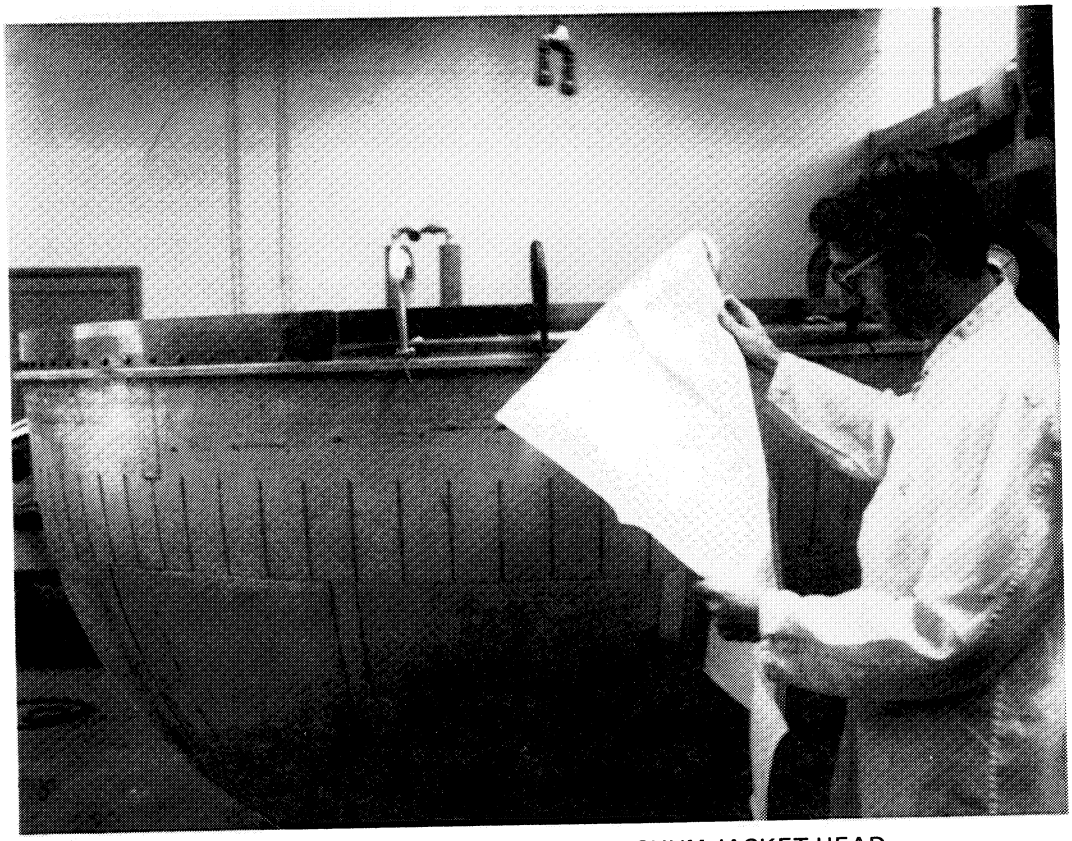

b: ASSEMBLING JOINING STRIPS TO VACUUM JACKET HEAD

Figure 4.6-5. Vacuum Jacket Head Assembly LH_2 Test Model

The -12 and -13 plates shown in Detail C4 of Figure 4.2-2 were bonded to the girth ring with EA 934 adhesive. The plates were clamped in place during the 24 hour room temperature cure cycle. The joining plates connecting the two vacuum jacket heads are bolted to the -12 and -13 plates. Figure 4.6-5b shows the bolt pattern being located.

Deviations

During the vacuum jacket head assembly, it was necessary to deviate from the original planning procedures. Work around procedures were developed as difficulties arose.

Vacuum Sealing Strip Cracking

This problem and its work around solution was previously discussed.

Inner Skin Wrinkles

Inner skin wrinkling occurred on both heads, primarily as a result of the vacuum seal strips cracking. Sharp wrinkles were faired over with EA 934 adhesive. After the Flex-Core was bonded to the inner face skin, the core areas over the wrinkles were potted with BMS 5-90. After curing this material the core was shaved to contour. When the head was removed from the mandrel, the inner skin wrinkles were filled with EA 934 adhesive and a covering strip bonded over the area.

Preconditioning

The vacuum jacket head assembly inner surfaces which were to be exposed to the vacuum annulus were preconditioned by baking for 16 hours at 324.8°K (125°F). As a further precaution, to minimize out gassing, the inner face skin surfaces were cleaned as follows prior to final assembly to the LH_2 test model: (1) surface wiped 3 times with trichlorethylene and (2) surface wiped 3 times with alcohol.

Recommendations

The fabrication and test experience with two light weight vacuum jacket heads suggests some improvements in the design and fabrication process.

1) The inner vacuum sealing strip should be deleted, and vacuum sealing of the inner skin accomplished by the structural joining strip.

2) Further investigation should be conducted with the various adhesives involved to develop a process whereby all the bond surfaces can be primed immediately following the chemical clean operation. Also, the phosphoric acid anodize metal surface preparation method now being implemented in the Boeing production bond shops should be used since it has been shown to produce bonds of higher strength and increased durability.

4.6.2 MLI Panels

The detail drawing of the MLI panel assemblies is shown in Figure D-14, Appendix D. The nylon stud and washer used in assembling the panel are shown in Figure D-26.

Two MLI panel fiberglass/epoxy layup tools were made. One layup tool was used to fabricate the fourteen (14) inner MLI panel assemblies. The other tool was used for the outer fourteen (14) MLI panel assemblies.

Figures 4.6-6a and 6b are photographs showing the layup of the Dacron set (B4A) and the aluminized Mylar. The folds that occur in the aluminized Mylar when it is draped over the layup tool are taped as shown in Figure 4.6-7a. These folds were staggered in successive Mylar layers to avoid excessive local thickness buildup. After completing the layup of the net and the Mylar layers (and in the case of the outer MLI panels, the Kapton layers) the nylon assembly buttons were installed and locked in place by heat forming as seen in Figure 4.6-7b. The Velcro hook and pile patches for installation attachment were then bonded to the panel. The final operation was to trim the panel as the Figure 4.6-7c photograph shows.

The MLI panel assemblies were preconditioned by heating to approximately 367°K (200°F) in a vacuum chamber before being installed on the pressure vessel. The purpose of this preconditioning was to remove surface contamination from the radiation shields while there was minimum restriction to pumping along the panel edges, and thereby reduce preconditioning time of the vacuum annulus after final assembly. The method of preconditioning was to pump the chamber continuously at temperature while monitoring the vacuum pressure. When the

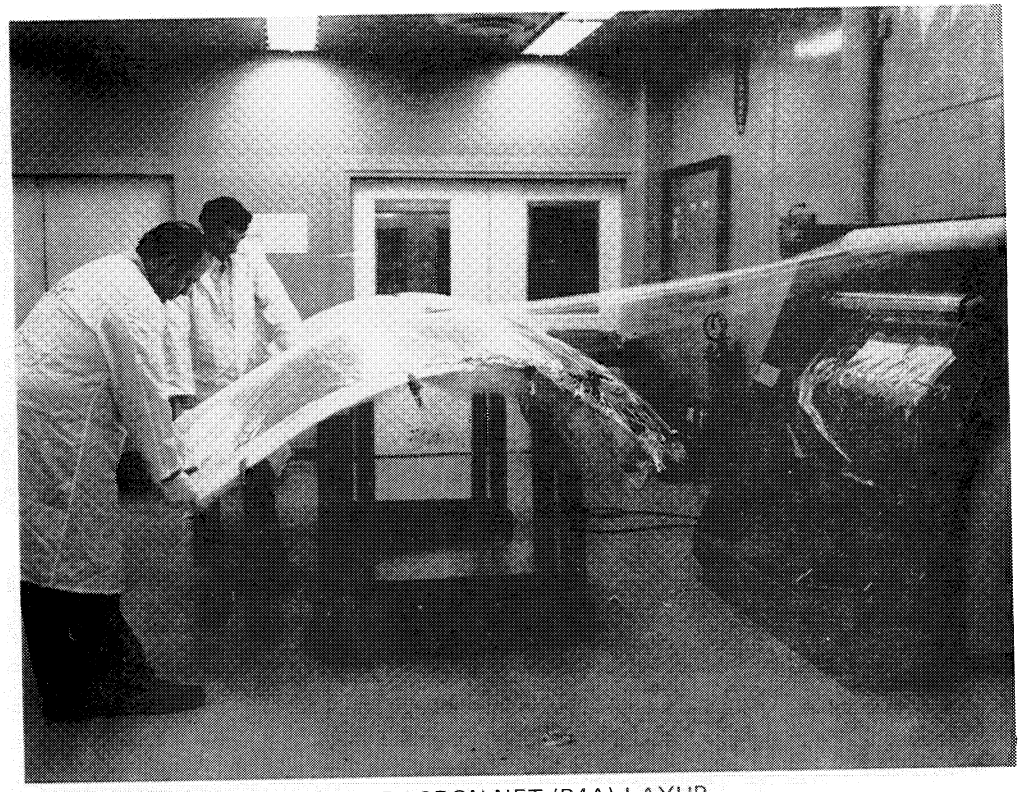

A: DACRON NET (B4A) LAYUP

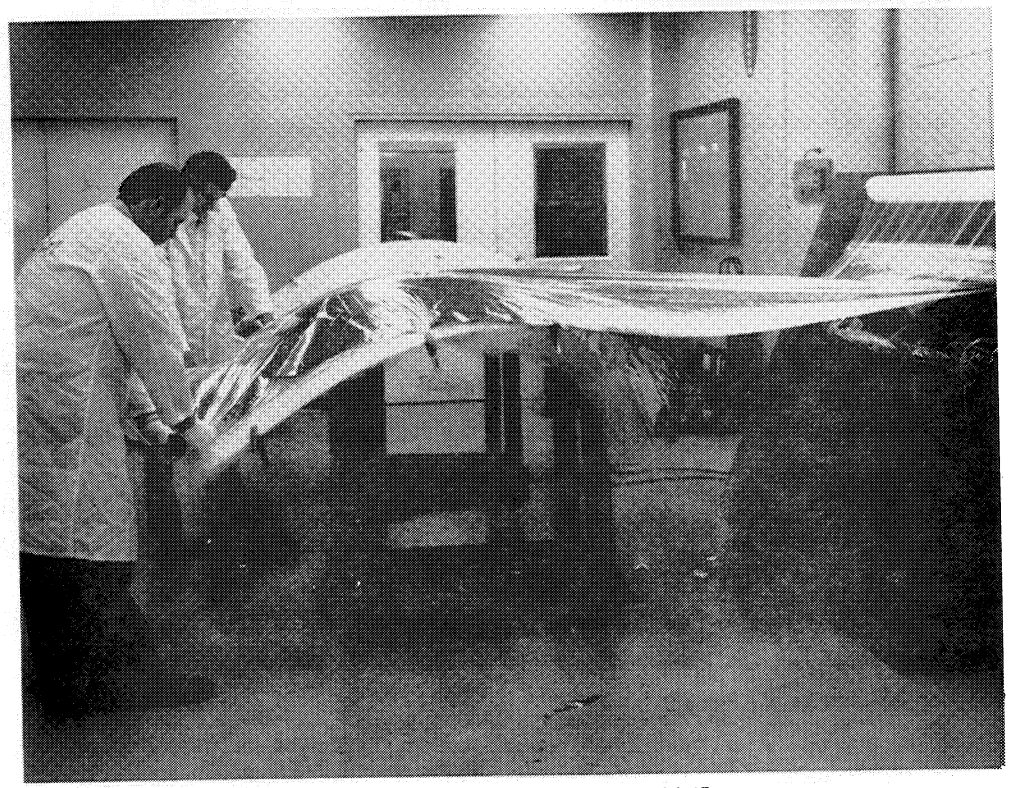

B: ALUMINIZED MYLAR LAYUP

Figure 4.6-6. MLI Panel Assembly

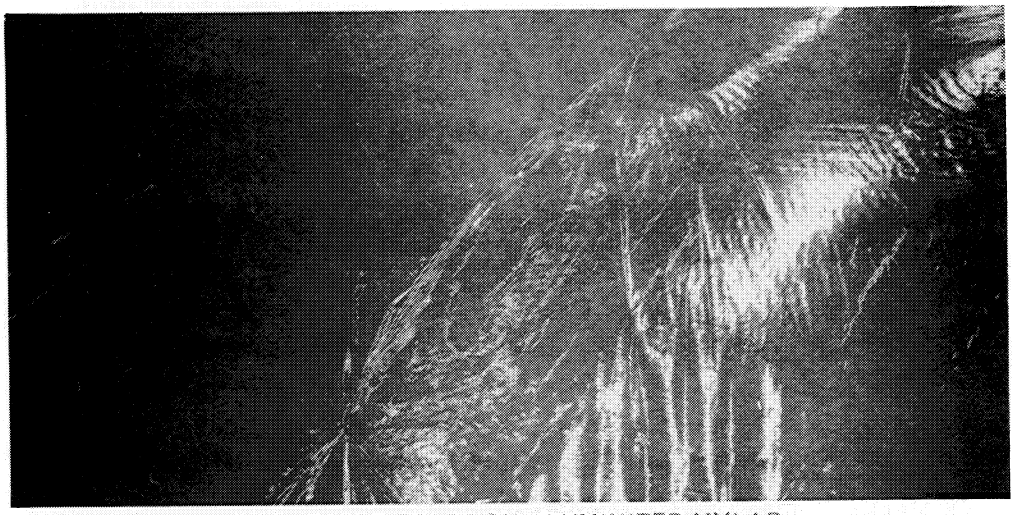

A: TAPED FOLDS ON ALUMINIZED MYLAR

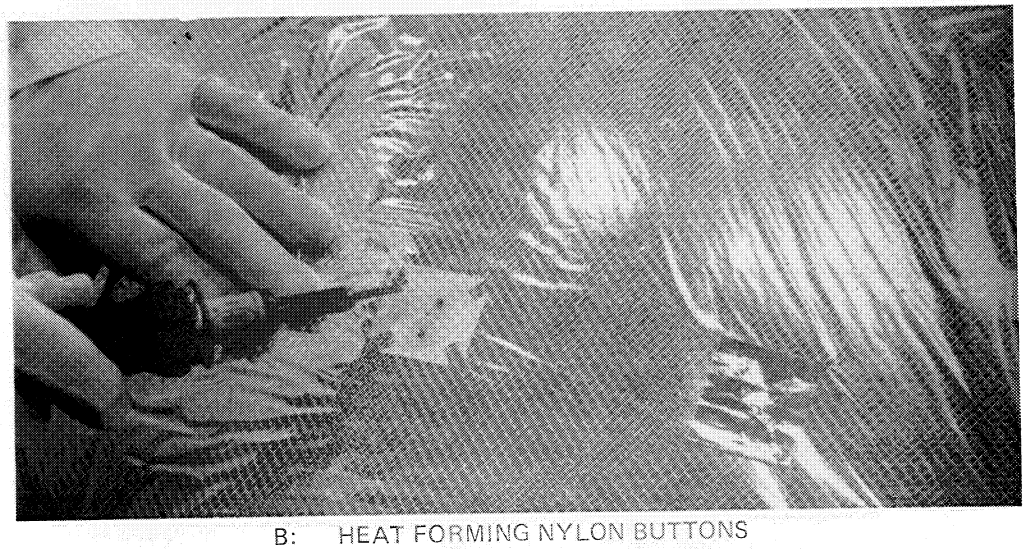

B: HEAT FORMING NYLON BUTTONS

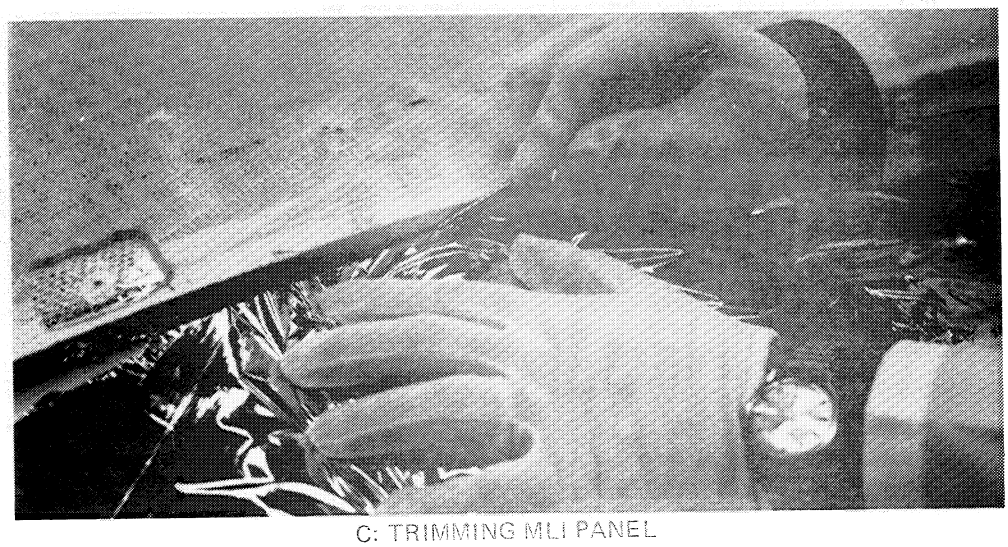

C: TRIMMING MLI PANEL

Figure 4.6.7. MLI Panel Assembly

chamber pressure stabilized (approximately 100 hours), indicating that the major contamination had been removed, the heating source was removed and the chamber allowed to slowly return to ambient pressure. Figure 4.6-8a is a photograph of the panels being placed in the support rack. Five or six panel assemblies were preconditioned at one time. Figure 4.6-8b shows the rack being installed in the heating box. The installation of the heating box into the vacuum chamber is shown in Figure 4.6-9a. After preconditioning the MLI panels were placed on a holding fixture and wrapped with a plastic bag (Figure 4.6-9b) which was filled with dry nitrogen gas.

4.6.3 Support Straps

The support strap assembly drawing is shown in Figure D-30, Appendix D.

The Kevlar-3 (PRD-3) single end yarns were laid up in a ten-ply thickness and a 50.8 mm (2.0 in.) width with ERLA 4617 (Union Carbide Corp.) resin system to form a composite strap. The strap was cured with vacuum bag pressure, two hours at 339°K (150°F), two hours at 422°K (300°F) and one hour at 450°K (350°F). The titanium end fittings were chemically milled to dimensions. Support strap details are shown in Figure 4.6-10a. Prior to bonding the titanium faying surfaces were cleaned with an aluminum blast followed by a silicone rinse (Union Carbide A1100) EA 934 was used to bond the end fittings to the strap. The assembly fixtures shown in Figure 4.6-10b were used to accurately locate end fittings. The strap assembly was cured with vacuum bag pressure one hour at 367°K (200°F).

After assembly the sixteen support straps were baked for 16 hours at 324°K (125°F) to minimize the outgassing of the EA 934 adhesive. Immediately prior to installation on the pressure vessel, the straps were preconditioned by heating to 367°K (200°F) in a vacuum.

4.6.4 Pressure Vessel

The pressure vessel was fabricated by Cosmodyne Corporation, Torrance, California. The assembly drawing is shown in Figure D-8, Appendix D. Figures 4.6-11a and 11b are photographs of the head assembly and the head and cylindrical section assembly. The completed assembly (as shipped by Cosmodyne) with pressure vessel support straps attached is shown mounted in the support stand at Boeing in

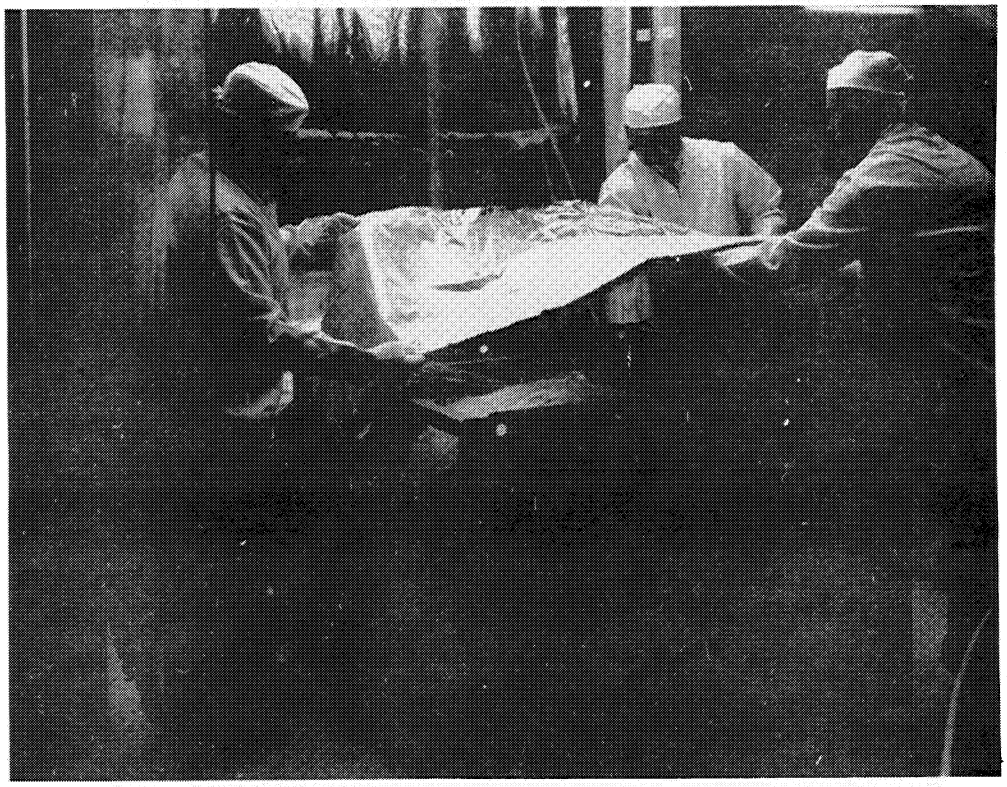

A: PLACING PANELS ON SUPPORT RACK

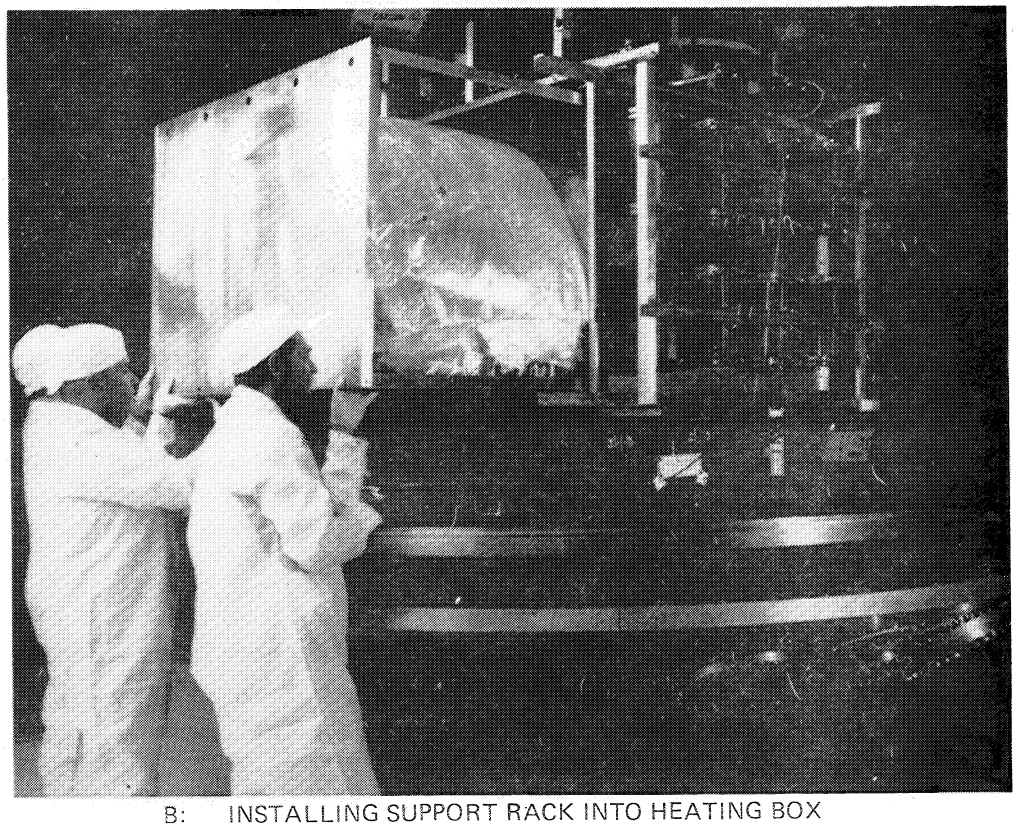

B: INSTALLING SUPPORT RACK INTO HEATING BOX

Figure 4.6-8. Preconditioning MLI Panel Assemblies

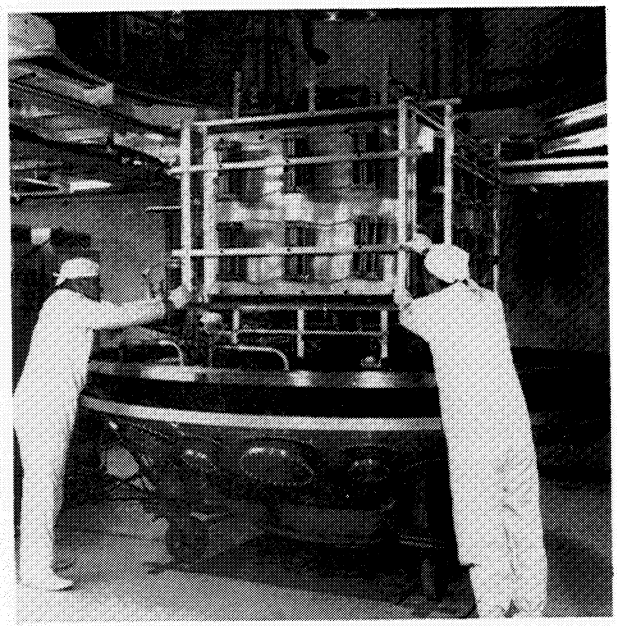

A: INSTALLING HEATING BOX INTO VACUUM CHAMBER

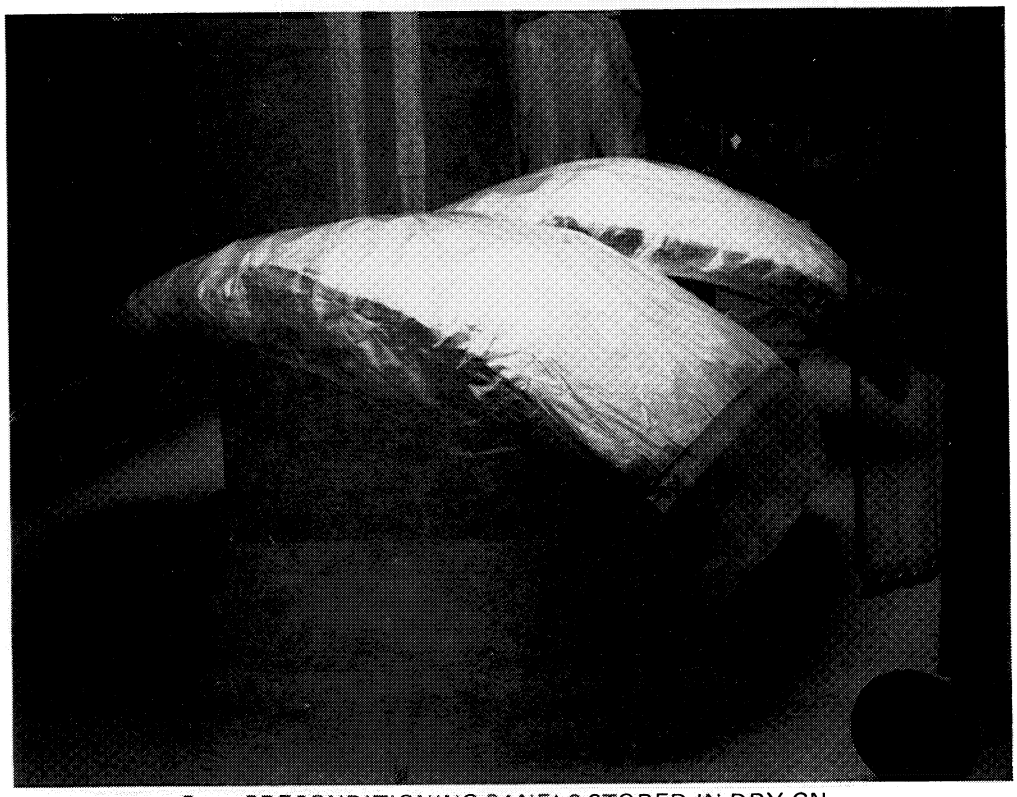

B: PRECONDITIONING PANELS STORED IN DRY GN_2

Figure 4.6-9. Preconditioning MLI Panel Assemblies

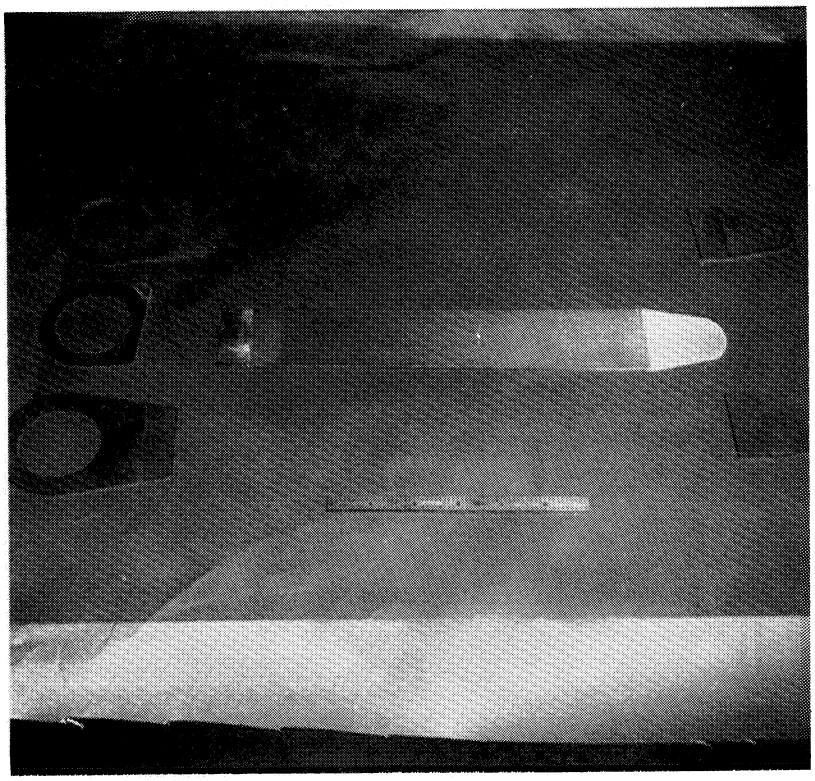

A: SUPPORT STRAP DETAILS

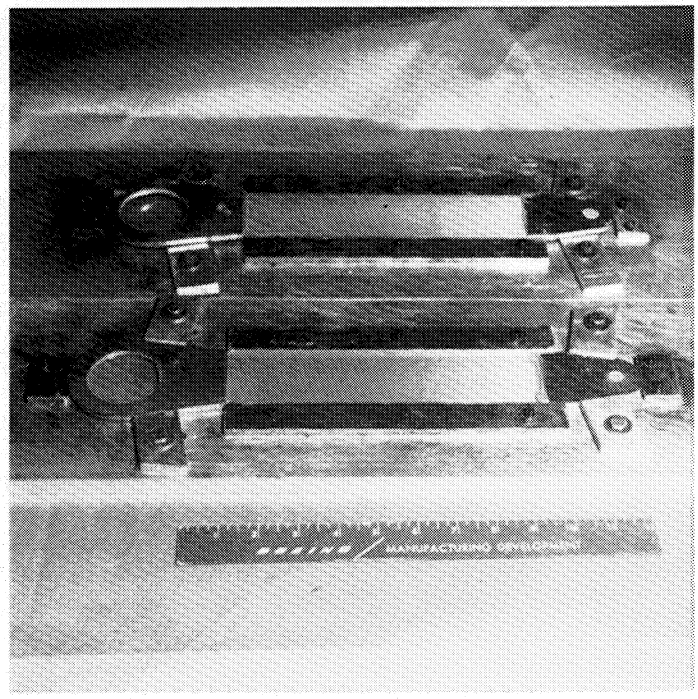

B: SUPPORT STRAP ASSEMBLY FIXTURES

Figure 4.6-10. Support Strap Assembly

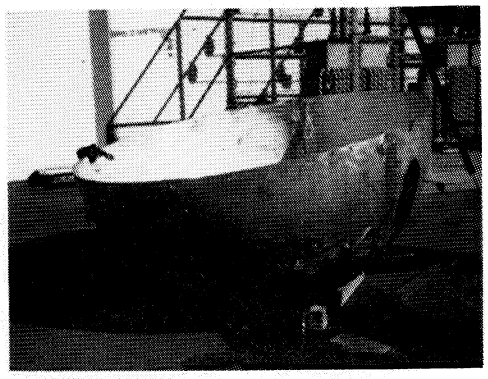

A: HEAD ASSEMBLY

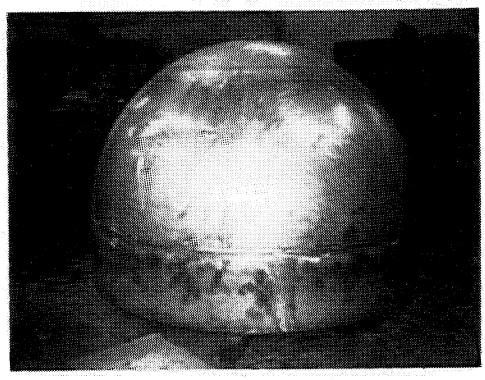

B: HEAD AND CYLINDRICAL SECTION ASSEMBLY

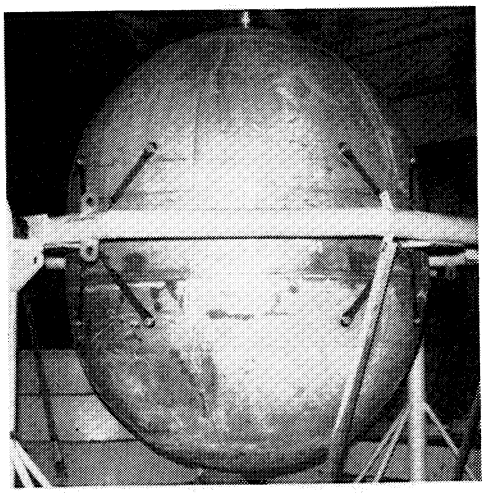

C: COMPLETED ASSEMBLY

Figure 4.6-11. Pressure Vessel Assembly

Figure 4.6-11c. After receipt by Boeing, the inlet tube and the simulated plumbing line boss were welded to the pressure vessel.

4.6.5 Final Assembly

The LH_2 test model trunnions were attached at four points to the hexagonal frame of the support stand shown in Figure 4.6-12a. Assembly drawings for this support stand are located in Appendix D, Figures D-39 and D-40. The support stand was used during fabrication, transportation and testing of the LH_2 test model. The hexagonal frame was free to rotate 6.28 radians (360°) within the support stand and provided optimum accessibility to the LH_2 test model as installation of the various details progressed.

Figure 4.6-12b shows the pressure vessel installed in the support stand, rotated in the horizontal position, with the Velcro pile pads bonded in place. The simulated plumbing line can be seen in the foreground.

Inner MLI panel installation details are described in Figures 4.6-13 through 4.6-16a. During the fit up of each panel, the support strap was removed from the pressure vessel boss as shown in Figure 4.6-13a. This permitted minimum cutting of the panel in the region of the support boss. The 50.80 mm (2.00 in.) (approximately) diameter hole in the panel was a snug fit around the boss (Figure 4.6-13b). As seen in Figure 4.6-13b, the panels were installed on the lower half of the pressure vessel first. This approach eliminated scaffolding and made it easier to install the panels. It was found that the panels could stand a reasonable amount of handling. However, some of the nylon pins at the location of the Velcro pads were broken. This occurred because of the pressure required to attach the Velcro hook to the pile. The broken pins were replaced. Figure 4.6-14a, shows the inner panels complete on the lower hemisphere. Following this, the fixture was rotated and the other half completed. Two support straps were instrumented with thermocouples (Figure 4.6-14b). Instrumentation and inner panel insulation at the inlet tube are described in Figure 4.6-15a. A pressure tape to indicate vacuum pressure level at the interface between the MLI and the pressure vessel was installed in the region of the simulated plumbing line. This 3.175 mm (0.125 in.) diameter x 0.508 mm (0.020 in.) wall stainless steel tube can be seen in Figure 4.6-15b. The completed installation of the inner MLI panels is shown in Figure 4.6-16a. The outer two Dacron net

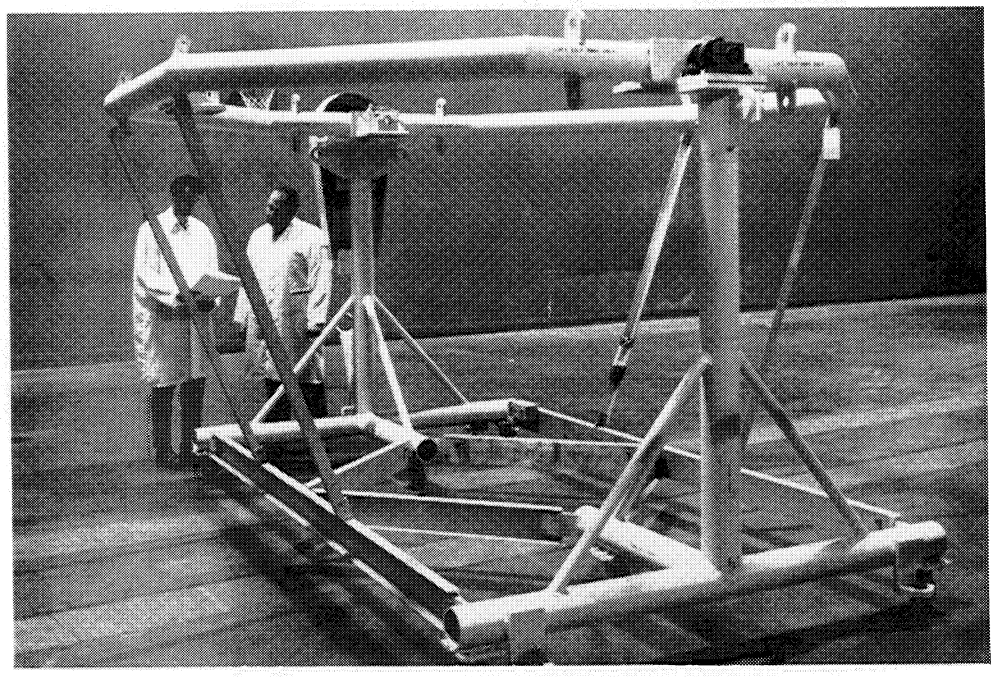

A. SUPPORT STAND

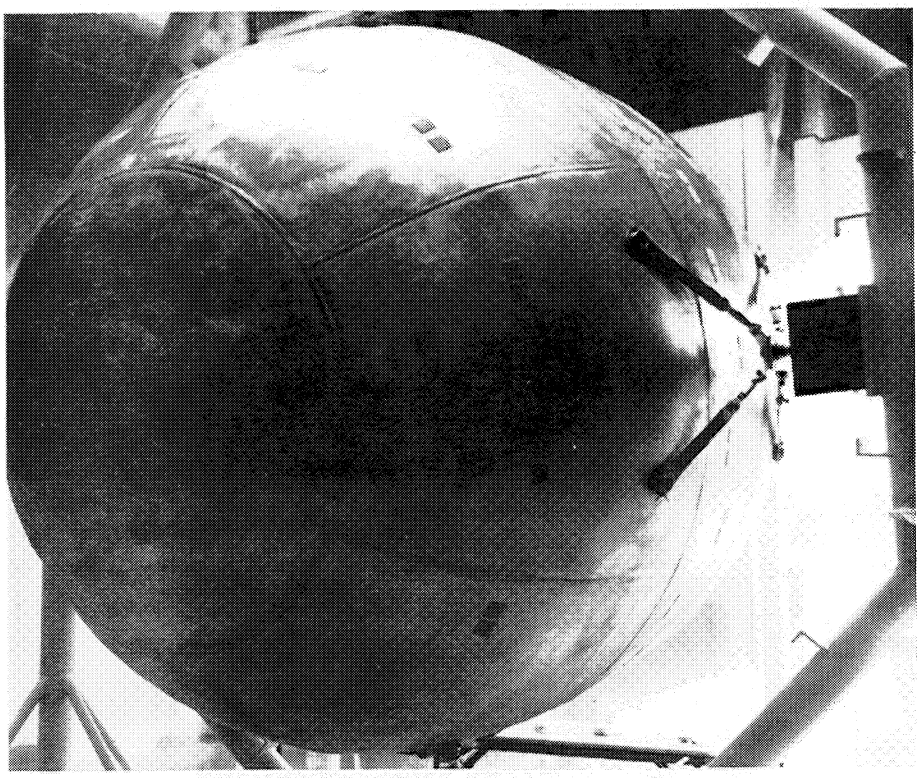

B. PRESSURE VESSEL INSTALLED IN SUPPORT STAND

Figure 4.6-12. Half Scale LH_2 Test Model Assembly

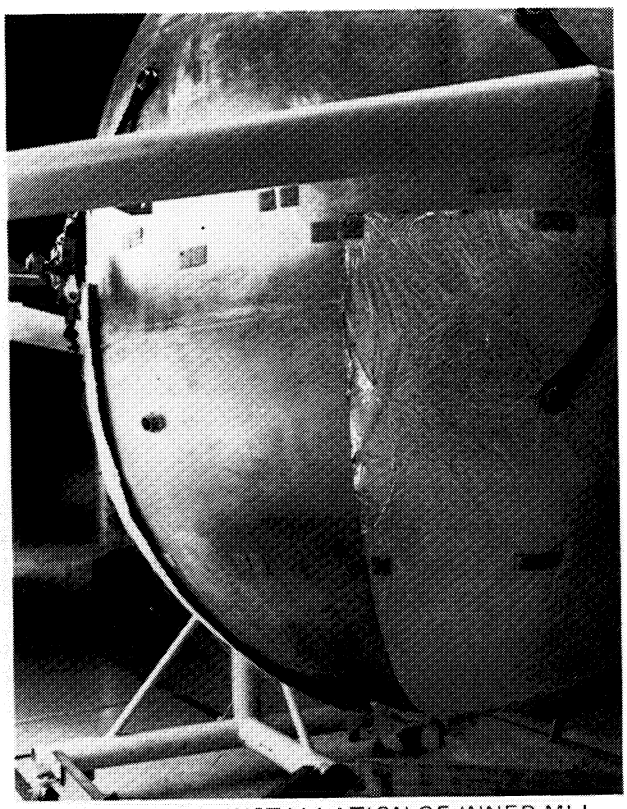

A. PARTIAL INSTALLATION OF INNER MLI

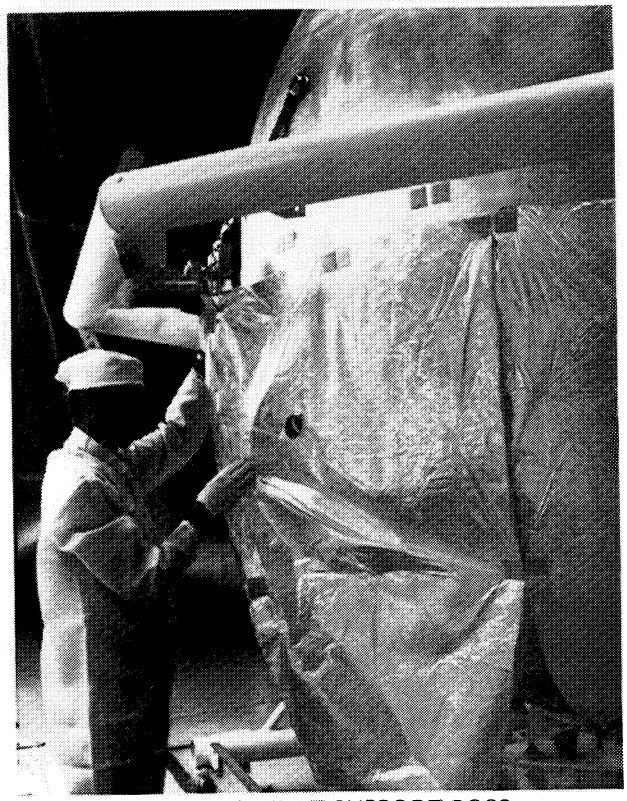

B. CUTOUT AT SUPPORT BOSS

Figure 4.6-13. Half Scale LH_2 Test Model Assembly

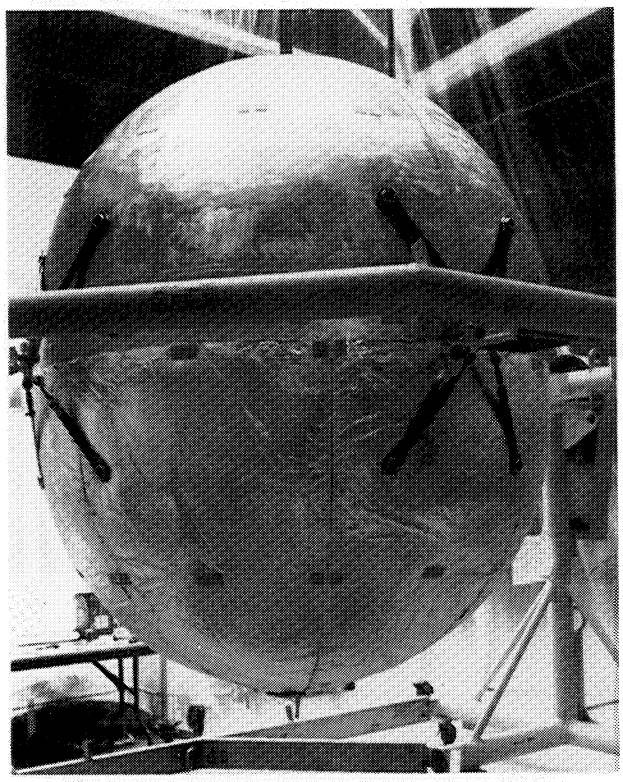

A. INNER MLI PANELS COMPLETE ON LOWER HEMISPHERE

B. SUPPORT STRAP INSTRUMENTATION

Figure 4.6-14. Half Scale LH_2 Test Model Assembly

A. INLET TUBE INSTRUMENTATION

B. ARRANGEMENT AT SIMULATED PLUMBING LINE

Figure 4.6-15. Half Scale LH_2 Test Model Assembly

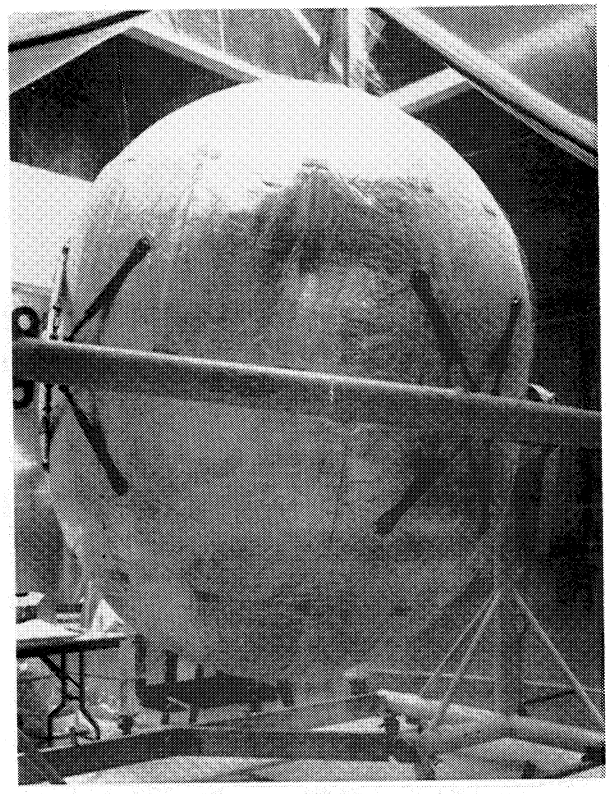

A: COMPLETED INSTALLATION OF INNER MLI PANELS

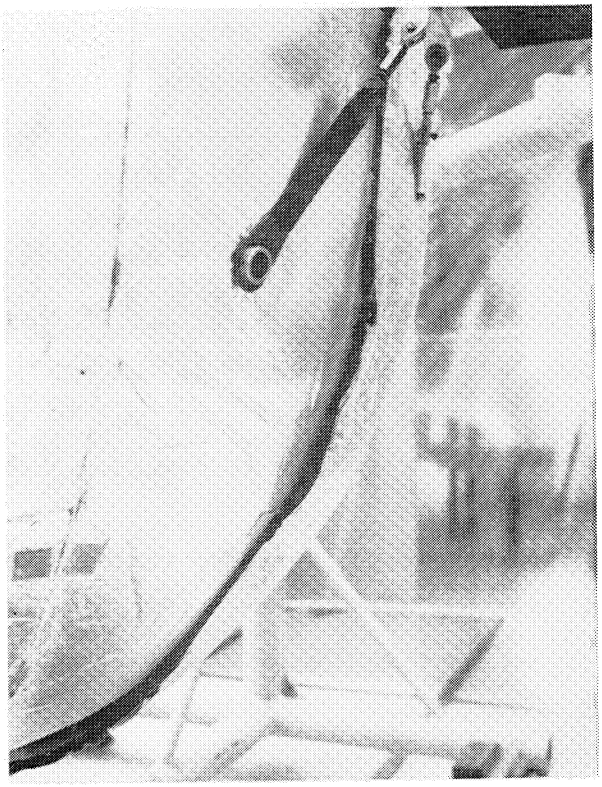

B: ONE OUTER MLI PANEL INSTALLED

Figure 4.6-16. Half Scale LH_2 Test Model Assembly

(B4A) layers of adjacent panels were sewn together at the seams, maintaining an 1.27 mm (0.05 in.) gap approximately between panels for insulation venting. Insulation thickness uniformity was checked after installation by noting the relationship of the nylon pin washers to the outer insulation layers. The uniform 13.97 mm (0.55 in.) height of the pins provided a means for assessing panel thickness. In general, the inner MLI panels showed considerable pillowing around the pins indicating fluffiness. There were only a few locations which indicated some insulation compaction.

Outer MLI panel installation details are described in Figures 4.6-16b through 4.6-19. Figure 4.6-16b shows the first outer MLI panel installed. The panels were slit to receive the support strap as shown in Figure 4.6-17a, then installed (Figure 4.6-17b). Figure 4.6-18a compares the arrangement at the support strap before and after the insulation cover patch has been added. Figure 4.6-18b describes the insulation on the inlet tube. Figure 4.6-19a shows the outer polar cap being installed at the simulated plumbing line. The completed MLI installation is shown in Figure 4.6-19b. The outer two Dacron net (B4A) layers of adjacent outer panels were also sewn together, maintaining the 1.27 mm (0.05 in.) gap approximately between the panels. There was less pillowing of the outer panels around the nylon pins than with the inner panels but again it appeared that outer MLI panels generally maintained the 13.97 mm (0.55 in.) thickness requirement.

The leads from the thermocouples on the surface of the pressure vessel, buried within the insulation, and on the support straps were routed to the outer surface of the insulation (Figure 4.6-20a) then down to the apex close out fitting at the simulated plumbing line as seen in Figure 4.6-20b.

Thermocouples were also bonded to the inner surface (Figure 4.6-21a) of the vacuum jacket heads, and the outer surface (Figure 4.6-21b).

Figure 4.6-22a is a photograph of the upper vacuum jacket installed. The head was bolted in place at the trunnion fittings then the support fixture rotated 3.14 radians (180°) and the lower vacuum jacket head lowered in place. The vacuum annulus can be seen in Figure 4.6-22b.

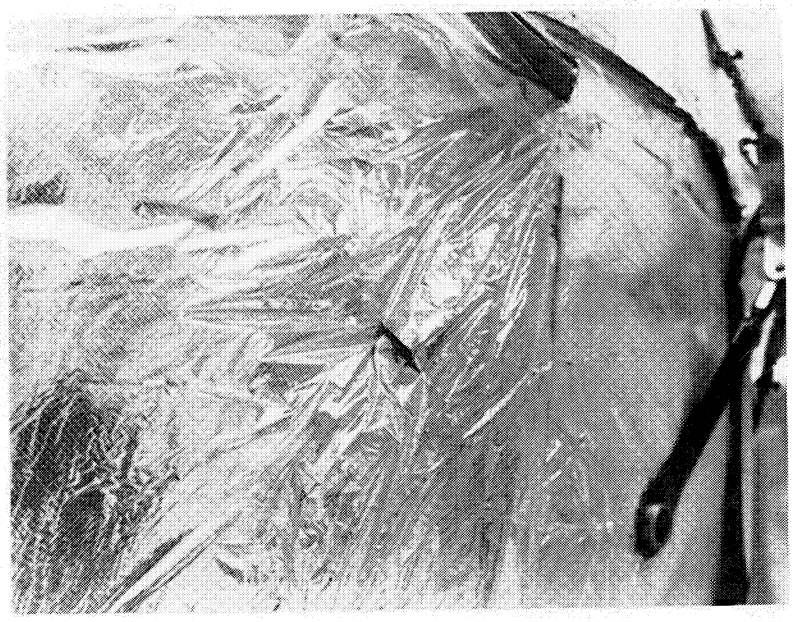

A: SLIT FOR SUPPORT STRAP

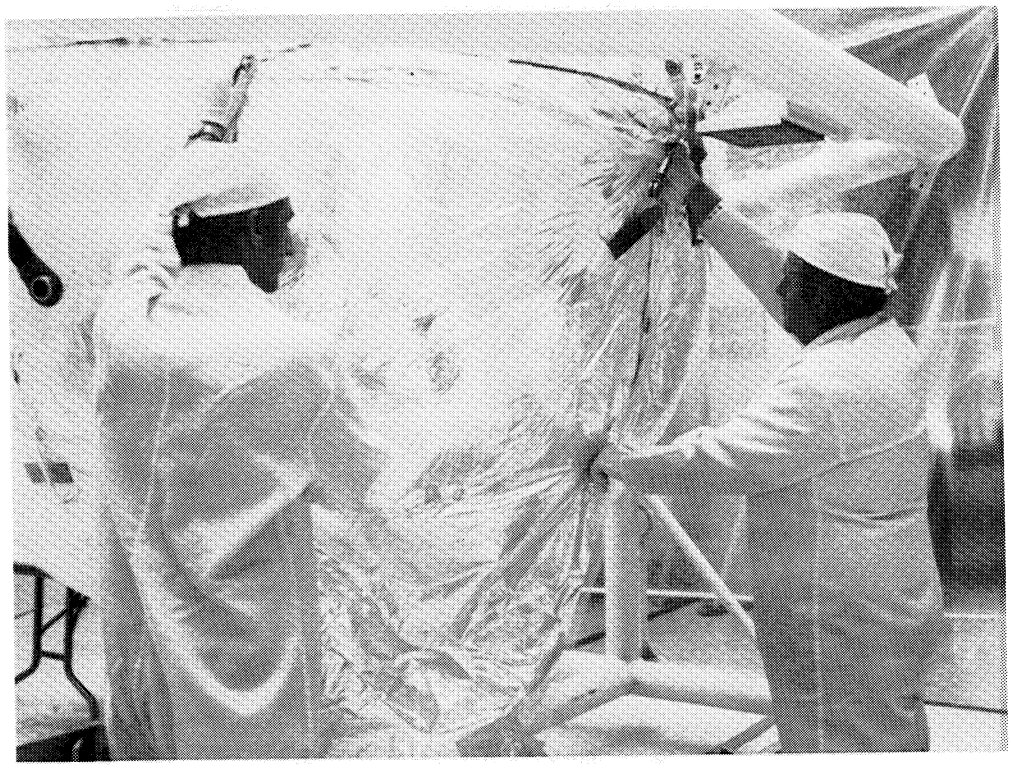

B: INSTALLING OUTER MLI PANEL AT SUPPORT STRAP

Figure 4.6-17. Half Scale LH_2 Test Model Assembly

A: DETAILS AT SUPPORT STRAP

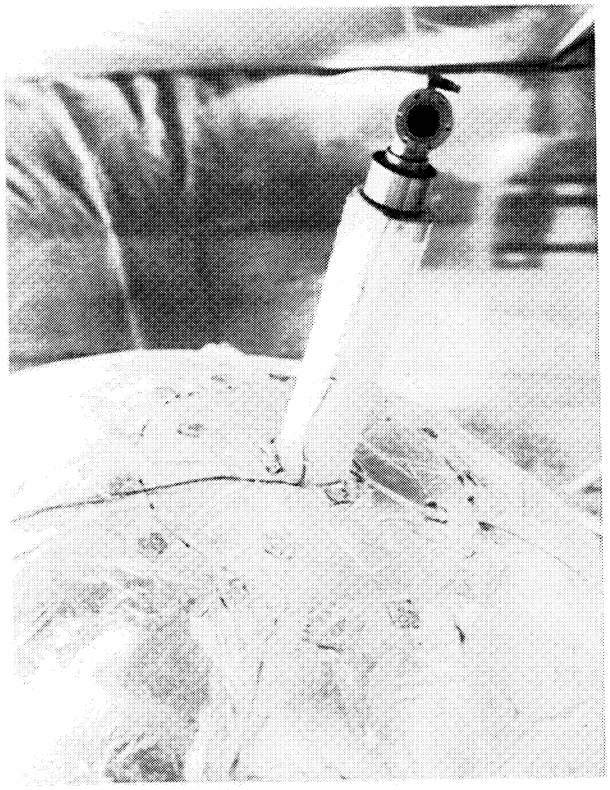

B: INLET TUBE INSULATION

Figure 4.6-18. Half Scale LH_2 Test Model Assembly

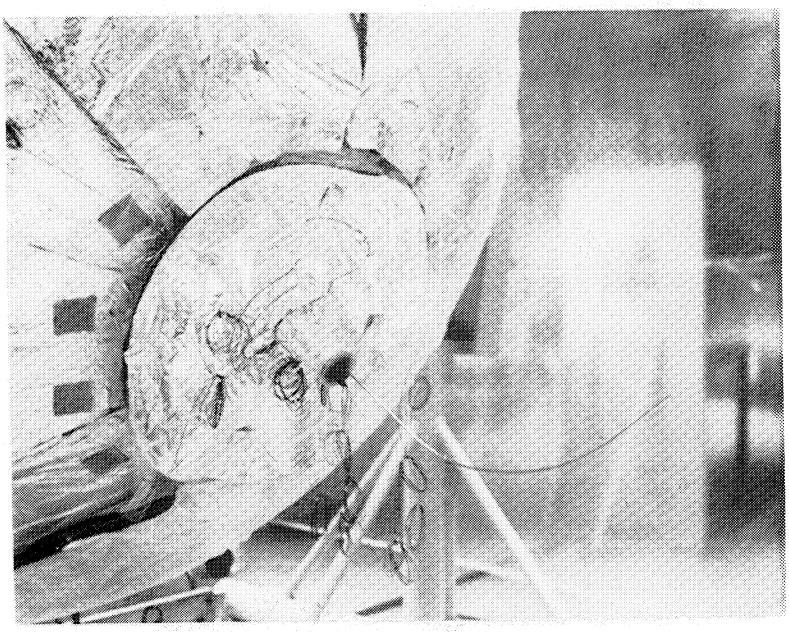

A: SIMULATED PLUMBING LINE INSULATION

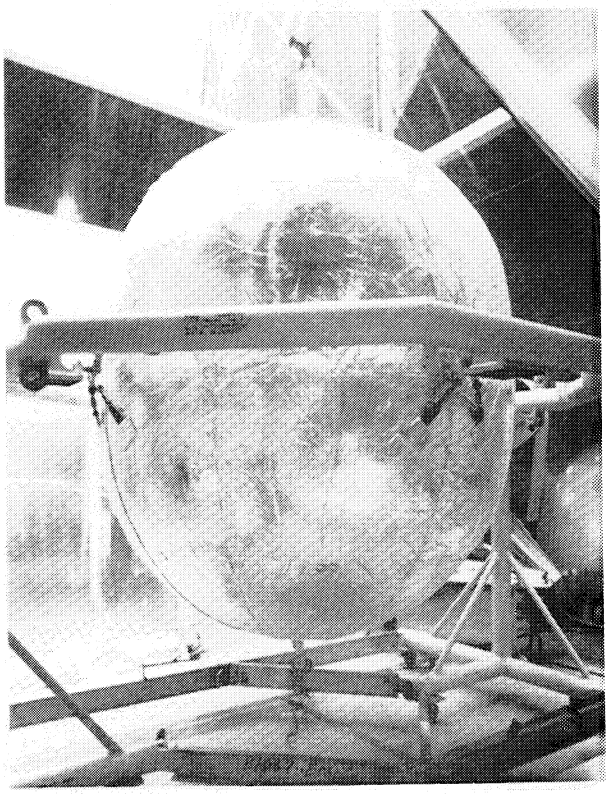

B: COMPLETED INSTALLATION OF MLI

Figure 4.6-19. Half Scale LH_2 Test Model Assembly

A: PENETRATION OF THERMOCOUPLE AT SEAM

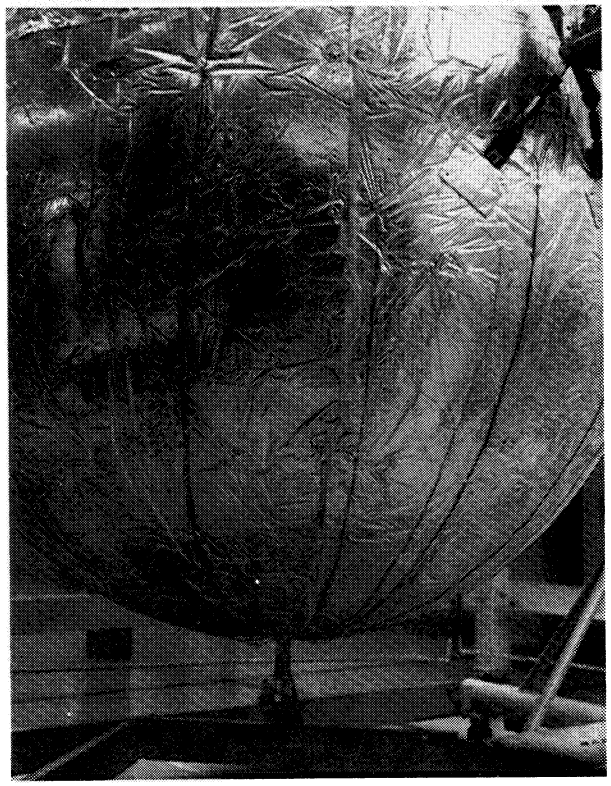

B: ROUTING OF THERMOCOUPLE LINES

Figure 4.6-20. Half Scale LH_2 Test Model Assembly

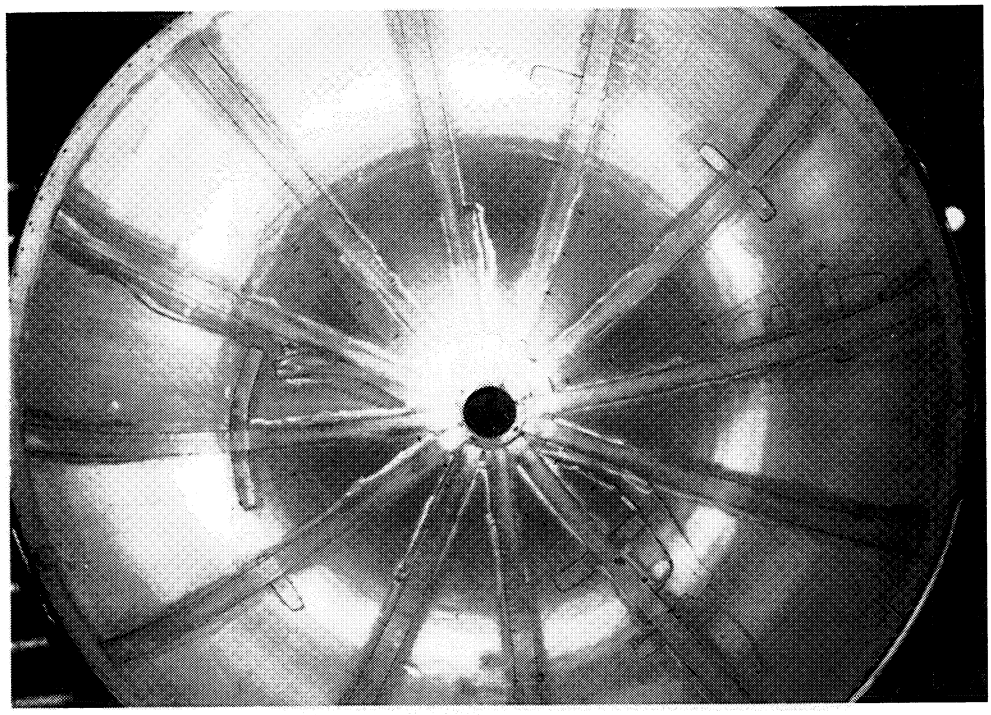

A: THERMOCOUPLES ON INNER SURFACE OF LOWER VACUUM JACKET HEAD

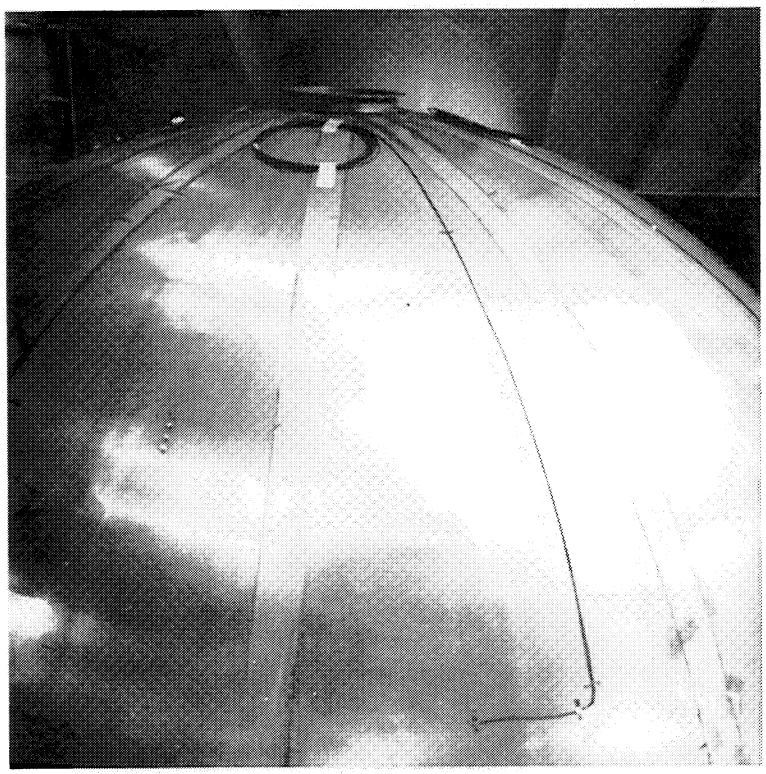

B: THERMOCOUPLES ON OUTER SURFACE OF LOWER VACUUM JACKET HEAD

Figure 4.6-21. Half Scale LH_2 Test Model Assembly

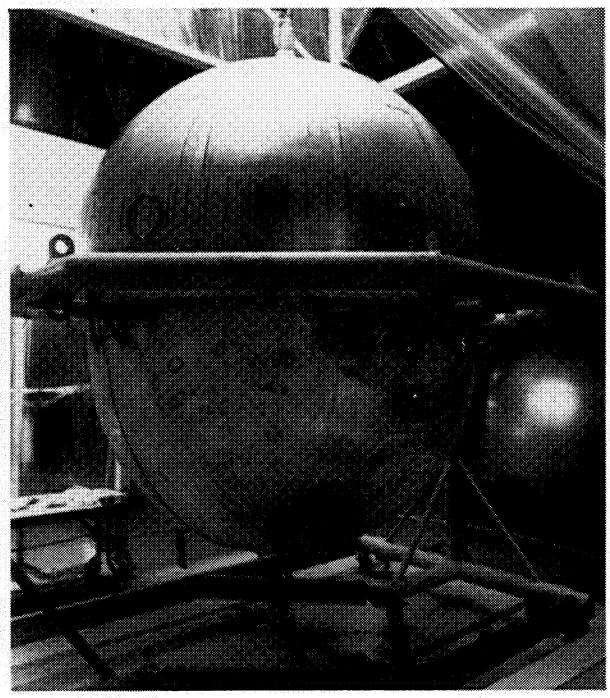

A: UPPER VACUUM JACKET HEAD INSTALLED

B: VACUUM ANNULUS

Figure 4.6-22. Half Scale LH_2 Test Model Assembly

After bolting the joining plates together at the girth (Figure 4.6-23a) the vacuum seal strip was welded in place (Figure 4.6-23b). A water dam was jury rigged in the weld area to protect the adjacent bond areas from over heating. The completed weld is shown in Figure 4.6-23c. The upper and lower vacuum jacket closeout fittings were installed along with the ion pumps and shut-off-valves. (Figures 4.6-24a and 24b.)

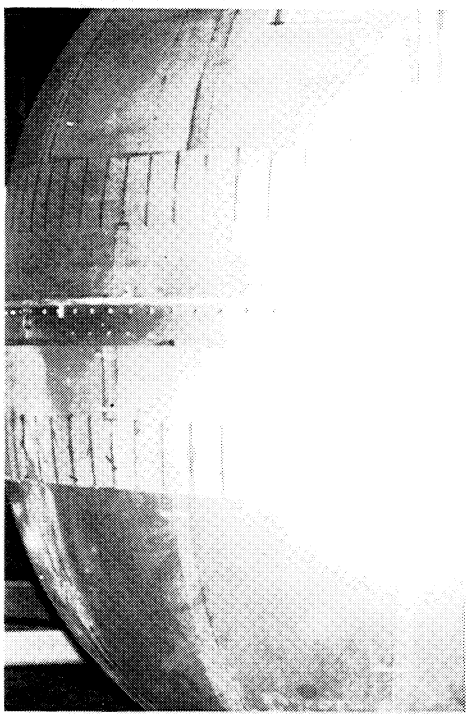

A: VACUUM JACKET JOINING PLATES AT GIRTH

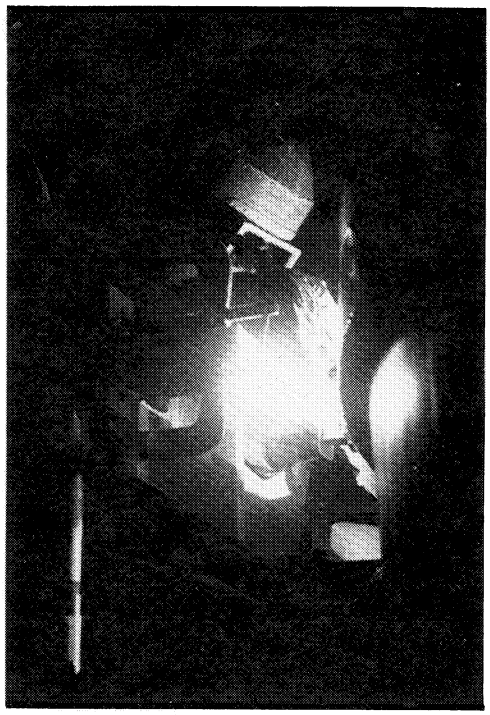

B: WELDING VACUUM CLOSEOUT RING AT GIRTH

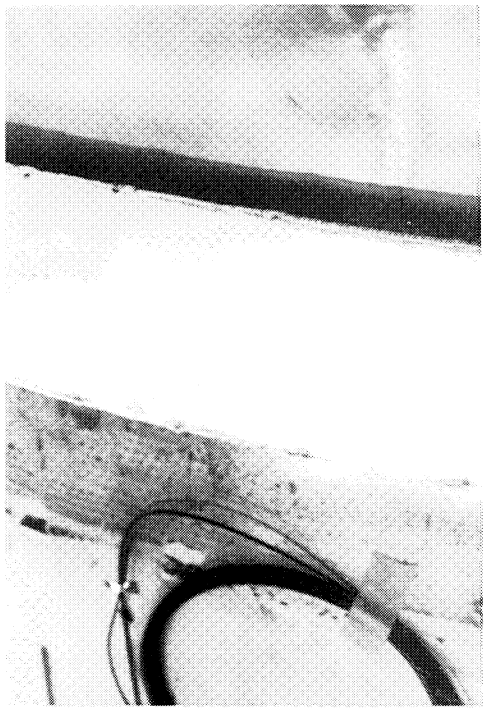

C: COMPLETED VACUUM CLOSEOUT WELD AT GIRTH

Figure 4.6-23. Half Scale LH_2 Test Model Assembly

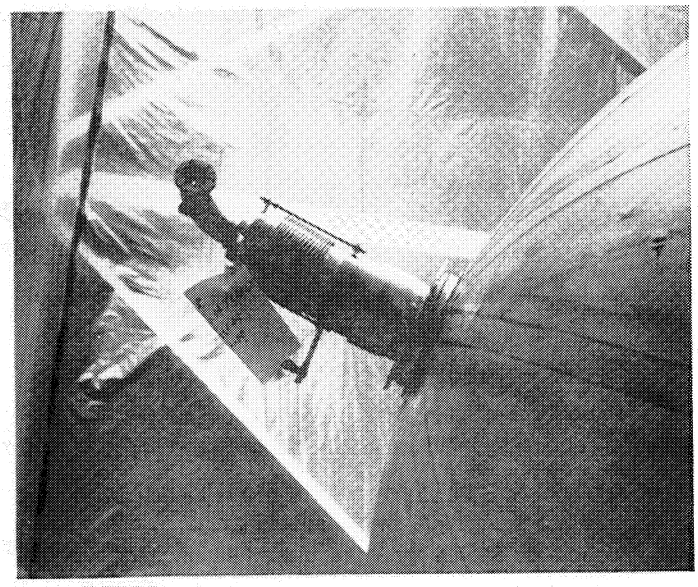

A: VACUUM JACKET CLOSEOUT FITTING AT INLET

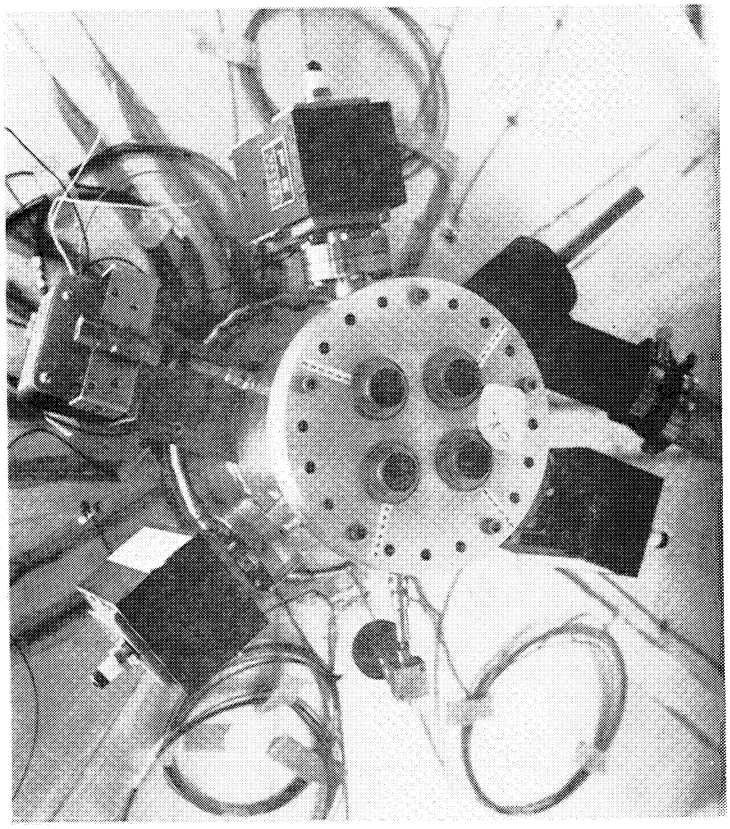

B: VACUUM JACKET CLOSEOUT FITTING AT SIMULATED PLUMBING LINE

Figure 4.6-24. Half Scale LH_2 Test Model Assembly

4.7 ACCEPTANCE TESTS

Acceptance tests were conducted on the pressure vessel, the support straps and the vacuum jacket heads to ensure structural and vacuum acquisition integrity before proceeding to the next stages of LH_2 test model assembly.

4.7.1 Pressure Vessel

After final weld assembly of the pressure vessel (Reference Figure , Appendix D) Cosmodyne completed cold shock to 77.4°K (-320°F), internal proof pressure to 275.79 kN/m^2 (40 psig) and a helium leak check in compliance with drawing specifications.

The method used to helium leak check the pressure vessel at Cosmodyne was to run a vacuum cup arrangement along the weld seams while the pressure vessel was pressurized to 34.47 kN/m^2 (5 psi) with a helium/air mixture. The vacuum cup was connected to a helium leak detector. This method gave a positive indication of the general vacuum tightness of the structure.

After receipt of the pressure vessel at Boeing, the inlet tube assembly was welded in place. The pressure vessel assembly was then mounted in a vacuum chamber and a test conducted to determine the total helium leak rate of the pressure vessel assembly. Test results showed that the pressure vessel assembly has an acceptable leak rate of 9.23×10^{-8} atm ml of helium per second.

The external surface of the pressure vessel was sanded and cleaned prior to installing the assembly in the vacuum chamber. The cleanliness of this surface was further improved in the vacuum chamber where any remaining contamination was reduced by outgassing. After the test, the pressure vessel was removed from the vacuum chamber, re-installed in the test model support fixture, and the fixture then moved into a clean booth for installation of the MLI panels.

4.7.2 Support Straps

The sixteen (16) support strap assemblies were acceptance tested as follows, prior to installation on the pressure vessel.

1) Cold shock each end fitting bond area to 77.4°K (-320°F)

2) Proof test at room temperature to 16.01 kN (3600 lb) tension

Fifteen (15) straps were successfully tested. The remaining strap failed at the small end fitting bond joint at 14.23 kN (3200 lb) tension. The end fitting was cleaned off and rebonded to the strap. This end was cold shocked to 77.4°K (-320°F) and then the strap assembly proof tested to 16.01 kN (3600 lb) tension at room temperature.

4.7.3 Force/Stiffness Tests - Vacuum Jacket Head

Objective

The test objective was to demonstrate that the LH_2 test model vacuum jacket had a strength of 172 kN/m^2 (25 psi) or more when loaded by external pressure. If the vacuum jacket strength was less than 172 kN/m^2 (25 psi) external pressure, the test was to nondestructively determine the critical pressure and buckling mode. The test data could then be used to design a shell reinforcement to increase the buckling strength to 172 kN/m^2 (25 psi).

Test Setup

Figure 4.7-1 describes the vacuum jacket head force/stiffness test setup. The existing Boeing kirksite explosive forming die, hydraulic jack system, and the 50.8 mm (2.0 in) thick steel cover plate were used in the nondestructive proof test setup described in Reference 3. The larger vacuum jacket head on this program required a 0.76 m (30.0 in) long x 12.7 mm (0.50 in) thick steel cylindrical section between the cover plate and the

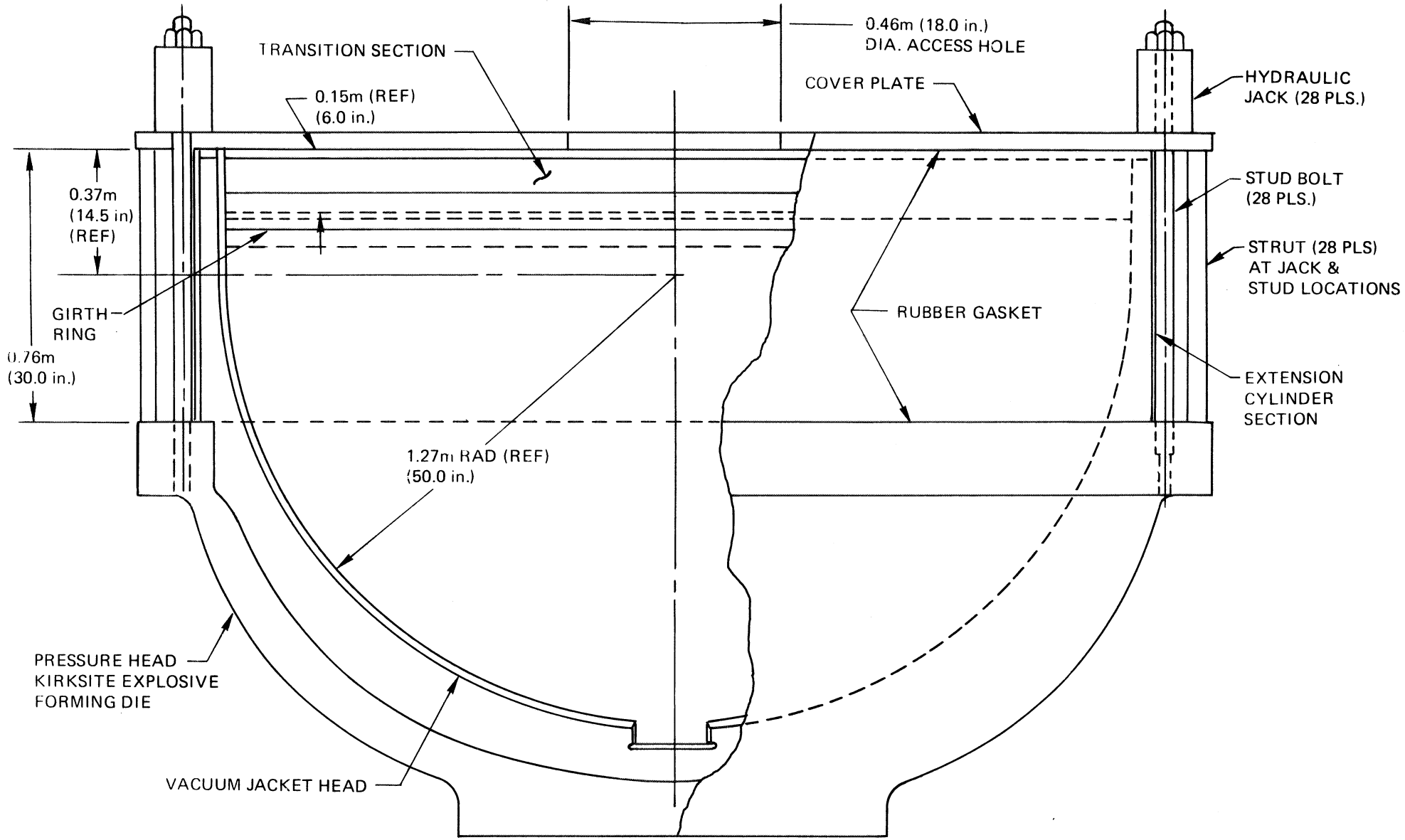

Figure 4.7-1. Force/Stiffness Test Setup for Vacuum Jacket Head - LH_2 Test Model

kirksite. Figure 4.7-2a shows the vacuum jacket head attached to the transition section and bolted to the cover plate. Figure 4.7-2b is a photograph of the test setup.

Transition Section

The transition section was used in the test setup to provide strain relief between the vacuum jacket head test specimen and the test fixture cover plate. Details of this assembly are shown in Appendix D, Figures D-27 and D-28. The transition section consisted of four segments comprising 2.03 mm (0.080 in) thick 6061-T6 aluminum face skins, and aluminum Flex-Core 5056/F80 - .0014, 68.88 kg/m^3 (4.3 lb/ft^3). Ring segments bonded to the transition assembly are bolted to the test fixture cover plate.

Transition Section Analysis

Figure 4.7-3 is a sketch of the transition joint used for the analysis. The BOSOR3 (Reference 4) analysis method was used to compute the loads on the transition section for an external pressure of 172 kN/m^2 (25 psi) at 294°K (70°F). These loads are plotted in Figures 4.7-4 and 4.7-5 versus the Z coordinate of the vacuum jacket head. "N_{10} and N_{20}" were the membrane loads in the meridional and circumferential directions, respectively. "M_{10} and M_{20}" were the moments in the meridional and circumferential directions, respectively. The static equivalent line loads on each face skin were computed using the equations:

$$N_{1i} = N_{10}/2 + M_{10}/d$$
$$N_{1o} = N_{10}/2 - M_{10}/d$$
$$N_{2i} = N_{20}/2 + M_{20}/d$$
$$N_{2o} = N_{20}/2 - M_{20}/d$$

where i = inner face skin
o = outer face skin
d = depth of the sandwich

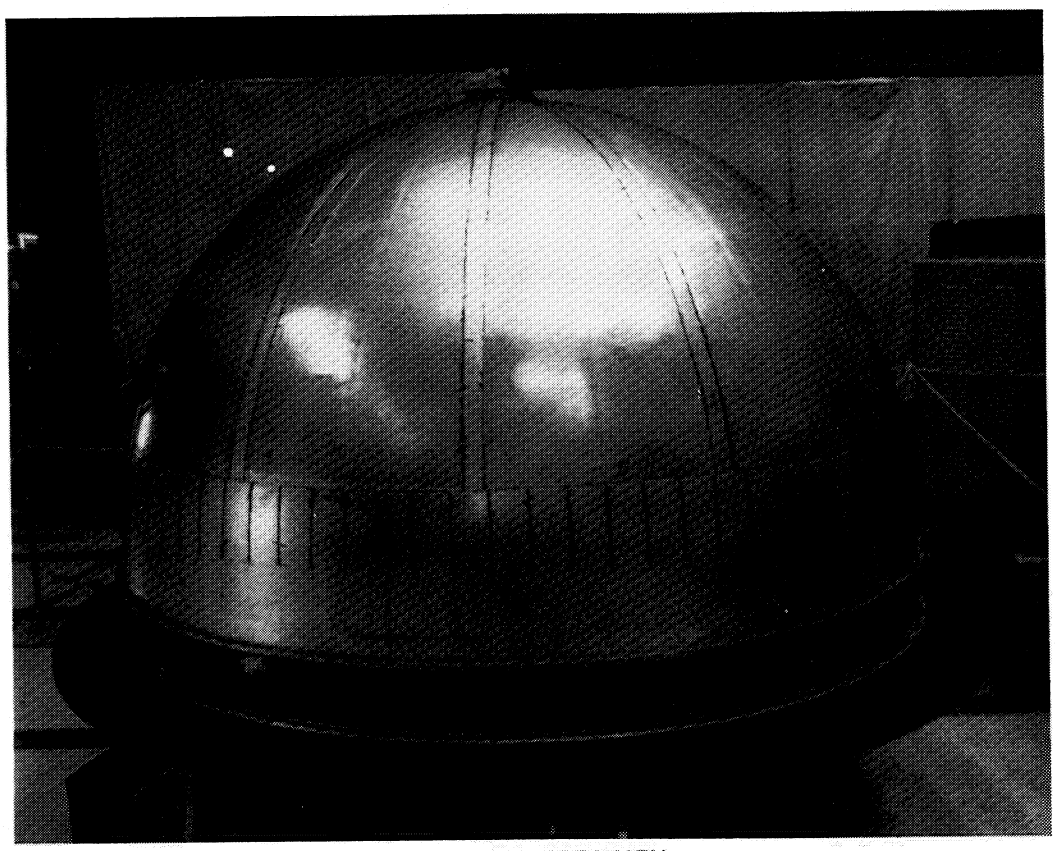

A: TEST SPECIMEN

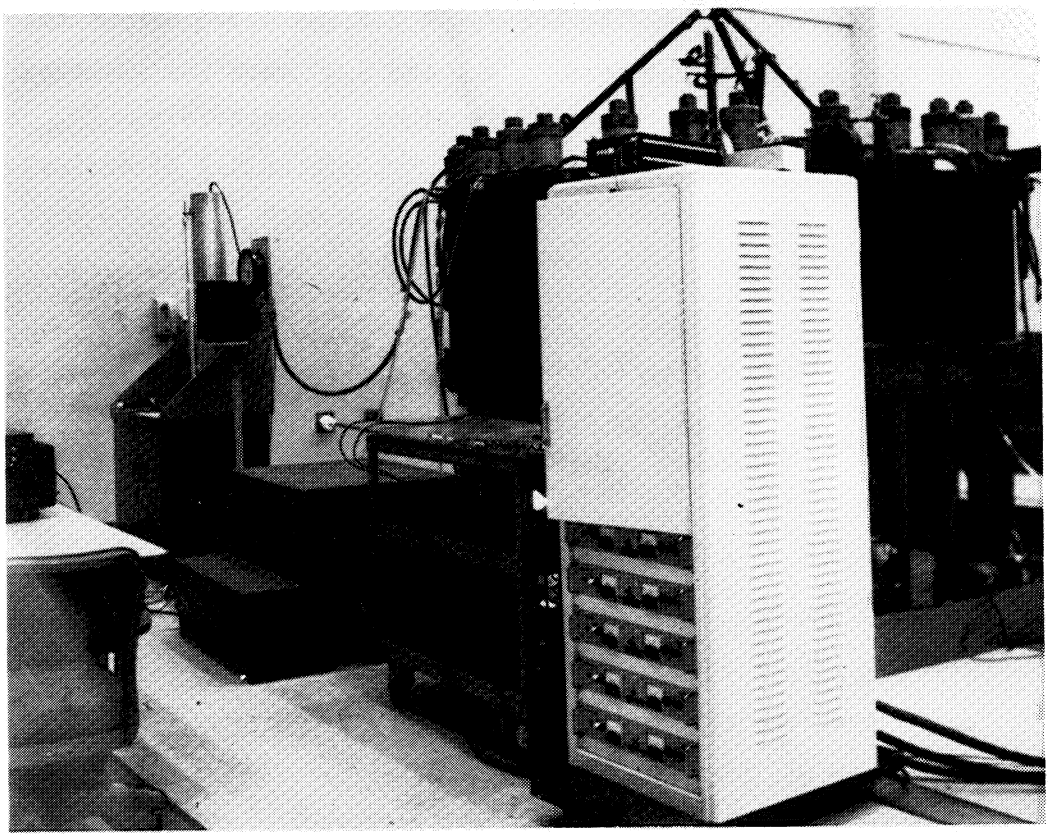

B: TEST SETUP

Figure 4.7-2. Force/Stiffness Test Setup for Vacuum Jacket Head–LH_2 Test Model

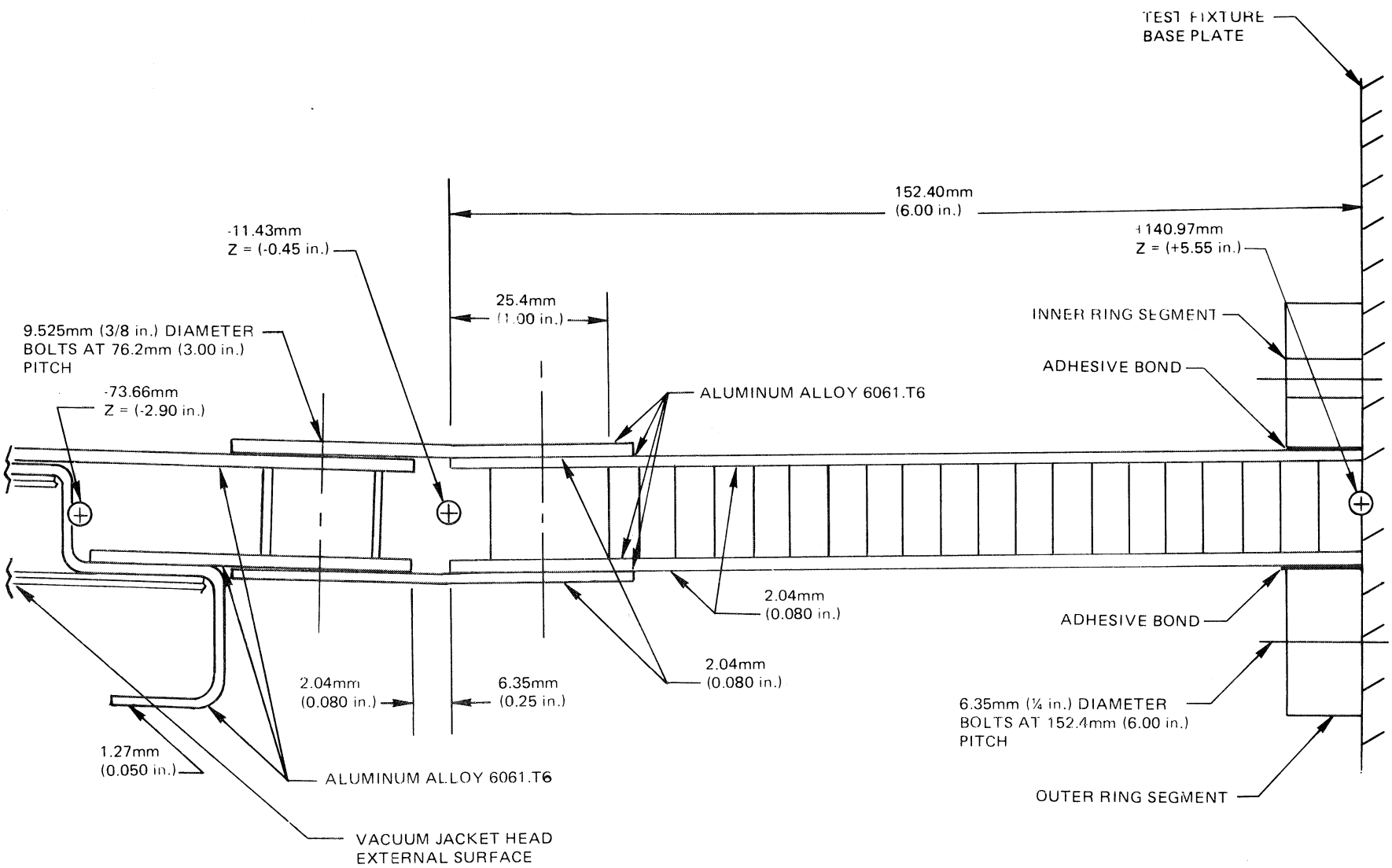

Figure 4.7-3 Details of Transition Section for Analysis - F/S Test

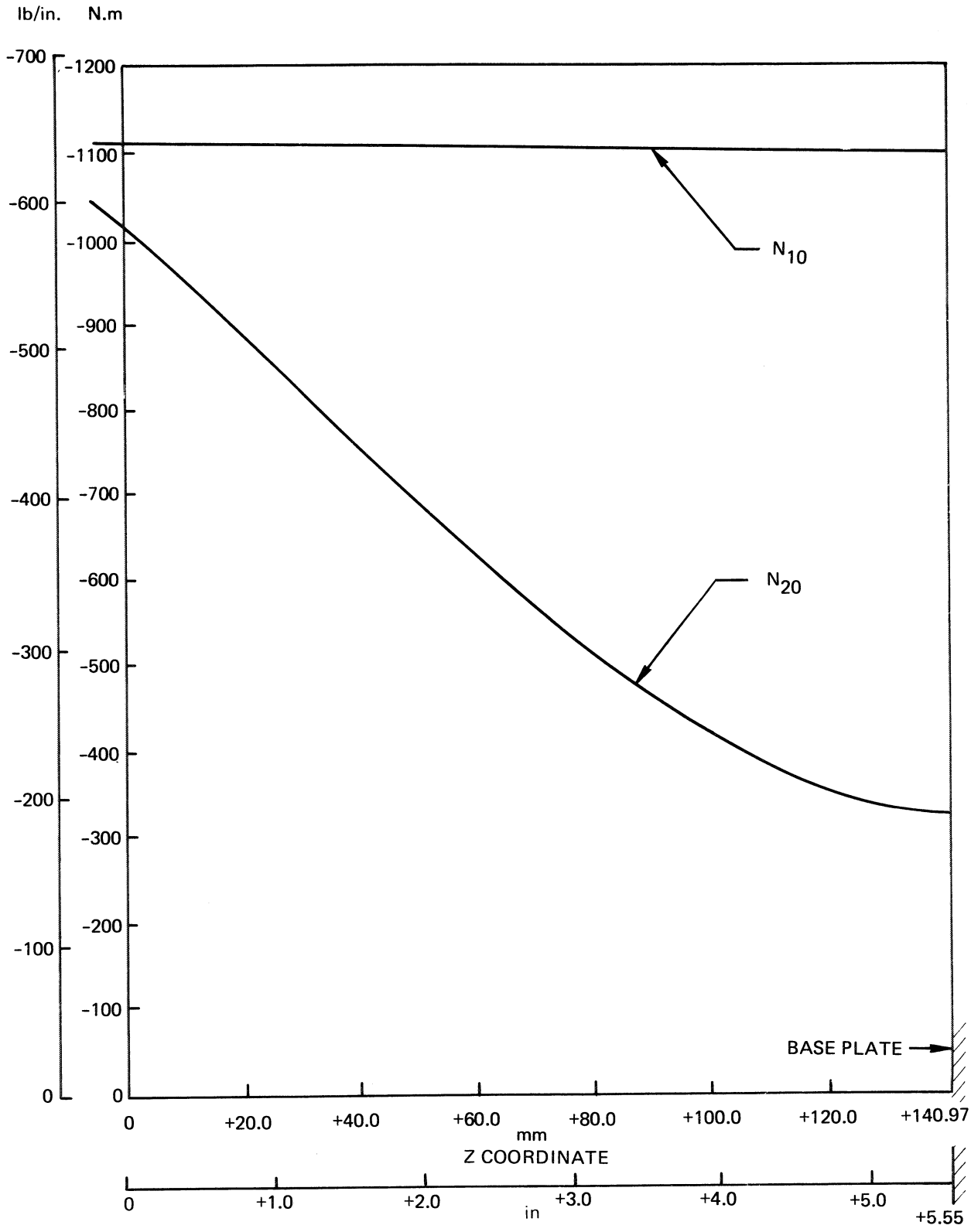

Figure 4.7-4. Loads on Transition Section at 172.37 k N/m^2 (25 psi) Pressure - F/S Test

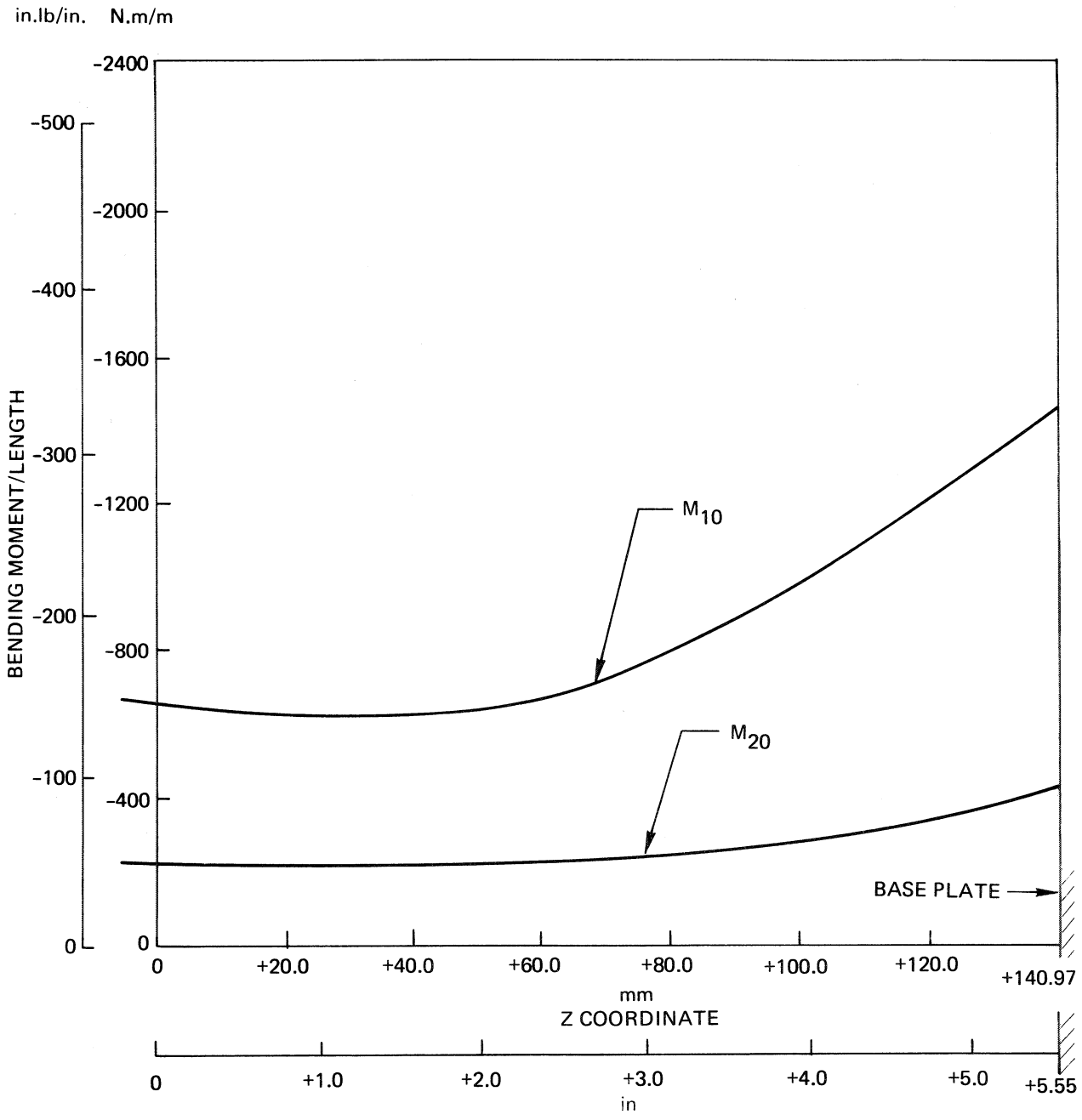

Figure 4.7-5. Bending Moments on Transition Section at 172.37 k N/m^2 (25 psi) Pressure - F/S Test

The line loads for each skin in each direction are plotted versus the Z coordinate in Figure 4.7-6. The maximum load occurred in the inner skin at Z = +140.97 mm (+5.55 in) in the meridian direction, N_{1i} = -140.10 kN/m (-800 lb/in). This load was transferred to the test fixture baseplate by end bearing of the 2.03 mm (0.080 in) 6061-T6 aluminum skin where f_b = 68.95 MN/m^2 (10 ksi), or by shear through the adhesive bond where f_s avg = 140.10/0.0127 = 11.03 MN/m^2 (1.6 ksi) (see Figure 4.7-3). Load transfer by either mode had a large margin of safety. The typical adhesive shear strength of a 12.7 mm (0.5 in) lap joint with Hysol EA 934 adhesive is 21.37 MN/m^2 (3.1 ksi). Assuming that the allowable strength is 75 percent of the typical strength, the margin of safety was M.S. = 0.75 x 21.37/11.03 - 1 = +0.45 (adhesive failure). For end bearing of the 6061-T6 aluminum using the allowable bearing yield strength at an e/D = 2.0 from the Boeing Design Manual,

$$M.S. = F_{bry}/f_b - 1 = 3999.9/68.95 - 1 = +4.8 \text{ (aluminum bearing)}$$

It appeared that the outer skin would be in tension at Z = 140.97 mm (5.55 in), N_{1o} = 27.15 kN/m (+155 lb/in). This load would be transferred by adhesive shear to the outer ring segment and then into bolt tension to the baseplate. The tensile load on each bolt for a 152.4 mm (6.0 in) spacing would be,

$$P_{bolt} = 27.15 \times 0.152 = 4.14 \text{ kN (930 lb)}$$

The carbon steel bolts were 6.35 mm (1/4 in) diameter; AN507 (or BACB30GC). The allowable strength of these bolts in axial tension is 6.58 kN (1480 lb). The margin of safety was

$$M.S. = 6.58/4.14 - 1 = +0.59$$

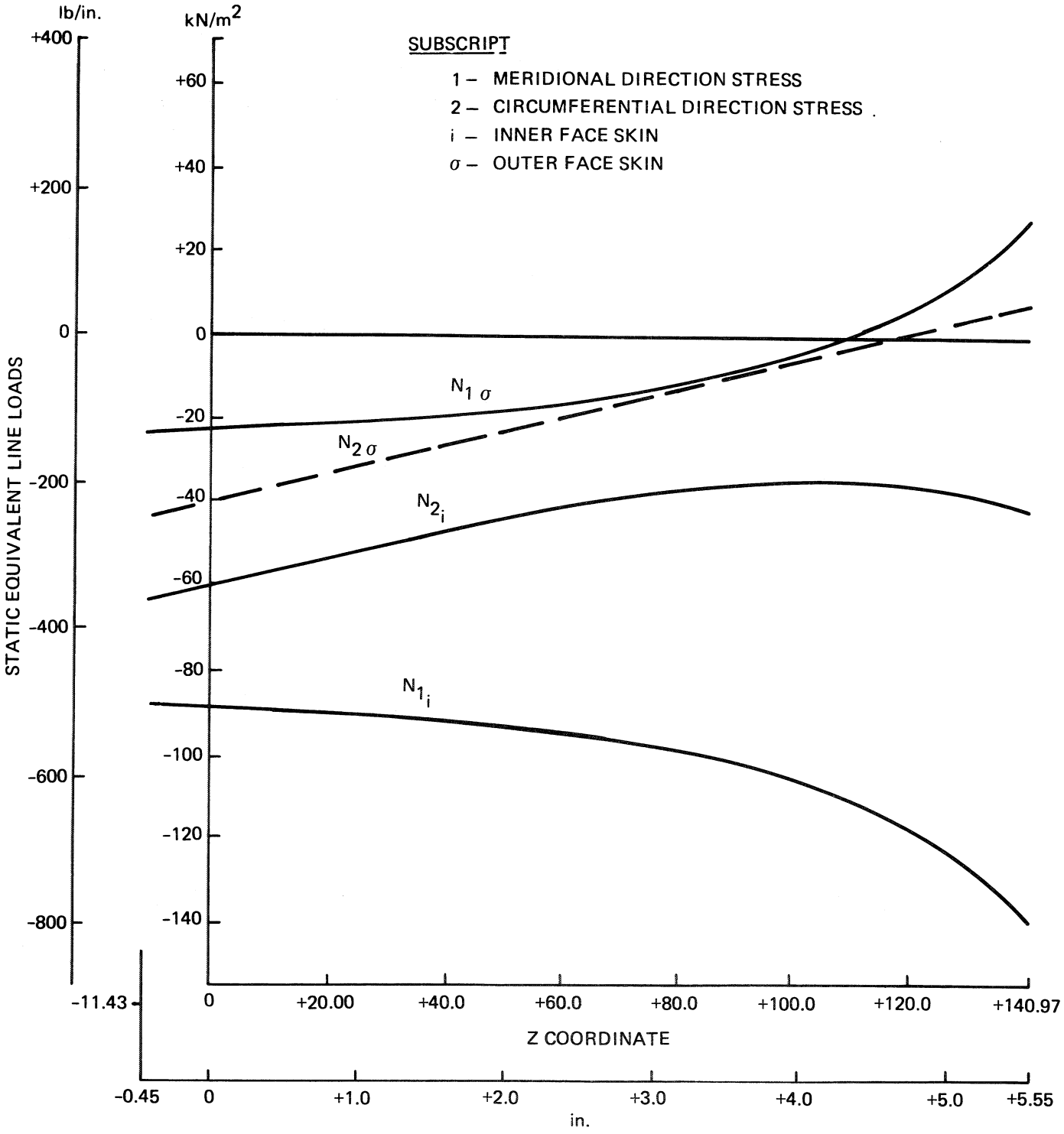

Figure 4.7-6. Static Equivalent Line Loads on Transition Section vs. Z Coordinate FIS Test

The maximum skin stress in the sandwich face occurred in the inner skin at Z = +127 mm (+5.0 in), N_{1i} = 122.59 kN/m (700 lb/in). Dividing by the nominal face skin gage, 2.03 mm (0.080 in), the nominal compression stress was f_{c1} = -122.59/0.00203 = -60.33 MN/m^2 (-8.75 ksi) in the meridional direction. In the circumferential direction, the stress was $f_{c2} = N_{2i}/t$ = -40.28/-.00203 = -19.85 MN/m^2 (2.88 ksi).

The 294°K (70°F), proportional limit stress for aluminum 6061-T6 (QQ-A-250/11) in compression is 186.16 MN/m^2 (27 ksi) per the Boeing Design Manual. Sandwich failure by intracell buckling of face wrinkling are remote possibilities for 2.03 mm (0.080 in) face skins on 68.88 kg/m^3 (4.3 lb/ft^3) density aluminum honeycomb core. The section is short and thick enough to preclude instability. The probable mode of failure is shear crimping. The allowable stress for shear crimping is calculated by the equation per the Boeing Design Manual,

$$N_{cr} = 0.75 \frac{d^2}{c} G_{yz}$$

where N_{cr} = allowable load/meter for both skins
d = distance between face skin centroids
c = core depth
G_{yz} = core shear modulus

For the 68.88 kg/m^3 (4.3 lb/ft^3) density, 5056 aluminum Flex-Core, G_{yz} = 99.29 MN/m^2 (14.4 ksi). With d = 17.27 mm (0.68 in) and c = 15.24 mm (0.60 in).

$$N_{cri} = 1.46 \text{ MN/m (8320 lb/in)}$$

For the inner face,

$$N_{cri} = N_{cr}/2 = 7.28.53 \text{ kN/m (4160 lb/in)}$$

Since the maximum load was 122.59 kN/m (700 lb/in), there was a large margin of safety against shear crimping.

Load transfer in the meridional direction at the joint between the transition section and the vacuum jacket head would be by sheet bearing and fastener shear. Both the transition section sheet and the joining plates were aluminum 6061-T6 2.03 mm (0.08 in) sheet. The maximum load at Z = -11.43 mm (-0.45 in) occurs in the inner skin where N_{1i} = -87.56 kN/m (-500 lb/in). The attachment bolts per Figure D-27, Appendix D, are pitched at 79.76 mm (3.14 in) so that the load per bolt would be,

$$P_{bolt} = 0.0798 \times 87.51 = 6.933 \text{ kN } (1570 \text{ lb})$$

The nominal sheet bearing stress was,

$$f_{br} = P_{bolt} t \times D = 6.983/(0.00203 \times 0.00953) = 360.9 \text{ MN/m}^2 \text{ (52.3 ksi)}$$

The allowable bearing yield stress for aluminum 6061-T6 is 399.9 MN/m^2 (58.0 ksi). The margin of safety was,

$$M.S. = 399.9/360.9 - 1 = +0.11$$

The ultimate allowable shear strength of AN6 9.53 mm (3/8 in) diameter bolts is 17.21 kN (3870 lb) in single shear. Assuming the shear yield allowable strength is 2/3 of the ultimate shear strength, P_{sy} = 11.43 kN (2570 lb). The margin of safety was

$$M.S. = 11.43/6.98 - 1 = +0.64.$$

The transition section was segmented in the circumferential direction. The splice plates are 2.54 mm (0.10 in) 6061-T6 aluminum sheet fastened by four 6.35 mm (1/4 in) diameter bolts. The load per bolt was

$$P_{bolt} = 0.15m \times N_{21}/4 \text{ bolts} = 0.15 \times 63.05/4 = 2.40 \text{ kN } (540 \text{ lb})$$

Neither sheet bearing or bolt shear are critical for the circumferential splice.

Test Specimen Instrumentation

It was determined in Reference 3 that successful force/stiffness tests require the use of strain gages placed back-to-back. To minimize the number of gages requires a good knowledge of the possible failure modes. The instrumentation plan was based on a careful examination of the geometrical imperfections built into the vacuum jacket and analytical studies of the probably buckling modes.

Over 100 measurements were made on the vacuum jacket head tool to determine the location and size of the initial imperfections built into the head.

These data were plotted as contours in the meridional and circumferential directions. Eigenvalue and axisymmetric buckling mode analyses were used to select the areas of the vacuum jacket head mostly likely to buckle. Twenty-eight locations were selected for strain gaging. Three locations were selected for electronic deflection indication (EDI) data. Figure 4.7-7 is a schematic of the instrumentation.

Figures 4.7-8 through 4.7-10 are photographs of the gages installed on the head. The white material shown in Figure 4.7-8 is a waterproofing material to protect the gages when the outer surface was immersed in water. The numbers assigned to the gages were approximately the order in which the locations were selected. Gage locations 1, 2 and 3 were the most probable buckle locations, etc. Gage sets 6, 18 and 26 were used to monitor the strains at the girth ring.

Force/Stiffness Test Data

A total of four external pressure tests were conducted.

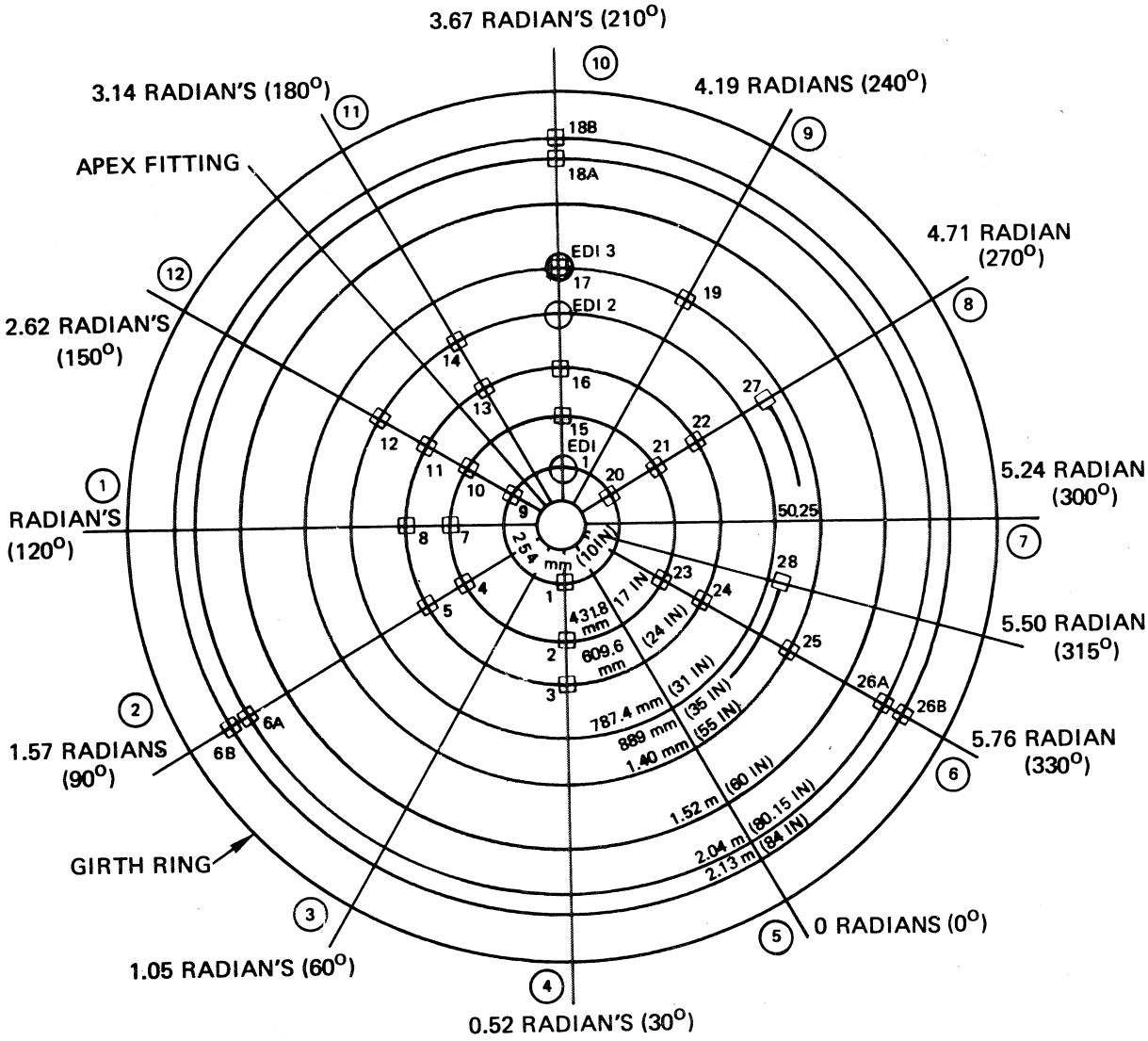

□ STRAIN GAGE PAIR - BACK TO BACK UNLESS OTHERWISE SHOWN
"A" = INNER B = OUTER

○ ELECTRONIC DEFLECTION INSTRUMENT (EDI)
NORMAL TO SURFACE

◯ OUTER SKIN PANEL IDENTITY NUMBER

EACH RING INDICATES THE DISTANCE
ALONG THE VACUUM JACKET SKIN
CONTOUR FROM THE ℄ OF THE APEX FITTING

Figure 4.7-7. Vacuum Jacket Head Instrumentation-- F/S Test

A: EXTERIOR LOCATION FOR STRAIN GAGES 1B-28B

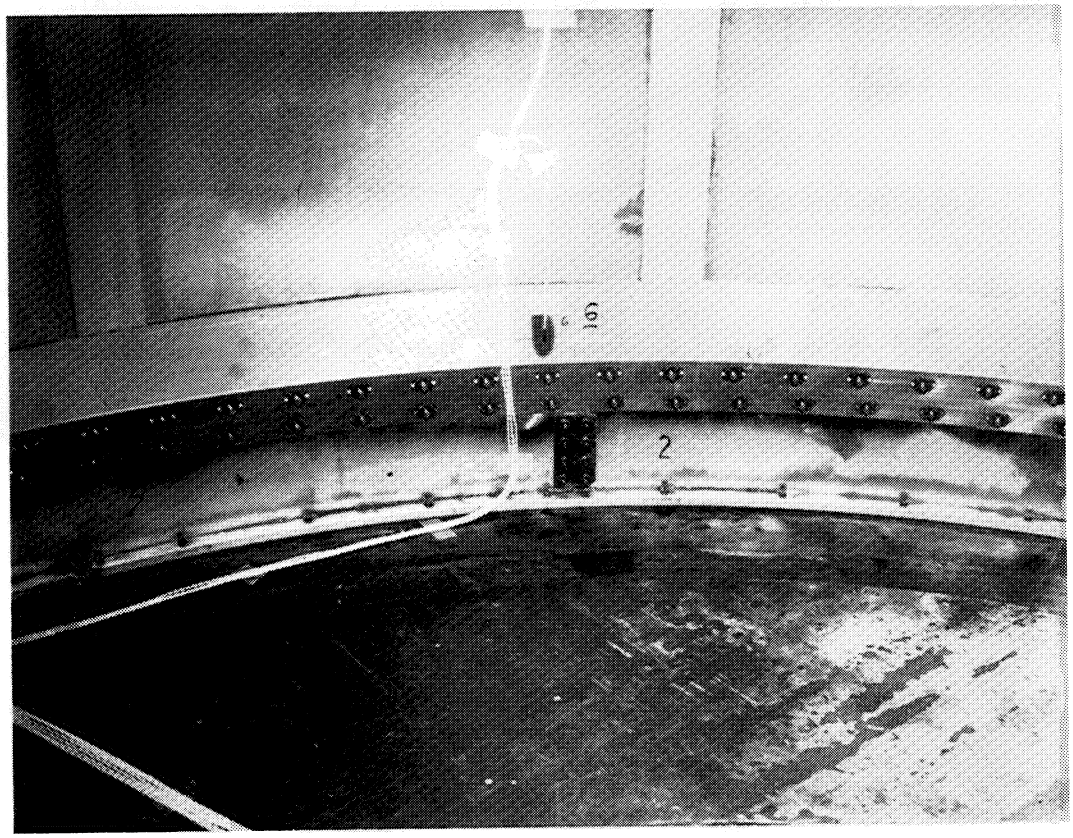

B: INTERIOR LOCATION FOR STRAIN GAGE 6A

Figure 4.7-8. Vacuum Jacket Head Instrumentation—F/S Test

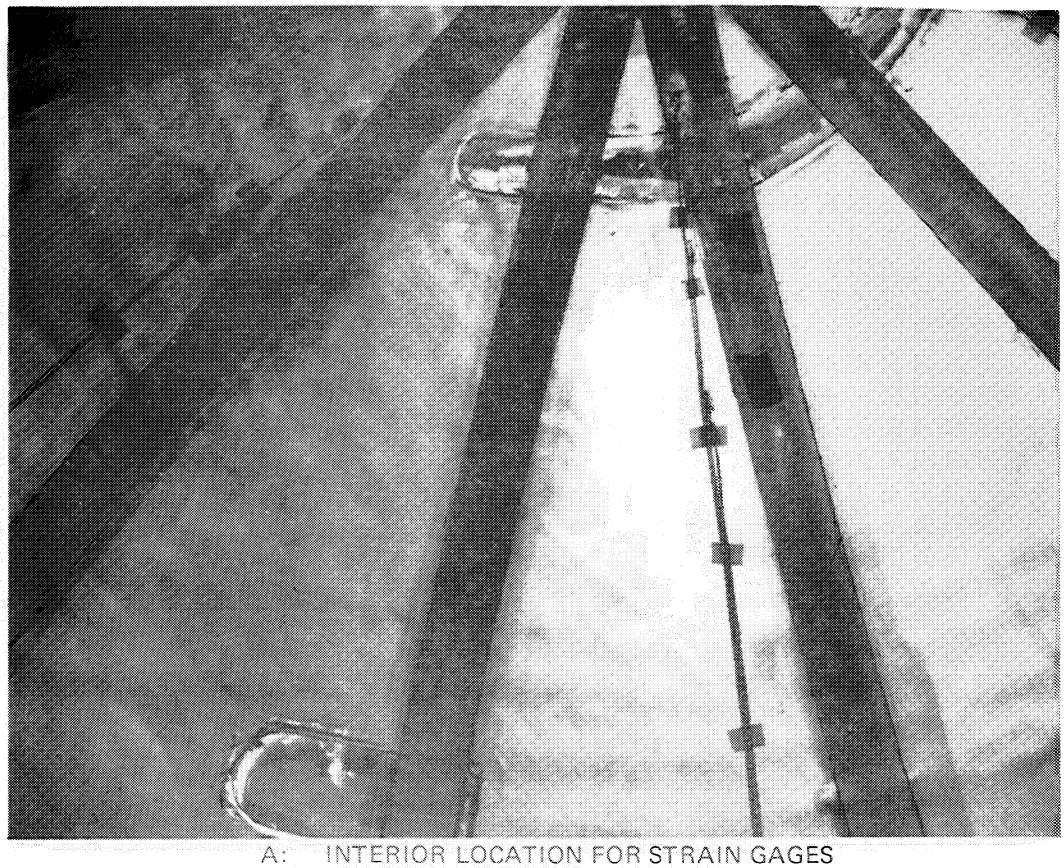

A: INTERIOR LOCATION FOR STRAIN GAGES
1A, 2A, 23A, AND 24A

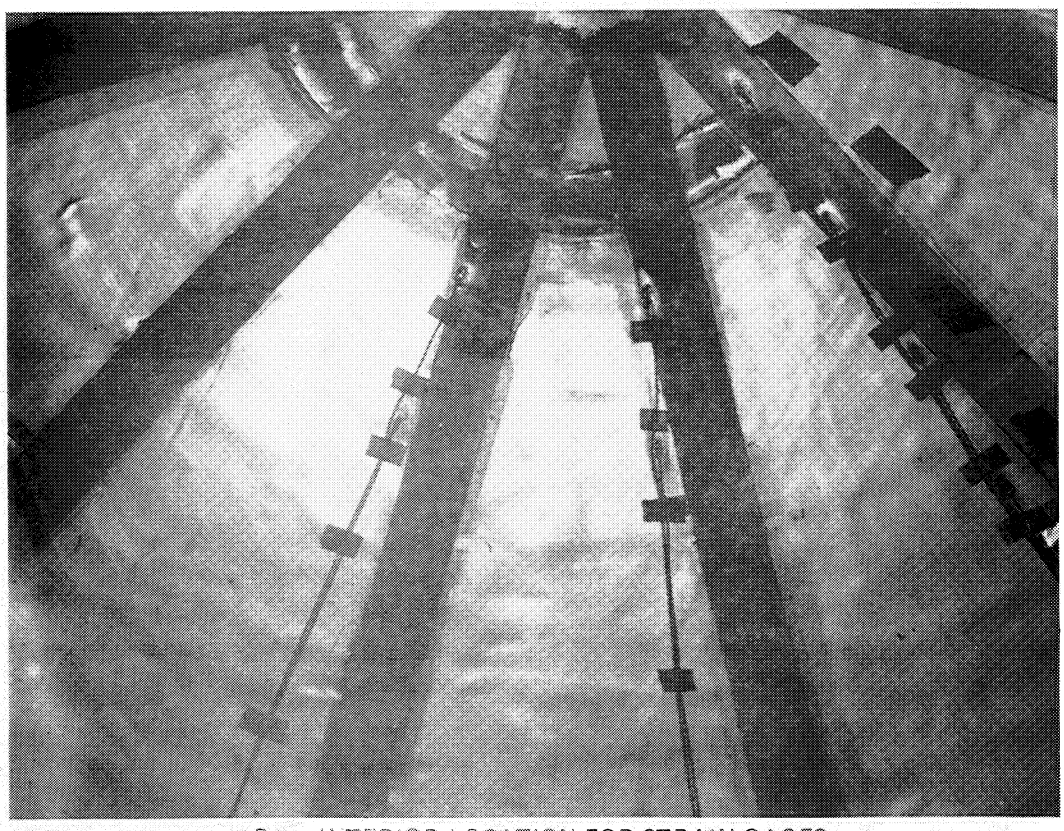

B: INTERIOR LOCATION FOR STRAIN GAGES
4A, 5A, 7A-12A

Figure 4.7-9. Vacuum Jacket Head Instrumentation F/S Test

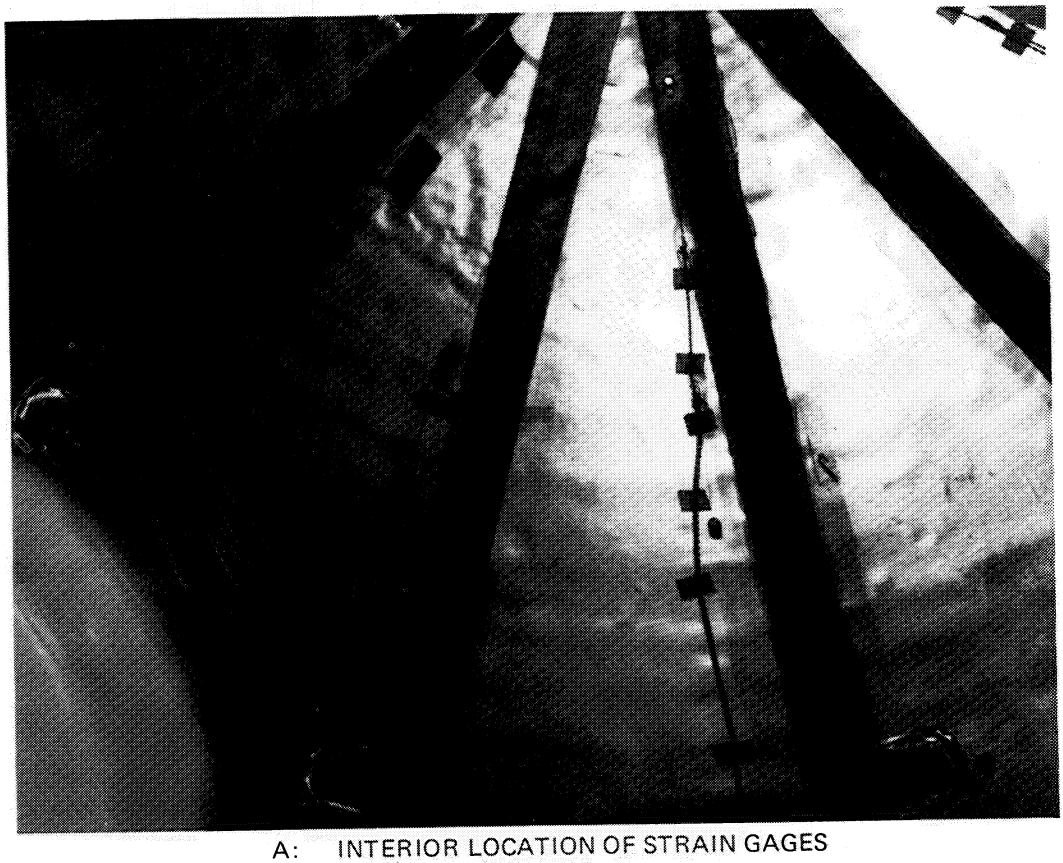

A: INTERIOR LOCATION OF STRAIN GAGES
9A-16A

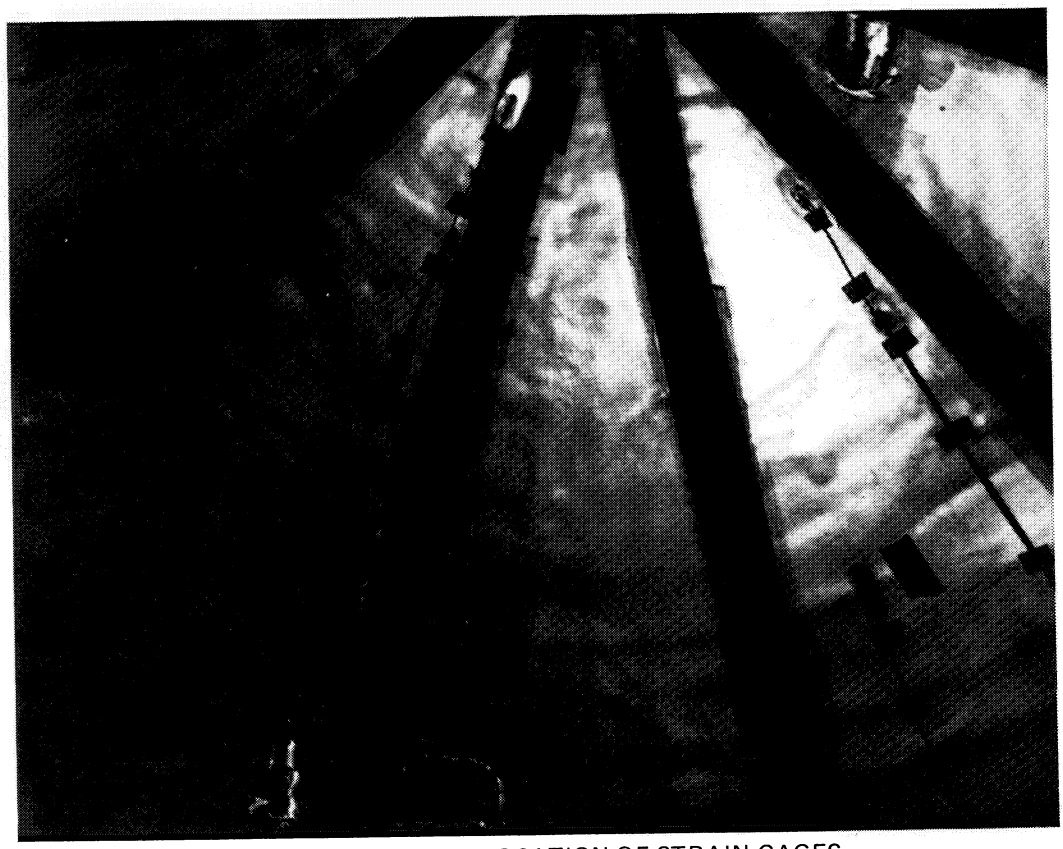

B: INTERIOR LOCATION OF STRAIN GAGES
20A-24A

Figure 4.7-10. Vacuum Jacket Head Instrumentation—F/S Test

The first two tests were used to check out the pressure control system, the data acquisition system and the personnel conducting the test. Tests 1 and 2 applied a maximum external pressure of 55.16 kN/m^2 (8 psi). Although a number of water leaks developed it was determined that the pressure could be controlled with sufficient accuracy for the test. A sump pump was used to remove the excess water.

Test 3 loaded the shell to 110.32 kN/m^2 (16 psi) external pressure. Force-stiffness data were monitored continuously; however, no buckling was indicated during the test. Following test No. 3 much of the data recorded at 30 second intervals during the test were plotted. Some of the data indicated a possible buckle could develop at 137.9 kN/m^2 (20 psi); however, the force-stiffness prediction was not conclusive. It was decided to proceed with the fourth test and to closely monitor all the data.

Test No. 4 loaded the shell to a maximum external pressure of 141.34 kN/m^2 (20.5 psi). Force-stiffness data were recorded at 30 second intervals throughout the test. Force-stiffness data were manually plotted at loads of 34.47 and 68.94 kN/m^2 (5 and 10 psi), then at 6.9 kN/m^2 (1 psi) intervals from 82.74-137.9 kN/m^2 (12-20 psi). The force-stiffness plot for strain gage pair 2 began to turn sharply downward at 124.11 kN/m^2 (18 psi). At 137.9 kN/m^2 (20 psi) the F/S (force/stiffness) plot was predicting 179.26 - 186.16 kN/m^2 (26-27 psi) as the critical external pressure. One additional load, 141.34 kN/m^2 (20.5 psi), was applied. Since the F/S plot was continuing downward the test was stopped. Figure 4.7-11 is the F/S vs. F plot of the data recorded manually and plotted during the test. The shaded area indicates possible extrapolations of the F/S plot. The estimated critical load is 172.37 - 186.16 kN/m^2 (25-27 psi) external pressure. Since the test objective was 172.37 kN/m^2 (25 psi) or greater, the vacuum jacket head, as tested, was satisfactory for the vacuum acquisition and system evaluation tests.

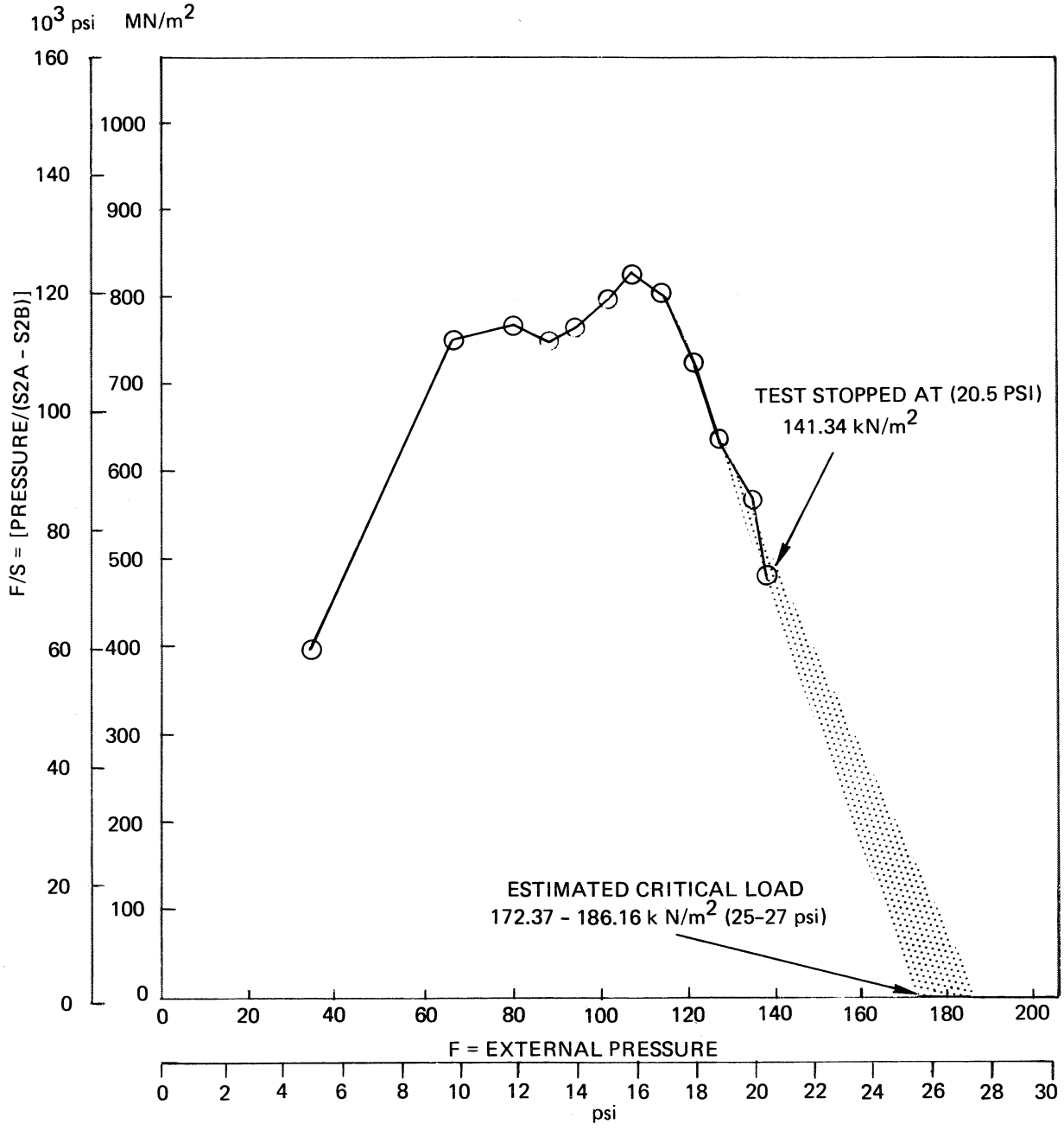

Figure 4.7-11. F/S Plot for Strain Gage Set 2

Post-Test Evaluation

Considerable data were recorded during the force-stiffness test. Examination of the data did not reveal any other critical buckling areas on the shell.

Since the critical buckling mode was located at the S2 gages it appeared from the eigenvalue analysis that the critical mode shape was 2 or 3 circumferential waves. The initial imperfections of the tool surface were characterized by 2 circumferential waves with a peak amplitude of approximately 1.27 mm (.050 in). From these observations it was concluded that the critical or first buckling mode was probably a result of the tool surface imperfections. Therefore, it was reasonable to conclude that vacuum jacket heads built on the same tool would have similar imperfections and would buckle at approximately the same load level. Based on this evaluation and since the quality of the second vacuum jacket head was better than the first vacuum jacket head it was decided not to force/stiffness test the second head.

Following removal of the vacuum jacket head from the test fixture, the inner and outer surfaces were examined. The only damage observed was evident debonding at the inner and outer edge plates to girth ring joint. These plates were removed and a more intensive cleaning procedure devised to improve the bond joint. The faying surfaces were (a) chem-cleaned, (b) sanded with 400 grit sand paper, and (c) solvent cleaned with BMS 11-7. The EA934 adhesive (Hysol Division, The Dexter Corp.) was then applied to the faying surfaces and the parts clamped together for eight hours at room temperature.

4.7.4 Vacuum Acquisition Tests - Vacuum Jacket Assembly

Objective

The test objective was to demonstrate vacuum acquisition capability of the LH_2 test model vacuum jacket assembly.

Test Setup

The two vacuum jacket heads were assembled by bolting the girth ring joining plates and trunnion fittings in place. This assembly was mounted to the support fixture. The welded in-place vacuum sealing strip at the girth was not used in this test. Rather a mylar/aluminum foil/mylar (Zeroperm) strip along with a vacuum sealing compound was used to seal the girth ring area. Flat plates and the sealing compound were used to seal off the upper and lower apex fitting openings. In the lower plate the pumpdown line and a thermocouple vacuum pressure gauge were mounted. Another thermocouple gauge and an ionization gauge were located in the CVC PA60 pumping cart. The CEC leak detector was valved into the vacuum pumpdown at the pumping cart.

Test

During the test the vacuum jacket was cycled through ten vacuum pumpdowns and backfills to ambient. The first two pumpdowns were used to check the system, make the necessary modifications, and perform gross leak checks with a sonic leak detector. Eight pumpdowns were required to complete the helium leak checking and repair.

Helium Leak Check

Initially, the complete assembly was sprayed along the seams with helium from a probe. Leaks discovered by this method were repaired. This check uncovered only leaks in the upper head bond joints in the vicinity of the girth ring. After repair of these leaks, a plastic bag was placed over the upper head, sealed along the girth ring and apex fitting, and then filled with helium. No leaks were found in the upper head. A similar arrangement was used on the lower head, but in this case a helium leak was indicated. It then became necessary to individually bag off all the bond seams on the lower head and check them. The leaks were subsequently isolated to the apex fitting region. These were repaired and checked.

Repair Procedures

The repair procedures adopted were as follows:

1) With the assembly under vacuum pressure XA 3919 (3M) adhesive was applied to the outer skin area in the region of the suspected leak. (This approach assumed that the vacuum would draw the liquid adhesive through the outer skin and core and into the leak channel in the inner skin joint.)

2) The vacuum jacket assembly was backfilled to ambient.

3) The adhesive was cured in the following stages:

   a) Air dried at room temperature for 15 minutes.

   b) Heated to 3.38.38°K (225°F) for 45 minutes.

   c) Heated to 450°K (350°F) for 60 minutes.

Post Test Evaluation

This test demonstrated

1) The vacuum acquisition capability of the LH_2 test model vacuum jacket assembly.

2) Helium leak checking and repair procedures for vacuum jackets with sandwich shell construction, and

3) That Zeroperm with a sealing compound was an adequate alternative to welding for short duration, room temperature vacuum acquisition testing.

The vacuum level of 533.3 kN/m^2 (4 x 10^{-3} torr) and the measured decay rate of 17.33 mN/m^2 per minute (0.13 x 10^{-3} torr per minute) obtained during this test demonstrated the vacuum integrity of this assembly.

4.7.5 Helium Leak Check - LH_2 Test Model Assembly

Objective

The test objective was to determine the helium leak rate of the LH_2 test model vacuum jacket assembly. A target leak rate of 1 x 10^{-7} atmospheric ml of helium per second was selected. A leak rate of this magnitude would not draw significantly on the pumping capability of the three 5 L/S D-1 (Ultek) pumps so that there would be sufficient remaining pump capacity to handle the 9.23 x 10^{-8} atmospheric ml of helium per second leakage rate of the pressure vessel (Reference Section 4.7.1) and the outgassing from the contaminants within the vacuum annulus. Test objectives could also be met with a higher vacuum jacket assembly helium leak rate. The final criteria for delivering the LH_2 test model assembly to the test site was having the capability to maintain the vacuum annulus pressure at 26.66 mN/m^2 (2 x 10^{-4} torr) with the three 5 L/S D-1 ion pumps operating. This could be achieved with varying combinations of vacuum jacket assembly leak rates and levels of outgassing from vacuum annulus contaminants.

Pumpdown Arrangement

Figure 4.7-12 is a photograph of the vacuum annulus pumpdown arrangement. The pumping port was contained in the vacuum jacket apex closeout fitting at the simulated plumbing line. This port consisted of a high vacuum, positive relief, seal-off valve (Cryolab) which was opened with a manual operator when vacuum pumping the annulus. When closed, the valve sealed off the annulus. The closed valve also provided for relief of positive annulus pressure.

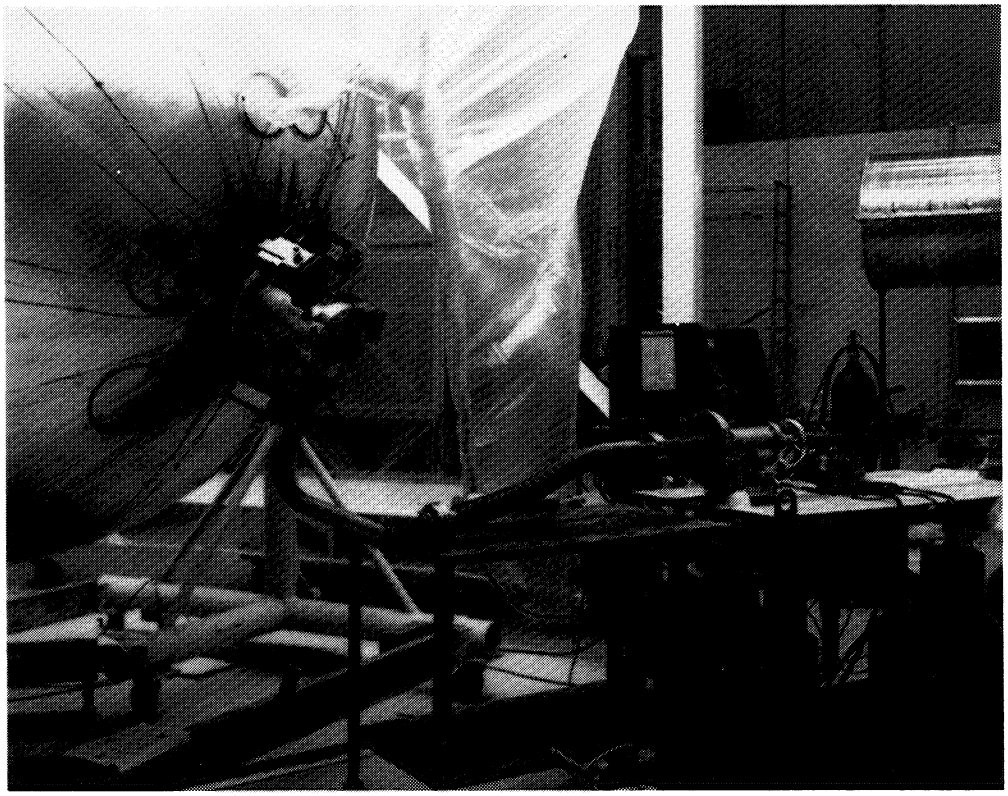

Figure 4.7-12. Vacuum Pumpdown Arrangement LH_2 Test Model Assembly

A 50.8 mm (2.00 in) diameter line connected the pumping port to the pumping cart. A flexible bellows was used for a portion of the line and short rubber hose sections served as interconnects. The LH_2 test model was rotated at approximately 0.79 radians (45°) in order to reduce the length of the pumpdown line and to provide the best overall accessibility to the critical vacuum seal areas, i.e., the apex fittings and the girth ring. Later on, after the leak areas were isolated to the girth ring region, the assembly was rotated to the vertical position.

The pumping cart consisted of a two stage (Heraeus) 100 CFM mechanical blower. In front of the blower was a LN_2 cold trap. Between the blower and the cold trap was a thermocouple pressure gage (DV8). The pressure readout for this gage was in microns of mercury with the scale reading from 1×10^{-4} torr to 1×10^{-2} torr. The blower was backed up by a 21 CFM (Kinney KTC 21) mechanical pump. Another thermocouple gage (DV6) was located between the blower and the mechanical pump. The pressure readout for this gage was in microns of mercury with the scale reading from 0 to 1 torr in a cleared sealed system. At the start of a vacuum pumpdown the mechanical pump was turned on. The blower would automatically cut in at a pressure of approximately 20 torr as measured by gage DV6.

Leak Detector

A CEC leak detector with a sensitivity of 1×10^{-10} atmospheric ml of helium per second was valved into the pumping cart.

Leak Check and Repair

A preliminary leak check was conducted as shown in Figure 4.7-13a. This was followed by selectively bagging areas of the weld joints to pinpoint the location of weld leaks. After isolating all the weld leaks at each vacuum pressure level, the annulus was backfilled with dry GN_2 and the leaks repaired.

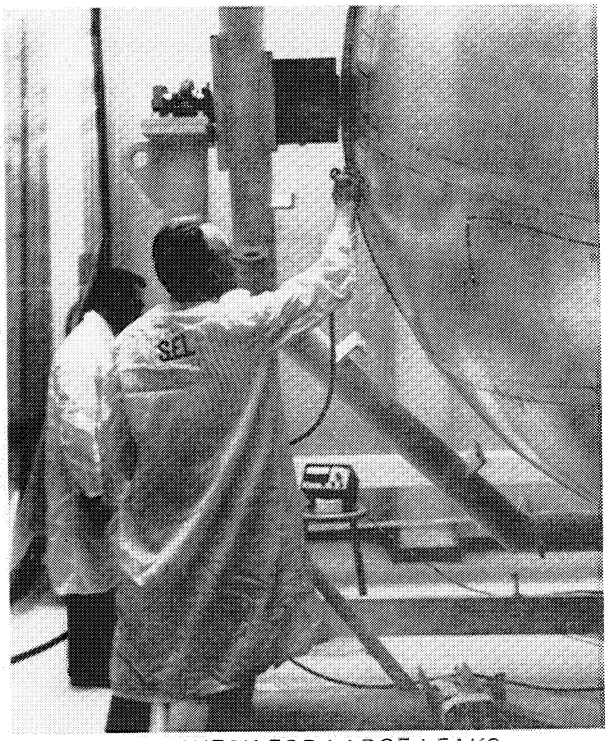

A: CHECK FOR LARGE LEAKS

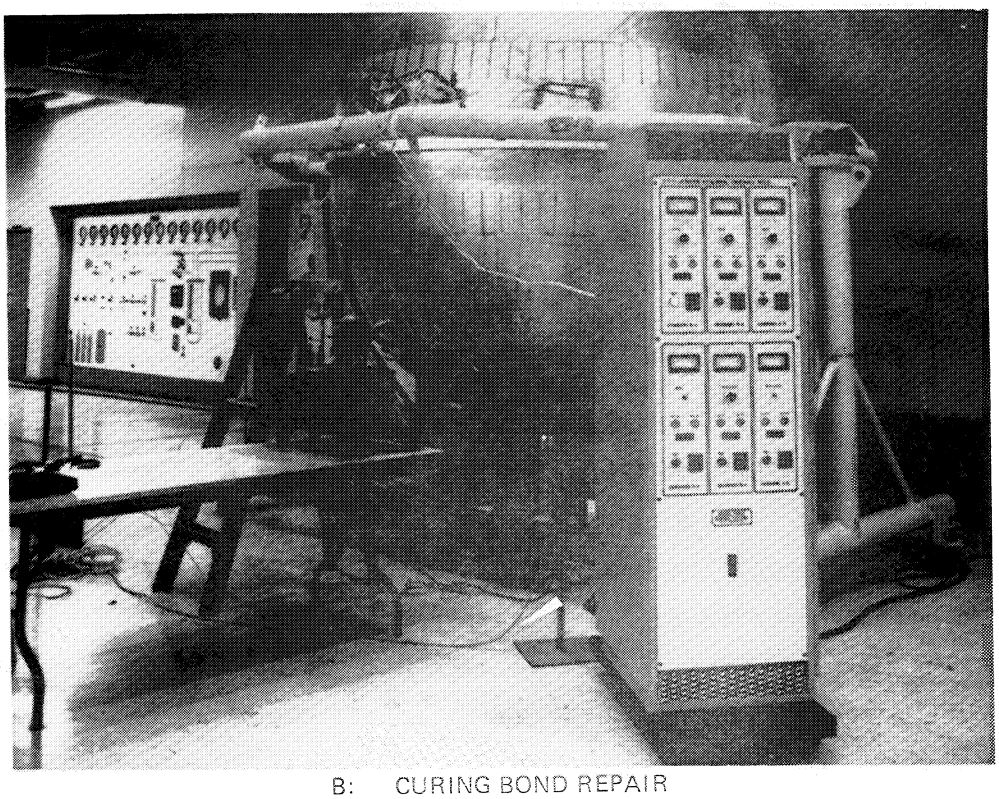

B: CURING BOND REPAIR

Figure 4.7-13. Helium Leak Check and Repair LH_2 Test Model Assembly

During the leak checking and repairing of weld and bond leaks the vacuum annulus was cycled 20 times from ambient to a vacuum pressure. The first four cycles were for weld repairs in upper apex (1) fitting, at the trunnions (2), and in the girth ring. Cycles 5 through 7 were for bond repairs at the head to girth ring joint. Both girth ring weld and bond repairs were made after Cycle 8. Cycles 9, 10, and 11 were for girth ring weld leak repairs. The remaining cycles were for upper head to girth bond leak repairs.

The bond repair technique used was the same as that discussed in Section 4.7.4. Heat lamps monitored by a controller, as shown in Figure 4.7-13b, were used for local curing of the repaired areas.

Only two areas on the lower head to girth ring bond joint required sealing. However, the upper head, which was the head that was F/S tested (Reference Section 4.7.3) was exceptionally difficult to seal. The problem appeared to result from a silicone (RTV) sealant that had been inadvertently beaded around the faying edge of the outer skin to girth ring during F/S test preparations. The silicone worked its way between the skin and the ring. It served as a helium collector channelling helium to areas remote from where the isolated leak checks were being conducted. It was only after discovering this and removing the silicone that progress in sealing the upper head was finally made.

Total Leak Check

After the vacuum jacket appeared to be adequately sealed, a total helium leak check was made of the vacuum jacket assembly. A plastic bag to contain the helium around the vacuum jacket was placed over the LH_2 test model and the support fixture. The pressure vessel outlet was vented through the bag to exclude the pressure vessel leakage from test data taken during this test. The pumpdown lines and connectors were checked to ensure that they were helium leak tight. As an added safeguard the lines and connectors were also bagged with a plastic covering.

The system sensitivity was determined by valving in a calibrated leak of 9.04×10^{-7} atmospheric ml of helium per second into annulus at the upper apex fitting. The system sensitivity was found to be 4.52×10^{-9} atmospheric ml of helium per second per division. The leak detector scale registered 2190 division rise during the test. From this the total leak rate was calculated to be $2190 \times 4.52 \times 10^{-9} = 9.9 \times 10^{-6}$ atmospheric ml of helium per second.

Discussion of Results

The measured leak rate of the vacuum jacket assembly was greater than the target set in the test objective. At this stage there was still the uncertainty about the level of outgassing in the annulus. It was possible that preconditioning within a reasonable time period would reduce the outgassing to a low enough level so that the three 5 L/S d-1 ion pumps could maintain the 26.66 mN/m^2 (2×10^{-4} torr) vacuum level in the annulus with the 1×10^{-5} atmospheric ml of helium per second leak rate through the vacuum jacket and the 1×10^{-8} atmospheric ml of helium per second leak rate through the pressure vessel. Also, the dynamic vacuum pressure with pumps operating as measured by gage DV8 was at 40 mN/m^3 (3×10^{-4} torr) and continuing to decrease, which was a strong indication of a leak tight system. For these reasons it was decided that the 1×10^{-5} atmospheric ml of helium per second was an acceptable leak rate and that preconditioning should commence.

Conclusions

The difficulty of sealing the upper head to girth bond joint suggested several precautions that should be taken in future programs.

1) Silicone (RTV) rubber sealant should not be used around vacuum jacket structure.

2) Consideration should be given to having the outer face skin of the vacuum sealing surface. It is accessible and more easily repaired than an inner face skin sealing surface. This advantage must be weighed against the disadvantage of venting outgassing products from

large adhesive surface areas into the vacuum annulus, thereby making the preconditioning task more difficult.

3) Further research is needed to develop a 450°K (350°F) temperature vacuum repair technique which would avoid the localized heating after final assembly of the vacuum jacket.

5.0 FAILURE ANALYSIS

A structural failure occurred in the upper vacuum jacket head of the LH_2 test model at 9:05 P.M. on September 23, 1974. The annulus between the pressure vessel and the vacuum jacket had been under continuous vacuum for over 50 hours with the pressure at the pumping cart reading 40.0 mN/m^2 (3×10^{-4} torr). A total of approximately 1500 hours at vacuum pressure had been accumulated on the vacuum jacket. During bond repair local areas adjacent to the girth ring had accumulated up to 12 hours of 450°K (350°F). This local heating occurred with the annulus backfilled to ambient pressure. A discussion outlining conditions at the time of failure, probable failure sequence, and probable cause of failure follows.

5.1 CONDITIONS AT THE TIME OF FAILURE

The LH_2 test model assembly was in the vertical position in the support stand. The set-up was located in the Space Environment Laboratory close to the LN_2 supply line in preparation for cooling the pressure vessel as part of the vacuum annulus preconditioning process. The helium leak check discussed in Section 4.7.5 had been conducted during the morning of September 23, 1974. Evaluation of the data indicated a leak rate of 1×10^{-5} atmospheric ml of helium/second. Although this was two decades higher than the target 1×10^{-7} atmospheric ml of helium/second, it was judged to be acceptable, i.e., within the capability of the three 5 L/S D-1 (Ultek) ion pumps (Reference Figure 3.4.5). Some uncertainty still existed, however, since at this time the outgassing rate of the contaminants within the vacuum annulus was not established. For this reason it was decided to proceed with the preconditioning process, but at the same time to conduct a helium leak check on the upper vacuum head to determine if any large vacuum leaks remained.

The last elevated temperature cure cycle occurred on the upper girth ring bond area on September 20, 1974, between trunnions 1 and 2 and trunnions 1 and 4. At the conclusion of the cure cycle the annulus was evacuated. The vacuum pressure was approximately 40.0 mN/m^2 (3×10^{-4} torr) and gradually improved as vacuum pumping continued.

At the time of failure the pressure vessel was vented to the atmosphere. Two mechanics were in the process of installing a plastic bag over the upper vacuum jacket head, for use in the helium leak check previously discussed.

The bag consisted of shaped gores which were taped together on the floor. The bag was lowered over the upper vacuum jacket head and spot taped to the girth ring. One mechanic was on the catwalk above the setup, supporting the top of the bag at the fill and vent fitting. The other mechanic was standing on the octagonal support frame with his feet braced on the heat shroud support clips. He was pressing the tape down by hand to seal the final seam of the plastic bag.

5.2 TEST HISTORY

The test history of each vacuum jacket head is shown in Table 5.2-1. The upper vacuum jacket head was the head externally pressure (F/S) tested as discussed in Section 4.7.3, and was also the most difficult head to vacuum seal. It was this head which initially failed. It is also significant to note that the failure occurred after approximately 1500 hours at vacuum pressure and also after considerable localized heating to 450°K (350°F).

5.3 STRUCTURAL FAILURE SEQUENCE

The failure of the LH_2 test model assembly originated at the upper vacuum jacket head, which resulted in a pressure unbalance on the pressure vessel that applied a high downward acting load on the pressure vessel support straps, breaking the straps. A maximum load of 422.58 kN (95,000 lb) was possible with a 101.4 kN/m^2 (14.7 psi) unbalance pressure acting on the pressure vessel. The ultimate capability of the tension support straps was approximately 106.76 kN (24,000 lb). Thus, the pressure vessel support straps were only able to absorb part of the momentum. Without support from the straps, the pressure vessel continued downward breaking the bottom vacuum jacket in tension and was finally stopped by the floor and the steel support stand. The girth ring and the support stand retained the LH_2 test model in the upright position. Figure 5.3-1a is an overview photograph of the LH_2 test model assembly. Figure 5.3-1b is a view between trunnions 3 and 4, the area where the mechanic was taping the plastic cover. This is also the area where the failure originated. Figures 5.3-2a and b are views on trunnion 2 and between trunnions 1 and 2.

Table 5.2-1. Test History of LH_2 Test Model Prior to Failure

VACUUM JACKET HEAD	PRESSURE CYCLES					THERMAL CYCLES [3]					
	METHOD OF APPLYING PRESSURE	PRESSURE		NO. OF CYCLES	TOTAL HOURS AT VACUUM PRESSURE	GIRTH RING AREA QUADRANT BETWEEN TRUNNIONS	WITH HEAT LAMPS			WITH HEAT GUN	
		N/m^2	psi				NO. OF CYCLES	TOTAL HRS AT 394.3°K (250°F)	TOTAL HRS AT 450°K (350°F)	NO. OF CYCLES	TOTAL HRS AT 394.3°K – 422.1°K (250°F – 300°F)
UPPER	EXTERNAL WATER PRESSURE, ANNULUS AT AMBIENT PRESSURE [1]	55.16	8.0	1		1–2	9	7.5	12	2	4–5
		58.61	8.5	1							
		110.32	16.0	1		2–3	6	5	8	2	4–5
		141.34	20.5	1							
	AMBIENT EXTERNAL PRESSURE, VACUUM IN ANNULUS [2]	101.35	14.7	29	≈ 1500	3–4	7	5.75	9	2	4–5
						4–1	8	6.25	9	1	2–2.5
LOWER	AMBIENT EXTERNAL PRESSURE, VACUUM IN ANNULUS [2]	101.35	14.7	29	≈ 1500	1	1	1	2		
						3–4	1	1	2		

[1] F/S TEST (REFERENCE SECTION 4.7.3)

[2] UPPER AND LOWER VACUUM JACKET HEADS ASSEMBLED TOGETHER (REFERENCE SECTIONS 4.7.4 AND 4.7.5)

[3] LOCAL HEATING TO CURE ADHESIVE USED TO SEAL VACUUM LEAK AREAS (REFERENCE SECTION 4.7.5)

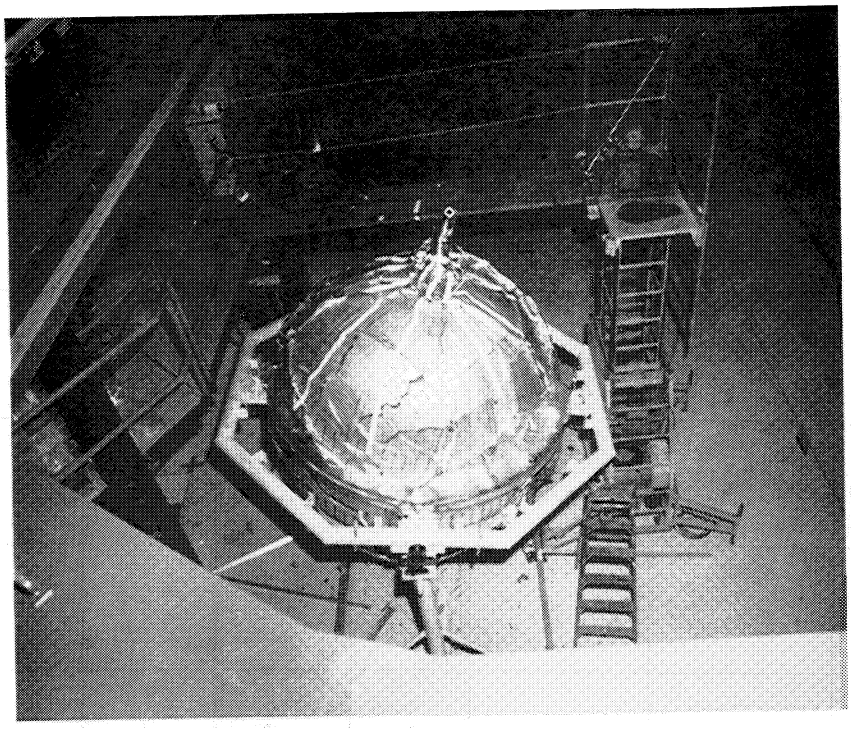

a: OVERVIEW

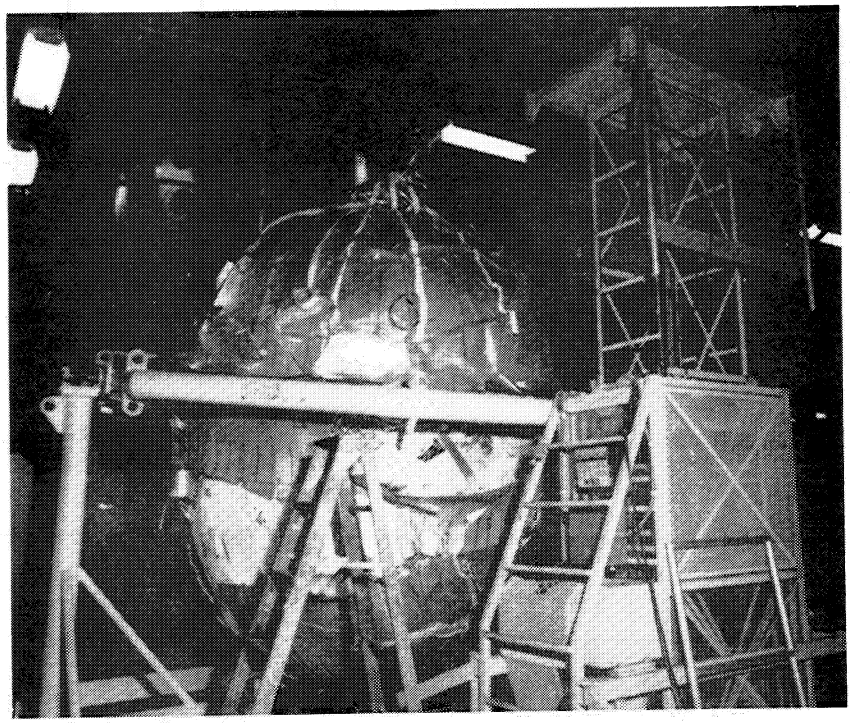

b: VIEW BETWEEN TRUNNIONS 3 AND 4

Figure 5.3-1. LH_2 Test Model After Failure

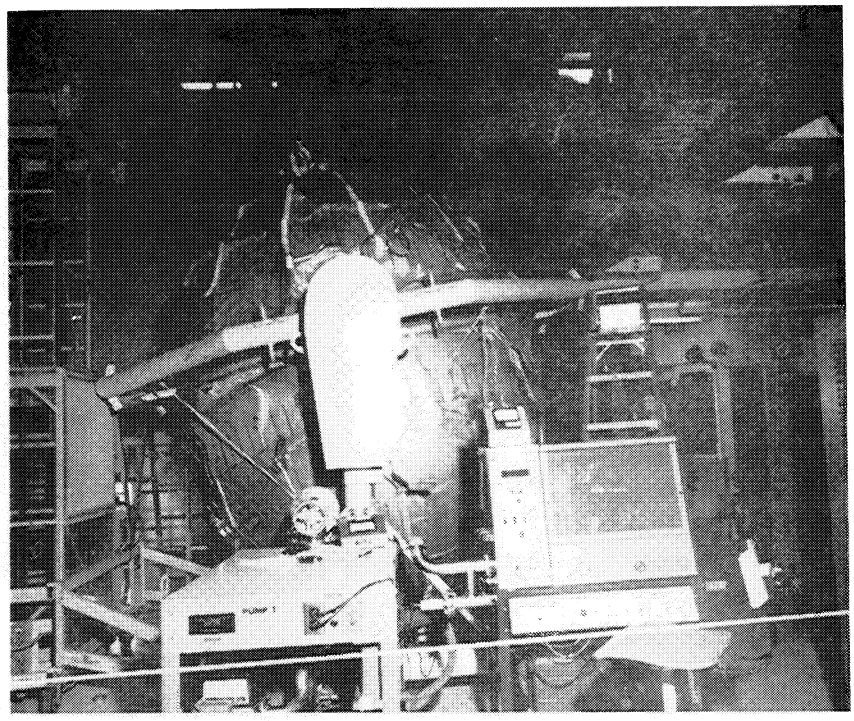

a: VIEW ON TRUNNION 2

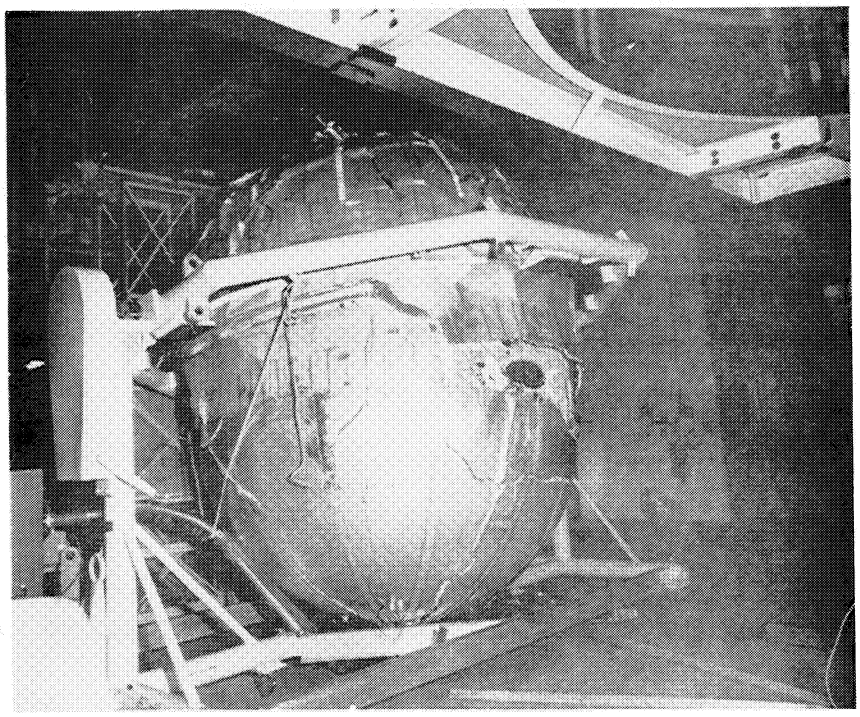

b: VIEW BETWEEN TRUNNION 1 AND 2

Figure 5.3-2. LH_2 Test Model After Failure

5.4 PROBABLE CAUSE OF FAILURE

A review of the test history and visual inspection of the hardware resulted in identifying two probable causes of failure. It appears certain that one or both of these probable causes were instrumental in weakening the vacuum jacket head to the point where the mechanic's hand pressure could trigger the shell buckle.

5.4.1 Adhesive Bond Degradation at Girth Joint

One probable cause was the degradation of the adhesive bond at the girth joint from local high temperature bond cure cycles. Any adhesive bond degradation at the girth joint would reduce the capability of the honeycomb sandwich shell to transfer the compression load and moment into the girth ring which would result in a marginally stable condition.

Table 5.2-1 shows the number of local bond cure cycles that were necessary in order to vacuum seal the bond joint of the upper vacuum jacket head at the girth ring.

The inadvertent use of silicone sealer at the faying edge of the outer face skin to girth ring bonded joint during F/S proof testing forced the silicone into the bonded joint. The silicone prevented sealing vacuum leaks and as a result a large number of local high temperature bond cure cycles were made. The 450°K (350°F) temperature cycles used to locally cure the leak sealing x A3919 adhesive may have resulted in adhesive bond degradation and locked in thermal induced stresses from non-uniform thermal expansion of the builtup thicknesses.

5.4.2 Local Debond of Inner Face Skin

The other probable cause was the possible local debonding of the inner face skin to core adhesive joint. This would reduce the compression capability of the vacuum jacket head.

Several factors suggest the possibility of a local face skin to gore adhesive joint debond which was not critical during the F/S proof test, but which grew to critical size during repeated vacuum pressure cycling. The visual and

coin tap inspection method used during the vacuum jacket head assembly may have missed small local face skin to core unbonded areas. During the F/S proof test, difficulty was encountered in sealing the specimen to cover plate joint area and some water leakage occurred which wetted portions of the inner face skin. Water in contact with the unprotected adhesive edge at the face skin gore joint strips had the potential for causing or adding to initial inner face skin to core debonding. Also, the F/S proof test as conducted was not fully representative of the loading conditions applied to the vacuum jacket head in service. During the F/S proof test, hydrostatic pressure was applied externally to the vacuum jacket which did not put the inner face skin to core bond joint in tension as it was during vacuum loading on the inner face skin. All of which leads to the possibility that small noncritical inner face skin to core debonds grew in size with repeated vacuum pressure cycles until a near-instability condition existed for the vacuum jacket head.

5.5 RECOMMENDATIONS

The failure analysis points to several design and test conditions which should be considered in any future lightweight vacuum jacket designs.

1) If the inner face skin is maintained at the vacuum sealing skin, then the F/S proof test procedures should be revised to include internal vacuum loading on the inner face skin.
2) Consideration should be given to using the outer face skin as the vacuum sealing surface. This would allow venting the inner face skin and core. One difficulty as discussed in Reference 3 is the problem of outgassing the sandwich shell adhesives. Investigation of this approach should center around using the lowest outgassing adhesive that is compatible with the design temperature requirements.
3) Use the F/S test procedure for each vacuum cycle to detect change in stiffness.
4) Develop vacuum leak repair materials and techniques so that local heating of the bonded structure can be eliminated.
5) Consideration should be given in the design of the pressure vessel support system to the possibility of high load unbalance from the vacuum jacket buckling.

6.0 DATA EVALUATION

Program results showed that the technology and materials exist for producing all the key elements in an evacuated MLI system for the OMS fuel tank. Most of the results from the design and analytical studies have been verified by hardware fabrication and testing. Thermal performance and vacuum maintenance of the system were not validated by test. However, in light of preliminary tests, there is no reason to suspect that there will be a major conflict between the predicted system performance and the actual test data. The lack of this substantiating test data, therefore, should not preclude embarking on future evacuated MLI system programs with a high level of confidence.

The key elements in the evacuated MLI system which were subject to analytical and experimental investigation on this program were (1) the vacuum jacket, (2) the MLI, (3) the support straps, and (4) vacuum acquisition.

6.1 VACUUM JACKET

The two vacuum jacket heads were manufactured in sequence on the same layup and bond cure mandrel. Experience in manufacturing the first head resolved most of the fabrication difficulties so that the second vacuum jacket head was much easier to fabricate and after completion was judged to be of better quality than the first. This judgement led to eliminating the F/S proof test for this head and was vindicated during the vacuum acquisition test when it was found that the first vacuum jacket head was difficult to seal whereas the second head had only two minor helium leak areas in the bond joints.

The F/S proof test on the first vacuum jacket head predicted shell buckling failure at or above 172.37 kN/m^3 (25 psi) which verified the analytical predictions of Section 3.3.

The bond repair techniques used to seal vacuum jacket bond joint leaks produced a vacuum tight jacket. The measured leak rate was 1×10^{-5} atmospheric ml of helium per second.

The service life on this lightweight vacuum jacket was of sufficient length to:

1) verify the design,
2) demonstrate a vacuum tight jacket,

3) accumulate 29 pressure cycles,
4) accumulate approximately 1500 hours total at vacuum pressure, and
5) sustain up to 12 hours of localized heating at 450°K (350°F) at ambient pressure.

These results demonstrated that the technology was available to produce a light-weight vacuum jacket design.

6.2 MLI

During installation of the MLI panels on the pressure vessel, some of the nylon fasteners adjacent to the Velcro pads broke from the force necessary to firmly secure the Velcro hook and pile. These fasteners were easily replaced, but the occurence did suggest the necessity of a design change in the MLI panel in this area for any future MLI panel assemblies of this design.

In process inspection of the MLI panel assemblies and installation showed that these panels were easily fabricated, and when installed, held firmly to the pressure vessel with little sagging. The installation gaps between MLI panels were on the order of 1.27 to 2.54 mm (0.05 to 0.10 in.) which was judged as satisfactory to provide the necessary outgassing path for vacuum acquisition with minimum thermal performance degradation to the insulation. The inner MLI panel layer exhibited little wrinkling and appeared quite fluffy after installation. The outer MLI panel layer had more wrinkling and less fluffiness but showed no sign of local excessive composition. Indeed, there was every indication (i.e., the relationship of each outer nylon washer, which was 13.97 mm (0.55 in.) from the inner washer, to the outer radiation shield) that the thickness of the MLI installed was 27.94 mm (1.10 in.) as designed.

The MLI panel installation withstood remarkably well the 29 pressure cycles for ambient to vacuum and the severe abuse received at the time of the LH_2 test model failure. The outer layers of the outer panels were torn and most of the nylon pins broken. The inner panels were mainly intact, with little sign of damage except for broken nylon pins which could be easily replaced.

The results indicate that the LH_2 test model MLI panels will meet the fabrication, installation and durability requirements of the OMS fuel tank. Thermal performance of the MLI was not verified on this program, but the MLI panel elevated temperature tests discussed in Section 4.5.3 indicated no visual degradation of the material due to temperature. These test results and the results from the thermal analyses performed on this program which were based on test results from the literature, give positive indication that the thermal performance requirements of the OMS fuel tank can also be met by LH_2 test model MLI panel design.

6.3 SUPPORT STRAPS

No difficulties were encountered in strap assembly and installation. The failure of one production strap during proof load (see Section 4.7.2) was easily repaired and successfully proof tested.

The support strap arrangement held the LH_2 test model pressure vessel firmly in place at all support stand hexagonal ring positions. However, there does remain a question as to whether the OMS fuel tank might require sway braces at the apex outlet fittings due to its much larger size.

The one remaining uncertainty is the heat flow to the cryogen from the support strap. However, the LH_2 test model heat flow prediction (Section 4.4) shows only 5.3% of the total heat flow to the cryogen is attributed to the support strap.

It seeems evident from these results that the PRD/epoxy support strap would meet the requirements of the OMS fuel tank.

6.4 VACUUM ACQUISITION

There remains some uncertainty since the vacuum acquisition was not completed as to the exact procedures which would minimize the time necessary for vacuum acquisition. Intuitively, however, based on vacuum pressure observation during helium leak checking and repairing, there was no doubt that the vacuum acquisition requirements for the LH_2 test model would be met. From this it can be concluded that the vacuum acquisition requirements of the OMS fuel tank can be met.

7.0 REMAINING UNCERTAINTIES

Additional studies and experimental work remain to be done in order to complete the element qualification testing necessary before committing a sophisticated cryogenic tank system such as the OMS fuel tank to fabrication.

Two remaining uncertainties resulted from the inability to complete the testing originally planned for this program. These are:

1) procedures and time necessary to complete the preconditioning of the vacuum annulus so that the design requirement of maintaining a vacuum level at 26.6 mN/m^2 (2×10^{-4} torr) with a maximum of three 5 L/S D-1 ion pumps would be met, and
2) whether the three 5 L/S D-1 ion pumps would be capable of handling the steady increase in gas load or sudden outbursts of outgassing during vacuum jacket temperature cycling to 450°K (350°F).

Three other remaining uncertainties became evident as the program progressed, but testing for these was beyond the scope of this program. However, before committing the OMS fuel tank to fabrication, additional analytical and experimental studies should be undertaken to investigate:

1) whether additional pressure vessel support in the form of sway braces at the inlet and outlet port would be needed,
2) the effectiveness of the vented double metallic seal arrangement at the manhole cover to meet the H_2 leakage requirements, and
3) the need for safety straps or restraints to prevent a major failure in the event of a head buckling.

8.0 CONCLUSIONS

This investigation verified the feasibility of producing a lightweight vacuum jacket using state-of-the-art technology and materials. The major elements of an evacuated MLI system were optimized for the OMS fuel (LH_2) tank. Performance predictions were made for the half-scale LH_2 test model scaled from the OMS fuel tank.

It was concluded that the service life of future lightweight vacuum jackets would be substantially increased by minor modification to the sandwich design and adhesive bond procedures. These recommended changes were:

1) To vent the inner face skin and core, thereby eliminating the tension load on the inner face skin to core adhesive bond which was suspected of lowering the fatigue life of the vacuum jacket. This change would move the vacuum sealing surface from the inner skin to the outer skin. Also, with this change an investigation would be required to select the lowest outgassing adhesives which would be compatible with the loading, temperature and vacuum requirements of the vacuum jacket under consideration.
2) To incorporate in the adhesive bond procedures the recommendations made as a result of recent Boeing Commercial Airplane Company research on the relationship between surface preparation and adhesive bond joint strength. Essentially, these recommendations call for changes in the chemical cleaning process and for short-elapsed time between the cleaning operation and applying either the primer or the adhesive. Additional research would be required to ensure compatibility between selected high temperature adhesives and between the adhesive and primer selected.

Three conclusions were reached as a result of the vacuum acquisition test.

1) RTV sealing compound should never be used around vacuum structures. This compound absorbed and channelled helium, thereby producing misleading data during helium leak checking.

2) Vacuum leak repair procedures should be developed which would be compatible with the vacuum structure service temperatures, but which would avoid local adhesive curing at elevated tempeatures after the vacuum jacket has been assembled.
3) The vacuum sealing surface should be the outer face skin which would be accessible after vacuum jacket assembly.

The buckling of the upper vacuum jacket head at 101.4 kN/m^2 (14.7 psi) after it was F/S proof tested to 141.37 kN/m^2 (20.5 psi) and the F/S data indicated a critical shell buckling pressure at or above 172.37 kN/m^2 (25 psi) led to the following conclusions.

1) That vacuum pressure should be applied to the inner face skin of the vacuum jacket during the F/S test if the inner skin is the vacuum sealing surface. This would load the sandwich structure exactly as the service loading conditions and probably give some indication of any subcritical local debond areas either during the F/S test or by the visual inspection of the hardware after the test. This test procedure would be more costly than the purely external water pressure test conducted on this program and would be somewhat difficult to achieve.
2) That instrumentation should be maintained after vacuum jacket assembly so that periodic in-service F/S proof tests can be conducted to monitor any vacuum jacket degradation.
3) That cryogenic tank systems using vacuum jackets should consider the high loads induced by the pressure vessel on the support system when a vacuum jacket buckles.

Experience in fabricating the LH_2 test model led to four conclusions:

1) To replace the 0.076 mm (0.003 in.) vacuum sealing strips on the inner surface of the inner skin with the 0.305 mm (0.012 in.) aluminum structural joining strips. This change would prevent the cracking of the gore joints during the first XA 3919 adhesive cure on the inner face skin which occurred on both vacuum jacket heads fabricated for this program.

2) To revise the girth ring design arrangement or the head layup mandrel to eliminate the EA934 room temperature cured bond joint between the inner and outer joining strips and the girth ring.

3) To revise the nylon assembly pin arrangement at the Velcro fastener patches on the MLI panel assemblies to avoid placing the nylon pins under excessive compression during MLI panel installation, and

4) That the MLI panel assembly and installation arrangement used on the LH_2 test model would satisfy the OMS fuel tank requirements, thereby simplifying MLI panel assembly and reducing heat leak through the assembly fasteners.

REFERENCES

1. NASA SP-8057, "Structural Design Criteria Applicable to a Space Shuttle," January, 1971.

2. MSC-06900, "Space Shuttle Baseline Accommodations for Payloads," January, 1972.

3. NASA CR121105, "Lightweight Evacuated Multilayer Insulation Systems for the Space Shuttle Vehicle," Contract NAS 3-14369, D. L. Barclay, J. E. Bell, and D. K. Zimmerman, May, 1973.

4. "Stress, Stability and Vibration of Complex Shells of Revolution," Bushnell, David, Analysis and User's Manual for BOSOR3, SAMSO TR-69-375, Lockheed Missiles and Space Company, September 6, 1969.

5. "Computations on the Stresses of Local Loads in Spherical Pressure Vessels or Pressure Vessel Heads," Bijlaard, P. P., Welding Research Council Bulletin #34, March, 1957.

6. Condensed Catalog, Ultek Vacuum Equipment, 1972.

7. "Kinetic Theory of Gases," McGraw-Hill, New York, 1938.

8. Heat Transmission, McAdams, W. H., 3rd edition, McGraw-Hill, New York, 1954.

9. Applied Cryogenic Engineering, Vance, R. W. and Duke, W. M. (editors), John Wiley & Sons, New York, 1962.

10. "Numerical Solutions for Laminar Flow Heat Transfer in Circular Tubes," Kays, W. M., Transactions of ASME, November, 1965, page 1265.

11. "OPTRAN," Laakso, J. H., Boeing Computer Code, unpublished Boeing document.

NAS3-15848 DISTRIBUTION LIST FOR FINAL REPORT

"LIGHTWEIGHT VACUUM JACKET FOR CRYOGENIC INSULATION", VOL. 1, NASA CR 134759

National Aeronautics & Space Administration
Lewis Research Center
21000 Brookpark Road
Cleveland, Ohio 44135

1	Attn:	Contracting Officer, MS 500-313
5		E. A. Bourke, MS 500-205
1		Technical Utilization Office, MS 3-16
1		Technical Report Control Office, MS 5-5
2		AFSC Liaison Office, MS 501-3
2		Library, MS 60-3
1		Office of Reliability & Quality Assurance, MS 500-211
3		J. R. Barber, Project Manager, MS 500-203

National Aeronautics & Space Administration
Headquarters
Washington, D.C. 20546

	Attn:	Office of Aeronautics & Space Technology
1		Director, Manned Space Technology/RS
1		Director, Space Propulsion & Power/RP
1		Director, Materials & Structures/RW
1		F. W. Stephenson/RPI
	Attn:	Office of Manned Space Flight
1		Director, Advanced Manned Mission/MT
	Attn:	Office of Space Science
1		Director, Physics & Astronomy Programs/SG
1		Director, Planetary Programs/SL
1		Director, Launch Vehicles & Propulsion/SV
	Attn:	Office of Technology Utilization Division
1		Director, Technology Utilization/KT

1	National Aeronautics & Space Administration Ames Research Center Moffett Field, California 94035 Attn: Library
1	National Aeronautics & Space Administration Flight Research Center P.O. Box 273 Edwards, California 93523
	National Aeronautics & Space Administration George C. Marshall Space Flight Center Huntsville, Alabama 35912
1	Attn: Library
1	A. G. Orillion
1	T. W. Barret
1	J. M. Stuckey
1	E. H. Hyde
1	I. G. Yates
1	National Aeronautics & Space Administration Goddard Space Flight Center Greenbelt, Maryland 20771 Attn: Library
	National Aeronautics & Space Administration John F. Kennedy Space Center Cocoa Beach, Florida 32931
1	Attn: Library
1	W. S. Brosier, LL-OPN-2
	National Aeronautics & Space Administration Lyndon B. Johnson Space Center Houston, Texas 77001
1	Attn: Library
1	W. Chandler
	National Aeronautics & Space Administration Langley Research Center Langley Station Hampton, Virginia 23365
1	Attn: Library
1	I.O. MacConoehie, MS411
1	C. D'Aiutolo, MS 249A
10	NASA Scientific & Technical Information Facility P.O. Box 8757 Baltimore/Washington International Airport Baltimore, MD 21240 Attn: NASA Representative

1 Picatinny Arsenal
Dover, New Jersey 07801
Attn: Library

1 U.S. Naval Research Laboratory
Washington, D.C. 20390
Attn: Library

1 U.S. Army Research Office (Durham)
Box CM, Duke Station
Durham, North Carolina 27706
Attn: Library

1 U.S. Army Missile Command
Redstone Scientific Information Center
Redstone Arsenal, Alabama 35808
Attn: Document Section

1 U.S. Naval Missile Center
Point Mugu, California 93041
Attn: Technical Library

1 U.S. Naval Weapons Center
China Lake, California 93557
Attn: Library

1 Aerojet-General Corporation
Electronics Division
P.O. Box 296
Azusa, California 91703
Attn: Library

1 Aerojet-General Corporation
Space Division
9200 East Flair Drive
El Monte, California 91734
Attn: Library

1 Aerojet-General Corporation
Aerojet Ordnance & Manufacturing
11711 South Woodruff Avenue
Fullerton, California 90241
Attn: Library

1 Aerojet Liquid Rocket Company
P.O. Box 15847
Sacramento, California 95813
Attn: Technical Library 2484-2015A

1 Aerospace Corporation
2400 E. El Segundo Blvd.
Los Angeles, California 90045
Attn: Library
V. H. Monteil

1 Garrett Corporation
Airesearch Mfg. Division
9851 Sepulveda Blvd.
Los Angeles, California
Attn: Library

1 Garrett Corporation
Airesearch Mfg. Division
402 South 36th Street
Phoenix, Arizona 85034
Attn: Library

1 Aro Incorporated
Arnold Engineering Development Center
Arnold AF Station, Tennessee 37389
Attn: Library

1 Battelle Memorial Institute
505 King Avenue
Columbus, Ohio 43201
Attn: Library

1 Beech Aircraft Corporation
Boulder Facility
Box 631
Boulder, Colorado

1 Bell Aerosystems Inc.
Box 1
Buffalo, New York 14240
Attn: Library

1 Bendix Corporation
Instruments & Life Support Division
P.O. Box 4508
Davenport, Iowa 52808
Attn: Library

1 Boeing Company
1625 K Street N.W.
Washington, D.C.

1 Office of the Director of Defense
Research & Engineering
Washington, D.C. 20301
Attn: Office of Ass't. Director (Chemical Technology)

Jet Propulsion Laboratory
4800 Oak Grove Drive
Pasadena, California 91103
1 Attn: Library
1 J. Kelly
1 R. Breshears
1 D. Dipprey

1 Defense Documentation Center
Cameron Station
Building 5
5010 Duke Street
Alexandria, Virginis 22314
Attn: TISIA

1 Advanced Research Projects Agency
Washington, D.C. 20525
Attn: Library

1 Aeronautical Systems Division
Air Force Systems Command
Wright-Patterson Air Force Base
Dayton, Ohio
Attn: Library

1 Air Force Missile Test Center
Patrick Air Force Base
Florida
Attn: Library

1 Air Force Systems Command
Andrews Air Force Base
Washington, D.C. 20332
Attn: Library

Air Force Rocket Propulsion Laboratory (RPR)
Edwards, California 93523
1 Attn: Library
1 R. L. Wiswell, LKDS
1 D. A. Hart

1 Air Force Rocket Propulsion Laboratory (RPM)
Edwards, California 93523
Attn: Library

1 Air Force FTC (FTAT-2)
Edwards Air Force Base
California 93523
Attn: Library

Air Force Office of Scientific Research
Washington, D.C. 20333
Attn: Library

1 U.S. Air Force
Washington, D.C.
Attn: Library

1 Air Force Aero Propulsion Laboratory
Research & Technology Division
Air Force Systems Command
U.S. Air Force
Wright-Patterson AFB, Ohio 45433
Attn: Library (APRP)

1 Arnold Engineering Development Center
Air Force Systems Command
Tullahoma, Tennessee
Attn: Library

Space & Missile Systems Organization
Air Force Unit Post Office
Los Angeles, California 90045
1 Attn: Library (Technical Data Center)

1 Office of Research Analyses (OAR)
Holloman Air Force Base
New Mexico 88330
Attn: Library (RRRD)

1 RTD (RTNP)
Bolling Air Force Base
Washington, D.C. 20332

1 Bureau of Naval Weapons
Department of the Navy
Washington, D.C.
Attn: Library

1 Naval Research Branch Office
1030 E. Green Street
Pasadena, California 91101
Attn: Library

1 Boeing Company
P.O. Box 1680
Huntsville, Alabama 35801

1 Chemical Propulsion Information Agency
Applied Physics Laboratory
8621 Georgia Avenue
Silver Spring, Maryland 20910

1 Chrysler Corporation
Missile Division
P.O. Box 2628
Detroit, Michigan
Attn: Library

1 Chrysler Corporation
Space Division
P.O. Box 29200
New Orleans, Louisiana 70129
Attn: Library

1 Curtiss-Wright Corporation
Wright Aeronautical Division
Woodridge, New Jersey
Attn: Library

1 Denver Research Institute
University of Denver
P.O. Box 10127
Denver, Colorado 80210
Attn: Security Office

1 Fairchild Stratos Corporation
Aircraft Missile Division
Hagerstown, Maryland
Attn: Library

1 Fairchild Hiller Corporation
Research Center
Germantown, Maryland
Attn: Library

1 Fairchild Hiller Corporation
Republic Aviation
Farmington, L. I., N.Y.

General Dynamics/Convair
P.O. Box 1128
San Diego, California 92112
1 Attn; Library
1 R. Tatro

1 General Electric Company
Missiles & Space Systems Center
Valley Forge Space Technology Center
P. O. Box 8555
Philadelphia, Pennsylvania 19101
Attn: Library

1 General Electric Company
Apollo Support Department
P. O. Box 2500
Daytona Beach, Florida 32015
Attn: C. Bay

1 Grumman Aircraft Engineering Corporation
Bethpage, L. I. N.Y.
Attn: Library

1 Hamilton Standard Corporation
Windsor Locks, Conn. 06096
Attn: Library

1 Hercules Powder Company
Allegheny Ballistics Lab
P. O. Box 210
Cumberland, Maryland 21501
Attn: Library

1 Honeywell Inc.
Aerospace Division
2600 Ridgeway Road
Minneapolis, Minnesota
Attn: Library

1 IIT Research Institute
Technology Center
Chicago, Illinois 60616
Attn: Library

1 International Nickel Company
One New York Plaza
New York, N. Y. 10004
Attn: C. B. Sanborn

1 Kidde Aerospace Division
Walter Kidde & Company
567 Main Street
Belleville, New Jersey 07109
Attn: Library

1 Linde, Division of Union Carbide
P. O. Box 44
Tonawanda, N.Y. 11450
Attn: G. Nies

1 Ling-Temco-Vought Corporation
P. O. Box 5907
Dallas, Texas 75222
Attn: Library

Lockheed Missiles & Space Company
P. O. Box 504
Sunnyvale, California 94087
1 Attn: Library
1 R. T. Parmley

1 Lockheed Propulsion Company
P. O. Box 111
Redlands, California 92374
Attn: Library

1 Marquardt Corporation
16555 Saticoy Street
Box 2013 South Annex
Van Nuys, California 91409
Attn: Library

1 Minnesota Mining & Manufacturing Company
900 Bush Avenue
St. Paul, Minnesota 55106
Attn: Library

Martin-Marietta Corporation
P. O. Box 179
Denver, Colorado 80201
1 Attn: Library
1 G. C. Skartvedt

1 Martin-Marietta Corporation
Box 5827
Orlando, Florida
Attn: Library

1 McDonnell Douglas Astronautics
5301 Bosa Avenue
Huntington Beach, California 92647
1 Attn: Library
1 L. Q. Westmoreland
1 P. Klevatt

McDonnell Douglas Aircraft Corporation
P. O. Box 516
Lambert Field, Missouri 63166
1 Attn: Library
1 L. F. Kohrs

1 Northrop Space Laboratories
3401 West Broadway
Hawthorne, California
Attn: Library

1 Philco-Ford Corporation
Aeronutronic Division
Ford Road
Newport Beach, California 92663
Attn: Library

1 Purdue University
Lafayette, Indiana 47907
Attn: Library

1 Radio Corporation of America
Astro-Electronics Products
Princeton, New Jersey
Attn: Library

1 Rocketdyne
A Division of Rockwell International
6633 Canoga Avenue
Canoga Park, California 91304
Attn: Library

1 Space Division
A Division of Rockwell International
12214 Lakewood Blvd
Downey, California
Attn: Library

1 Rocket Research Corporation
Willow Road At 116th Street
Redmond, Washington 98052
Attn: Library

1 Stanford Research Institute
333 Ravenswood Avenue
Menlo Park, California 94025
Attn: Library

1 Susquehanna Corporation
Atlantic Research Division
Shirley Highway & Edsall Road
Alexandria, Virginia 22314
Attn: Library

1 Thiokol Chemical Corporation
Redstone Division
Huntsville, Alabama
Attn: Library

TRW Systems Inc.
1 Space Park
Redondo Beach, California 90278
1 Attn: Library
1 A. H. Zimmerman

1 TRW
TAPCO Division
23555 Euclid Avenue
Cleveland, Ohio 44117
Attn: Library

1 United Aircraft Corporation
Corporation Library
400 Main Street
East Hartford, Connecticut 06108

1 United Aircraft Corporation
United Technology Center
P. O. Box 358
Sunnyvale, California 94038
Attn: Library

United Aircraft Corporation
Pratt & Whitney Division
Florida Research & Development Center
P. O. Box 2691
West Palm Beach, Florida 33402
1 Attn: Library
1 G. B. Cox

1 Vickers Incorporated
Box 302
Troy, Michigan
Attn: Library

1 Vought Astronautics
Box 5907
Dallas, Texas
Attn: Library